International Journal of Photoenergy

Nano/Molecular Photosciences and Clean Energy

Guest Editors: Mohamed Sabry Abdel-Mottaleb and Jean-Marie Herrmann

Nano/Molecular Photosciences and Clean Energy

International Journal of Photoenergy

Nano/Molecular Photosciences and Clean Energy

Guest Editors: Mohamed Sabry Abdel-Mottaleb and Jean-Marie Herrmann

Contents

Nano/Molecular Photosciences and Clean Energy, Mohamed Sabry Abdel-Mottaleb and Jean-Marie Herrmann
Volume 2008, Article ID 734364, 1 page

Versatile Bottom-Up Approach to Nanostructured Functional Materials for Optoelectronic Applications, Giorgio Macchi, Francesco Meinardi, Patrizia Valsesia, and Riccardo Tubino
Volume 2008, Article ID 784691, 4 pages

Diffusion Enhanced Upconversion in Organic Systems, A. Monguzzi, R. Tubino, and F. Meinardi
Volume 2008, Article ID 684196, 5 pages

One Dimensional Polymeric Organic Photonic Crystals for DFB Lasers, F. Scotognella, A. Monguzzi, M. Cucini, F. Meinardi, D. Comoretto, and R. Tubino
Volume 2008, Article ID 389034, 4 pages

Photocatalytic Degradation of a Water Soluble Herbicide by Pure and Noble Metal Deposited TiO2 Nanocrystalline Films, Katerina Pelentridou, Elias Stathatos, Helen Karasali, Dionysios D. Dionysiou, and Panagiotis Lianos
Volume 2008, Article ID 978329, 7 pages

Microstructured Reactors Designed by Stereolithography and Characterized by Fluorescent Probes, S. Corbel, F. Evenou, F. Baros, N. Martinet, M. Donner, and M. C. Carré
Volume 2008, Article ID 757510, 7 pages

Analysis of Surface Texturization of Solar Cells by Molecular Dynamics Simulations, Hsiao-Yen Chung, Chiun-Hsun Chen, and Hsin-Sen Chu
Volume 2008, Article ID 540971, 5 pages

Analysis of Pyramidal Surface Texturization of Silicon Solar Cells by Molecular Dynamics Simulations, Hsiao-Yen Chung, Chiun-Hsun Chen, and Hsin-Sen Chu
Volume 2008, Article ID 282791, 6 pages

Sunlight-Initiated Photochemistry: Excited Vibrational States of Atmospheric Chromophores, Veronica Vaida, Karl J. Feierabend, Nabilah Rontu, and Kaito Takahashi
Volume 2008, Article ID 138091, 13 pages

Photochemistry Aspects of the Laser Pyrolysis Addressing the Preparation of Oxide Semiconductor Photocatalysts, R. Alexandrescu, I. Morjan, F. Dumitrache, M. Scarisoreanu, I. Soare, C. Fleaca, R. Birjega, E. Popovici, L. Gavrila, G. Prodan, V. Ciupina, G. Filoti, V. Kuncser, and L. Vekas
Volume 2008, Article ID 604181, 11 pages

Electro-Optical and Electrochemical Properties of a Conjugated Polymer Prepared by the Cyclopolymerization of Diethyl Dipropargylmalonate, Yeong-Soon Gal, Won-Chul Lee, Won Seok Lyoo, Sung-Ho Jin, Kwon Taek Lim, Young-Il Park, and Jong-Wook Park
Volume 2008, Article ID 276027, 5 pages

Two-Dimensional Free Energy Surfaces for Electron Transfer Reactions in Solution, Shigeo Murata, Maged El-Kemary, and M. Tachiya
Volume 2008, Article ID 150682, 8 pages

Electrochemiluminescence Study of Europium (III) Complex with Coumarin3-Carboxylic Acid,
Stefan Lis, Krzysztof Staninski, and Tomasz Grzyb
Volume 2008, Article ID 131702, 6 pages

Hindawi Publishing Corporation
International Journal of Photoenergy
Volume 2008, Article ID 734364, 1 page
doi:10.1155/2008/734364

Editorial
Nano/Molecular Photosciences and Clean Energy

Mohamed Sabry Abdel-Mottaleb[1] and Jean-Marie Herrmann[2]

[1] *Department of Chemistry, Faculty of Science, Ain Shams University, Abbassia, Cairo 11566, Egypt*
[2] *IRCELYON, CNRS-Université Lyon-1, 69 626 Villeurbanne, France*

Correspondence should be addressed to Mohamed Sabry Abdel-Mottaleb, phochem08@photoenergy.org

Received 25 December 2008; Accepted 25 December 2008

This special issue on "nano/molecular photosciences and clean energy" is composed of selected, full-length versions of papers presented at the International Conference on Nano/Molecular Photochemistry, Photocatalysis and Solar Energy Conversion (Solar '08). The highly successful solar conference series, started in 1991, provide a place where researchers interested in fundamental and applied aspects of photochemistry can meet and inspire one another. The solar conference recognizes that successful photochemical applications go hand in hand with advancement of fundamental understanding of photoinduced processes and excited states.

This conference was held in Cairo, Egypt, during the period 24–28 February, 2008. It was aimed at discussing in an interdisciplinary sense the newest trends, break-through, discoveries, and applications in photochemistry, photocatalysis, solar energy conversion, environmental aspects, and related nanoscience and nanotechnology.

This conference, as the previous ones, enjoyed high esteem, due to high scientific level and excellent organizational features. There were more than 200 participants from 36 countries world-wide: Algeria, Australia, Canada, China, Czech Republic, Egypt, France, Georgia, Germany, Greece, Hungary, India, Iran, Ireland, Italy, Japan, Kenya, Korea, Libya, Lithuania, Malaysia, Norway, Poland, Portugal, Romania, Russia, Saudi Arabia, Singapore, South Africa, Spain, Sweden, Switzerland, Taiwan, the Netherlands, UK, and USA. The conference was not the "monolith" on narrow subject matter. Rather the other way round: there was a great diversity of topics: organic and inorganic chemistry, basic science, R&D, and industrial topics. The main motif was to demonstrate the use of light energy, especially sunlight, in a variety of topics dedicated to sustainable energy sources, as inorganic and organic photovoltaics, photodegradation of pollutants, air cleaning in hospitals, photocatalysis, water cleaning, and bacteria deactivation by singlet oxygen generation. Other topics were associated with fluorescence phenomena, photonic crystals, inorganic nanomaterials for photovoltaics, in particular morphologically different forms of titania, zinc oxide, highly luminescent inorganic and organic nanoparticles, photochemical water splitting, OLEDs, and charge-transfer phenomena. Great attention was dedicated to inorganic nano-materials for environmental protection. There is no doubt that global pollution is a real mess very difficult to deal with everywhere, even in developed countries. Thus, alternative ways to harvest and harness the sunlight into purification of air and portable water are essential for humanity in overcrowded world. Many poster contributions were dedicated to this important topic. The main focus was on titania and titania doped with a variety of other inorganic oxides to enhance its photodegradation power. Several tens of papers dealt with this topic. Several poster contributions were dedicated to spirocompounds and their photochromic properties. Remarkable contribution (again several tens of contributions) were dedicated to solar energy conversion using organic, inorganic, and hybrid photovoltaic materials.

The focus of this conference series is of great importance to the current global energy security situation. A coordinated action on a global level is urgently needed to avert the crisis. The developing world must take an active role in any such coordinated action. Thus, the location of this conference is chosen to engage the scientists and decision makers in the developing world into this action plan. It will be interesting to see how the field has further developed at Solar '10 in 2010.

Mohamed Sabry Abdel-Mottaleb
Jean-Marie Herrmann

Hindawi Publishing Corporation
International Journal of Photoenergy
Volume 2008, Article ID 784691, 4 pages
doi:10.1155/2008/784691

Research Article

Versatile Bottom-Up Approach to Nanostructured Functional Materials for Optoelectronic Applications

Giorgio Macchi,[1,2] Francesco Meinardi,[1,2] Patrizia Valsesia,[1,3] and Riccardo Tubino[1,2]

[1] *Dipartimento di Scienza dei Materiali, Università di Milano Bicocca, via R.Cozzi 53, 20125 Milano, Italy*
[2] *Istituto Nazionale per la Fisica della Materia, Italy*
[3] *Consorzio Interuniversitario per la Scienza e Tecnologia dei Materiali, Italy*

Correspondence should be addressed to Giorgio Macchi, giorgio.macchi@mater.unimib.it

Received 28 March 2008; Accepted 8 May 2008

Recommended by Mohamed Sabry Abdel-Mottaleb

A versatile strategy to load ordered mesoporous silica-based materials with functional molecular building blocks in order to obtain host-guest systems exhibiting specific functions is described. Optical microscope examination of the obtained material confirms that the addition of a chromophoric moiety to the reaction mixture is not detrimental in achieving the desired macroscopic morphology of the silica particles. A micro-photoluminescence investigation of the obtained material gave strong evidence that both surfactant micelles and the porous oxide matrix preserve the spectral features of the included molecular species in a nonconventional chemical environment.

1. INTRODUCTION

Since the discovery of conducting polymers, much effort has been put into the development of polymer-based optoelectronic devices (OEDs) [1–3]. Organic polymers are ideal low-cost and high-versatility materials for the rapidly evolving markets of plastic-based information and energy technologies [4, 5]. Nevertheless, there are still problems associated with the application of organic materials in OEDs (e.g., aggregation-induced emission quenching, low quantum yield [6]). The idea described in this paper aims at overcoming some of these problems by developing photoresponsive organic/inorganic hybrid systems obtained by hierarchical organization of functional organic molecules in arrays of nanostructured host-guest compounds. Hybrid materials provide advantages which cannot be achieved with the single components. For example, the design of hybrid solar cells offers both, efficient light absorption of organic materials and efficient conversion of light to electric energy in inorganic materials [5, 7].

In recent years, among the great variety of porous hosts, both inorganic and organic [8–10], the synthesis of ordered mesoporous inorganic-based materials [11, 12], especially MCM-41, by employing supramolecular assembly of surfactant to template the reaction of inorganic species has been the subject of considerable research, due to their large surface area (1000 m^2/g) and storage capacity for applications in catalysis, gas, and vapours adsorption, drug delivery, molecular confinement, flow cytometry, and skincare products [13–20]. Such mesostructurally ordered porous materials have been produced in the form of micrometric powders [21], thin films [22], and bulk monoliths [23]. The key idea underlying the present paper is the addition of functional molecular building blocks to the reaction mixture, in order to obtain a host-guest material exhibiting specific functions. This bottom-up approach will lead to many advantages: (i) the oxide matrix effectively shields the guest species form environmental moisture and chemical impurities (solvents, oxygen); (ii) the proper choice of the molecular components and host geometrical constraints produces a precise control of the supramolecular organization of the inserted molecules, thus tailoring the properties of the resulting system by preventing aggregation processes even at high concentration; (iii) the obtained nanostructured material should maintain the desired macroscopic morphology.

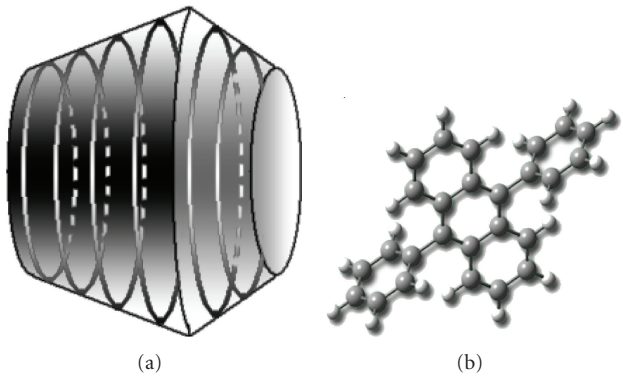

Figure 1: (a) Sketch of a silica particle with the expected *gyroidal* morphology, showing the arrangement of surfactant micelles. (b) Molecular structure of DPA.

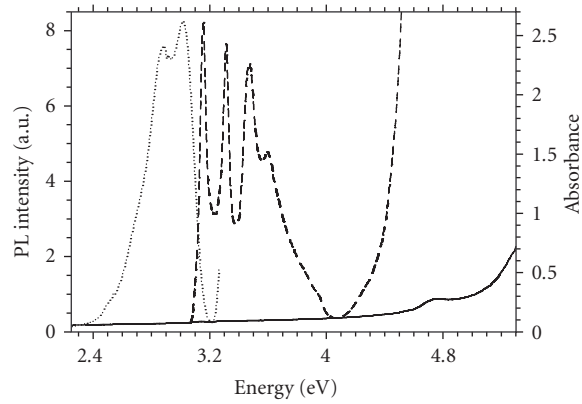

Figure 2: Comparison between optical absorption measurements of an aqueous solution of DPA alone (solid line) and after addition of a sample amount of CTACl (dashed line), along with PL spectrum of the resulting system (dotted line) excited at 3.15 eV.

The results that we will describe in this paper would open up the way to the preparation of active materials in various applications, such as optoelectronic devices and luminescent probes.

2. EXPERIMENTAL

2.1. Synthesis of dye-loaded silica particles

Silica-based organic-inorganic hybrid systems are obtained by a templating process: MCM-like materials were synthesized following the synthetic route described in [24]. The surfactant used was cetyltrimethylammonium chloride (CTACl, 98%, Fluka Co., *Buchs, Switzerland*). Tetraethyl orthosilicate (TEOS, >99%, from Fluka Co., *Buchs, Switzerland*) was the silica precursor. Oxide growth takes place in acidic conditions, and hydrochloric acid (HCl) was consequently used. In order to prepare micrometer-sized *gyroidal* particles [21] (see Figure 1(a)), the following molar ratio was used: 100:4:0.11:0.13 H_2O/HCl/CTACl/TEOS.

Accordingly to the literature [25], the length of CTACl alkane chains determines both micelle diameter and the pore size of the obtained material, which is of about 3.5 nm. Under quiescent condition, cylindrical micelles arrange themselves into gyroidal shapes containing concentric channels coiling around the main axis (see Figure 1(a)).

In a typical synthesis, 355 mg of CTACl were mixed in 15.52 mL of deionized water in a polypropylene bottle. The solution was kept under mild stirring at room temperature (RT) and 3.29 mL of HCl (37%W, Fluka Co., *Buchs, Switzerland*) was added dropwise as well as 0.29 mL of TEOS. 2.06 mg of diphenylanthracene (DPA, ≥98.0%, Fluka Co., *Buchs, Switzerland,* see Figure 1(b)) was finally mixed to the mixture. After a few minutes of mild stirring, the polypropylene flask was closed and kept at RT for 3 hours. The obtained suspension was centrifugated 5000 rpm for 5 minutes, the supernatant removed, and the resulting white powder was extensively washed with 10 mL of deionized water and dried in air. The white powder was then placed between a microscope slide and the cover glass for optical data acquisition. A test solution of DPA in deionized water (DPA-W) with different concentration of CTACl was prepared in order to check DPA solubility dependence on the hydrophobicity of the solvent.

2.2. Optical data acquisition

Optical absorption and photoluminescence (PL) spectra on aqueous solutions were recorder using a Varian Cary 50 Scan UV-visible spectrophotometer (bandwidth 1 nm) and a Varian Cary Eclipse spectrofluorimeter (bandwidth 1 nm), respectively.

Reflected-light microimages were acquired using a doubled Nd:YAG laser (532 nm) as light source, coupled via single-mode optical fiber to an 80i Nikon confocal microscope, and a 100X oil-immersion objective (1.3 NA) to collect the light from sample. The signal is then amplified with a photomultiplier and a software-based scanning system reconstructs the overall image. Micro-PL spectra of silica particles were obtained with the same setup, using a filtered (3.26–3.76 eV bandpass) high-pressure Hg lamp as excitation source and by coupling the microscope to a N_2-cooled CCD camera through a 190 nm polychromator via a multimodal optical fiber.

3. RESULTS AND DISCUSSION

In order to test our approach, we test DPA as a suitable molecule for the inclusion in the silica matrix by means of spectroscopic investigation of its optical features in different environments.

In Figure 2, optical absorption spectrum of a DPA-water mixture (solid line) is reported, showing no significant bands or peaks in the range 3.0–4.0 eV.

With DPA being water-insoluble, aggregates are probably formed and precipitation consequently takes place. Upon addition of surfactant (CTACl), a well-resolved vibronic progression becomes evident (see Figure 2, dashed line), with the 0–0 purely electronic transition centered at 3.15 eV. Both the shape and position of the spectrum are known in

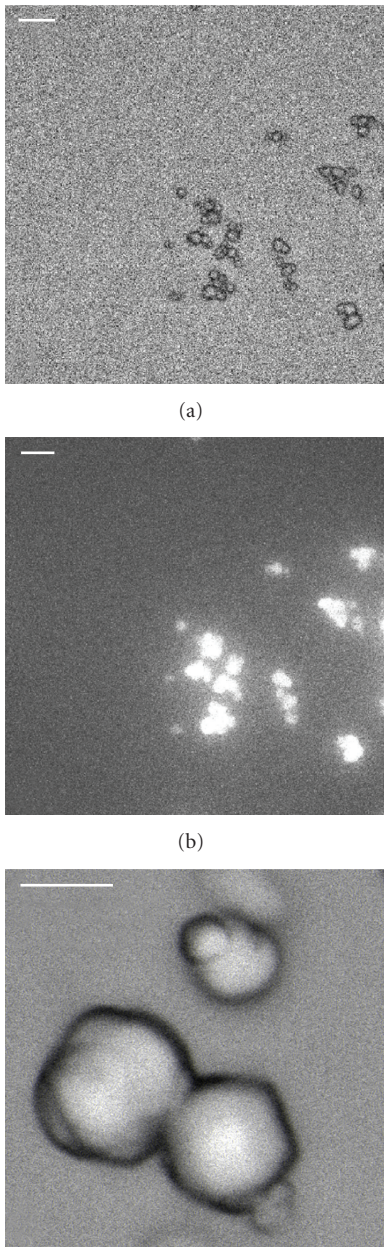

(a)

(b)

(c)

Figure 3: Microscope images of MCM-DPA sample, (a) and (b) reflected and emitted light, respectively, from silica particles on glass substrate and (c) software-assisted zoom, showing silica powder morphology (scale bars 10 μm).

literature to be fingerprint of isolated molecule behaviour [26]. PL spectrum of the DPA-water-CTACl ternary mixture is plotted in Figure 2 (dotted line), with the maximum at 2.85 eV, accordingly to the reported emission of isolated DPA in dilute solution [26]. These findings suggest that the interior of micelles formed in the water-surfactant system is able to host DPA molecules, preventing aggregation process. Moreover, following the key idea described in Section 1, silica growth should take place around such all-organic host-guest systems.

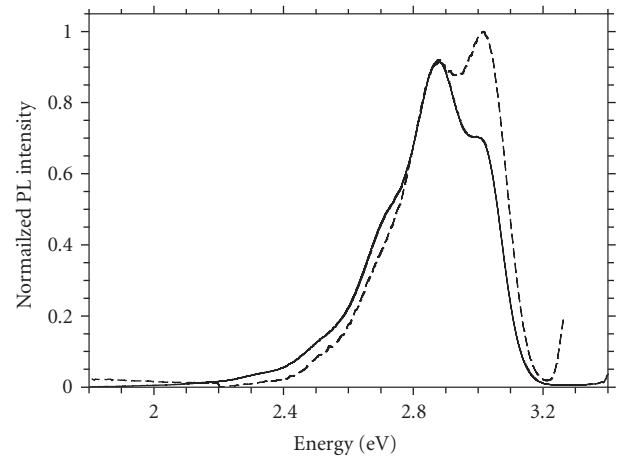

Figure 4: PL spectra of MCM-DPA sample (solid line) and DPA-water-CTACl ternary system (dashed line), excited with Hg lamp in the range 3.26–3.76 eV and with Xe lamp at 3.15 eV, respectively.

Figure 3 reports microscope images of the sample prepared (MCM-DPA) accordingly to procedure described in Section 2.1. In Figure 3(a), a layer of silica particles dried in air shows quite good homogeneity both in shapes and in dimensions. Figure 3(b) reports the same portion of the material under UV light, showing that emitted light is coming entirely from the silica beads. Figure 3(c) depicts a magnification of single silica particles: *gyroidal* shape confirms (see Figure 1(a) as reference) that the synthesis took place as expected and that the insertion of the chromophore does not affect the macroscopic morphology of the sample.

Micro-PL investigation of the particles in Figure 3(c) let us to inspect the emissive properties of the nanostructured material. The obtained PL spectrum is reported in Figure 4 (solid line) compared to emission spectrum of DPA-water-CTACl ternary system described above (dashed line). MCM-DPA emission shows a structured, quite resolved band spanning from 2.0 to 3.2 eV, with a maximum centered at 2.88 eV. The vibronic progression underlying this PL band is quite easily recognizable, with the purely electronic transition at about 3.0 eV and 0–1, 0–2, and 0–3 replica at 2.7, 2.5, and 2.3 eV, respectively.

The main difference between the two spectra reported in Figure 4 concerns the intensity of the 0–0 purely electronic transitions, being the shoulder in MCM-DPA spectrum about 70% of the corresponding peak in DPA-water-CTACl system emission. This is probably due to self-absorption phenomena, which is an evidence for the high concentration of the chromophore achievable within the silica microparticles.

4. CONCLUSIONS

In summary, an effective procedure to obtain hierarchically-organized nanostructured systems has been tested and described. The material prepared maintains the desired spectral features as well as the expected macroscopic morphology. A ~30% of self-absorption observed in the silica microparticles emission spectrum demonstrates that a high

concentration of the loaded chromophore can be achieved, producing very bright luminescent material by preventing aggregation processes (which are known to quench PL) that usually take place in more conventional systems.

These results therefore appear to be very promising for the inclusion of functional molecular and supramolecular units in inorganic host matrices as active materials in various applications, such as optoelectronic devices, luminescent probes, and hybrid solar cells.

ACKNOWLEDGMENTS

This work was supported by the European Commission through the Human Potential Programme (Marie-Curie RTN NANOMATCH, Grant no. MRTN-CT-2006-035884). R.Tubino thanks Fondazione Cariplo and FIRB Synergy for the financial support. P.Valsesia also thanks FIRB Idee Progettuali.

REFERENCES

[1] M. D. McGehee and A. J. Heeger, "Semiconducting (conjugated) polymers as materials for solid-state lasers," *Advanced Materials*, vol. 12, no. 22, pp. 1655–1668, 2000.

[2] Z. Bao, "Materials and fabrication needs for low-cost organic transistor circuits," *Advanced Materials*, vol. 12, no. 3, pp. 227–230, 2000.

[3] R. H. Friend, R. W. Gymer, A. B. Holmes, et al., "Electroluminescence in conjugated polymers," *Nature*, vol. 397, no. 6715, pp. 121–128, 1999.

[4] T. W. Kelley, P. F. Baude, C. Gerlach, et al., "Recent progress in organic electronics: materials, devices, and processes," *Chemistry of Materials*, vol. 16, no. 23, pp. 4413–4422, 2004.

[5] S. E. Shaheen, C. J. Brabec, N. S. Sariciftci, F. Padinger, T. Fromherz, and J. C. Hummelen, "2.5% efficient organic plastic solar cells," *Applied Physics Letters*, vol. 78, no. 6, pp. 841–843, 2001.

[6] D. Oelkrug, A. Tompert, J. Gierschner, et al., "Tuning of fluorescence in films and nanoparticles of oligophenylenevinylenes," *Journal of Physical Chemistry B*, vol. 102, no. 11, pp. 1902–1907, 1998.

[7] W. U. Huynh, J. J. Dittmer, and A. P. Alivisatos, "Hybrid nanorod-polymer solar cells," *Science*, vol. 295, no. 5564, pp. 2425–2427, 2002.

[8] G. Calzaferri, H. Maas, M. Pauchard, M. Pfenniger, S. Megelski, and A. Devaux, "Supramolecularly organized luminescent dye molecules in the channels of zeolite L," in *Advances in Photochemistry, Vol. 27*, pp. 1–50, John Wiley & Sons, New York, NY, USA, 2002.

[9] G. Bongiovanni, C. Botta, G. Di Silvestro, M. A. Loi, A. Mura, and R. Tubino, "Energy transfer in nanostructured oligothiophene inclusion compounds," *Chemical Physics Letters*, vol. 345, no. 5-6, pp. 386–394, 2001.

[10] B. D. Wagner, "Recent applications of host-guest inclusion in fluorescence-based trace analysis," *Current Analytical Chemistry*, vol. 3, no. 3, pp. 183–195, 2007.

[11] A. Corma, "From microporous to mesoporous molecular sieve materials and their use in catalysis," *Chemical Reviews*, vol. 97, no. 6, pp. 2373–2420, 1997.

[12] Q. Huo, D. I. Margolese, U. Ciesla, et al., "Organization of organic molecules with inorganic molecular species into nanocomposite biphase arrays," *Chemistry of Materials*, vol. 6, no. 8, pp. 1176–1191, 1994.

[13] D. E. De Vos, M. Dams, B. F. Sels, and P. A. Jacobs, "Ordered mesoporous and microporous molecular sieves functionalized with transition metal complexes as catalysts for selective organic transformations," *Chemical Reviews*, vol. 102, no. 10, pp. 3615–3640, 2002.

[14] H. Yoshitake, T. Yokoi, and T. Tatsumi, "Adsorption of chromate and arsenate by amino-functionalized MCM-41 and SBA-1," *Chemistry of Materials*, vol. 14, no. 11, pp. 4603–4610, 2002.

[15] M. Vallet-Regí, A. Rámila, R. P. del Real, and J. Pérez-Pariente, "A new property of MCM-41: drug delivery system," *Chemistry of Materials*, vol. 13, no. 2, pp. 308–311, 2001.

[16] P. Sozzani, S. Bracco, A. Comotti, et al., "Complete shape retention in the transformation of silica to polymer microobjects," *Nature Materials*, vol. 5, no. 7, pp. 545–551, 2006.

[17] M. Wark, Y. Rohlfing, Y. Altindag, and H. Wellmann, "Optical gas sensing by semiconductor nanoparticles or organic dye molecules hosted in the pores of mesoporous siliceous MCM-41," *Physical Chemistry Chemical Physics*, vol. 5, no. 23, pp. 5188–5194, 2003.

[18] B. J. Scott, G. Wirnsberger, and G. D. Stucky, "Mesoporous and mesostructured materials for optical applications," *Chemistry of Materials*, vol. 13, no. 10, pp. 3140–3150, 2001.

[19] M. Choi, F. Kleitz, D. Liu, H. Y. Lee, W.-S. Ahn, and R. Ryoo, "Controlled polymerization in mesoporous silica toward the design of organic-inorganic composite nanoporous materials," *Journal of the American Chemical Society*, vol. 127, no. 6, pp. 1924–1932, 2005.

[20] S. Iyer, Y. Kievsky, and I. Sokolov, "Fluorescent silica colloids for study and visualization of skin care products," *Skin Research & Technology*, vol. 13, no. 3, pp. 317–322, 2007.

[21] H. Yang, N. Coombs, and G. A. Ozin, "Morphogenesis of shapes and surface patterns in mesoporous silica," *Nature*, vol. 386, no. 6626, pp. 692–695, 1997.

[22] L. Huang, S. Kawi, K. Hidajat, and S. C. Ng, "Formation of mesoporous silica thin films on oxide substrates by casting," *Microporous and Mesoporous Materials*, vol. 88, no. 1–3, pp. 254–265, 2006.

[23] N. A. Melosh, P. Davidson, and B. F. Chmelka, "Monolithic mesophase silica with large ordering domains," *Journal of the American Chemical Society*, vol. 122, no. 5, pp. 823–829, 2000.

[24] T. Itoh, K. Yano, Y. Inada, and Y. Fukushima, "Photostabilized chlorophyll *a* in mesoporous silica: adsorption properties and photoreduction activity of chlorophyll *a*," *Journal of the American Chemical Society*, vol. 124, no. 45, pp. 13437–13441, 2002.

[25] I. Sokolov, Y. Y. Kievsky, and J. M. Kaszpurenko, "Self-assembly of ultrabright fluorescent silica particles," *Small*, vol. 3, no. 3, pp. 419–423, 2007.

[26] Y. Hirshberg, "The absorption spectra of phenylated anthracenes," *Transactions of the Faraday Society*, vol. 44, pp. 285–289, 1948.

Hindawi Publishing Corporation
International Journal of Photoenergy
Volume 2008, Article ID 684196, 5 pages
doi:10.1155/2008/684196

Research Article

Diffusion Enhanced Upconversion in Organic Systems

A. Monguzzi, R. Tubino, and F. Meinardi

Department of Material Science, University of Milano-Bicocca, via Cozzi 53, 20125 Milano, Italy

Correspondence should be addressed to A. Monguzzi, angelo.monguzzi@mater.unimib.it

Received 29 March 2008; Accepted 5 May 2008

Recommended by Mohamed Sabry Abdel-Mottaleb

The upconverted fluorescence generation in a solution of multicomponent organic systems has been studied as a function of the temperature to investigate the role of resonant energy transfer processes and of the molecular diffusion on the overall emission yield. The strong blue emission observed exciting the samples at 532 nm derives from a bimolecular triplet-triplet annihilation between 9,10 diphenylanthracene molecules, which produces singlet excited states from which the higher energy emission takes place. Diphenylanthracene excited triplet states are populated by energy transfer from a phosphorescent donor (Pt(II)octaethylporphyrin) which acts as excitation light harvesting. At low temperature, the experimental data on the efficiency of the transfer have been interpreted in the frame of a Dexter energy transfer in the Perrin approximation. At room temperature, the fast diffusion of the molecules has been found to be the main factor which affects the energy transfer rates and the overall photon upconversion efficiency.

1. INTRODUCTION

The well-known upconversion processes such as second-harmonic generation or two-photon absorption usually require very high excitation power densities [1], typically of the order of MW/cm^2, being effective only by using laser sources. Recently, a novel approach has been proposed based on the exciton triplet-triplet annihilation (TTA) between organic molecules, which gives rise to an upconverted fluorescence indirectly excited via energy transfer (ET) from a second molecular species acting as a light harvesting [2–7]. In such a way, the requested power density to have upconverted photons is reduced to the level of the solar emission (as low as $\approx$ 0.1 W/cm^2) [5]. Obviously, this makes these processes suitable for applications in the field of organic photovoltaics [8], which requires for methods for the conversion of the low energy tail of the solar spectrum.

In these multicomponent systems, the upconverted light is the result of several intermediate photophysical processes: (i) absorption of the excitation light by a phosphorescent donor (D) molecule producing triplet excited states; (ii) energy transfer processes towards metastable triplet state of an acceptor molecule (A); (iii) triplet-triplet annihilation giving rise to high-energy singlet excited states of the second species, from which the upconverted fluorescence takes place. The donor must exhibit large absorption cross-section, while the acceptor must have as long as possible long lived triplet states suitable to collect the excitation from the donor [9] by ET and to generate singlet excited state via TTA. Hybrid materials like organometallic compounds [3, 10] are usually employed as donors, since the presence of heavy atoms strongly enhances their ISC rate [11], thus giving a high population of excited triplet states. Conjugated molecules like polyacenes are reported to work well [12–14] as acceptors, due to the extremely low oscillator strength of their T^*-S_0 electronic transitions. The key passages which can limit the overall process efficiency are the steps involving the ET and the TTA, which can be sketched as

$$\begin{aligned} D_3^* + A &\longrightarrow D + A_3^*, \\ A_3^* + A_3^* &\longrightarrow A + A_1^*, \end{aligned} \tag{1}$$

where the subscripts identify the singlet (1) and triplet (3) states.

The results presented in this paper focused our attention on the ET step, in order to understand its role in the upconversion-induced delayed fluorescence of a model multicomponent systems. To this goal, we prepared solutions at a different acceptor concentration, which has been considered as a simple quencher of the red emission of the donor. Measurements of the ET efficiency on solutions at different temperatures allowed us to evaluate quantitatively

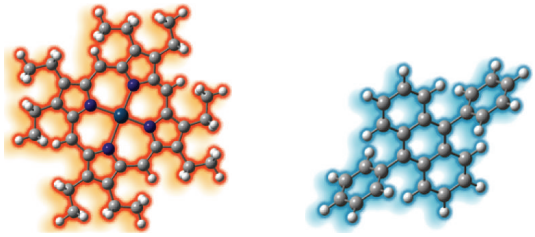

(a) (b)

Figure 1: Molecular structures of (a) Pt(II)octaethylporphyrin and (b) 9,10 diphenylanthracene.

the contribution of the molecular diffusion on the overall efficiency of the process.

2. EXPERIMENTAL

CW photoluminescence (PL) measurements have been carried out by exciting the samples using a Coherent Verdi Nd:YAG laser at the wavelength of 532 nm with a power density of 0.3 W/cm^2. The emission from the solutions has been detected by a nitrogen cooled CCD (Spex 2000) coupled to a monochromator (Triax 190 from J-Horiba) with a bandpass of 0.5 nm. All the measurements have been recorded with the sample inside a bath cryostat in helium atmosphere at room temperature (RT) and 77 K.

PtOEP (Pt(II)octaethylporphyrin) and DPA (9,10 diphenylanthracene), both purchased from Aldrich and used as-is, have been selected as the donor and acceptor moieties, respectively. Their molecular structures are reported in Figure 1. Mixed solutions have been prepared in 1,1,1-Trichloroethane with a fixed concentration of PtOEP (1.4×10^{-4} M) while the concentration of DPA has been varied from 10^{-5} to 4×10^{-2} M. Solutions have been carefully deoxygenated before the measurements by bubbling dry helium for 1 hour [15, 16]. After the deoxygenation, the measured lifetime of the PtEOP emission in absence of the DPA is 27 microseconds which corresponds to a decay rate (K_0) of 3.7×10^4 Hz.

Time resolved PL measurements, carried out to control the effects of the deoxygenation, have been performed with the same monochromator but using a pulsed laser at 355 nm for the excitation (Laser-Export Co. LCS-DTL-374QT), and, for the detection, a photomultiplier connected to a board for time correlated photon counting measurement (ORTEC 9353 100-ps Time Digitizer/MCS). The overall time resolution was better than 100 nanoseconds.

3. RESULTS AND DISCUSSION

Considering that the ET occurs between D_3^* and A_3^* triplet states, whose transition to the ground state is weakly allowed or forbidden at all, therefore, we expect that only Dexter ET via exchange interaction can take place [17–19].

In such a case, the transfer rate (k_{ET}) between a donor-acceptor pair at a distance R can be written as [18]

$$k_{ET}(R) = \frac{2\pi}{\hbar} Z^2 \int F_D(E) G_A(E) dE, \tag{2}$$

where $F_D(E)$ and $G_A(E)$ are the normalized donor emission and acceptor absorption spectra, respectively. The integral of the products of these two functions is the mathematical expression of the resonance involved levels as required by the energy conservation principle. Z is the exchange integral which can be expressed by his asymptotic form

$$Z^2 = K^2 \exp\left(\frac{-2R}{L}\right), \tag{3}$$

where K is a constant with the dimension of an energy, and L is the so-called effective Bohr radius measuring the spatial extent of the donor and acceptor wavefunctions. In particular, (3) shows the dependence of the ET rate on the distance between donor and acceptor, as a consequence of the molecular-wavefunctions exponential decay in the space.

For processes controlled by exchange interactions, $F_D(E)$ and $G_A(E)$ spectra are only hardly detectable as they involve forbidden transitions. Moreover, the shape of the molecular wavefunctions should be known for an exact evaluation of the parameter Z. For these reasons, many models have been developed to simplify the original Dexter equations [20–22]. The Perrin model [22] follows from the observation that (3) gives at short distances, when $R \ll L$, an extremely fast ET rate, while the ET rate becomes negligible at $R > L$. The Perrin model assumes for each isolated donor-acceptor pair the existence of a sort of active sphere of radius R_0: if the donor acceptor distance is shorter than R_0, the energy is totally transferred from the donor to the acceptor, while there is no transfer for larger distances. In this frame, the $k_{ET}(R)$ assumes the simple form

$$k_{ET}(R) = \begin{cases} 0 & \text{for } R > R_0, \\ \infty & \text{for } R < R_0. \end{cases} \tag{4}$$

In (4), R_0 is defined as the *effective radius*, in the sense that at this distance the ET rate equals the rate of the spontaneous decay of the donor in absence of acceptors.

R_0 can be obtained experimentally from measurements of PL relative quantum yield (QY) of the donor, by defining the QY as the ratio between the donor PL intensity ϵ in the presence of a defined acceptor concentration (C_A), and that without it (ϵ_0). By using (4), this relative QY can be written as [19]

$$\frac{\epsilon}{\epsilon_0} = \exp\left(\frac{-C_A}{C_0}\right). \tag{5}$$

C_0 is a constant related to the Dexter parameters (L, K) called critical transfer concentration. Using units of moles per liter for C_0, the value of R_0 in Ångstrom is equal to 7.346 $C_0^{-1/3}$.

In Figure 2, PL spectra of PtEOP/DPA mixed solution are reported as a function of the DPA content. At low DPA concentration, the typical red phosphorescence (PH) of the PtOEP at 635 nm [16, 23] is clearly detected (Figure 2(b)). As the acceptor concentration increases, the intensity of the peak at 635 nm is reduced and a strong enhancement of the DPA emission band at 435 nm (FL) is observed, as in a typical donor-acceptor system (Figure 2(a)). The only difference in this case is that the emission of the acceptor occurs at an

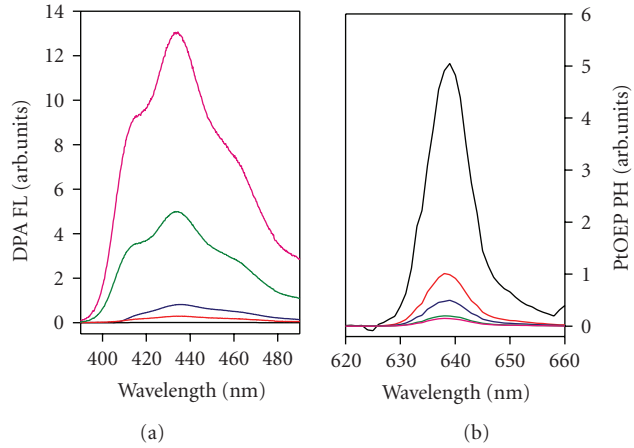

Figure 2: (a) DPA FL spectrum and (b) PtEOP PH intensity at different DPA concentration in PtOEP (1.4×10^{-4} M)/1,1,1-Trichloroethane solution. Spectra have been collected at RT exciting the solution at 532 nm.

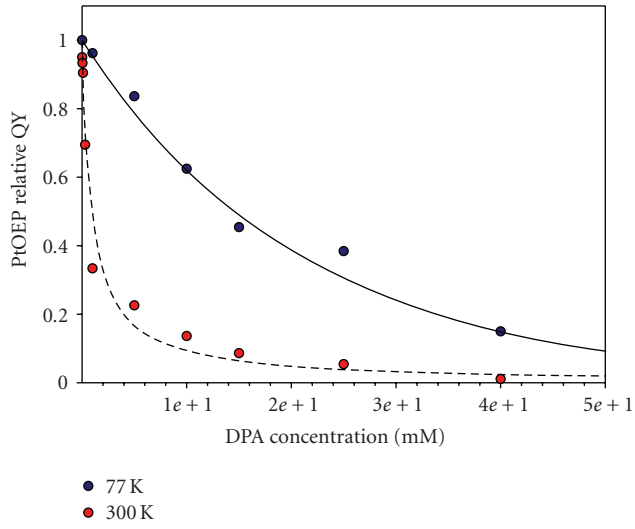

Figure 3: Relative PL quantum yields of the PtOEP PL as a function of the DPA concentration at 77 K (blue circles) and 300 K (red circles). The dashed line has been calculated by combining the contribution of the molecular diffusion and the ET process as a contact interaction. The continuous line is the fit of the data collected at 77 K considering a pure Dexter ET (Dexter radius 26.5 Å).

energy higher than that of the emission of the donor because of the upconversion process.

To verify whether the ET process can be fully described as a Dexter mechanism and to check if the Perrin approximation can be employed for these systems, we measured the relative PL efficiency of the PtEOP used in (5) as a function of the DPA concentration. In Figure 3 (blue circles), the measurements performed on frozen solution are reported, where the molecules diffusion is completely prevented. These data can be perfectly fitted using (5) and are therefore consistent with an exchange driven transfer with an effective radius R_0 of 26.5 Å. A second set of measurements is carried

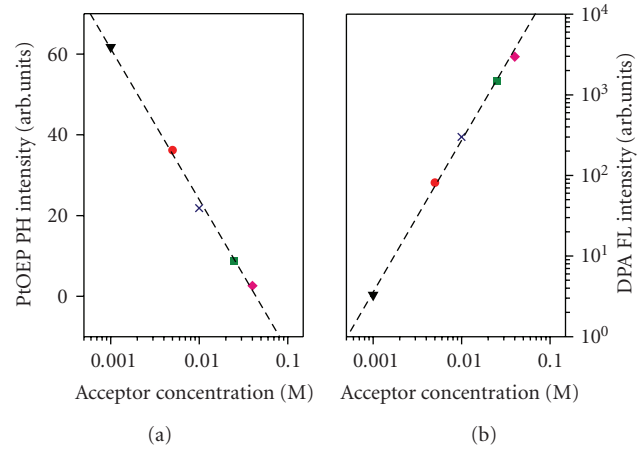

Figure 4: (a) PtOEP PH intensity at different acceptor concentration. Dashed line is the fit with a linear function. (b) Corresponding DPA FL intensity. Dashed line is the fit with a linear function with $m = 1.9$.

out at RT (Figure 3, red circles). Indeed the full process (Dexter ET plus diffusion) can be formally described as a donor quenching due to direct collision with the acceptor moiety [24] using the Dexter radius as the contact distance. In such a case, the ET rate in steady state condition is

$$K_{\mathrm{ET}} = 4\pi D R_0 C_A, \tag{6}$$

where D is the overall diffusion coefficient defined as the sum of the diffusion coefficients of donors (D) and acceptors (A). Diffusion coefficients are evaluated from the viscosity of the solvent ($\eta = 1.2$ cP at RT [25]) and from the effective molecular radii (R_m) estimated accordingly to Bondi [26]. In such a way, the Einstein relation ($D = 3kT/6\pi\eta R_m$) gives an overall diffusion coefficient of 1.8×10^{-5} cm^2/s.

The relative PL quantum efficiency of PtEOP, taking in to account the diffusion contribution, is then calculated as the ratio between the PtEOP decay rates with and without the donor [$\epsilon/\epsilon_0 = K_0/(K_0 + K_{\mathrm{ET}})$] and has been shown in Figure 3 (dashed line). This curve matches well the corresponding experimental data. It must be pointed out that in this comparison no adjustable parameters (K_0, D, R_0) are involved. By considering that for DPA concentration values higher than 1×10^{-2} M $K_{\mathrm{ET}} \gg K_0$, from (6) we can deduce that in the absence of competitive de-excitation channels, PtOEP PH intensity is inversely proportional to the concentration of acceptor C_A. In Figure 4(a), the values of PH intensity varying C_A of three orders of magnitude are reported, and by using a semilogarithmic scale to plot concentrations, we expect a linear decrease of PH intensity. The data reported in Figure 4(a) are indeed strictly consistent with the prevision of collision ET/diffusion model proposed by (6) (dashed line). For TTA is a second-order process, the blue light intensity should be proportional to the square of acceptor triplet excited states population [27]. In such a way by considering that the number of excited acceptors is proportional to C_A (see (6)), then also upconverted light intensity should be proportional to the square of acceptor

concentration. In Figure 4(b), the FL intensity versus the DPA concentration (by using logarithmic scale) has been plotted at fixed concentration of donor. The experimental data fit well with a linear function with an angular coefficient $m = 1.9$ which is in very good agreement with the considerations done on the TTA process (the quadratic dependency gives an exact value of 2 for the slope m).

Obtained results indicate that in the investigated multicomponent system, ET is the main mechanism to populate DPA triplets, and that there are not competitive alternative channels through which donor centers can loss the absorbed energy. At RT it is clear that the molecular diffusion plays a key role in enhancing the ET efficiency. In fact, because of the involvement of long-living donor triplet states, the diffusion lengths of excited molecules are the order of magnitudes larger than the effective radius R_0 of the ET. In the case of PtOEP/DPA solutions, the overall diffusion length goes up to 210 nm with a 10^{-3} DPA concentration. Only for really large acceptor concentrations ($\gg 10^{-2}$ M), the effect of migration can be considered negligible and only the direct donor-acceptor ET is effective. This implies that in order to enhance the efficiency of the ET of these systems in solution, it is necessary to improve the molecular mobility by using solvents with low viscosity and/or small molecular species.

4. CONCLUSIONS

The effects of the molecular diffusion on the triplet-triplet exciton ET between PtEOP and DPA, an organic system model for upconversion-induced delayed fluorescence, have been studied as a function of the temperature. At low T, the results can be well described as a Dexter ET by using the Perrin approximation with an effective radius of 26.5 Å. On the contrary, at RT the molecular diffusion is the main phenomenon which affects the ET efficiency, which is very high also for low acceptor concentrations as a consequence of overall molecular diffusion lengths. As shown, RT experimental data can be strictly interpreted by using an ET/diffusion combined model. These findings clearly explain why high upconversion efficiencies are usually reported for systems in solution [3, 6], while the performance of the corresponding films, where donors and and acceptors moieties are not able to move, is much lower [2, 7].

ACKNOWLEDGMENT

This work has been supported by the Italian MURS (project Synergy) by Fondazione Cariplo and by RTN Nanomatch (Marie-Curie RTN NANOMATCH, Grant no. MRTN-CT-2006-035884).

REFERENCES

[1] Y. R. Shen, *The Principles of Nonlinear Optics*, John Wiley & Sons, Berlin, Germany, 2002.

[2] F. Laquai, G. Wenger, C. Im, A. Büsing, and S. Heun, "Efficient upconversion fluorescence in a blue-emitting spirobifluorene-anthracene copolymer doped with low concentrations of Pt(II)octaethylporphyrin," *Journal of Chemical Physics*, vol. 123, no. 7, Article ID 074902, 6 pages, 2005.

[3] R. R. Islangulov, D. V. Kozlov, and F. N. Castellano, "Low power upconversion using MLCT sensitizers," *Chemical Communications*, no. 30, pp. 3776–3778, 2005.

[4] S. Baluschev, P. E. Keivanidis, G. Wegner, et al., "Upconversion photoluminescence in poly(ladder-type-pentaphenylene) doped with metal (II)-octaethyl porphyrins," *Applied Physics Letters*, vol. 86, no. 6, Article ID 061904, 3 pages, 2005.

[5] S. Baluschev, T. Miteva, V. Yakutkin, G. Nelles, A. Yasuda, and G. Wegner, "Up-conversion fluorescence: noncoherent excitation by sunlight," *Physical Review Letters*, vol. 97, no. 14, Article ID 143903, 2006.

[6] S. Baluschev, V. Yakutkin, G. Wegner, et al., "Two pathways for photon upconversion in model organic compound systems," *Journal of Applied Physics*, vol. 101, no. 2, Article ID 023101, 4 pages, 2007.

[7] S. Baluschev, V. Yakutkin, G. Wegner, et al., "Upconversion with ultrabroad excitation band: simultaneous use of two sensitizers," *Applied Physics Letters*, vol. 90, no. 18, Article ID 181103, 3 pages, 2007.

[8] T. Trupke, M. A. Green, and P. Würfel, "Improving solar cell efficiencies by up-conversion of sub-band-gap light," *Journal of Applied Physics*, vol. 92, no. 7, pp. 4117–4122, 2002.

[9] R. Bensasson and E. J. Land, "Triplet-triplet extinction coefficients via energy transfer," *Transactions of the Faraday Society*, vol. 67, pp. 1904–1915, 1971.

[10] C. Adachi, M. A. Baldo, M. E. Thompson, and S. R. Forrest, "Nearly 100% internal phosphorescence efficiency in an organic light-emitting device," *Journal of Applied Physics*, vol. 90, no. 10, pp. 5048–5051, 2001.

[11] D. Beljonne, Z. Shuai, G. Pourtois, and J. L. Bredas, "Spin-orbit coupling and intersystem crossing in conjugated polymers: a configuration interaction description," *Journal of Physical Chemistry A*, vol. 105, no. 15, pp. 3899–3907, 2001.

[12] J. Jortner, S. Choi, J. L. Katz, and S. A. Rice, "Triplet energy transfer and triplet-triplet interaction in aromatic crystals," *Physical Review Letters*, vol. 11, no. 7, pp. 323–326, 1963.

[13] J. Partee, E. L. Frankevich, B. Uhlhorn, J. Shinar, Y. Ding, and T. J. Barton, "Delayed fluorescence and triplet-triplet annihilation in π-conjugated polymers," *Physical Review Letters*, vol. 82, no. 18, pp. 3673–3676, 1999.

[14] T. Azumi and S. P. McGlynn, "Delayed fluorescence of solid solutions of polyacenes—II: kinetic considerations," *Journal of Chemical Physics*, vol. 39, no. 5, pp. 1186–1194, 1963.

[15] R. Bonnet, A. A. Charalambides, E. J. Land, R. S. Sinclair, D. Tait, and T. G. Truscott, "Triplet states of prophyrin esters," *Journal of the Chemical Society, Faraday Transactions 1*, vol. 76, no. 4, pp. 852–859, 1980.

[16] A. K. Bansal, W. Holzer, A. Penzkofer, and T. Tsuboi, "Absorption and emission spectroscopic characterization of platinum-octaethyl-porphyrin (PtOEP)," *Chemical Physics*, vol. 330, no. 1-2, pp. 118–129, 2006.

[17] Th. Förster, "Zwischenmolekulare energiewanderung und fluoreszenz," *Annalen der Physik*, vol. 437, no. 1-2, pp. 55–75, 1948.

[18] D. L. Dexter, "A theory of sensitized luminescence in solids," *Journal of Chemical Physics*, vol. 21, no. 5, pp. 836–850, 1953.

[19] M. Inokuti and F. Hirayama, "Influence of energy transfer by the exchange mechanism on donor luminescence," *Journal of Chemical Physics*, vol. 43, no. 6, pp. 1978–1989, 1965.

[20] O. Stern and M. Volmer, "On the quenching-time of fluorescence," *Physik Zeitschr*, vol. 20, pp. 183–188, 1919.

[21] G. W. Robinson and R. P. Frosch, "Electronic excitation transfer and relaxation," *Journal of Chemical Physics*, vol. 38, no. 5, pp. 1187–1203, 1963.

[22] F. Perrin, "Loi de decroissance du pouvoir fluorescent en fonction de la concentration," *Comptes Rendus de l'Académie des Sciences*, vol. 178, pp. 1978–1980, 1924.
[23] P. A. Lane, L. C. Palilis, D. F. O'Brien, et al., "Origin of electrophosphorescence from a doped polymer light emitting diode," *Physical Review B*, vol. 63, no. 23, Article ID 235206, 8 pages, 2001.
[24] U. Gösele, M. Hauser, U. K. A. Klein, and R. Frey, "Diffusion and long-range energy transfer," *Chemical Physics Letters*, vol. 34, no. 3, pp. 519–522, 1975.
[25] R. Cohen and J. Mercer, *DNAPL Site Evaluation*, CRC Press, Boca Raton, Fla, USA, 1993.
[26] A. Bondi, "van der Waals volumes and radii," *Journal of Physical Chemistry*, vol. 68, no. 3, pp. 441–451, 1964.
[27] J. Mężyk, J. Kalinowski, F. Meinardi, and R. Tubino, "Triplet exciton interactions in solid films of an electrophosphorescent Pt (II) porphyrin," *Applied Physics Letters*, vol. 86, no. 11, Article ID 111916, 3 pages, 2005.

Hindawi Publishing Corporation
International Journal of Photoenergy
Volume 2008, Article ID 389034, 4 pages
doi:10.1155/2008/389034

Research Article

One Dimensional Polymeric Organic Photonic Crystals for DFB Lasers

F. Scotognella,[1] A. Monguzzi,[1] M. Cucini,[2] F. Meinardi,[1] D. Comoretto,[2] and R. Tubino[1]

[1] *Department of Material Science, University of Milan, Bicocca, Via Roberto Cozzi 53, 20125 Milan, Italy*
[2] *Department of Chemistry and Industrial Chemistry, University of Genoa, Via Dodecaneso 31, 16146 Genoa, Italy*

Correspondence should be addressed to F. Scotognella, francesco.scotognella@mater.unimib.it

Received 30 March 2008; Accepted 5 May 2008

Recommended by Mohamed Sabry Abdel-Mottaleb

We present a very simple method to realize a one-dimensional photonic crystal (1D PC), consisting of a dye-doped polymeric multilayer. Due to the high photonic density of states at the edges of the photonic band-gap (PBG), a surface emitting distributed feedback (DFB) laser is obtained with this structure. Furthermore, the incidence angle dependence of the PBG of the polymeric multilayer is reported.

1. INTRODUCTION

The use of polymers and dye-doped polymers for the fabrication of photonic crystal is currently being actively investigated. Photonic crystals, which consist of a periodic dielectric lattice with a periodicity in the range of optical wavelengths, are intensively studied in order to achieve control of light propagation. This property, which can be used to confine, manipulate, and guide photons, should allow the creation of all-optical integrated circuits and optoelectronic devices [1–3]. In a medium, the periodicity of the refractive index can be in one, two, and three dimension and there are many examples of one-, two-, and three-dimensional photonic crystal fabricated with several materials [4, 5]. While one-dimensional photonic crystals are inherently structurally simpler than two- and three-dimensional analogues, only few investigations have been reported on multilayer stacks of materials, known also as Bragg stacks. These Bragg stacks can be useful for various photonic and optoelectronic applications. In 1994, Dowling et al. [6] proposed and analyzed a surface-emitting laser consisting of a one-dimensional photonic crystal (1D PC) in which a gain material was incorporated. Similar to a Fabry-Pérot type laser with a single longitudinal mode, this distributed feedback (DFB) type laser can oscillate at one of the photonic band edges, where photon density is significantly enhanced [6]. Although inorganic DFB laser is commercially available, a small amount of papers reports the use of polymeric 1D PC for this application [7]. Furthermore, some properties, like incidence angle dependence of the photonic band gap (PBG) of these dye-doped structures, are usually not investigated.

In this paper, we describe the modeling, fabrication, and optical characterization of a dye-doped one-dimensional photonic crystal, consisting in alternated stacks of polyvinylcarbazole (PVK) and cellulose acetate (CA), where each CA stack is doped with Rhodamine 6G (R6G). The laser emission of the dye in the photonic structure and the angular dependence of the PBG are also measured and discussed.

2. MODELING

In order to predict the photonic properties of the structure (Figure 1(a)) which we want to fabricate with the two polymers, we use two-computational tools: MIT photonic band gap and Comsol Multiphysics. MIT Photonic Bandgap is a freeware developed by S. G. Johnson. The program calculates ab initio the band structure of a periodic dielectric structure. The inputs for the calculation are the refractive index of the two materials (in our case $n_{PVK} = 1.683$ and n_{CA}=1.475 [7, 8]) and the ratio between their thicknesses (d_{PVK}/d_{CA}). Although the maximum width of a PBG with a 1D PC is obtained by stacking layers with the same optical path ($n_{PVK}d_{PVK} \approx n_{CA}d_{CA}$), we want to fabricate a 1D PC

where the dye-doped CA layer is 3/4 of the unit cell in order to increase the absorption of the pump power by the dye. The program assumes that the structure is infinite in all directions. In Figure 1(b), the calculated dispersion relation and the photonic density of states for the polymeric 1D PC are shown. The photonic density of state is very high in proximity of photonic band edges. The photonic band gap (violet in the figure) is narrow, and this is due to the relative low refractive index contrast of the two polymers ($\approx$1.14). Nevertheless, for a DBF laser application, this fact is negligible while the zero group velocity at the photonic band edge is the main feature. The organic dye which we choose to dope the CA layer is Rhodamine 6G, that emits between 550 and 600 nm. In order to obtain a PBG centered at about 600 nm (and a photonic band edge at 590 nm), the thicknesses of the PVK layer and the dye-doped CA layer have to be 50 and 150 nm, respectively. Comsol Multiphysics is a commercially available software that solves numerically second-order differential equations. The inputs for this calculation are similar to the previous program. But in this case, we can decide the number of layers. In Figure 1(c) an e.m. wave with wavelength of 600 nm (the center of the PBG) is reflected when it passes through a 39-layers 1D PC.

3. EXPERIMENTAL

Following [7], polymers solutions of PVK (Acros Organics, Janssen-Pharmaceuticalaan 3, 2440 Geel, Belgium) and CA (Acros Organics) are prepared. The solvents are chlorobenzene (Sigma Aldrich, 3050 Spruce St, St Louis, MO, United States) and diacetone alcohol (Acros Organics) for PVK and CA, respectively. The number-average molecular weights of PVK and CA are 90 000 and 100 000, respectively. So, we have selected a concentration of 24,4 and 53,46 g/L. The CA layer is 0.5 w% doped by R6G. In order to obtain the multilayer, we have tried with dip coating, but with this technique a deposited polymer film stays too much in contact with the solvent of the other polymer and consequently the solvent of the other polymer can slightly dissolve the film. We can overcome this problem with the spin coating technique, where about 99% of the solvent is ejected in the first second of rotation. A substrate of glass (Carlo Erba, Via Generale Carlo Ferraris, 22036 Erba Como, Lombardy, Italy) has been used and the rotation speeds for PVK and for CA on the glass substrate are 3800 and 4100 rpm and the already coated layers 3600 and 4000 rpm, respectively. In this way, a $(PVK/CA)_9PVK$ multilayer is obtained. After each deposition, a baking of 5 minutes at 80°C has done. We can neglect the refractive index of the substrate because his thickness is 2 mm, and it cannot affect the photonic properties of the multilayer. The transmittance spectrum has been measured with a Cary Varian 50 spectrophotometer (bandwidth of 1 nm). For the laser emission measurement, a pulsed second harmonic of an Nd:YAG laser (Quanta System, Via Iv Novembre, 116, 21058 Solbiate Olona (VA), Italy) has been used as a pump with a repetition rate and duration of 1 Hz and 7 nanoseconds, respectively. The sample has been obliquely pumped with laser emission of the

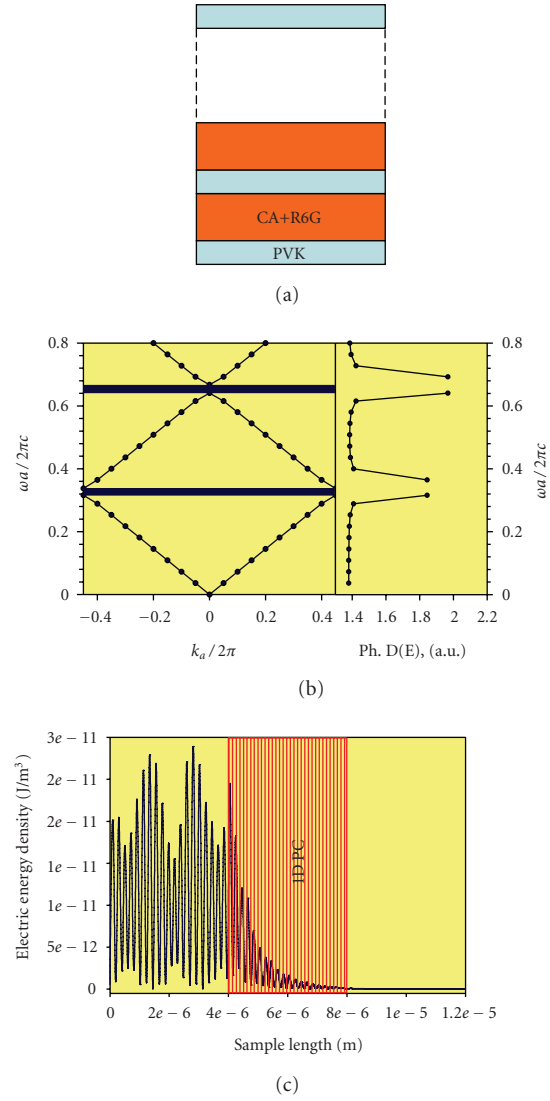

Figure 1: (a) Dye-doped 1D PC, (b) dispersion relation of the 1D PC (with an infinite number of layer) with MIT photonic band gap, and (c) propagation of an e.m. wave (λ = 600 nm) through a 39-layers 1D PC.

dye normal to the surface (in the direction of the refractive index periodicity). The photoluminescence was revealed by Jobin Yvon CCD camera (bandwidth of 1 nm). The angular dependence transmittance spectra have been measured with an optical set-up based on fiber optical coupled to an Avantes 2048 compact spectrometers (spectral resolution 1.6 nm) working in the range 250–1100 nm. White light was provided by a tungsten-halogen/deuterium combined lamp.

4. RESULTS AND DISCUSSION

In Figure 2, the transmission spectrum of the $(PVK/CA)_9PVK$ multilayer, where CA layers are 0.5 w% doped by R6G, is shown. The PBG is centered at about 610 nm and the photonic band edge at 590 nm. The band gap is shifted by 10 nm with respect to theoretical predictions; this is due to

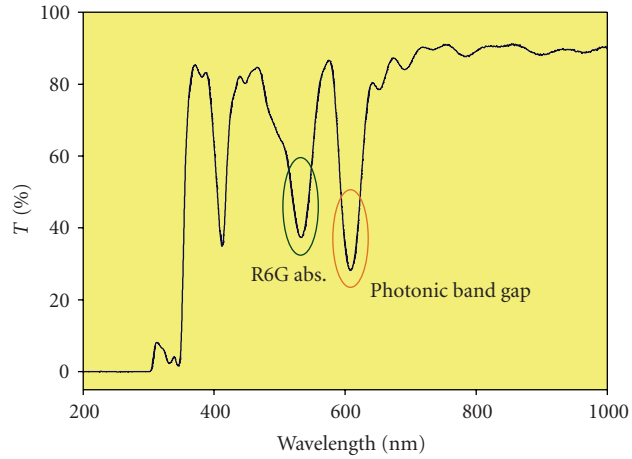

Figure 2: Transmission spectrum of the $(PVK/CA)_9PVK$ multilayer. The green oval indicates the Rhodamine 6G absorption, while the orange oval indicates photonic band gap. At about 400 nm, the higher order photonic band gap is present

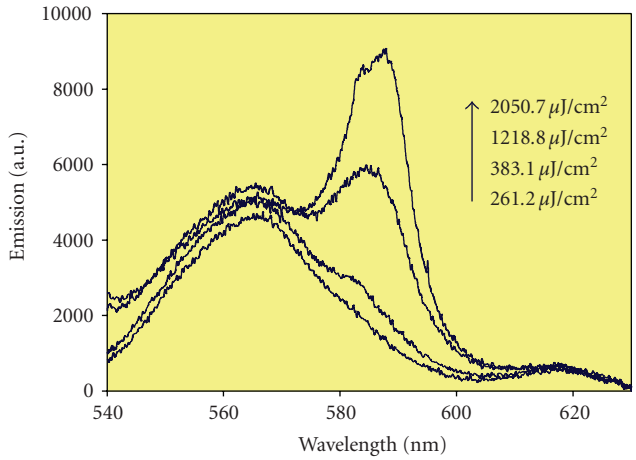

Figure 3: Photoluminescnce spectra of the surface emitting DFB laser made with the dye-doped 1D PC upon increasing the pump energy.

the difficult control of the thickness of each deposited stack. In the spectrum, we see also the absorption of the dye around 532 nm and the second order PBG. The depth of the PBG is about 60%. In Figure 3, the photoluminescence spectra of the R6G-doped 1D PC, at different pump energy density, are reported. The photoluminescence signal is revealed normally to the surface of the multilayer. The region between 540 and 570 nm shows the luminescence peaks of the dye, while between 570 and 630 nm remarkable effects arise from the superimposition of the luminescence of the dye with the photonic structure. In the range of energy where the photonic band gap is present, the luminescence of the dye is suppressed, while, at the energy corresponding to the first (higher energy) photonic band edge, the emission of the dye exhibits a narrow peak arising from the enhancement of the emission in the region of the high density of states.

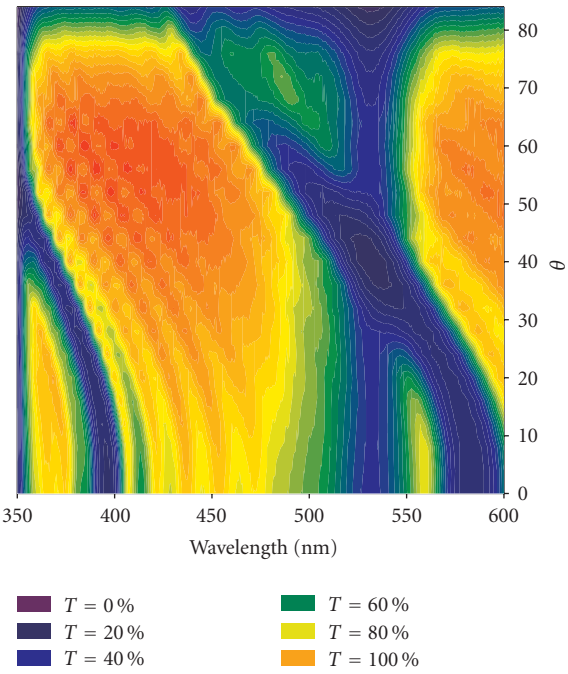

Figure 4: Incidence angle dependence of the transmission spectrum of the dye-doped 1D PC.

Figure 4 shows the trend of the transmission spectrum of the dye-doped 1D PC versus the incident angle θ. In the range between 520 and 540 nm, the absorption of R6G is shown, and it, obviously, does not change, whereas the photonic band gap, the higher order photonic band gap, shows a red shift of the order of 150 nm. The higher order PBG shows a red shift toward the region of PVK absorption.

From these data, we can obtain the refractive index and thickness of the multilayer by solving the equations system [9]:

$$m\lambda_{\text{Bragg}} = 2D\sqrt{n_{\text{eff}}^2 - \sin^2\theta},$$
$$W = \frac{4}{\pi}\left|\frac{n_{\text{PVK}} - n_{\text{CA}}}{n_{\text{PVK}} + n_{\text{CA}}}\right|, \quad (1)$$
$$\frac{\varepsilon_{\text{eff}} - 1}{\varepsilon_{\text{eff}} + 2} = x_{\text{PVK}}\frac{\varepsilon_{\text{PVK}} - 1}{\varepsilon_{\text{PVK}} + 2} + (1 - x_{\text{PVK}})\frac{\varepsilon_{\text{CA}} - 1}{\varepsilon_{\text{CA}} + 2},$$

where the first equation is Bragg-Snell equation, the second is the expression for the PBG width for a 1D PC and the third is the Lorentz-Lorentz equation. In these equations, m is the diffraction order, λ_{Bragg} is the wavelength where the PBG is centered, x_{PVK} is the fraction, the unit cell fraction of the polymer PVK, n_{eff} is the effective refractive index, θ is the incidence angle measured off from the normal, $n_{\text{PVK(CA)}}$ and $\varepsilon_{\text{PVK(CA)}}$ are, respectively, the refractive index and the dielectric constant of PVK (CA). Solving the system, we calculate the refractive indexes (n) and the thicknesses (d) of the two layers and we can compare these with the values that we have found in literature and from simulations (Table 1). The results of theoretical simulations and the

Table 1: Refractive indexes and thicknesses of the polymers in the 1D PC. Comparison with literature and theoretical predictions.

	Spectroscopic data		Literature data	Theoretical sim.
	n	d (nm)	n	d (nm)
PVK	1.668	48.47	1.683	50
CA	1.470	149.40	1.475	150

literature data are in excellent agreement with the equation system solutions.

5. CONCLUSION

In this work, we have modeled, fabricated, and optically characterized a dye-doped polymeric 1D PC. The modeling has been useful to predict the photonic properties of a structure made with the chosen materials. Comsol Multiphysics uses finite elements algorithms and permits to study finite structures, so the prediction of the interaction between e.m. waves and aperiodic and disordered structures with this program is also possible. We have found that the spin coating deposition technique is good for easy fabrication of polymeric photonic crystals. The fabricated dye-doped 1D PC, with the photonic band edge centered in proximity of the laser dye emission, is a low threshold surface emitting DFB laser. Bleaching of the dye is observed at high pump energy density. We intend to overcome this problem by doping of the structure with novel laser dye, for example, organic complexes of lanthanides [10] in which the optically pumped excited state of the ligand is quickly depopulated by an efficient energy transfer process to the emitting ion.

Furthermore, the incidence angle dependence of the PBG of the polymeric multilayer has been measured. This behavior allows us to determine independently n and d and will be used for controlling the spontaneous emission of the dye in the 1D PC.

ACKNOWLEDGMENTS

The author wants to acknowledge Maurizio Crippa, Roberto Lorenzi, and Alberto Paleari for stimulating discussion as well as Claudio Maria Mari and his research group for help with the experiments, RTN Network NANOMATCH, FIRB Synergy, and CARIPLO Foundation. Support from the Italian Ministry of University and Research (PRIN 2006) and University of Genoa (Progetti di Ateneo 2007) is also acknowledged.

REFERENCES

[1] E. Yablonovitch, "Inhibited spontaneous emission in solid-state physics and electronics," *Physical Review Letters*, vol. 58, no. 20, pp. 2059–2062, 1987.

[2] S. John, "Strong localization of photons in certain disordered dielectric superlattices," *Physical Review Letters*, vol. 58, no. 23, pp. 2486–2489, 1987.

[3] J. D. Joannopoulos, R. D. Meade, and J. N. Winn, *Photonic Crystals: Molding the Flow of Light*, Princeton University Press, Princeton, NJ, USA, 1995.

[4] C. López, "Materials aspects of photonic crystals," *Advanced Materials*, vol. 15, no. 20, pp. 1679–1704, 2003.

[5] J. E. G. J. Wijnhoven and W. L. Vos, "Preparation of photonic crystals made of air spheres in titania," *Science*, vol. 281, no. 5378, pp. 802–804, 1998.

[6] J. P. Dowling, M. Scalora, M. J. Bloemer, and C. M. Bowden, "The photonic band edge laser: a new approach to gain enhancement," *Journal of Applied Physics*, vol. 75, no. 4, pp. 1896–1899, 1994.

[7] T. Komikado, S. Yoshida, and S. Umegaki, "Surface-emitting distributed-feedback dye laser of a polymeric multilayer fabricated by spin coating," *Applied Physics Letters*, vol. 89, no. 6, Article ID 061123, 3 pages, 2006.

[8] http://www.texloc.com/closet/cl_refractiveindex.html.

[9] V. Morandi, F. Marabelli, V. Amendola, M. Meneghetti, and D. Comoretto, "Colloidal photonic crystals doped with gold nanoparticles: spectroscopy and optical switching properties," *Advanced Functional Materials*, vol. 17, no. 15, pp. 2779–2786, 2007.

[10] K. Nakamura, Y. Hasegawa, H. Kawai, et al., "Enhanced lasing properties of dissymmetric Eu(III) complex with bidentate phosphine ligands," *Journal of Physical Chemistry A*, vol. 111, no. 16, pp. 3029–3037, 2007.

Hindawi Publishing Corporation
International Journal of Photoenergy
Volume 2008, Article ID 978329, 7 pages
doi:10.1155/2008/978329

Research Article

Photocatalytic Degradation of a Water Soluble Herbicide by Pure and Noble Metal Deposited TiO_2 Nanocrystalline Films

Katerina Pelentridou,[1] Elias Stathatos,[2] Helen Karasali,[3] Dionysios D. Dionysiou,[4] and Panagiotis Lianos[1]

[1] *Engineering Science Department, University of Patras, 26500 Patras, Greece*
[2] *Electrical Engineering Department, Technological-Educational Institute of Patras, 26334 Patras, Greece*
[3] *Benaki Phytopathological Institute, Pesticide control and Phytopharmacy, 14561 Athens, Greece*
[4] *Department of Civil and Environmental Engineering, University of Cincinnati, Cincinnati, OH 45221-0071, USA*

Correspondence should be addressed to Elias Stathatos, estathatos@teipat.gr

Received 1 April 2008; Revised 12 May 2008; Accepted 5 July 2008

Recommended by Jean-Marie Herrmann

We present the photocatalytic degradation of a water soluble sulfonylurea herbicide: azimsulfuron in the presence of titania nanocrystalline films. Efficient photodegradation of herbicide was achieved by using low-intensity black light tubes emitting in the Near-UV. The degradation of the herbicide follows first-order kinetics according to the Langmuir-Hinshelwood model. Intermediate products were identified by the LC-MS-MS technique during photocatalytic degradation. In order to increase photodegradation rate of the herbicide, we examined the effect of titania modification by depositing noble metals at various quantities and valence states. The presence of platinum at neutral valence state and optimum concentration induced higher photodegradation rates while silver-modified titania exhibited similar photocatalytic rates with those obtained with pure nanocrystalline TiO_2 films. Finally, the effect of initial pH value was also examined. Acidic or alkaline media were unfavorable for azimsulfuron photodegradation.

1. INTRODUCTION

Photodegradation of various organic pollutants by photocatalysis, using wide bandgap semiconductors, has been extensively studied [1–3]. Among them, TiO_2 a relatively inexpensive semiconductor exhibits high photocatalytic activity, stability in aqueous solution, nontoxicity [4, 5], and so forth. However, TiO_2 usage has a few drawbacks; for example, it absorbs only in the UVA part of the light spectrum where solar radiation is only 2-3% of the total reaching the surface of the Earth [6]. Moreover, the application of TiO_2 for photocatalytic oxidation of organic molecules is limited by high charge carrier recombination rates that results in low quantum efficiency. In recent years, surface metallization of TiO_2 has received considerable attention as an option to overcome the high degree of charge carrier recombination [7–10]. Platinum, and some other noble metals, may be used for this purpose thus providing an electron sink. In addition, they may extent TiO_2 absorbance in the Visible [11]. The presence of a metal at the surface of TiO_2 results in the formation of a Schottky barrier at the metal-semiconductor interface, which facilitates the interfacial electron transfer and subsequently encourages the charge carrier separation [12].

Among the various organic substances, which are known as water pollutants, herbicides are a major pollution source for both underground and surface waters. Advanced oxidation processes are used, among others, also for the degradation of herbicides [13, 14]. Azimsulfuron (AZS, see Scheme 1 for chemical structure) belongs to the class of sulfonylurea herbicides, which have a broad spectrum of weed control, low application rate, and low animal toxicity [15, 16]. Sulfonylurea herbicides, in addition to playing an important role in modern agriculture, are also degradable by heterogeneous photocatalysis, as it has been proven in the past [17, 18]. In the present work, sol-gel prepared TiO_2 films, which were further modified with noble metal ions, were examined for the photodegradation of AZS in water. The effect of various parameters, such as the amount of metal deposits and pH value of herbicide aqueous solution, were studied in order to evaluate the optimum conditions for the photocatalytic oxidation of AZS.

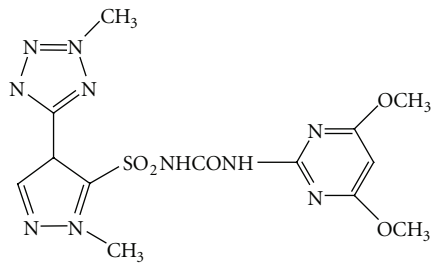

Scheme 1: Chemical structure of AZS.

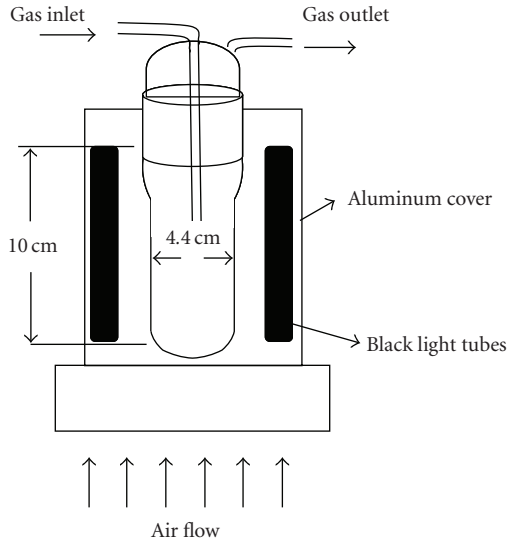

Figure 1: Schematic representation of the reactor used in all experiments.

2. EXPERIMENTAL

Azimsulfuron, N-[[(4,6-dimethoxy pyrimidin-2-yl)-amino] carbonyl]-1-methyl-4-(2-methyl-2H-tetrazole-5-yl)-1H-pyrazole-5-sulfonamide (AZS, 99.3% purity, Scheme 1), was donated by DuPont de Nemours, Puteaux, France. All the rest of reagents were obtained from Sigma-Aldrich, Mo, USA. Millipore water was used in all experiments.

2.1. Description of the photocatalytic reactor

The cylindrical reactor schematically shown in Figure 1 was used in all experiments [19]. Air was pumped through the gas inlet using a small pump to ensure continuous oxygen supply to the reaction solution while simultaneously agitating it. In cases where experiments were carried out in the absence of oxygen, the solution was deoxygenated by nitrogen flow and the openings were sealed. Four black light fluorescent tubes of 4 W nominal power were placed around the reactor. The whole construction was covered with a cylindrical aluminum reflector. Cooling was achieved by air flow from below the reactor using a ventilator. The catalyst was in the form of four-glass rings, covered on both sides with nanocrystalline TiO_2 film. Film deposition is described below. The glass rings were of 38 mm of diameter and 15 mm height, stacked and coaxially placed inside the reactor. Thus, the total surface of the photocatalyst film was approximately $2 \times 71.6 = 143\,\text{cm}^2$. The intensity of radiation reaching the surface of the film on the side facing lamps was measured with an Oriel radiant power meter and found equal to $0.79\,\text{mW/cm}^2$.

2.2. Nanocrystalline Titania films and metal deposition

Titania films were deposited by following the previously reported procedure [20, 21]. Briefly, for 25 mL solution, 3.6 g of the nonionic surfactant Triton X-100 (polyoxyethylene-10-isooctylphenyl ether) was mixed with 20 mL of ethanol, followed by addition of 1.6 mL of glacial acetic acid and 1.8 mL of titanium isopropoxide under vigorous stirring. Self organization of the surfactant in this original sol creates organized assemblies that act as templates defining nanoparticle size. The surfactant is burned out during calcination. After a few minutes stirring, the glass rings described above, which were previously thoroughly washed, sonicated in ethanol and dried in a N_2 stream, were dipped in the above sol and withdrawn slowly by hand. After the film was dried in air for a few minutes, it was calcined in an oven. The temperature was increased in a ramp rate of 20°C/ min up to 550°C and left at that temperature for about 10 minutes. When the titania-covered rings were taken out of the oven, they were transparent and optically uniform. The above procedure was repeated several times in order to reach the quantity of catalyst necessary for the purposes of the present work. The final mass of titania on the four glass rings was 80 mg (20 mg on each glass ring). Noble metal ions were deposited on titania films by adsorption from aqueous solutions containing one of the following metal salts: $Na_2PtCl_4 \cdot xH_2O$ or $AgNO_3$ at various concentrations (from 10^{-4} to 10^{-3} M for the platinum salt and from 5×10^{-4} to 10^{-2} M for the silver salt). After the last layer of TiO_2 was deposited and immediately after the film was taken out from the oven, the rings were submerged in the salt aqueous solution and were left for half an hour in the dark. Then, the rings were washed, dried, and subjected to UV radiation for 30 minutes; or they were additionally heated at 500°C for 15 minutes. UV and heat treatment were performed to reduce cationic species to neutral metallic particles.

2.3. Photodegradation procedure

The reactor was filled with 100 mL water in which 6 mg of AZS were dissolved. Standard solutions were employed in all experiments. AZS is not adsorbed on titania films, however, about an hour of equilibrium was allowed before illumination. The concentration of AZS in solution was monitored by absorption spectrophotometry at 240 nm using quartz cuvettes. In order to assure linear relationship between absorbance and concentration, preliminary measurements have been made. The linear relationship was established in the range of $0 \rightarrow 60\,\text{mg L}^{-1}$. Thus, the presently chosen

concentration 60 mg L^{-1} was the maximum concentration of the established linear concentration versus absorbance range. It was found that this concentration is also close to the solubility limit of AZS in water. A 3 mL aliquot was collected for performing absorption spectrophotometry, and it was poured back into the reactor after measurement. The first concentration measurement was done in the dark. It was then verified that the herbicide was not adsorbed on the titania film. Finally, the products of photodegradation have been monitored by LC-MS-MS analysis.

2.4. Apparatus and methods

Absorption measurements were made with a Cary 1E spectrophotometer. LC-MS-MS analysis was carried out on a Varian 1200L mass spectrometer equipped with electrospray ionization interface (ESI). The ion trap was connected to a Varian 1200 LC system consisting of two individual pumps, a membrane degasser, an autosampler with temperature control, and a thermostatic column control. The chromatographic separation was performed on a reversed phase Varian Polaris C-18 column (150 mm × 2.1 mm, 5 μm particle size) at 30°C. The concentration of AZS at each degradation stage was calculated by using an external calibration curve from LC-MS-MS measurements of AZS at five different concentrations. Stock solution was prepared by diluting the appropriate amount of the analytical standard with water/methanol (70/30) at concentration 60 ppm. In order to determine the degradation products formed during AZS photocatalysis, ESI ionization in both negative- and positive-ion modes was investigated. The results indicated that the ESI source at positive-ion mode with collision energy at 30 V was most appropriate for the analysis of the degradation products.

3. RESULTS AND DISCUSSION

The films made by the sol-gel procedure described in the Experimental section consisted of anatase nanocrystals of about 15 nm average size. Size polydispersity is limited and the active surface area is around 110 m^2/g, as measured by nitrogen adsorption-desorption isotherms according to the BET analysis [21].

3.1. Photodegradation studies of AZS with pure TiO_2 films

It has been proposed that titanium dioxide mediated photodegradation involves the generation of electron-hole pairs [2], which migrate to the photocatalyst surface forming surface bound hydroxyl and superoxide radicals according to following reactions:

$$\begin{aligned} TiO_2 + h\nu &\longrightarrow e^-_{cb} + h^+_{vb}, \\ O_2 + e^-_{cb} &\longrightarrow O_2{}^{-\bullet}, \\ H_2O+ + h^+_{vb} &\longrightarrow {}^{\bullet}OH + H^+. \end{aligned} \quad (1)$$

It is commonly known that the hydroxyl and superoxide radicals are the primary oxidizing species in the photocatalytic process. These oxidative reactions result in the photodegradation of AZS. The efficiency of this process depends on oxygen concentration. The absorption spectra of the AZS solution at various stages of photodegradation are presented in Figure 2, where it is obvious that the concentration of intact AZS decreased during illumination in the presence of titania. The characteristic peak at 240 nm completely disappears after 15 hours of illumination, using low-power black light source. Practically, no photolysis of AZS has been observed at the present illumination level, as seen by curve number 2 of Figure 3. The presence of oxygen during photocatalytic experiments is absolutely necessary and this is proved by the data of curve number 3 in Figure 3. Absence of oxygen leads to negligible photodegradation. Photodegradation followed Langmuir-Hinshelwood kinetics:

$$\ln(A_0/A) = k_{app}t. \quad (2)$$

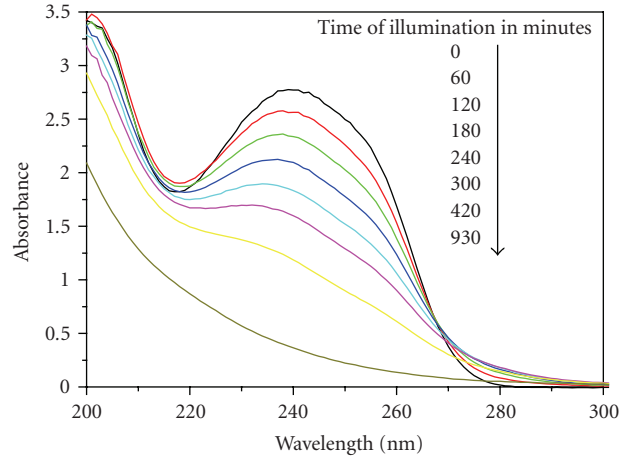

Figure 2: Absorption spectrum of AZS in water and variation with time of UV illumination in the presence of TiO_2 nanocrystalline films.

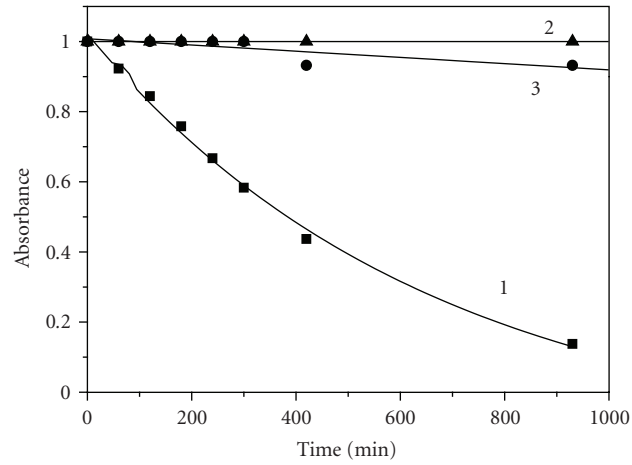

Figure 3: Photodegradation curves of AZS with black light illumination: in the presence of TiO_2 films (1); in the absence of photocatalyst (2); and in the absence of oxygen (3).

The corresponding first-order rate constant was $0.0020\,\text{min}^{-1}$. By taking into account the fact that no AZS was adsorbed on the titania films, as already said, it is obvious that photodegradation is carried out in the liquid phase and it is also obvious that $O_2^{-\bullet}$ species, which are only formed in the presence of oxygen, play a major role. Furthermore, the fact that photodegradation is carried out in the liquid phase explains why it is relatively slow. As a matter of fact, it is known that photodegradation rates are higher when the target substance is adsorbed on the photocatalyst.

3.2. Photodegradation of AZS in presence of noble metals deposited on TiO_2 films

Silver or platinum metal ions were deposited on the TiO_2 surface by submerging titania for several minutes in aqueous solutions of metal salts. Metal cations could be adsorbed in TiO_2 films at substantial quantities because of the relatively high specific surface area of the films. The platinum complex is in the form of divalent tetrachloride ion. By accepting two photo-generated electrons, it is converted into zero valence metal according to the following reaction:

$$PtCl_4^{2-} + 2e^- \longrightarrow Pt^0 + 4Cl^-. \quad (3)$$

However, XPS measurements for UV illuminated samples gave peaks with binding energies of 72.85 and 76.13 eV, consistent with published values [22] for $Pt^{(II)}$. In addition to UV exposure, thermal heating (500°C) of the metal-deposited films gave a variation of the binding energies of platinum, which were then located at 70.5 and 73.86 eV, consistent with $Pt^{(0)}$ [22]. It is obvious that weak UV light intensity from black light irradiation was not enough for the complete transformation of tetrachloroplatinate ion into zero valence platinum. However, it is possible that $Pt^{(II)}$ is finally transformed into $Pt^{(0)}$, due to the prolonged UV illumination during photodegradation. In the case of silver ions, the results were more predictable as only one electron is enough to reduce silver ions and create zero valence noble metal on the surface of TiO_2, according to the following reaction:

$$Ag^{+1} + e^- \longrightarrow Ag^0. \quad (4)$$

This electron is easy to be generated, either by UV illumination under black light irradiation or by thermal heating of the films [23]. XPS measurements gave similar results for both procedures of silver reduction. The photodegradation of AZS herbicide in the presence of platinum modified titania films is presented in Figure 4. The films subjected to both UV and thermal treatment gave better photocatalytic efficiencies as compared with the films, which were only UV treated. Furthermore, the original salt concentration, which obviously affects the quantity of deposited metal, affected photodegradation efficiency. When the platinum salt concentration was $5 \times 10^{-4}\,\text{mol L}^{-1}$, we obtained the highest photocatalytic efficiency. At higher metal load, efficiency dropped, possibly due to screening effects. The photocatalytic degradation of AZS in presence of silver loaded TiO_2 is presented in

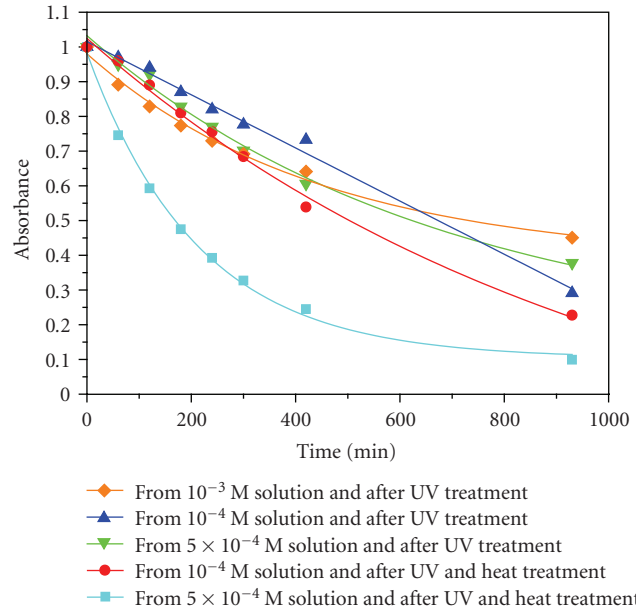

Figure 4: Photodegradation curves of AZS with black light illumination in presence of Pt modified TiO_2 films at various platinum concentrations and treatments of the films.

Figure 5(a). As in the case of platinum, metal load affected photocatalysis, $10^{-2}\,\text{mol L}^{-1}$ silver salt concentration giving the best results. Silver deposited on TiO_2 films gave the plasmon resonance absorption [23] spectra of Figure 5(b). Absorbance values verified that there is a direct relation between metal load and salt concentration in the aqueous solution. Comparative studies of AZS photodegradation with pure or metal-loaded TiO_2 showed that the presence of platinum is effective for the destruction of the herbicide contrary to silver, which gave similar results as pure TiO_2 films (see Figure 6). The role of platinum in photocatalysis is not fully understood. The degree of enhancement of the activity of TiO_2 by platinisation seems to depend highly on the substance to be photodegraded [24], the characteristics and the amount of deposited Pt [25], and the structural and morphological properties of original TiO_2 [26]. In general, it is accepted, as already said, that in platinized TiO_2, a better separation of charge carriers is observed.

3.3. AZS photodegradation intermediates

Intermediate products of AZS photodegradation were studied by LC-MS-MS. Two major ions were detected in all photodegradation stages, one with m/z: 199 and the other with m/z: 244. These two fragments exactly correspond to the amino-dimethoxypyrimidine and 1-methyl-4-(2-methyl-2H-tetrazole-5-yl)-1H-pyrazole-5-sulfonamide moieties, respectively, which AZS consists of. Ion 244 yielded a major further fragment ion at m/z: 83.3, which could correspond to the sulfonamide $SO_2NH_2^-$ group. The amino-dimethoxypyrimidine-containing ion yielded a major fragment ion at m/z: 74.5, which could correspond to the break down of the carbon link between the two nitrogen

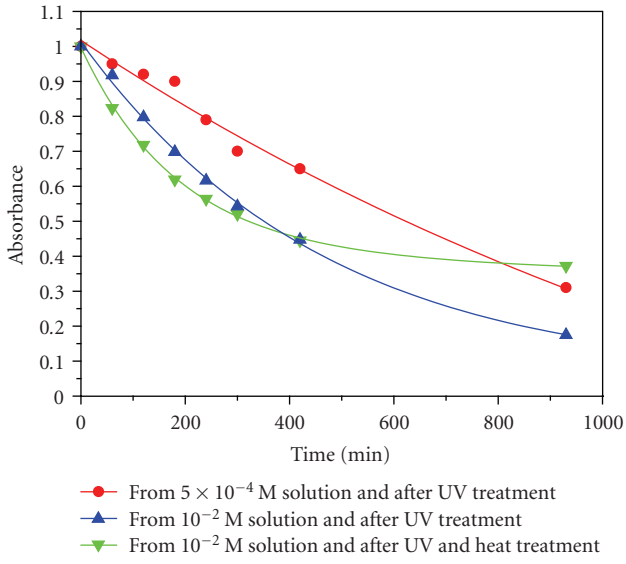

(a)

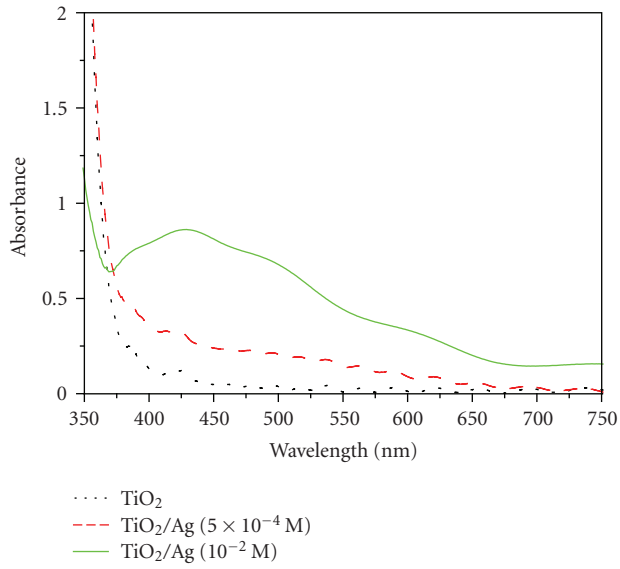

(b)

FIGURE 5: (a) Photodegradation curves of AZS with black light illumination in the presence of Ag modified TiO_2 films at various silver concentrations and treatments of the films: (a) -•- from 5×10^{-4} M solution and after UV treatment; (b) -▲- from 10^{-2} M solution and after UV treatment; (c) -▼- from 10^{-2} M solution and after UV and heat treatment.

atoms leading to the formation of methylaminocarboxylic acid $CH_3NHCOOH$. These data are preliminary and further studies on the detailed reaction pathway are being conducted in our laboratories.

3.4. pH effect on the photodegradation of AZS

The photodegradation of AZS was also studied at various pH values. The results are presented in Figure 7. pH values

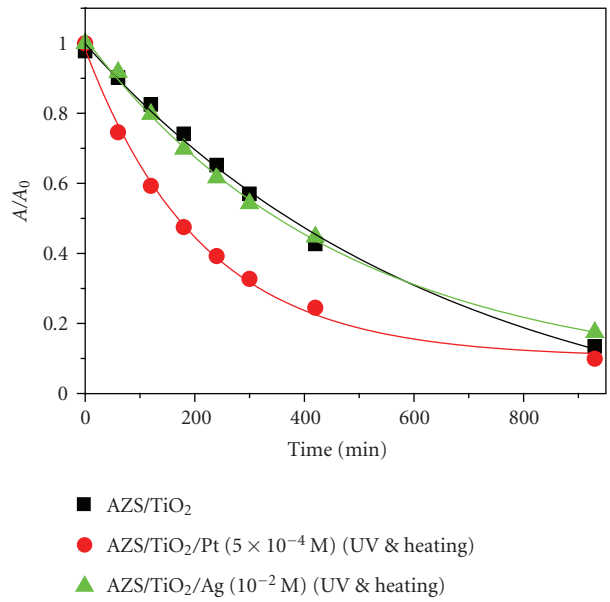

FIGURE 6: Comparative photodegradation curves of AZS with black light illumination in the presence of pure and modified TiO_2 films.

were modified by adding either H_2SO_4 or NaOH, both at a concentration of 0.1 mol L^{-1}. The fastest photodegradation was obtained at natural pH (4.7), that is, in a pure solution of AZS in water. Photodegradation rates in basic pH were low and even lower in acidic pH. This behavior could be explained by the fact that AZS possesses chargeable chemical groups. It is highly probable that at low pH values, AZS is positively charged, and at high pH values, it is negatively charged. However, as it is well known that the surface of titania is also charged with the same charge at the same pH [27]. Therefore, at low or high pH, there is a repulsion that separates the catalyst surface from the target molecule and makes it more difficult for the reactive radical species, which are generated on the surface of the catalyst, to reach the target molecules; hence the lower photodegradation rates in these cases. The right axis scale of all graphs of Figure 7 represents the change of pH in the solution during illumination. In strongly alkaline and acidic solutions, pH decreased during photodegradation, but in the case of natural solutions, a pH increase was observed. The interpretation of the pH effect on the photocatalytic process is a rather difficult task because of the multiple roles that various factors could play, such as electrostatic interactions with the semiconductor surface, chemical structure of the original substance and of its fragments, and formation of active radicals.

4. CONCLUSIONS

The herbicide azimsulfuron can be effectively photodegraded by employing pure or noble metal-modified titania nanocrystalline films as photocatalysts with black light tubes as low-intensity UV illumination source. The catalyst was deposited by the sol-gel method on glass rings; it could be

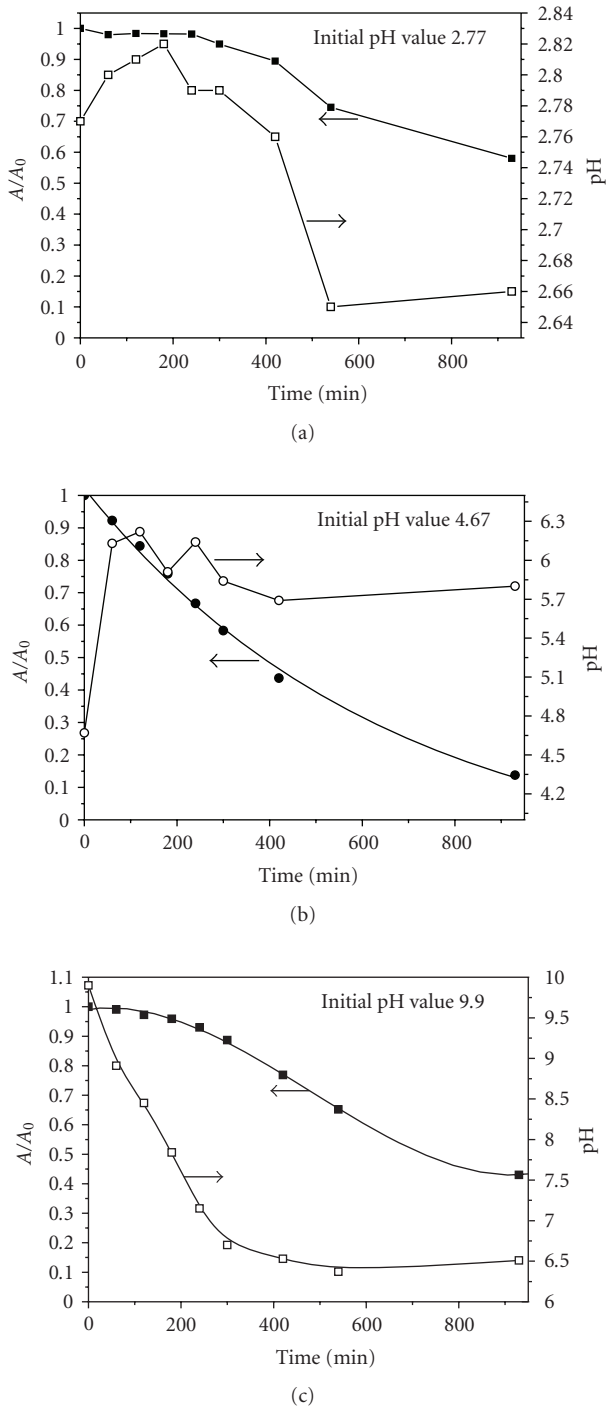

Figure 7: Effect of pH variation in the photodegradation rates with pure nanocrystalline titania films (a) in acidic pH; (b) in natural pH of AZS in water; (c) in alkaline pH value.

thus easily recuperated and repeatedly used in subsequent photodegradation procedures. The best photocatalytic rates were achieved in the case of platinum modified nanocrystalline TiO_2 films. The pH of AZS aqueous solution affected photodegradation rates. The fastest rate was obtained in the case of natural pH of the solution.

ACKNOWLEDGMENT

The authors acknowledge financial support from the Greek General Secretariat of Research and Technology through the E&T bilateral GR-USA cooperation program, 05NON-EU-521.

REFERENCES

[1] D. Bahnemann, "Photocatalytic detoxification of polluted waters," in *The Handbook of Environmental Chemistry. Vol. II. Part L*, O. Hutzinger, Ed., pp. 285–351, Springer, Berlin, Germany, 1999.

[2] M. R. Hoffmann, S. T. Martin, W. Choi, and D. W. Bahnemann, "Environmental applications of semiconductor photocatalysis," *Chemical Reviews*, vol. 95, no. 1, pp. 69–96, 1995.

[3] E. Evgenidou, I. Konstantinou, K. Fytianos, I. Poulios, and T. Albanis, "Photocatalytic oxidation of methyl parathion over TiO_2 and ZnO suspensions," *Catalysis Today*, vol. 124, no. 3-4, pp. 156–162, 2007.

[4] O. Zahraa, H. Y. Chen, and M. Bouchy, "Photocatalytic degradation of 1,2-dichloroethane on supported TiO_2," *Journal of Advanced Oxidation Technologies*, vol. 4, pp. 1169–1176, 1999.

[5] S. Malato, J. Blanco, J. Cáceres, A. R. Fernández-Alba, A. Agüera, and A. Rodríguez, "Photocatalytic treatment of water-soluble pesticides by photo-Fenton and TiO_2 using solar energy," *Catalysis Today*, vol. 76, no. 2–4, pp. 209–220, 2002.

[6] Z. Zou, J. Ye, K. Sayama, and H. Arakawa, "Direct splitting of water under visible light irradiation with an oxide semiconductor photocatalyst," *Nature*, vol. 414, no. 6864, pp. 625–627, 2001.

[7] L. Sun and J. R. Bolton, "Determination of the quantum yield for the photochemical generation of hydroxyl radicals in TiO_2 suspensions," *Journal of Physical Chemistry*, vol. 100, no. 10, pp. 4127–4134, 1996.

[8] D. Ollis and H. Al-Ekabi, Eds., *Photocatalytic Purification and Treatment of Water and Air*, Elsevier Science, Amsterdam, The Netherlands, 1993.

[9] R. Memming, *Semiconductor Electrochemistry*, Wiley-VCH, Weinheim, Germany, 2001.

[10] S. Sakthivel, M. V. Shankar, M. Palanichamy, B. Arabindoo, D. W. Bahnemann, and V. Murugesan, "Enhancement of photocatalytic activity by metal deposition: characterisation and photonic efficiency of Pt, Au and Pd deposited on TiO_2 catalyst," *Water Research*, vol. 38, no. 13, pp. 3001–3008, 2004.

[11] N. Serpone and E. Pelizzetti, Eds., *Photocatalysis-Fumdamentals and Applications*, Wiley-Interscience, New York, NY, USA, 1989.

[12] D. Hufschmidt, D. Bahnemann, J. J. Testa, C. A. Emilio, and M. I. Litter, "Enhancement of the photocatalytic activity of various TiO_2 materials by platinisation," *Journal of Photochemistry and Photobiology A*, vol. 148, no. 1–3, pp. 223–231, 2002.

[13] I. K. Konstantinou, V. A. Sakkas, and T. A. Albanis, "Photocatalytic degradation of propachlor in aqueous TiO_2 suspensions. Determination of the reaction pathway and identification of intermediate products by various analytical methods," *Water Research*, vol. 36, no. 11, pp. 2733–2742, 2002.

[14] V. A. Sakkas, I. M. Arabatzis, I. K. Konstantinou, A. D. Dimou, T. A. Albanis, and P. Falaras, "Metolachlor photocatalytic degradation using TiO_2 photocatalysts," *Applied Catalysis B*, vol. 49, no. 3, pp. 195–205, 2004.

[15] M. V. Pinna, M. Zema, C. Gessa, and A. Pusino, "Structural elucidation of phototransformation products of azimsulfuron in water," *Journal of Agricultural and Food Chemistry*, vol. 55, no. 16, pp. 6659–6663, 2007.

[16] A. Pusino, M. V. Pinna, and C. Gessa, "Azimsulfuron sorption-desorption on soil," *Journal of Agricultural and Food Chemistry*, vol. 52, no. 11, pp. 3462–3466, 2004.

[17] V. Maurino, C. Minero, E. Pelizzetti, and M. Vincenti, "Photocatalytic transformation of sulfonylurea herbicides over irradiated titanium dioxide particles," *Colloids and Surfaces A*, vol. 151, no. 1-2, pp. 329–338, 1999.

[18] S. Rafqah, P. Wong-Wah-Chung, A. Aamili, and M. Sarakha, "Degradation of metsulfuron methyl by heterogeneous photocatalysis on TiO_2 in aqueous suspensions: kinetic and analytical studies," *Journal of Molecular Catalysis A*, vol. 237, no. 1-2, pp. 50–59, 2005.

[19] N. Strataki, V. Bekiari, D. I. Kondarides, and P. Lianos, "Hydrogen production by photocatalytic alcohol reforming employing highly efficient nanocrystalline titania films," *Applied Catalysis B*, vol. 77, no. 1-2, pp. 184–189, 2007.

[20] P. Bouras, E. Stathatos, and P. Lianos, "Pure versus metal-ion-doped nanocrystalline titania for photocatalysis," *Applied Catalysis B*, vol. 73, no. 1-2, pp. 51–59, 2007.

[21] E. Stathatos, P. Lianos, and C. Tsakiroglou, "Highly efficient nanocrystalline titania films made from organic/inorganic nanocomposite gels," *Microporous and Mesoporous Materials*, vol. 75, no. 3, pp. 255–260, 2004.

[22] B. Ohtani, K. Iwai, S. Nishimoto, and S. Sato, "Role of platinum deposits on titanium(IV) oxide particles: structural and kinetic analyses of photocatalytic reaction in aqueous alcohol and amino acid solutions," *Journal of Physical Chemistry B*, vol. 101, no. 17, pp. 3349–3359, 1997.

[23] E. Stathatos, P. Lianos, P. Falaras, and A. Siokou, "Photocatalytically deposited silver nanoparticles on mesoporous TiO_2 films," *Langmuir*, vol. 16, no. 5, pp. 2398–2400, 2000.

[24] F. Denny, J. Scott, K. Chiang, W. Y. Teoh, and R. Amal, "Insight towards the role of platinum in the photocatalytic mineralisation of organic compounds," *Journal of Molecular Catalysis A*, vol. 263, no. 1-2, pp. 93–102, 2007.

[25] J. Lee and W. Choi, "Photocatalytic reactivity of surface platinized TiO_2: substrate specificity and the effect of Pt oxidation state," *Journal of Physical Chemistry B*, vol. 109, no. 15, pp. 7399–7406, 2005.

[26] M. C. Hidalgo, M. Maicu, J. A. Navío, and G. Colón, "Photocatalytic properties of surface modified platinised TiO_2: effects of particle size and structural composition," *Catalysis Today*, vol. 129, no. 1-2, pp. 43–49, 2007.

[27] M. Carrier, N. Perol, J.-M. Herrmann, et al., "Kinetics and reactional pathway of Imazapyr photocatalytic degradation Influence of pH and metallic ions," *Applied Catalysis B*, vol. 65, no. 1-2, pp. 11–20, 2006.

Hindawi Publishing Corporation
International Journal of Photoenergy
Volume 2008, Article ID 757510, 7 pages
doi:10.1155/2008/757510

Research Article

Microstructured Reactors Designed by Stereolithography and Characterized by Fluorescent Probes

S. Corbel,[1] F. Evenou,[1] F. Baros,[1] N. Martinet,[2] M. Donner,[2] and M. C. Carré[1]

[1] *Département de Chimie Physique des Réactions, UMR 7630 CNRS-INPL, Nancy Université, 1 Rue Grandville, BP 20451, 54001 Nancy Cedex, France*
[2] *Centre de Ressources Biologiques, INSERM U724, Avenue de la Forêt de Haye, 54505 Vandoeuvre les Nancy, France*

Correspondence should be addressed to S. Corbel, serge.corbel@ensic.inpl-nancy.fr

Received 4 April 2008; Accepted 30 May 2008

Recommended by Mohamed Sabry Abdel-Mottaleb

The main objective of this research was to define a structured and functionalized support for future biomedical applications (model of "low-density bioarray"). The experiments were carried out by using stereolithography process with a special SU-8 photoresist and the reproducibility of the method was studied by analyzing the surface profile of the support. Finally, a matrix of regular controlled sized wells was fabricated. Chemical reactions leading to covalent grafting were run to demonstrate that the inner surface of the wells remains still reactive after polymerization. The grafting of fluorophores with carboxylic functions activated by N-hydroxysuccinimide was studied as function of time, in order to determine the best reactions, conditions. Then, the grafting of two distinct fluorescent probes was led simultaneously inside the wells, showing the possibility of spatial localization of diverse reactions on the same support. The covalent and localized bindings were confirmed by fluorescence spectroscopy and microscopy analyses.

1. INTRODUCTION

Probes biomolecules arrays are nowadays more and more used in research field to detect, determine, or quantify complementary targeted biomolecules (DNA, proteins, cells, tissues, etc.). An important point is the probe biomolecule immobilisation on the support which must be well located, stable (a covalent binding with the support is suitable) while keeping binding properties of biomolecules. Among the different technology processes for reaching these structured biosensor supports, thin polymer film-based substrates are currently used to afford robust patterns [1–5]. So, the shape of the polymeric structure was devised to fit the "tools" used in Life Sciences Laboratories: multichannel micropipets for multiple simultaneous depositions, microplates readers for analyses.

In this paper, we demonstrate that photolithography remains a simple and reproducible process for polymer patterning that generates surface-confined amino groups which can be subsequently used for immobilisation of compounds. Through the use of stereolithography process, we have fabricated a polymeric matrix including millimetre-sized wells on the surface of glass slides.

Thanks to the hydrophobic nature of the polymer, the ministructures so made can also provide ideal 3D aqueous environment which might be very convenient for the capture of biomolecules.

The work can be resumed in three steps:

(1) the stereolithography process to get the polymeric matrix,

(2) the covalent grafting of fluorescent probes to demonstrate that the surface remains reactive in the wells and finally,

(3) the fluorescence to validate the grafting.

2. LOCALIZATION OF REACTIVE SITES ON A MICROSCOPE SLIDE BY STEREOLITHOGRAPHY

2.1. The supports and products

The supports, glass microscope slides silanised with an amino linker, 3-aminopropyltriethoxysilane (APTS), chemicals,

and solvents were purchased from Sigma-Aldrich (Chimie Tech Services, Anthony, France). After having tested different monomers, SU-8 photoresist (MicroChem Corp., Newton, Ma USA) was selected. Its formulation is based of EPON SU-8 resin (glycidyl-ether-bisphenol-A novolac) dissolved in γ-butyrolactone (52 wt%), and a triaryl sulfonium salt as the photoinitiator. The main interesting physical characteristics are the low density ($d = 1.164$) which allows an easy recoating and the high glass temperature ($T_g > 200°C$) suitable for thermal treatment.

Stability of the cured resin was tested by immersing coated slide in different solvents at room temperature. The polymer appeared very stable in solvents such as methylene chloride, absolute ethanol, and acetone (2 days for each of them) in propylene glycol methyl ether acetate (PGMEA), sodium bicarbonate buffer pH 8.5 (5 days). In pure DMF, the film was completely and rapidly stripped from the surface keeping its patterned structure.

After the demonstration that polymer issued from SU-8 was sufficiently resistant, we investigated the step of shaping by polymerization.

2.2. The coating and photopolymerization

The process comprised the coating, curing, and baking operations. Polymerization occurred on one side of the slide, except on the frosted end. Prior to use, silanized glass slides were rinsed with acetone and dried. SU-8 photoresist (2 mL) was dropped on the centre of each slide and spun on its surface using a spin coater (Karl Süss, RC Spin Coater CT62 V08, Saint Jeoire, France) at a spin speed of 600 rpm during 30 seconds. Solvent was evaporated by a baking on a hot plate at 95°C during 5 minutes. Higher baking times were found to lead to air bubbles formation inside SU-8 film.

Stereolithography process was used to polymerize photoresist at the surface of the slide (Figure 1). This technology enables the fabrication of many complex shapes and has been presented in previous papers [6]. The Spectra-Physics Model 2020 argon ion laser was used for irradiations in the near ultraviolet (wavelength 363.8 nm) with an exposure of 300 mJ/cm^2. Matrix of regular polymeric wells was obtained by successive duplications of an empty disc pattern inside a full polymer square, in the four directions (right, left, up, down). The shape is composed of a basic element like a hollow cylinder surrounded by a filled surface around it (Figure 2).

A program has been written in C++ for tracing the pattern with galvanometric mirrors directly on the basis of geometric parameters, without going through the usual steps of CAD, slicing, and manufacturing. To get compact cross-linking, we performed the hatch spacing up to a value less than the laser beam diameter, in the two orthogonal directions (x, y). The spot laser diameter was 0.2 mm in width, while the hatch space was set at 0.1 mm. When drawing the shape, the software uses two kinds of vectors. The first ones are used for tracing circles and the others are used for filling the outside surface of the circle with horizontal (x) and vertical (y) lines called hatching.

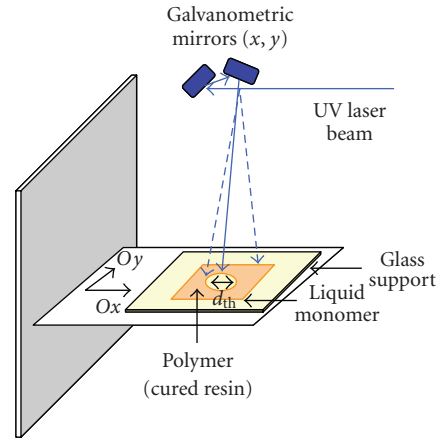

Figure 1: Structuration of the support by stereolithography.

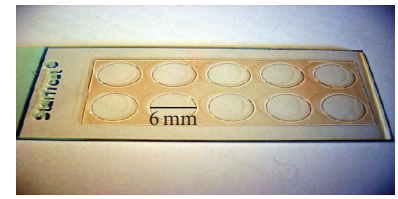

Figure 2: Shape of the polymeric structure obtained on the support (model of "low-density bioarray").

The improvement consisted of taking into account each point of coordinates within or outside the circle. Furthermore, there was a possibility to store hatch information in a file in order to verify the good accuracy in particular to determine whether there is an intersection between the hatching line (x or y) and contour lines as circles. Therefore, there was a double exposition at the intersection of circles and hatching lines as also at the intersections of horizontal (x) and vertical (y) lines of the hatching step.

In order to achieve the cross-linking of the exposed parts, a postexposure bake was carried out on a hot plate at 95°C during 2 minutes and then the slide was immersed in SU-8 developer under agitation for about 5 minutes, then had been dried. Finally, a strong adhesion of the polymer on the surface of the slide was obtained by a postcuring under UV lamps for 15 minutes and a baking on a hot plate at 95°C for 30 minutes.

2.3. Dimension characteristics of the polymeric shapes and accuracy

Surface profiles measurements have been recorded with the optical microfocus measurement system (UBM) and actual heights of the SU-8 wells measured by scanning at the surface of the polymeric structure build on the support.

First, we defined the elementary shape of a cross-section, which is a circle of 13 mm diameter centred in a square of 17 mm side. By duplicating this pattern once, we obtained two identical wells as represented on Figure 3. Thus, to define

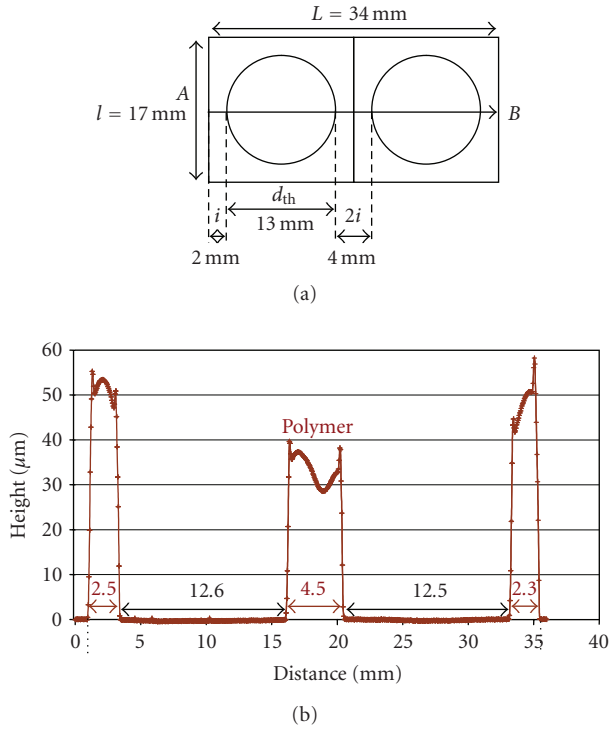

FIGURE 3: (a) Top view of the geometrical shape of two large wells. (b) Experimental AB line profile (d_{th} = 13 mm).

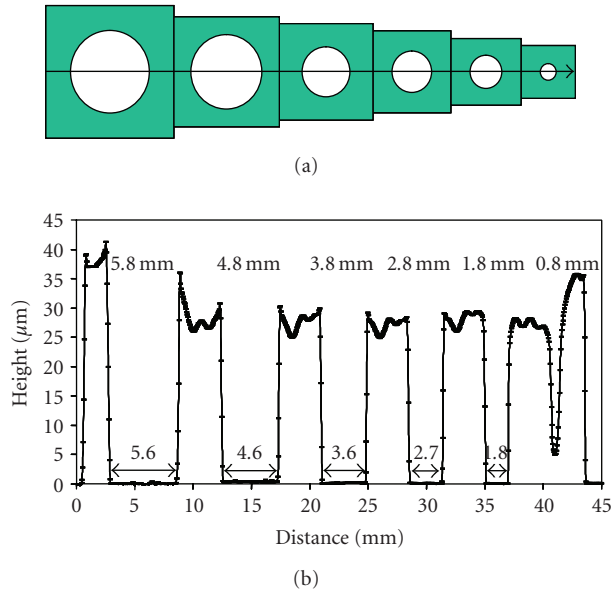

FIGURE 4: (a) Top view of the theoretical shape of linear matrix with decreasing diameter; (b) line profile of 6 polymer wells with decreasing diameter from 6 to 1 mm.

the diameter of circle equal to 13 mm, we have to take into account the diameter of the beam (200 μm).

The wells so defined and fabricated have been analyzed by the optical profilometer along the direction AB as shown on Figure 3.

The line profile represents the thickness of the polymer along the line AB crossing the centres of the 2 wells. The origin of the vertical axis z which defines the height corresponds to the level of the horizontal plane of the glass support ($z = 0$).

We can observe that the patterns are clean and correctly reproduced. The polymeric layer seems uniform with a relatively constant thickness, except on the edge of the square where the polymer is thicker.

These small peaks due to an over polymerization may be explained, as mentioned before, by the scanning of the pattern and therefore by a supplementary curing on the borders of the shape. It can be also mentioned that the surface of the polymer is not perfectly plane. Nevertheless, the thickness of the polymer remained more or less constant (between 31 and 38 μm) with a variation which can be estimated to 18%.

We have searched in a second step to manufacture smaller wells, by decreasing the diameter regularly as far as reaching a minimum value. Although the chosen resin allows the manufacturing of micro structures, the process is limited by the focus diameter of the laser beam. We kept the basic pattern which was a circle centred inside a square. The shape was duplicated by successive scanning according to one direction; we imposed a decreasing diameter from 6 to 1 mm, while maintaining constant the interval between the circle and the outside square (Figure 4). The analysis of the profile, concerning a surface measuring 45 × 12 mm, is represented on Figure 4. Whatever the size of the well, the shape was correctly reproduced.

First of all, we notice that it is possible to manufacture wells until 1.8 mm of theoretical diameter presenting satisfactory lateral profiles. Indeed, it was difficult to clean the inside of the smallest wells (around 1 mm). Between the wells, the polymer walls have a height of 27 μm on average. As it has been observed previously, the polymer was thicker on the sides with a value varying between 36 and 42 μm. We also found the small peaks of over polymerization affecting the outside limit of each well corresponding to the intersections of the hatching lines.

The above results imply the feasibility of more complex patterns. For example, Figure 5 shows the fabrication of a 2D matrix with a constant diameter of the wells and the resulting profile. The fabrication was performed by duplicating several times the same elementary shape according to x and y directions. The surface analysis was made along lines L_1 and L_2 crossing the centres of the wells as shown on Figure 5.

One recovers the peaks of over polymerization already mentioned. Far from the edges, the polymer surface remains constant according to one axis. However, the polymer is globally thicker in L_2 than in L_1 due to the angle of the laser beam with the vertical axis in the scanning system and the consequent different irradiation intensity.

In order to determine the accuracy we have scanned a grid in polymer (45 × 18 mm) in the two orthogonal directions with hatch spacing of 1 mm. The corresponding line profile is presented on Figure 6. At first sight, we can observe that the polymer thickness is practically constant

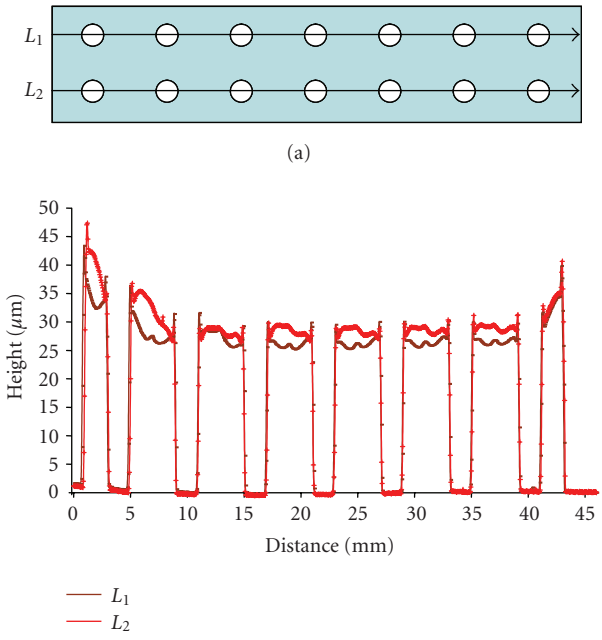

Figure 5: (a) Top view of the theoretical matrix surface with the directions L_1 and L_2; (b) surface profile along L_1 and L_2.

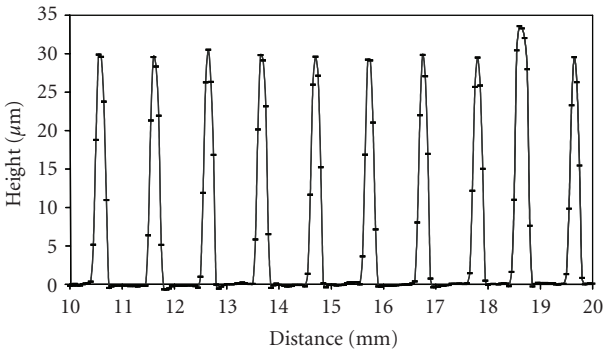

Figure 6: Line profile of a polymeric matrix with a 1 mm hatch spacing.

and equal to 30 μm on the whole length. These results are otherwise very encouraging since we could define small square wells of 1 mm side delimited by thin walls in polymer.

3. FLUOROPHORES COVALENT GRAFTING AND CHARACTERIZATION

Glass surfaces are well adapted for microarray applications because they present good mechanical properties, with low intrinsic fluorescence. They also possess a relatively homogeneous chemical surface which can be easily modified and furthermore, they are not very expensive. For our study, we have selected commercially available microscope slides already silanized by a hetero linker bearing an amino terminal function.

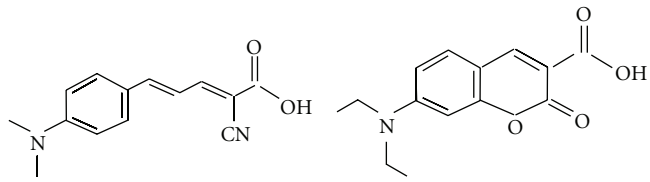

Figure 7: Structure formulas of the two fluorophores CiCOOH and CouCOOH.

Furthermore, for a future sensor application, the spots need to be uniform, accurate without spreading the analytes solution to the adjacent areas of the macroarrays. We have thought that these requirements could be achieved through the creation of wells embedded in a polymer covering the surface.

3.1. Fluorophores covalent grafting

Chemical reactions leading to covalent grafting were run to demonstrate that the inner surface of the wells remains active after the polymerization.

We have chosen as models two distinct wavelength fluorescent probes already studied in our laboratory [7, 8]. These fluorophores are "molecular rotors" easily synthezised: the first compound 2-cyano-5-(4-(N,N-dimethylamino)phenyl)-2,4-pentadienoic acid (CiCOOH) is a cinnamilydene derivative [7]; the second one, 7-(N,N-diethylamino)coumarin-3-carboxylic acid (CouCOOH), has a coumarin structure [9] (Figure 7). The two fluorescent probes comprise in their structure a carboxylic acid function well suited for a covalent robust amide bond with the amino of the surface.

As previously described about covalent graftings of other acidic compounds on solid substrates [10], the acidic function has been activated with N-hydroxysuccinimide.

Grafting of fluorophore active esters to amino solid support through amide bond, occurs at room temperature, safe from light, in sodium bicarbonate buffer, pH 8.5. After grafting, the slides were carefully washed by successive immersions under magnetic stirring, in deionised water, absolute ethanol, and dichloromethane. Then, they were air dried and stored until fluorescence analysis. The covalent bindings on the slides were confirmed by fluorescence spectroscopy and microscopy analyses.

3.2. Fluorescence spectroscopy study of the grafted probes

The covalent binding of each fluorophore was first conducted on a separate slide to define their respective fluorescence properties. For this study, the slide was immerged in the sodium bicarbonate buffer, pH 8.5, containing the fluorophore, under slight agitation during 4 hours. After the general work-up described above, the fluorescence has been measured at different sites all along the slides. The

fluorescence spectra were recorded on a Horiba Jobin-Yvon Fluorolog3 spectrofluorimeter and were corrected from lamp variations. Experiments were carried out at room temperature, the glass slide being in front-face position in order to avoid light reflection. The excitation/emission fluorescence fields of the two fluorophores were well separated as expected considering previous studies. The conditions of excitation-emission were 470–565 nm and 410–467nm for Fluorophores CiCONHX and CouCONHX, respectively.

We have gathered (Figures 8 and 9) the emission spectra obtained with each fluorophore. For the cinnamylidene derivative (CiCOOH grafting), the fluorescence signal A_i was recorded at six places on the slide (Figure 8). The signal B (background) of the native slide has been also reported; it has been subtracted from signal A_1 to exhibit the grafted cinnamilydene fluorescence ($A_1 - B$); so the maximum fluorescence is well characterized at 565 nm for a 470 nm excitation. Two remarks might here be done: on the one hand, the signal is not uniformall over the slide, with a 28% variation observed between two extreme measures: this fact may be imputed on the inhomogeneity of the native slide, but on the other hand the fluorophore response is distinct from the support one at this wavelength excitation.

For the coumarine derivative (CouCOOH grafting) the fluorescence signal was also recorded at six places of the slide (Figure 9). We have not reported the signal of the native slide which was negligible at this wavelength excitation. In this case, we can see a low deviation of the fluorescence signal; indeed, a difference of 11% between the two extreme spectra has been observed. Another interesting feature is the very important observed fluorescent signal.

These two fluorophores show specific fluorescent characteristics which have been useful for the characterization of localized graftings.

3.3. *Fluorescence microscopy study for the localization of the grafted probes*

In order to determine the optimal reactions' conditions on the structured support, the grafting of these two fluorophores was studied in function of time (Figure 10). Grafting reaction was carried out by successive deposition of the same volume of known fluorophore concentration solution into the macro wells in a saturated sodium bicarbonate buffer atmosphere. The reaction occurs with time, the first deposition corresponding to the longest-time reaction and the last one to the shortest-time reaction.

The fluorescence intensities in macrowells were measured with a Zeiss Axiotech epifluorescence microscope, coupled to a Hamamatsu IP28 photomultiplier. Two filter sets were used in order to differentiate the two fluorescent probes CiCOOH and CouCOOH. All measurements were repeated five times, at different places of the well, the diameter of the excitation spot being fixed to 200 μm. As we can see on Figure 10, the best conditions of grafting the two fluorophores were obtained after 24 hours of reaction.

Then, the grafting of the two distinct fluorescent probes (CiCOOH) and (CouCOOH) was led simultaneously inside the wells. For this, we have deposited the two probes

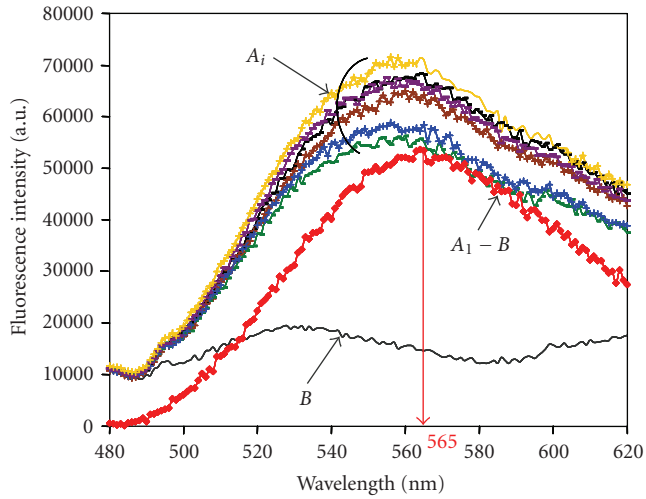

Figure 8: Emission spectra obtained with the cinnamylidene derivative (CiCOOH grafting); A_i: recorded at 6 different positions on the slide; B: background signal of the original slide; $A_1 - B$: signal corrected from background.

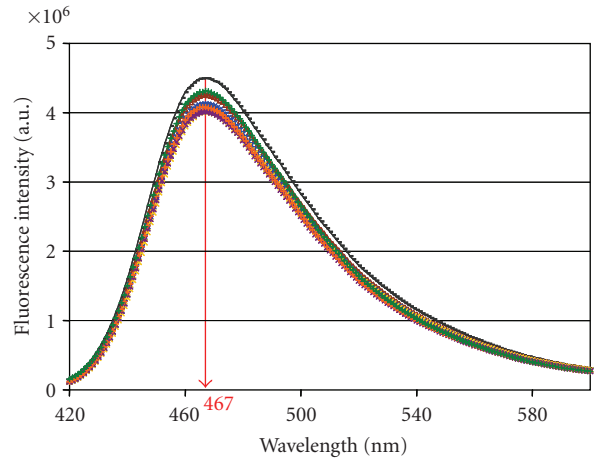

Figure 9: Emission spectra obtained with the coumarine derivative (CouCOOH grafting).

alternatively in a matrix of 10 wells to confirm that the inner area was still reactive after the polymerization step (Figure 11). The aim of this experiment was to prove that many different reactions may be conducted on a same support which is a condition of future developments in the industry for diagnostics test.

The fluorescence of each probe was recorded in five selected places in the same well, by fluorescence microscopy. Dispersion of measurements is shown on Figure 12 using the filters set relative to CouCOOH probe. Even if homogeneity in a well seems not as good as those obtained on a bare slide, due to the smaller size of the observation spot, the two probes are clearly differentiated, in spite of a weak overlap between the two filter sets.

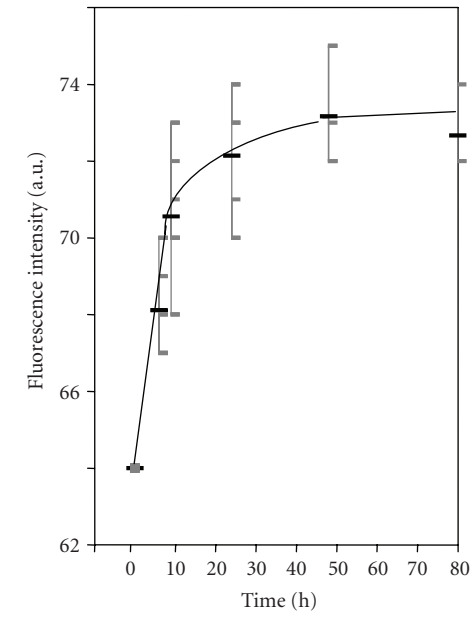

(a)

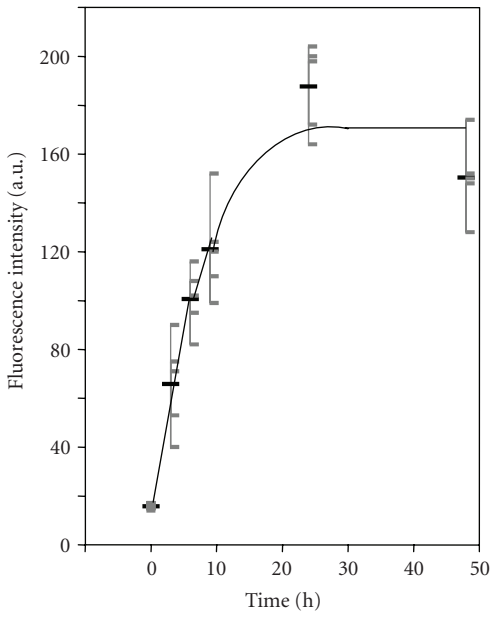

(b)

Figure 10: Time evolution in covalent grafting of CiCOONHS ((a) 6 hours, 9 hours, 24 hours, 48 hours, and 80 hours) and CouCOONHS ((b) 3 hours, 6 hours, 9 hours, 24 hours, 48 hours). The best conditions were reached after 24 hours of reaction.

4. CONCLUSIONS AND FUTURE WORKS

This preliminary work validates the fabrication process for generating polymeric matrix of wells, the size, the geometry, the number, the localization of which being well controlled. We have demonstrated the possibility to localise reactive sites in a polymer matrix shaped on a commercial glass slide. In this way, three main points have been developed. The local

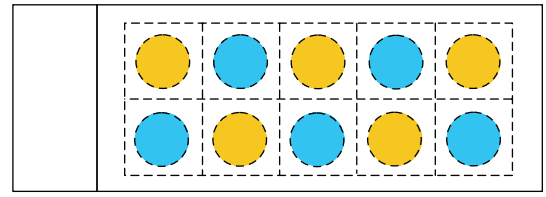

Figure 11: Matrix of 2 × 5 wells (diameter = 5 mm; distance between wells = 3 mm) with CiCOONHS and CouCOONHS grafted alternatively by deposition of 10 μL≈60 nmol of each fluorophore solution.

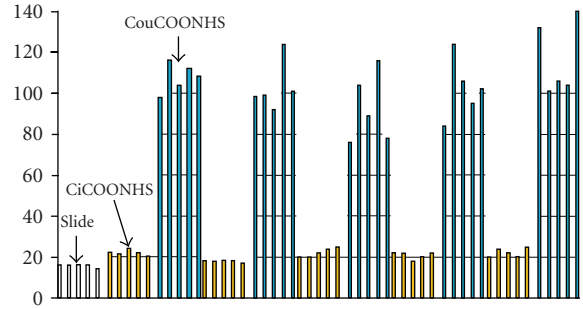

Figure 12: CiCOONHS and CouCOONHS alternatively grafted in the 10 wells of the matrix analyzed by fluorescence microscopy (filters Zeiss: λ_{exc} [395–440]; λ_{em} > 470 nm; magnification ×5; gauge 4).

area on functionalzed substrates delimited by polymer wells remained reactive as demonstrated by the covalent graftings of suited fluorophores followed by spectrofluorimetry or fluorescence microscopy analyses. We have cured the resin SU-8 with a closely spaced hatch pattern until 1mm resolution. An over polymerization at the crossing points of the plotting lines has been demonstrated. This problem will be resolved by developing a higher-density microarrays synthesized by photolithographic methods analogous to the techniques used in the semiconductor industry. This original method is based on dynamic photolithographic masks provided by Texas Instrument (Tex, USA) with digital light processor (DLP), often called digital micromirror device (DMD) [11, 12]. Future biomedical implementations include antibody array where different antibodies could be grafted into the wells to realize micro ELISA tests; an immunohistochemistry robot could be used to treat the glass slides.

ACKNOWLEDGMENTS

This work was supported by the French Research Ministry, MENESR (F. Evenou), CNRS (S. Corbel, F. Baros), and INSERM (M. C. Carré, N. Martinet, M. Donner).

REFERENCES

[1] J. Hyun and A. Chilkoti, "Micropatterning biological molecules on a polymer surface using elastomeric microwells,"

Journal of the American Chemical Society, vol. 123, no. 28, pp. 6943–6944, 2001.

[2] M. Yan and M. A. Bartlett, "Micro/nanowell arrays fabricated from covalently immobilized polymer thin films on a flat substrate," *Nano Letters*, vol. 2, no. 4, pp. 275–278, 2002.

[3] D. Falconnet, D. Pasqui, S. Park, et al., "A novel approach to produce protein nanopatterns by combining nanoimprint lithography and molecular self-assembly," *Nano Letters*, vol. 4, no. 10, pp. 1909–1914, 2004.

[4] J. D. Hoff, L.-J. Cheng, E. Meyhöfer, L. J. Guo, and A. J. Hunt, "Nanoscale protein patterning by imprint lithography," *Nano Letters*, vol. 4, no. 5, pp. 853–857, 2004.

[5] C. L. Feng, A. Embrechts, G. J. Vancso, and H. Schönherr, "Reactive μCP on ultrathin block copolymer films: localized chemistry for micro- and nano-scale biomolecular patterning," *European Polymer Journal*, vol. 42, no. 9, pp. 1954–1965, 2006.

[6] M. Furman, S. Corbel, H. Le Gall, O. Zahraa, and M. Bouchy, "Influence of the geometry of a monolithic support on the efficiency of photocatalyst for air cleaning," *Chemical Engineering Science*, vol. 62, no. 18–20, pp. 5312–5316, 2007.

[7] M. C. Carré, C. Geoffroy-Chapotot, M. Adibnejad, P. Berroy, J. F. Stoltz, and M. L. Viriot, "Fluorescent molecular rotors with specific hydrophilic functions: glucosamine and inositol derivatives," *Journal of Fluorescence*, vol. 8, no. 1, pp. 53–57, 1998.

[8] C. Muller, P. Even, M.-L. Viriot, and M. C. Carré, "Protection and labelling of thymidine by a fluorescent photolabile group," *Helvetica Chimica Acta*, vol. 84, no. 12, pp. 3735–3741, 2001.

[9] A. Song, X. Wang, and K. S. Lam, "A convenient synthesis of coumarin-3-carboxylic acids via Knoevenagel condensation of Meldrum's acid with *ortho*-hydroxyaryl aldehydes or ketones," *Tetrahedron Letters*, vol. 44, no. 9, pp. 1755–1758, 2003.

[10] G. MacBeath, A. N. Koehler, and S. L. Schreiber, "Printing small molecules as microarrays and detecting protein-ligand interactions en masse," *Journal of the American Chemical Society*, vol. 121, no. 34, pp. 7967–7968, 1999.

[11] J. Vasco, N. André, and P. Bartolo, "Micro-fabrication: the state-of-the-art," in *Proceedings of the 2nd International Conference on Advanced Research in Virtual and Rapid Prototyping*, pp. 483–490, Leiria, Portugal, September-October 2005.

[12] J. R. Zyzalo, O. Diegel, and J. Potgieter, "Rapid prototyping: rapid flashing for SLA layering techniques," in *Proceedings of the 2nd International Conference on Advanced Research in Virtual and Rapid Prototyping*, pp. 449–454, Leiria, Portugal, September-October 2005.

Hindawi Publishing Corporation
International Journal of Photoenergy
Volume 2008, Article ID 540971, 5 pages
doi:10.1155/2008/540971

Research Article

Analysis of Surface Texturization of Solar Cells by Molecular Dynamics Simulations

Hsiao-Yen Chung, Chiun-Hsun Chen, and Hsin-Sen Chu

Department of Mechanical Engineering, National Chiao Tung University, Hsinchu 300, Taiwan

Correspondence should be addressed to Hsin-Sen Chu, hschu@cc.nctu.edu.tw

Received 11 April 2008; Revised 18 May 2008; Accepted 4 June 2008

Recommended by Mohamed Sabry Abdel-Mottaleb

The purpose of this paper is to develop a simple new model, based on the classic molecular dynamics simulation (MD), alternative to complex electron-photon interactions to analyze the surface texturization of solar cells. This methodology can easily propose the absorptance differences between texturing and nontexturing solar cells. To verify model feasibility, this study simulates square, pyramidal, and semicircular texturization surfaces. Simulations show that surface texturization effectively increases the absorptance of incident light for solar cells, and this paper presents optimal texturization shapes. The MD model can also be potentially used to predict the efficiency promotion in any optical reflection-absorption cases.

1. INTRODUCTION

Achieving higher efficiency in solar cells is one of the most important issues in recent studies on the topic, and researchers have examined many methods for achieving this goal. Surface texturing of solar cells is a common approach to reduce incident light reflection and, consequently, increase solar cell efficiency.

Dry etching and wet etching are commonly used to apply surface texturization to solar cells. Dry etching means texturing without wet solutions. A plasma texturing technique using reactive ion etching, with advantages of low cost consumption and independence from crystallographic orientation, was previously proposed [1, 2]. A selective surface texturing technique using lasers recently gained some interest. Tan et al. [3] performed femtosecond pulsed laser induced forward transfer on a quartz substrate. A trench-like texturing was ablated on the donor substrate using a pulsed laser. This method exhibits good controls on the depth and width of ablated trenches.

Wet etching means surface texturing with chemical solutions. In a general surface texturing process on crystalline silicon, alkaline solutions form pyramids. This pyramidal surface shape occurs because alkaline solutions etch silicon along crystallographic orientations.

Some researchers use acid solutions to produce surface texturization. Due to the character of acid solutions, the etching rates in the different orientations are similar. Thus a semicircular structure is formed [4].

Most texturing studies focus on wet etching processes. Hylton et al. [5] conducted many experiments to compare the efficiency increase of saw-damage etching and texture etching processes using alkaline solutions on multicrystalline silicon wafers. That paper also explained the geometrical paths of incident light which defined the absorption and reflection on the pyramid structures. Nishimoto and Namba [6] developed a low-cost wet etching manufacturing process and reported the texturization of a monocrystalline silicon surface with low-cost alkaline solutions, Na_2CO_3. Recently, Gangopadhyay and his colleagues [7] further developed a new texturing method with tribasic sodium phosphate solution, claiming it was superior to the conventional method because it used less isopropyl alcohol for texturing.

The most previous studies focused on the manufacturing process. However, if we can simulate the behaviors of absorption and reflection before fabricating a new surface texturizaion on a solar cell, it is helpful to reduce the time and fabricating wastes. Therefore, it is necessary to develop a simulation methodology to govern this issue.

Molecular dynamics simulation is a technique well suited to nanoscale phenomena and mechanical behaviors. However, few studies use MD to examine solar-cell issues. One such study [8] explores the photo-induced electron-transfer phenomena on a dye-sensitized titanium solar cell with nonadiabatic MD simulations, which is based on the *ab*-initio functional theory. The study found that approximately 20% of the acceptor state was located on a titanium atom of the first surface layer. This simulation also predicted a complex non-single-exponential time-dependence of the electron-transfer process. However, many unknown factors in photon-electron interactions prevent studies from being conducted on the issue of photon absorption.

This paper presents a simple photon-atomic model with molecular dynamics simulations to explore the effects of three shapes of solar cell surface texturization. This paper also includes an estimation of the optimum texturization.

2. METHODOLOGY

First of all, if the de Broglie wavelength of a photon and an atom is smaller, we can make assumption that the absorption and reflection are closely represented as a series of collision behaviors between photons and atoms.

To avoid complications in photon-electron transformation, a rough and simple MD model was devised to govern this problem. In the classic mechanical MD simulations, a two-body attractive-repulsive potential model governs the interaction between two particles. For one particle, short-range repulsive forces rebound the too close particles from itself, and long-range attraction catches other particles closer to itself in attractive force field. Assuming that the force field between an atom and photon is spherical, the 12-6 Lennard-Jones potential model with an undetermined parameter k, which is a short-range multiple, is adopted,

$$U(r) = 4\left[k\left(\frac{1}{r}\right)^{12} - \left(\frac{1}{r}\right)^{6}\right]. \quad (1)$$

When photons reach the substrate, attraction and repulsion behaviors occur between silicon's atoms and photons. Figure 1 shows the mechanism of photon-atom interactions. When a photon enters the attractive field of an atom, the photon should be attracted to the center of the atom. But the repulsive force pushes the photon off center if the photon is too close to the atom center. The substrate is maintained as an NVE model (fixing particle numbers, system's volume, and total energy) in the heat-transfer process, so the photons which enter the substrate are constrained because of forces among atoms and decay of motive energy of themselves. Due to the actions of attractive and repulsive forces and the photon energy dissipation, the velocity of a photon which enters the substrate deeply tends toward zero. This behavior is considered photon absorption in a solar cell. However, some photons are repulsed at the substrate surface due to the repulsive force. This is considered reflection. The photons whose velocity decreases to zero were removed to avoid the increasing of particle numbers, and then affect the system energy.

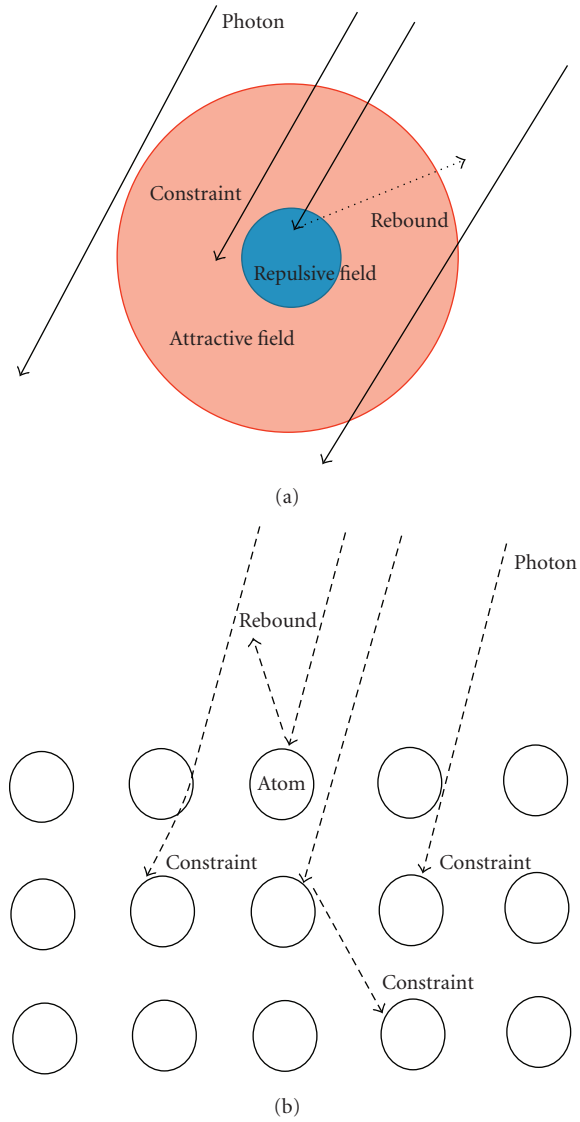

Figure 1: Illustrations of attractive and repulsive interaction of atoms and photons. (a) The photons move toward repulsive force field is probably rebound out, and the other photons move through attractive field is constrained or decelerated. (b) The rebounded behavior is as same as reflection. The constraint behavior is as same as absorption.

Note that the efficiency of monocrystalline silicon is, at most, 24.7% [9]. This study attempts to make a model with an absorptance reaching 24.7% in a smooth, nontextured substrate by simply adjusting k. In our simulation, k is determined to be 3.86. After this calculation, simulations of varying surface texturization with this potential model can proceed. The smooth surface model is a reference, and the other texturing models in this paper, which are simulated with the same conditions, can then be compared with the reference model. This methodology not only reasonably avoids the complexity of photon-atom interaction but also achieves the goal of trying to evaluate the efficiency of two models with different surface texturization.

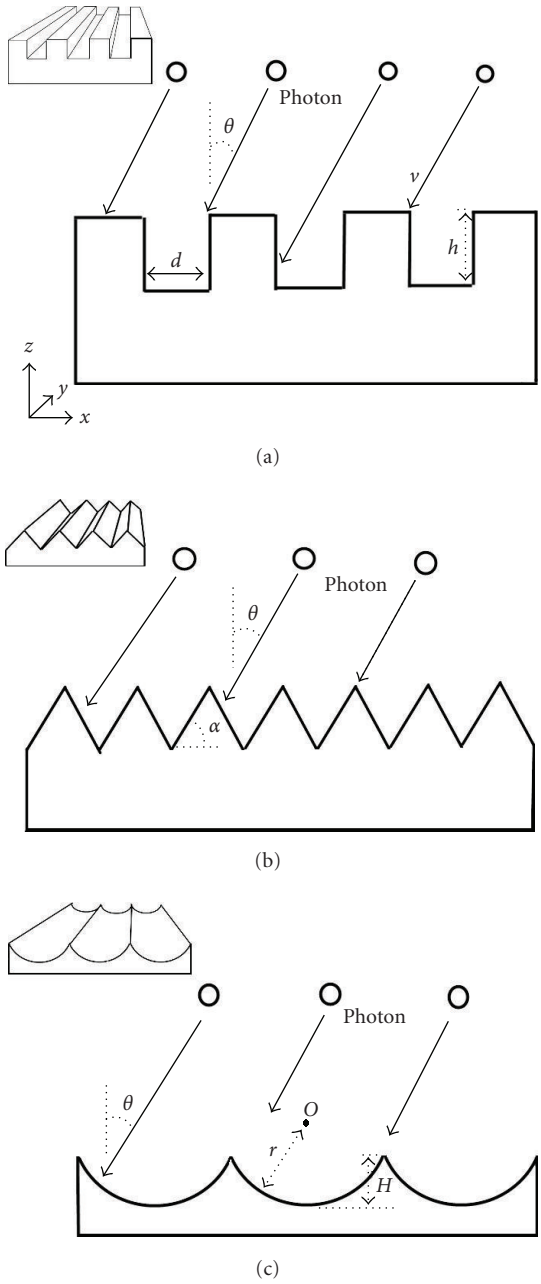

Figure 2: Physical model (a) square (b) pyramid (c) semicircle, the geometric variables are also shown in this figure.

Following this concept, monocrystalline silicon was selected as the solar cell material. This is because silicon is the most common material in all types of solar cells, and its structure is simpler for using with an MD model. The results and conclusions of this study can also be extended to other solar cells, GaAs, InGaAs, InGaP, and so forth. According to the reviews of previous studies, square, pyramidal, and semicircular texturing were demonstrated. Figure 2 shows the physical models of the three samples in this paper. A single silicon cell has a diamond structure with 8 atoms. Under the texturing surface, three layers absorb the motion

Table 1: Parameters.

Fundamental quantities	
Mass	4.65×10^{-23} g/atom in silicon
Length α	5.431 Å
Energy ε	1.792×10^{-19} J
Time t	1.77×10^{-3} ps/step
Normalized quantities	
Light speed (photon's speed) c^*	4.8×10^{6}
Temperature T^*	0.0231
Mass m^*	0.54

energy of photons. To avoid the effects of different lengths in the x- and y-directions, the substrate of solar cells is set as a square. Periodic boundary conditions are imposed in the x- and y-directions. Due to the periodic texturing shapes, different period lengths lead to different numbers of atoms. In the case of different intervals of square texturization, at least six periods are chosen. So in the case of distance $d = 1$ cell, the number of silicon atoms is 144352. The longer the distance, the more atoms are present in the substrate. The photon incident angle varies at x-z plane. The system temperature keeps at 300 K. Table 1 shows the physical parameters of this model.

3. RESULTS AND DISCUSSION

Figure 3 shows the relationship between the height of square texturing and absorptance for the square surface case. When $h = 0$, the surface of solar cells is smooth, and the absorptance is 0.247 at an incident angle of 0 degrees. When surface texturing exists, the specimen with a greater square height has higher absorptance. However, the rate of increase becomes smaller as the height increases. Photons can easily drop into the holes with higher walls, so the substrate absorbs more photons. If the incident angle of photons increases, the absorptance lessens because more photons rebound.

Figure 4 shows how the various distances affect the absorptance. As the distance increases, the absorptance obviously decreases when the square height is 2.31 Å. As in Figure 3, the absorptance decreases as the incident angle of the photons increases. The absorptance decreases slowly when the distance surpasses 6.94 Å. In other words, the effect decreases as the distance increases.

The next example simulates a pyramidal surface. Figure 5 shows the influence of the facet tilt angle α. In this figure, the absorptance increases as the tilt angle α increases. Moreover, the rate rises quickly when α is more than 30 degrees. This result indicates that a more acute pyramid structure causes a decrease in reflection. Hylton et al. [5] discussed the possible path of light incident upon geometrically textured surface in air and concluded that a blunter facet tilted angle (sharp pyramid) facilitates light double-bounce incidence, thereby reducing surface reflection. Our results agree with that conclusion. However, the current results are totally contrary to the research by Xi et al. [4]. This is because the present study assumes the pyramid to be isosceles; thus, the

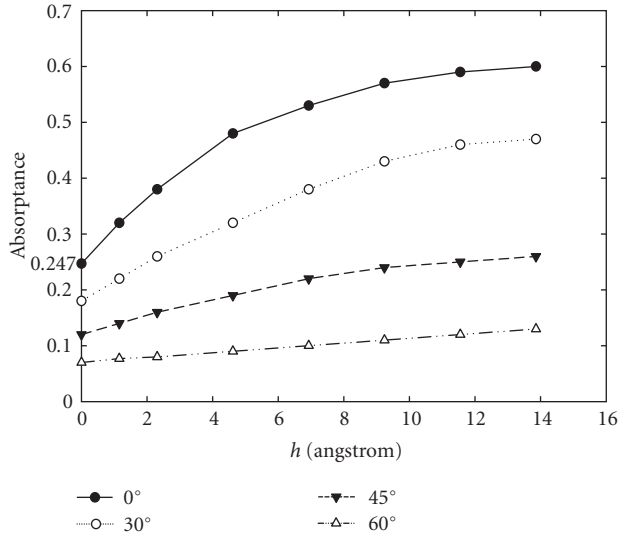

Figure 3: The relation among absorptance, h and photon's incidence angle θ.

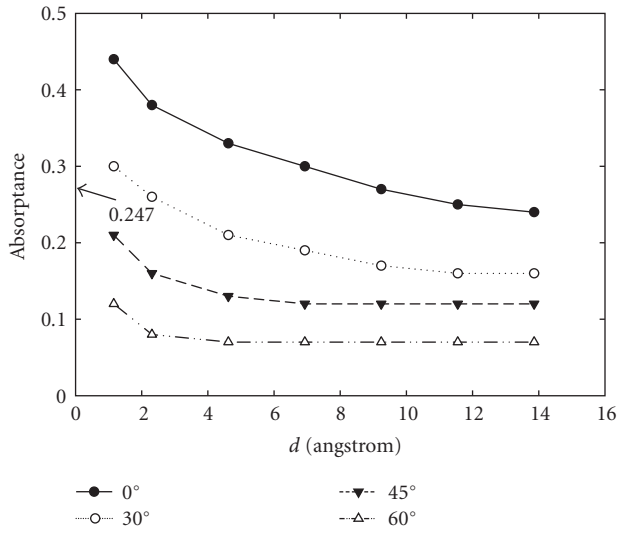

Figure 4: The relation among absorptance, distance and photon's incidence angle θ.

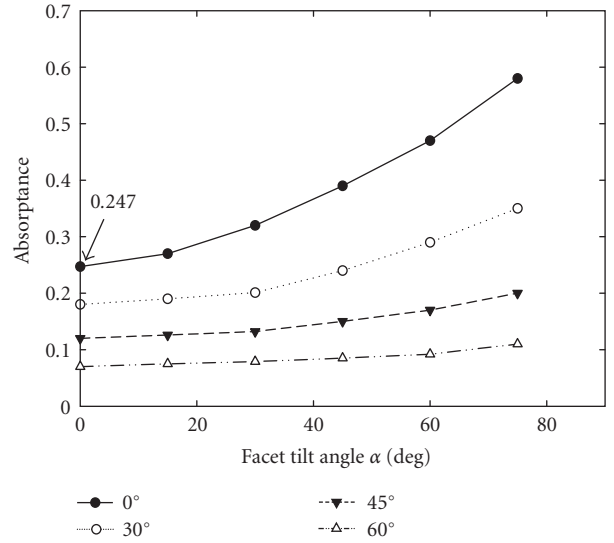

Figure 5: The relation among absorptance, facet titled angle α, and photon's incidence angle θ.

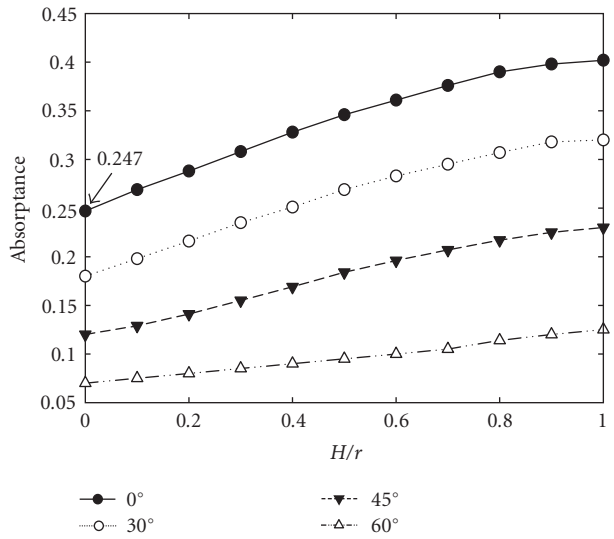

Figure 6: The dependence of absorptance on H/r in the case of semicircular texturing surface.

pyramids become sharper and taller with increasing α. This supposition leads to this phenomenon. As expected, a larger incident angle causes lower absorptance. Figure 5 shows this result.

Finally, Figure 6 shows the case of a semicircular surface. Varying the ratio of H/r, the absorptance shows a clear rising trend from 0.247 at $H/r = 0$, at which the surface of substrate is smooth, to a semicircular hole, $H/r = 1$, if vertical light meets the substrate. Obviously, the increasing rate of absorptance decreases if H/r rises. The same trend occurs at 30, 45, and 60 degrees of the incident angle, but the magnitude of absorptance is lower than that exposed by vertical light. This trend of absorption agrees well with the findings of Xi et al. [4].

4. CONCLUSION

In conclusion, this study proposes a new and simple MD model alternative to complex electron-photon interactions in quantum scale to analyze surface texturization of solar cells. Three surface texturization shapes are simulated with various angles of incident light. This methodology can easily determine the absorptance differences of various surface texturizations, and suggest better texturization shapes. Increasing the trench depth, shortening the distance between two trenches, sharpening pyramids, and adding more circling to the semicircular structure all help improve the efficiency of solar cells.

In this study, we ignore the wave behavior of photons and atoms. In fact, according to the wave-particle duality, the wave behaviors affect, either more or less, the absorption and reflection of solar cells. However, this study is a beginning to simulate the absorption by molecular dynamics. Our results also agree well with previous studies. This MD model can potentially be used to predict the efficiency promotion in any optical reflection-absorption cases.

REFERENCES

[1] T. Sakoda, K. Matsukuma, Y.-M. Sung, K. Otsubo, M. Tahara, and Y. Nakashima, "Additional plasma surface texturing for single-crystalline silicon solar cells using dielectric barrier discharge," *Japanese Journal of Applied Physics. Part 1*, vol. 44, no. 4A, pp. 1730–1731, 2005.

[2] W. A. Nositschka, C. Beneking, O. Voigt, and H. Kurz, "Texturisation of multicrystalline silicon wafers for solar cells by reactive ion etching through colloidal masks," *Solar Energy Materials and Solar Cells*, vol. 76, no. 2, pp. 155–166, 2003.

[3] B. Tan, K. Venkatakrishnan, and K. G. Tok, "Selective surface texturing using femtosecond pulsed laser induced forward transfer," *Applied Surface Science*, vol. 207, no. 1–4, pp. 365–371, 2003.

[4] Z. Xi, D. Yang, W. Dan, C. Jun, X. Li, and D. Que, "Investigation of texturization for monocrystalline silicon solar cells with different kinds of alkaline," *Renewable Energy*, vol. 29, no. 13, pp. 2101–2107, 2004.

[5] J. D. Hylton, A. R. Burgers, and W. C. Sinke, "Alkaline etching for reflectance reduction in multicrystalline silicon solar cells," *Journal of the Electrochemical Society*, vol. 151, no. 6, pp. G408–G427, 2004.

[6] Y. Nishimoto and K. Namba, "Investigation of texturization for crystalline silicon solar cells with sodium carbonate solutions," *Solar Energy Materials and Solar Cells*, vol. 61, no. 4, pp. 393–402, 2000.

[7] U. Gangopadhyay, K. H. Kim, S. K. Dhungel, et al., "A novel low cost texturization method for large area commercial monocrystalline silicon solar cells," *Solar Energy Materials and Solar Cells*, vol. 90, no. 20, pp. 3557–3567, 2006.

[8] W. Stier and O. V. Prezhdo, "Non-adiabatic molecular dynamics simulation of ultrafast solar cell electron transfer," *Journal of Molecular Structure: THEOCHEM*, vol. 630, no. 1–3, pp. 33–43, 2003.

[9] M. A. Green, K. Emery, D. L. King, Y. Hishikawa, and W. Warta, "Solar cell efficiency tables (version 29)," *Progress in Photovoltaics: Research and Applications*, vol. 15, no. 1, pp. 35–40, 2007.

Hindawi Publishing Corporation
International Journal of Photoenergy
Volume 2008, Article ID 282791, 6 pages
doi:10.1155/2008/282791

Research Article

Analysis of Pyramidal Surface Texturization of Silicon Solar Cells by Molecular Dynamics Simulations

Hsiao-Yen Chung, Chiun-Hsun Chen, and Hsin-Sen Chu

Department of Mechanical Engineering, National Chiao Tung University, Hsinchu 300, Taiwan

Correspondence should be addressed to Hsin-Sen Chu, hschu@cc.nctu.edu.tw

Received 11 April 2008; Accepted 15 May 2008

Recommended by Mohamed Sabry Abdel-Mottaleb

The purpose of this paper is to explore the relations between surface texturization and absorptance of multicrystalline silicon solar cells by a simple new model, based on the classic molecular (MD) dynamics simulation, alternative to complex electron-photon interactions to analyze the surface texturization of solar cells. In this study, the large tilted angle leads to the lower efficiency of solar cell. To consider the effect of incident angle, a range of high efficiency exists due to the increasing probability of second reflection. Furthermore, the azimuth angle of incident light also affects the efficiency of solar cells. Our results agree well with previous studies. This MD model can potentially be used to predict the efficiency promotion in any optical reflection-absorption cases.

1. INTRODUCTION

The solar cell technology has attracted recent attention due to the price rising of petroleum. In recent studies, achieving higher efficiency in solar cells is the one of most important issues on the topic. Surface texturing of solar cells is a common approach to reduce incident light reflection and, consequently, increase solar cell efficiency.

Wet etching is commonly used to produce texturization on surface of solar cells. Generally, pyramidal structure formed on the surface of silicon solar cells by alkaline solutions etching. This pyramidal surface shape occurs because alkaline solutions etch silicon along crystallographic orientations. Hylton et al. [1] conducted many experiments to compare the efficiency increase of saw-damage etching and texture etching processes using alkaline solutions on multicrystalline silicon wafers. That paper also explained the geometrical paths of incident light which defined the absorption and reflection on the pyramid structures. Nishimoto and Namba [2] developed a low-cost wet etching manufacturing process and reported the texturization of a monocrystalline silicon surface with low cost alkaline solutions, Na_2CO_3. Recently, Gangopadhyay and his colleagues [3] further developed a new texturing method with tribasic sodium phosphate solution, claiming it was superior to the conventional method because it used less isopropyl alcohol for texturing.

New solutions are also applied. Marrero et al. [4] describe a texturization method for monocrystalline silicon solar cells based on a mixture of sodium carbonate and sodium hydrogen carbonate solutions. A specific solution has been found that results in an optimal etching rate, the lowest surface reflectance, and a homogeneous density of pyramidal structures on the silicon surface. The subsequent phosphorus diffusion with rapid thermal processes has been modified in order to drastically reduce the process time and, simultaneously, to obtain a high homogeneity of the sheet resistance values and improved photocarriers lifetimes. 100×100 mm solar cells with an efficiency of 15.8% have been obtained compared to an efficiency of 14.7% for the reference cell.

Usual step during PV cell production is surface texturization, which is performed to reduce the reflection losses from the front surface of solar cells. Conventional chemical and electrochemical methods are efficient in texturing monocrystalline silicon [5]. Unfortunately, these methods are inefficient for multicrystalline silicon due to the presence of random crystallographic grain orientations and high

selectivity of etching along specific directions. Consequently, it is impossible to obtain texturization of homogeneous structure on the whole surface [6–10]. Another possibility is mechanical texturization [11]. Unfortunately, it is also not satisfactory due to possible mechanical damages, resulting in breakability and fragility of silicon and additionally very small thickness of silicon wafers. Therefore, there is a real need for a versatile gentle process that is capable of producing the layer of regular texture. The possible way of overcoming these difficulties is laser texturization [8, 12, 13].

Molecular dynamics simulation is a well-suited technique to nanoscale phenomena and mechanical behaviors [14–16]. However, few studies use MD to examine solar-cell issues. Stir and Prezhdo [15] explore the photoinduced electron-transfer phenomena on a dye sensitized titanium solar cell with nonadiabatic MD (NAMD) simulations, which is based on the *ab*-initio functional theory. The system under study is typical of the dye sensitized semiconductor nanomaterials used in solar cells, photocatalysis, and photoelectrolysis. The electronic structure of the dye-semiconductor system and the adiabatic dynamics is simulated by *ab*-initio density functional theory MD, while the NA effects are incorporated by the quantum-classical mean-field approach. A novel procedure separating the NA and adiabatic ET pathways is developed. The simulation provides a detailed picture of the ET process. For the specific system under study, ET occurs on a 30-femtosecond-time scale, in agreement with the ultrafast experimental data. Both adiabatic and NA pathways for the ET are observed. The NA transfer entirely dominates at short times and can occur due to strong localized avoided crossing as well as extended regions of weaker NA coupling. Although the adiabatic ET contribution accumulates more slowly, it approaches that of the NA ET pathway asymptotically. The electron acceptor states are formed by the d-orbital of Ti atoms of the semiconductor and are localized within the first 3-4 layers of the surface. About 20% of the acceptor state density is localized on a single Ti atom of the first surface layer. The simulation predicts a complex nonsingle-exponential time dependence of the ET process.

However, many unknown factors in photonelectron interactions prevent studies from being conducted on the issue of photon absorption. On the other hand, this issue is deserved to study.

The above literature review shows that there is still much necessity to investigate the problem of enhancing solar cells' efficiency. Also, the relations of surface texturization effects are still not well understood. In this study, a simple photonatomic model with molecular dynamics simulations to explore the effects solar cell surface texturization is developed and numerically solved to enhance the understanding of the underlying characteristics of different shapes of surface texturization by wet or dry etching.

The scope of this paper is mainly focused on the issue of relations of pyramidal structure and light absorptance. A real-closely pyramid texturization on the surface of multicrystalline silicon substrate etching by alkaline solutions is simulated by the molecular dynamics model to explore the influences of incident, azimuth and tilted angles with absorptance. The optimal shapes of this model are also discussed in our studies.

2. MATHEMATICAL AND PHYSICAL MODEL

As mentioned, the molecular dynamics simulation is a well-suited numerical method to calculate reflection caused by texturization of solar cells. The classical molecular dynamics scheme considers an n-atomic nonquantum system. Each atom i in this system is of its position r_i, velocity v_i and mass M. Thus, the motion of a particle can be described as Newton's second law:

$$M\frac{d^2r_i}{dt^2} = \sum_{j=1,j\neq i}^{N} F_{ij}, \tag{1}$$

where F_{ij} is the force exerted by atom j on atom i. The force term is derived from the interatomic potential that must satisfy both nanoscopic and macroscopic requirements. The potential function generally forms with a short-distance repulsive term and a long-distance attractive term. Given initial conditions, (1) can be solved to provide the position and the velocity of each particle as a function of time, which will be used to compute the system temperature, heat flux, and thermal conductivity.

Under the condition that the de Broglie wavelength of a photon and an atom is smaller, the assumption that the absorption and reflection closely represented as a series of attraction and repulsion behaviors between photons and atoms is reasonable.

To avoid complications in photonelectron transformation, a rough and simple MD model was devised to govern this problem. In the classic mechanical MD simulations, a two-body attractive-repulsive potential model governs the interaction between two particles. For one particle, short-range repulsive forces rebound the too close particles from themselves, and long-range attraction catches other particles closer to itself in attractive force field. Assuming that the force field between an atom and photon is spherical, the 12–6 Lennard-Jones potential model with an undetermined parameter k, which is a short-range multiple, is adopted:

$$U(r) = 4\left[k\left(\frac{1}{r}\right)^{12} - \left(\frac{1}{r}\right)^{6}\right]. \tag{2}$$

When photons reach the substrate with the nondimensional light speed c^* and the impact angle θ, attraction and repulsion behaviors occur between silicon's atoms and photons. Figure 1 shows the mechanism of photonatom interactions. When a photon enters the attractive field of an atom, the photon should be attracted to the center of atom. But the repulsive force pushes the photon off center if the photon is too close to the atom center.

The substrate is maintained as an NVE model (fixing particle numbers, system's volume and total energy) in the heat-transfer process, so the photons which enter the substrate are constrained because of forces among atoms and decay of motive energy of themselves. The system's temperature can be readily calculated from the velocity of

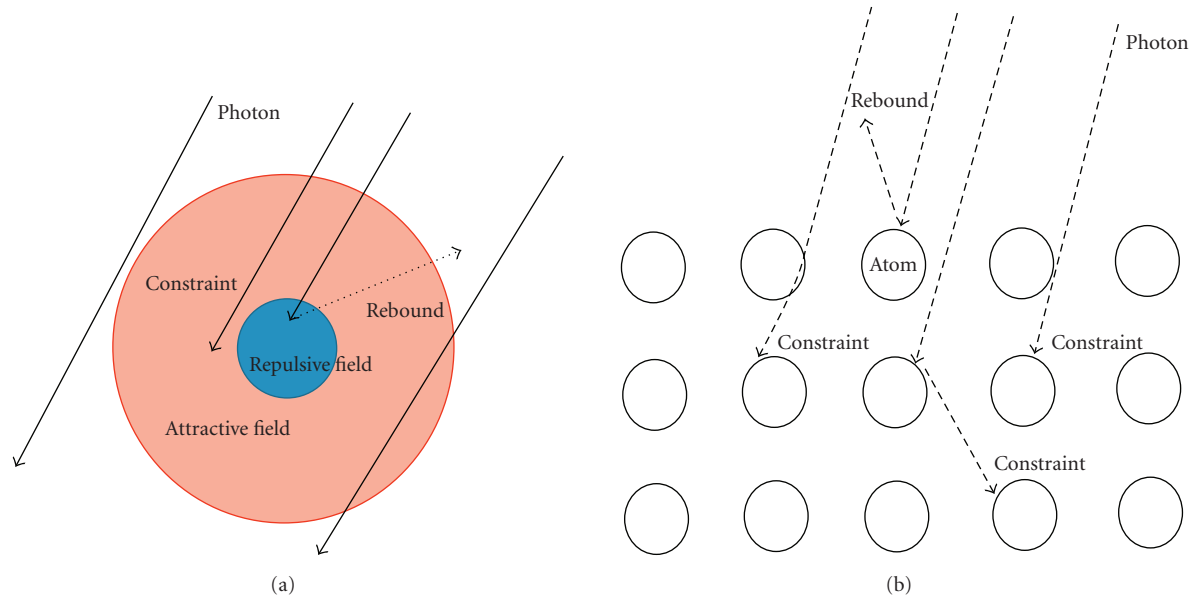

Figure 1: Illustrations of attractive and repulsive interactions of atoms and photons. (a) The photons moves toward repulsive force field are probably rebound out, and the other photons move through attractive field is constrained or decelerated. (b) The rebounded behavior is as same as reflection. The constraint behavior is as same as absorption.

each individual atom in the simulation domain since the Boltzmann distribution function allows the straightforward derivation of the mean kinetic energy $\langle E_c \rangle$ in the following way:

$$\langle E_c \rangle = \frac{1}{2} M \sum_{i=1}^{N} v^2 = \frac{3}{2} N k_B T_{\mathrm{MD}}, \tag{3}$$

where k_B is the Boltzmann constant and N is the number of particles in the system.

The initial temperature of the system was determined by Maxwell-Boltzmann distribution. During the indentation process, the velocity of every atom v^{new} was scaled as

$$v^{\mathrm{new}} = v^* \sqrt{\frac{T_D}{T_A}}, \tag{4}$$

where T_D is the desired temperature, T_A is the actual temperature, and v^* is the calculated velocity of atom. In this paper, the temperature was set as 300 K.

Due to the actions of attractive and repulsive forces and the photon's energy dissipation, the velocity of a photon which enters the substrate deeply tends toward zero. This behavior is considered photon absorption in a solar cell. However, some photons are repulsed at the substrate surface due to the repulsive force. This is considered reflection. The photons whose velocity decreases to zero were removed to avoid the increasing of particle numbers, and then affect the system's energy.

Note that the efficiency of monocrystalline silicon is, at most, 24.7% [17]. This study attempts to make a model with an absorptance reaching to this theoretic value, 24.7% in a smooth nontextured substrate by simply adjusting k. In our simulation, k is determined to be 3.86 in silicon. After this calculation, simulations of varying surface texturization with this potential model can proceed. The smooth surface model is a reference, and the other texturing models in this paper, which are simulated with the same conditions, can then be compared with the reference model. This methodology not only reasonably avoids the complexity of photonatom interaction but also achieves the goal of trying to evaluate the efficiency of two models with different surface texturization.

Following this concept, monocrystalline silicon was selected as the solar cell material. This is because silicon is the most common material in all types of solar cells, and its structure is simpler for using with a MD model. The results and conclusions of this study can also be extended to other solar cells, GaAs, InGaAs, InGaP, and so forth. The structure of monocrystalline silicon is an fcc diamond structure, showed in Figure 2. According the reviews of previous studies, square, pyramidal, and semicircular texturing structures were demonstrated. Under the texturing surface, three layers absorb the motion energy of photons. To avoid the effects of different lengths in the x- and y-directions, the substrate of solar cells is set as a square. Periodic boundary conditions are imposed in the x- and y-directions. Due to the periodic texturing shapes, different period lengths lead to different numbers of atoms. In the case of different intervals of square texturization, at least six periods are chosen. So in the case of distance $d = 1$ cell, the number of silicon atoms is 144352. The longer the distance, the more atoms are present in the substrate. The photon's incident angle varies at x-$z$planes.

All the simulations were executed with the computer of AMD Althlon64X2 3800+ CPU, Fedora Core Linux 6, and the GNU project FORTRAN compiler g77.

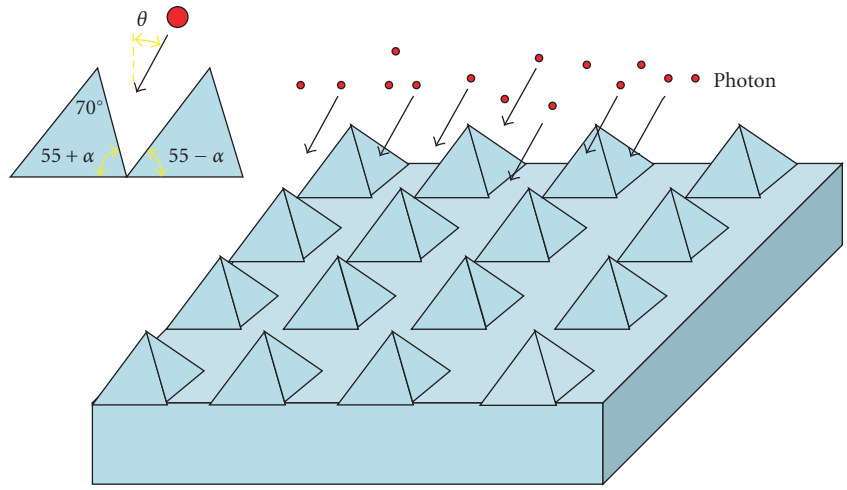

Figure 2: The model of mc-silicon by alkaline etching. The tilted angle is α.

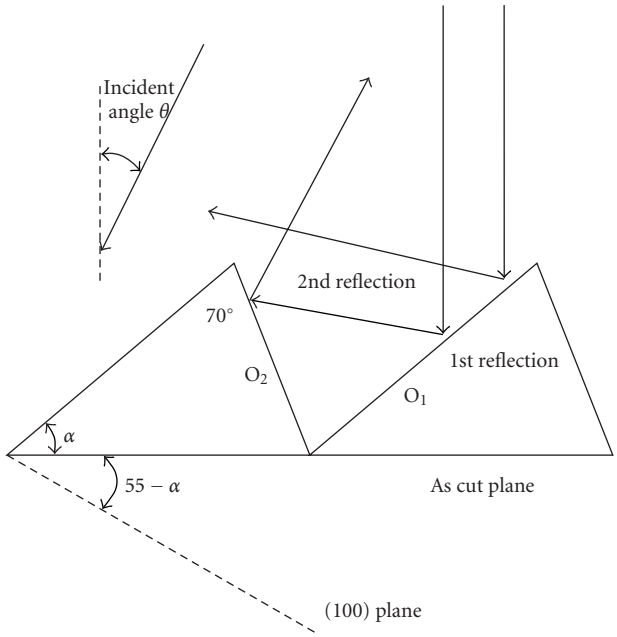

Figure 3: Schematic illustration of reflection on the surface of mc-silicon after alkaline etching.

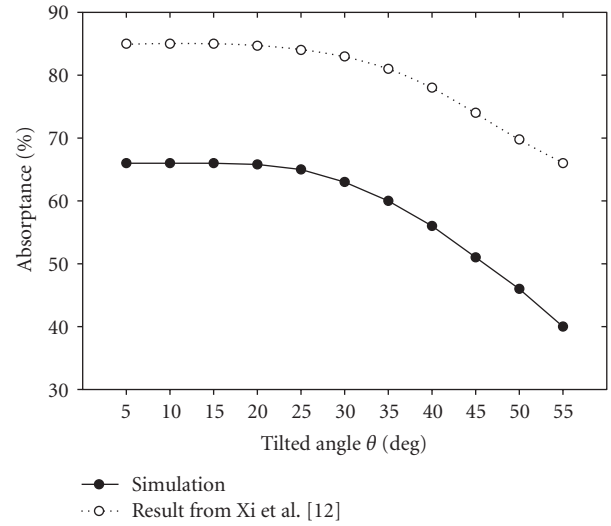

Figure 4: The relation of absorptance and the tilted angle, agreeing with the result of Xi et al. [18].

3. RESULTS AND DISCUSSION

The variety of light absorptance of multicrystalline Si substrate etched by alkaline solutions is discussed in Figures 3–5. According the discussion by Xi et al. [18], the tilted pyramids usually formed on the surface of mc-Si substrate etching by alkaline solution. If the orientation of the grains tends to (100), the pyramid will form a triangle with 70° on the top, tilted angle α and $110° - \alpha$ on the other angles. So, we try to make simulation with this model, and the results can easily compare with the results of Xi et al. [18].

Figure 4 shows that the reflection hardly changes when the tilted angle is less than 20°. That is because the most light reflects from O_1 plane to O_2 plane in Figures 3–5. More second reflection means that more light will be absorbed by the substrate. But if the tilted angle surpasses 20°, the reflectance increases quickly. Therefore, the pyramids with a large tilted angle lead to the lower efficiency. To compare with the results of Xi et al. [18], these two results are with a good agreement.

Furthermore, we try to change the incident angle θ, shown in Figure 5. In the case of pyramid with tilted angle $\alpha = 30°$ (the three angles are 70°, 80°, and 30°), more second reflection is produced when the incident angle $\theta = 20° \sim 85°$, so the absorptance rises higher to almost 60%. But once the incident angle is greater than 80°, the possibility of second reflection decreased because the incident light is perpendicular to plane O_2. Thus the absorptance quickly decreased. As the similar situation, when the incident angle is smaller than −20°, the incident light is also perpendicular

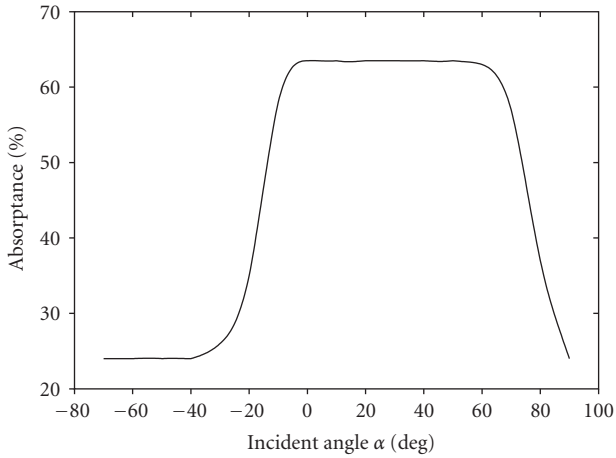

Figure 5: The relation of absorptance and incident angle.

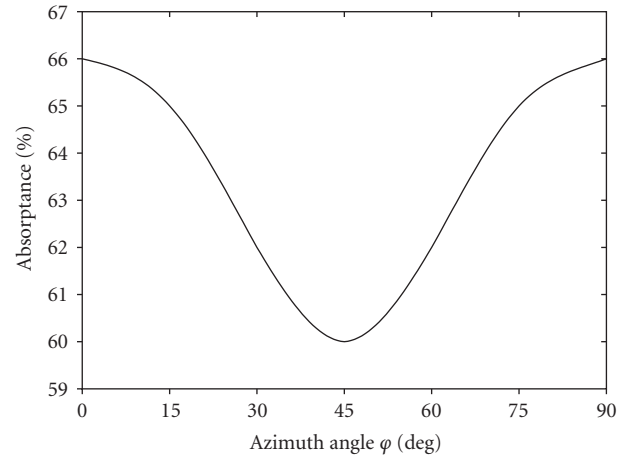

Figure 7: The position of the triangle of principal orientations. The incident angle θ and the azimuth angle φ are demonstrated.

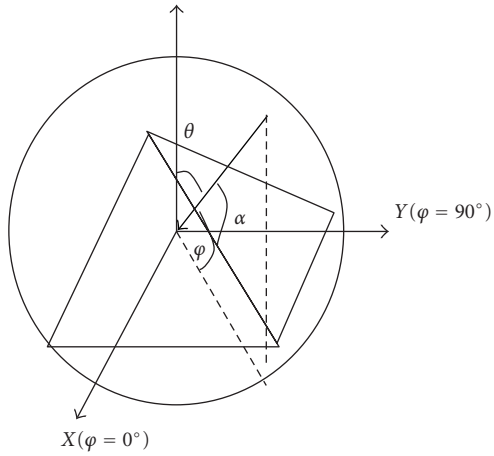

Figure 6: The diagram of a spherical polar coordinate system, which is quantified, is used to describe the surface morphology of the alkaline-etched wafers.

Table 1: Parameters of physical models, the bandgaps of the most important semiconductors for solar-cell applications.

Fundamental quantities	
	Multicrystalline silicon
Mass (density)	2.33 g/cm^3
Length σ	5.431 Å
Energy ε	1.792×10^{-19} J
Time t	1.77×10^{-3} ps/step
Normalized quantities	
Light speed (photon's speed) c^*	4.8×10^6
Temperature T^*	0.0231
Mass m^*	0.54

to plane O_1, the possibility of second reflection decreased, so the absorptance decreased to almost 20%.

We are interested about the effect of azimuth angle of incident light with absorptance. The surface morphology of the alkaline-etched wafers is quantified using a spherical polar coordinate system, as was the case for describing the relationship between different wafer and crystal orientations, shown in Figure 6. However, in this case, the tilt (α) and azimuth (φ) angles refer to the positions of the normals to a particular facet of textured surface exposed by etch. These angles are measured relative to a particular crystal or wafer orientation, whose surface is parallel to the x-z planes in the coordinate system and whose surface normal is parallel to the Z axis. The positions of the etch facets formed on a particular crystal or wafer orientation are thus described in terms of their angles α and φ with respect to the base orientation.

The simulation is proceeding with the conditions of the incident angle $\theta = 30^\circ$, isosceles pyramid of tilted angle $\alpha = 55^\circ$, and the azimuth angle $\varphi = 0^\circ$ to 90°, to explore the influence of azimuth angle on the absorptance of solar cells with pyramid surface. In Figure 7, it is found that the absorptance is the greatest when the azimuth angle $\varphi = 0^\circ$ or 90°, the incident light is perpendicular to the (100) plane for the azimuth angle. The reflective light is usually reflected by planes of another pyramid. The higher probability of second reflection leads to the higher absorptance. But when the azimuth angle is getting larger, more incidents reflect only once, the probability of second reflection slightly decreased. Thus, the absorptance also decreased. When the azimuth angle is greater than 45°, the incident light illuminates the (010) plane. The absorptance slightly increases again.

4. CONCLUSION

In conclusion, this study proposes a new and simple MD model alternative to complex electron-photon interactions in quantum scale to analyze surface texturization of solar cells. Three surface texturization shapes are simulated with various angles of incident light. This methodology can easily determine the absorptance differences of various surface texturizations and suggest better texturization shapes.

In the simulations of multicrystalline silicon by alkaline etching, the large tilted angle leads to the lower efficiency of solar cell. To consider the effect of incident angle, a range of high efficiency exists due to the increasing probability of second reflection. Furthermore, the azimuth angle of incident light also affects the efficiency of solar cells.

In this study, the wave behavior of photons and atoms is ignored. That means, according to the wave-particle duality, the gap between our study and real phenomenon possibly exists. However, this study is a beginning to simulate the absorption by molecular dynamics. Our results also agree well with previous studies. Thus, the development of this MD model is helpful to simulate the texturization before solar cells fabrication and can potentially be used to predict the efficiency promotion in any optical reflection-absorption cases.

REFERENCES

[1] J. D. Hylton, A. R. Burgers, and W. C. Sinke, "Alkaline etching for reflectance reduction in multicrystalline silicon solar cells," *Journal of the Electrochemical Society*, vol. 151, no. 6, pp. G408–G427, 2004.

[2] Y. Nishimoto and K. Namba, "Investigation of texturization for crystalline silicon solar cells with sodium carbonate solutions," *Solar Energy Materials and Solar Cells*, vol. 61, no. 4, pp. 393–402, 2000.

[3] U. Gangopadhyay, K. H. Kim, S. K. Dhungel, et al., "A novel low cost texturization method for large area commercial mono-crystalline silicon solar cells," *Solar Energy Materials and Solar Cells*, vol. 90, no. 20, pp. 3557–3567, 2006.

[4] N. Marrero, B. González-Díaz, R. Guerrero-Lemus, D. Borchert, and C. Hernández-Rodríguez, "Optimization of sodium carbonate texturization on large-area crystalline silicon solar cells," *Solar Energy Materials and Solar Cells*, vol. 91, no. 20, pp. 1943–1947, 2007.

[5] Z. Xi, D. Yang, W. Dan, C. Jun, X. Li, and D. Que, "Investigation of texturization for monocrystalline silicon solar cells with different kinds of alkaline," *Renewable Energy*, vol. 29, no. 13, pp. 2101–2107, 2004.

[6] M. Lipinski, P. Panek, E. Bełtowska, and H. Czternastek, "Reduction of surface reflectivity by using double porous silicon layers," *Materials Science and Engineering B*, vol. 101, no. 1–3, pp. 297–299, 2003.

[7] D. H. Macdonald, A. Cuevas, M. J. Kerr, et al., "Texturing industrial multicrystalline silicon solar cells," *Solar Energy*, vol. 76, no. 1–3, pp. 277–283, 2004.

[8] J. Nijs, S. Sivoththaman, J. Szlufcik, et al., "Overview of solar cell technologies and results on high efficiency multicrystalline silicon substrates," *Solar Energy Materials and Solar Cells*, vol. 48, no. 1–4, pp. 199–217, 1997.

[9] J. Qian, S. Steegen, E. Vander Poorten, D. Reynaerts, and H. Van Brussel, "EDM texturing of multicrystalline silicon wafer and EFG ribbon for solar cell application," *International Journal of Machine Tools and Manufacture*, vol. 42, no. 15, pp. 1657–1664, 2002.

[10] W. A. Nositschka, C. Beneking, O. Voigt, and H. Kurz, "Texturisation of multicrystalline silicon wafers for solar cells by reactive ion etching through colloidal masks," *Solar Energy Materials and Solar Cells*, vol. 76, no. 2, pp. 155–166, 2003.

[11] M. Spiegel, C. Gerhards, F. Huster, W. Jooss, P. Fath, and E. Bucher, "Industrially attractive front contact formation methods for mechanically V-textured multicrystalline silicon solar cells," *Solar Energy Materials and Solar Cells*, vol. 74, no. 1–4, pp. 175–182, 2002.

[12] C.-F. Li, D. B. Johnson, and R. Kovacevic, "Modeling of waterjet guided laser grooving of silicon," *International Journal of Machine Tools and Manufacture*, vol. 43, no. 9, pp. 925–936, 2003.

[13] L. A. Dobrzanski and A. Drygala, "Laser texturisation of crystalline silicon for solar cells," in *Proceedings of the 13th International Scientific Conference on Achievements in Mechanical and Materials Engineering (AMME '05)*, Gliwice-Zakopane, Poland, May 2005.

[14] M. M. D. Ramos and H. M. G. Correia, "Quantum modelling of photo-excited processes," *Applied Surface Science*, vol. 248, no. 1–4, pp. 450–454, 2005.

[15] W. Stier and O. V. Prezhdo, "Non-adiabatic molecular dynamics simulation of ultrafast solar cell electron transfer," *Journal of Molecular Structure: THEOCHEM*, vol. 630, no. 1–3, pp. 33–43, 2003.

[16] J. H. Simmons, "What is so exciting about non-linear viscous flow in glass, molecular dynamics simulations of brittle fracture and semiconductor-glass quantum composites," *Journal of Non-Crystalline Solids*, vol. 239, no. 1–3, pp. 1–15, 1998.

[17] M. A. Green, K. Emery, D. L. King, Y. Hishikawa, and W. Warta, "Solar cell efficiency tables (version 29)," *Progress in Photovoltaics*, vol. 15, no. 1, pp. 35–40, 2007.

[18] Z. Xi, D. Yang, W. Dan, C. Jun, X. Li, and D. Que, "Texturization of cast multicrystalline silicon for solar cells," *Semiconductor Science and Technology*, vol. 19, no. 3, pp. 485–489, 2004.

Hindawi Publishing Corporation
International Journal of Photoenergy
Volume 2008, Article ID 138091, 13 pages
doi:10.1155/2008/138091

Review Article

Sunlight-Initiated Photochemistry: Excited Vibrational States of Atmospheric Chromophores

Veronica Vaida,[1] Karl J. Feierabend,[1,2] Nabilah Rontu,[1] and Kaito Takahashi[1]

[1] *Department of Chemistry and Biochemistry, University of Colorado, Campus Box 215, Boulder, CO 80309, USA*
[2] *Earth System Research Laboratory, Chemical Sciences Division, National Oceanic and Atmospheric Administration, 325 Broadway, Boulder, CO 80305, USA*

Correspondence should be addressed to Veronica Vaida, vaida@colorado.edu

Received 14 April 2008; Accepted 29 May 2008

Recommended by Mohamed Sabry Abdel-Mottaleb

Atmospheric chemical reactions are often initiated by ultraviolet (UV) solar radiation since absorption in that wavelength range coincides to typical chemical bond energies. In this review, we present an alternative process by which chemical reactions occur with the excitation of vibrational levels in the ground electronic state by red solar photons. We focus on the O–H vibrational manifold which can be an atmospheric chromophore for driving vibrationally mediated overtone-induced chemical reactions. Experimental and theoretical O–H intensities of several carboxylic acids, alcohols, and peroxides are presented. The importance of combination bands in spectra at chemically relevant energies is examined in the context of atmospheric photochemistry. Candidate systems for overtone-initiated chemistry are provided, and their lowest energy barrier for reaction and the minimum quanta of O–H stretch required for reaction are calculated. We conclude with a discussion of the major pathways available for overtone-induced reactions in the atmosphere.

1. INTRODUCTION

The earth's temperature, climate, and chemistry are determined by the balance of incoming shortwave solar radiation and outgoing longwave infrared (IR). The emission of the sun is modeled as a blackbody at 5800 K, with a maximum photon output in the visible red [1]. Absorption by atmospheric components, notably ozone, limits the ultraviolet radiation reaching the earth's surface to wavelengths greater than 300 nm. In this review, we consider alternative photophysical and photochemical processes driven by solar photons in the visible red and near IR [2].

Traditionally, processes considered in atmospheric photochemistry are those requiring excitation of electronic states by ultraviolet (UV) light as these high energies are of the necessary energy to dissociate covalent bonds [3]. Reactive radicals including hydroxyl radical, OH, the main oxidant of organic and inorganic compounds in the earth's atmosphere can be generated in this way [4, 5]. Chemistry in the stratosphere and troposphere is, therefore, driven by direct photochemical reactions or by photolytically generated OH originating from photolysis of O_3 to give $O(^1D)$ which reacts with H_2O and CH_4 to give OH.

In this review, we discuss a sunlight-initiated process which occurs by excitation with red solar photons of vibrational levels of the ground electronic state of atmospheric chromophores [2, 6]. It has recently been shown that these ground electronic state photoreactions can be important in the atmosphere when excited electronic state reactions are precluded by the lack of appropriate electronic states accessible in the solar spectrum [7–16]. Atmospheric conditions, where UV photons are suppressed as is the case at high zenith angle which occurs at dusk, dawn, or the edge of a polar vortex, are also auspicious for such ground state photochemistry [17–32]. Atmospheric chemists describe the rate of formation of photoproducts from atmospheric processing as a first-order rate constant J (J-values), where J is given by a convolution of the photoabsorption cross-section, the wavenumber dependent photochemical quantum yield, and the photon flux of solar radiation [3]. In the present review, the experimental and theoretical methods used to obtain accurate integrated O–H cross-sections for vibrational transitions and the atmospheric impact of ground electronic state chemistry will be discussed.

This overtone-induced chemistry is important in that it contributes to atmospheric aerosol processing. In general,

hydrophilic acids and alcohols promote aerosol nucleation and growth. The overtone-induced chemistry leads to the production of hydrophobic byproducts such as CO_2, aldehydes, and ketones, which can evaporate, and therefore process these aerosols. The resulting changes in aerosol size, composition, and surface structure are paramount to understanding radiative transfer and consequently climate.

Our discussion focuses on sunlight-initiated chemistry of significance to secondary organic aerosol (SOA) chemistry and consequently to chemistry relevant to the earth's climate. We propose photochemistry of excited vibrational levels of the ground electronic state as potential contributions to explain the gap between modeled and measured organic concentrations [33–35]. Atmospheric aerosols influence global radiative forcing by back scattering and/or absorption of solar radiation and by enhancement of cloud albedo due to an increased number of cloud droplets [36]. Current aerosol models underestimate SOA mass by up to two orders of magnitude [37–39]. Atmospheric oxidation processes are largely driven by oxidants such as OH and O_3. However, direct photolysis processes are also important degradation pathways of potential SOA precursors and contributors. Photolysis processes of a variety of highly oxidized organics might represent an unrecognized chemical pathway in the multiphase (gas/particle/droplet) system that might help to explain the large gap between measured and modeled organic concentrations.

2. VIBRATIONALLY EXCITED STATES

The vibrations of polyatomic molecules are often represented as normal modes [40]. In the normal mode picture, the potential energy surface is expanded to the second-order term at the minimum, and the mass-weighted Cartesian force constant matrix is diagonalized to give the normal modes. These normal modes are sets of concerted, collective, and harmonic motions of all the atoms in the molecule with a fixed center of mass. Vibrations are uncoupled, and each type of vibration possesses its own distinct harmonic potential energy well. Spectra in the fundamental region have been assigned successfully using this normal mode picture assuming a linear dipole moment surface in these coordinates [40]. However, this double harmonic approximation (harmonic potential energy surface and linear dipole moment surface) becomes increasingly invalid for treatments of transitions to higher vibrational states [41–43]. In real molecules, the mechanical and electrical anharmonicities (the anharmonic terms of the potential energy surface and the nonlinear terms of the dipole moment surface, resp.) relax the $\Delta v = \pm 1$ vibrational selection rule and allow for the observation of transitions involving multiple quanta in one vibrational mode (i.e., overtone bands) or multiple quanta in two or more differing vibrational modes (i.e., combination bands). However, in most cases, these anharmonicities are relatively small, and, in general, overtone and combination bands are weak and not easily observed.

In the energy regime of about 30 to 60 kcal/mol, observations have shown that the X–H (X=O, C, N) stretching overtones dominate the ground electronic state vibrational spectra. These X–H stretching vibrations have been studied and assigned successfully using the local mode model [42–53]. Unlike in the normal mode view, local oscillators are considered to be weakly coupled and each X–H oscillator is treated independently in the local mode description. For example, the dominant absorption in the overtone spectra of the water molecule is better described with a linear combination of two independently oscillating O–H bonds (in the local mode picture) instead of considering a high excitation in either symmetric or asymmetric O–H stretching modes (in the normal mode picture). Albeit weak, these X–H stretching overtones allow for a method of depositing energy into a molecule by the absorption of sunlight, and thus may lead to reaction [54–60]. As mentioned above, sunlight has maximum photon intensity in the visible region, where these overtone transitions are observed. Therefore, in order to assess the importance of overtone-initiated chemistry, it is important to understand the absolute absorption cross-section of these X–H stretching overtones.

In the mid 1980s, Crim et al. reported overtone-initiated unimolecular decomposition for the hydrogen peroxide (HOOH) molecule, where the O–H stretching excitation of $\Delta v_{OH} = 5$ (+ torsion mode excitation) and 6 resulted in a bond cleavage of the O–O bond (De∼50 kcal/mol) [61–63]. Their wavelength dependent product state distribution showed initial state dependence. Slight differences in the product distribution of OH were seen when the combination band of the O–H stretch overtone and the torsion mode was excited compared to the excitation via pure O–H stretch overtone. Following their work, overtone-induced photodissociation reactions have been investigated in several molecules with the O–O–H bond, such as peroxynitric acid (O_2NOOH) [28, 32], peroxynitrous acid (ONOOH) [20, 64–66], methyl hydroperoxide (CH_3OOH) [27, 67], as well as hydrogen trioxy radical (OOOH) [68, 69]. Furthermore, systems with weak bonds adjacent to the O–H bond, such as N–O (De∼55 kcal/mol) in nitric acid (O_2NOH) [70, 71] and O–Cl (De∼43 kcal) in ClOH [72–75], have also been investigated as possible candidates to dissociate following O–H stretching overtone excitation.

The O–H bond with its strong polarity usually results in the strongest absorption within the X–H stretching spectra (per X–H bond) for a given quanta of excitation; thus, it is a good absorbing chromophore for the deposition of photon energy into the molecule. For example, the ratio between the average intensities for the O–H bond versus the C–H bond is about 4:1 for $\Delta v = 3$, 4.5:1 for $\Delta v = 4$, and 6:1 for $\Delta v = 5$ [23, 76, 77]. Therefore, polyatomic molecules with O–H bonds are candidates for absorbing solar red photons and reacting in the atmosphere [2, 7, 9, 14, 15, 17, 22, 23, 26, 65, 78–81]. Since greater effort is needed to obtain an absolute integrated cross-section in comparison to the peak position, only a few papers report both [82–84]. The weak absorption intensities of these relevant overtones also make it more difficult to obtain absolute values both experimentally and theoretically. In the following work, we compile the available experimental and theoretical integrated cross-sections of the O–H stretching mode for several polyatomic molecules. A comparison on the molecular

dependence as well as an investigation of the accuracy of the calculated values, which are usually obtained using the local mode model, will be presented. In addition, abiding with the possibility that excitation through combination bands may play an important role in the unimolecular reaction dynamics, combination bands in nitric acid are examined as an example. Furthermore, calculated reaction barriers of possible candidates for overtone-initiated reaction will be presented. The possibility of overtone-induced concerted reactions, where the excited O–H bond is strongly coupled to the reaction coordinate, will be discussed [7, 16, 18, 85]. These reactions will be contrasted with previous experimental results of overtone-induced dissociation reaction, where the energy in the excited O–H bond is transferred to rupture a weak adjacent bond [2, 17, 23, 24, 26, 30, 57, 64, 65, 70, 71, 78, 86, 87]. Finally, we will conclude with the discussion of the photochemical rate (J-values) and important points to note for discussing these overtone-initiated reactions in the atmosphere.

3. O–H STRETCHING SPECTRA AND THE LOCAL MODE MODEL

Due to the light mass of the hydrogen atom, X–H stretching vibrations have considerably higher frequencies than other vibrational modes. Also, the large difference in the mass between the X (O atom in the present case) atom and H atom allows for this vibrational mode to have relatively small coupling with other modes. In the late sixties, Siebrand and Williams [45], Swofford et al. [88], Henry [42], Burberry et al. [89], and Mortensen et al. [90] observed the following trends in the X–H stretching spectra.

First, the fundamental and overtone transition energies of the X–H stretching spectra were shown to fit to a two-parameter equation:

$$\Delta E_{v0} = v(A - Bv), \tag{1}$$

where ΔE_{v0} is the transition energy between the ground and vth excited state. This equation, sometimes regarded as Birge-Sponer equation [91], is the solution of a one-dimensional Morse oscillator [92] for diatomic molecules, where the harmonic term is

$$\omega_e = A + B \tag{2}$$

and the anharmonic term is expressed as

$$\chi_e\omega_e = B. \tag{3}$$

Second, Burberry et al. [89] observed the $\Delta v = 3-6$ aromatic C–H stretching spectra of benzene, toluene, xylene, and trimethyl benzene and reported that while the peak positions did not vary, the absorption intensity showed systematic decrease in relation to the number of aromatic C–H bonds.

These observations lead to the phenomenological "local mode model", where the vibrational spectra are understood in terms of localized excitation in the X–H bond. For the O–H bond, both experimental and theoretical calculations have shown that the peak positions can be given by a harmonic frequency of

$$\omega_e \cong 3700 - 3900\,\mathrm{cm}^{-1} \tag{4}$$

and an anharmonic frequency of

$$\chi_e\omega_e \cong 70 - 90\,\mathrm{cm}^{-1}. \tag{5}$$

Therefore, to exceed the reaction barriers of 30–60 kcal/mol discussed in the present review, overtone excitations of $\Delta v_{\mathrm{OH}} = 3$–6, which reside in the visible to near IR-region, need to be considered. Although we will not tabulate the actual values here, recent high-level calculations give peak positions with errors of less than few percent [51, 77, 93].

4. INTENSITIES OF THE O–H STRETCHING MODE

First, we present a brief summary of the experimental and theoretical methods used to obtain absolute integrated cross-sections before discussing the results that have been collected.

A combination of methods is usually needed to obtain experimental intensities for all $\Delta v_{\mathrm{OH}} = 1$–5 transitions. Use of Fourier transform infrared spectroscopy (FTS) easily provides data for the fundamental and near-IR regions including $\Delta v_{\mathrm{OH}} = 1$, 2, and 3, while methods such as cavity ring-down (CRD) [94–98] or photoacoustic (PA) [99–105] spectroscopy grants access to higher overtones into the visible region of the spectrum such as $\Delta v_{\mathrm{OH}} = 4$, 5. Each method has its advantages and disadvantages. Fourier transform spectroscopy, for example, has high wavenumber resolution as well as the Jacquinot advantage, enabling higher throughput of radiation [106]. Unlike conventional or laser spectrometry where one must scan the full wavenumber range, FTS information on all frequencies simultaneously impinge upon the detector and the entire spectrum of the species is recorded at once. In contrast to laser spectroscopy such as CRD and PA, FTS may be $\sim 10^6$ less sensitive due to its low-photon flux and the difficulty of measuring a small difference between the light intensity with and without an absorber present. Increased sensitivity, necessary for the detection of higher overtones due to their diminishing intensity, is the main advantage of CRD and PA spectroscopy [24, 94, 95, 97, 98, 101–105, 107]. The use of highly reflective mirrors employed in the CRD setup in our lab, for example [8, 10, 18, 108], increases the pathlength of the experiment to orders of kilometers, thereby increasing the sensitivity by at least a factor of 14000 in comparison to FTS experiments. However, CRD spectroscopy is limited in wavenumber range by the laser dye and by the mirrors that can be used. PA spectroscopy provides comparable sensitivity to CRD spectroscopy and is also limited in range by the laser dye. It provides the advantage of using small sample volume due to its ability to detect at parts per trillion levels.

A challenge often encountered in determining experimental cross-sections, regardless of spectroscopic method (FTS, CRD, or PA), is obtaining an accurate number density. This value is usually obtained using the available vapor pressure data and the ideal gas law. The accuracy of vapor

pressure measurements is low for compounds which readily form hydrogen-bonded clusters or hydrates. However, vapor pressures inside the sample chamber can readily fluctuate such that equilibrium in the chamber may be achieved on a different timescale by which point some sample can potentially be lost to the atmosphere, and temperature effects may cause the sample to degrade by thermal reaction. Often times, only relative intensities are reported in the literature due to difficulties met in determining an absolute cross-section.

For the theoretical calculation of the peak positions and integrated cross-sections, one must first obtain the potential energy surface (PES) and the dipole moment surface (DMS) from quantum chemistry ab initio calculations. With this PES, the vibrational eigenvalues and eigenfunctions are calculated by solving the vibrational Schrödinger equation. Local and normal mode pictures result in different coordinate systems, thereby giving different equation forms for the vibrational Schrödinger equation. The peak position or transition energy is obtained from the difference between the respective initial and final state energies. The integrated cross-section is obtained by [109]

$$S^{\text{calc}} = \frac{8\pi^3}{3hc} \left| \langle \Psi_f | \vec{\mu} | \Psi_i \rangle \right|^2 \tilde{\nu} = 4.16 \times 10^{-19} \left| \langle \Psi_f | \vec{\mu} | \Psi_i \rangle \right|^2 \tilde{\nu} \ (\text{cm molecule}^{-1}), \tag{6}$$

where $\tilde{\nu}$ is the transition energy in cm^{-1}, and $|\langle \Psi_f | \vec{\mu} | \Psi_i \rangle|^2$ is the square of the absolute magnitude of the transition moment in debye squared. The transition moment is obtained by the integration of the aforementioned DMS using the initial and final state eigenfunctions. It should be noted that there are numerous quantum chemistry methods that can be used to calculate the PES and DMS ranging from the relatively "cheap" wave function method of Hartree Fock [110, 111] and density functional theory methods [112], such as B3LYP [113, 114], to the "expensive" wave function methods, such as QCISD(T) [115–117], CCSD(T) [116, 118–120], and MRSDCI [121]. In using these methods to obtain the PES/DMS needed to calculate highly excited vibrational states, one needs to calculate geometries that are displaced from the equilibrium geometry. At these geometries, such as elongated X–H bond lengths, multireference methods are necessary to accurately describe the electronic state, and instability may occur with the use of single reference methods.

Many different methods have been used to solve the vibrational Schrödinger equation, and one of the usual methods is the variational method where one diagonalizes the Hamiltonian matrix using a given basis set [122–124]. Quack [51] used harmonic oscillator basis sets to obtain the eigenfunctions for the CH stretching overtone of CX_3H. Methods such as vibrational self-consistent field [125] and their higher level expansions VCI [126] and VCCSD [127] have also been used for the calculation of OH stretching overtone transitions of nitric acid [128]. Furthermore, several methods solve the time-dependent Schrödinger equation and obtain the spectra from the Fourier transform of the autocorrelation function of the wavepacket [129]. For the calculation of X–H stretching modes, Henry et al. developed the harmonic coupled anharmonic oscillator model, where the PES of the X–H stretching motion is approximated as a Morse potential and Taylor's expansion fitting of the ab initio dipole moments are used to obtain the DMS as a function of bond coordinates [90, 130]. Initially, experimental peak positions were used to obtain the needed parameters for the Morse oscillators, but in recent calculations these parameters are obtained from the fitting of ab initio energies. Recently, some of us used the local mode model and calculated the intensities of the O–H stretching spectra for several simple acids and alcohols using the grid variational method with the finite difference approximation [131]. In this calculation, the PES and DMS were obtained from the highly accurate numerical interpolation of the energy and dipole moment calculated by B3LYP/6-311++G(3df,3pd)[113, 114, 132–136].

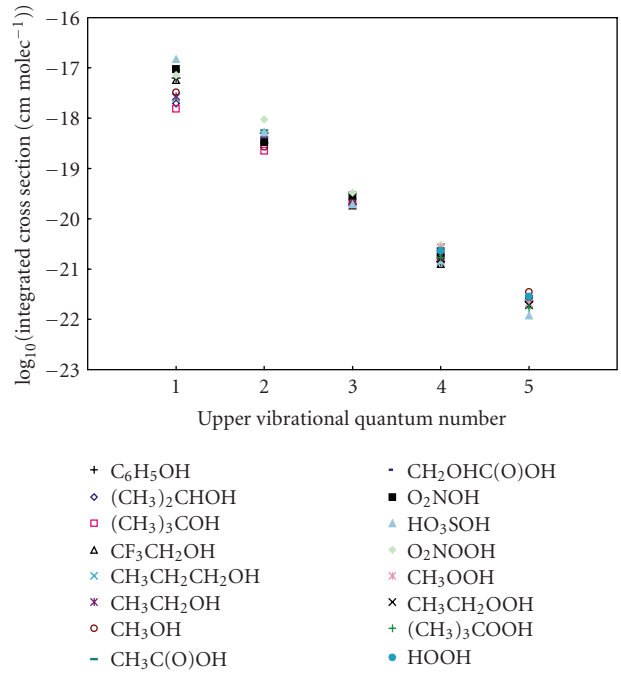

Figure 1: Compilation of experimental integrated cross-sections of O–H stretching overtones.

A summary of the O–H stretching intensities for various alcohols, carboxylic acids, and peroxides is presented in Figures 1 and 2 which illustrate the trend in O–H stretching integrated cross-sections as a function of upper quantum number [8, 18, 20, 24, 28, 67, 76, 78, 82–84, 102, 137–140]. Typically, intensities of the O–H stretches are comparable for most organic compounds. Figure 1 summarizes the experimental results from a variety of sources, [8, 18, 24, 78, 83, 102, 137, 141] including work from our group, while Figure 2 compiles theoretically derived integrated cross-sections [77, 131]. It should be noted that these figures list molecules in which both experimental and theoretical values are available. Furthermore, as mentioned above, many different quantum chemistry methods are available for the calculation of the PES and DMS, and the same applies

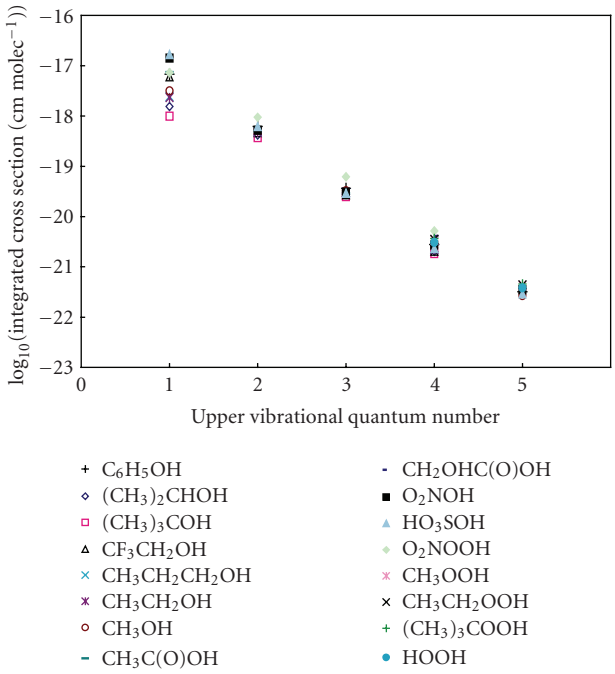

Figure 2: Compilation of theoretical O–H stretching integrated cross-sections.

for solving the vibrational problem. In order to keep the comparison consistent in terms of calculation method, the results given in Figure 2 are given by the grid variational method using the PES and DMS calculated by the B3LYP/6-311++G(3df,3pd) method. In addition, due to the limits in the experimental methodology mentioned above, for most molecules we were unable to collect literature values for all $\Delta\nu_{OH} = 1$–5 transitions.

Both Figures 1 and 2 illustrate that the O–H stretch preserves its intensity even though it decreases with each overtone. The "order-of-magnitude" rule [61], which states that the intensities of O–H stretching vibrational transitions successively decrease in magnitude by approximately a factor of 10, is illustrated in both figures by a linear decrease in log scale. This trend has also been observed in C–H and N–H stretching transitions. In general, the "order-of-magnitude" rule works best for higher energy overtones, and one sees great variance when comparing the fundamental and first overtone intensities. For example, Figure 1 reveals that the drop in intensity for sulfuric acid from the $\Delta\nu_{OH} = 1$ to the $\Delta\nu_{OH} = 2$ transition is 28 [137], while that for propanol is 4.7 [82]. Previously, we have shown that for propionic and pentafluoropropionic acid, this factor drops by about 14 [9, 79] and 18 for longer chained perfluorocarboxylic acids [15].

As shown in Figure 1, intensities for the $\Delta\nu_{OH} = 1$ vary over an order of magnitude, from 1.54×10^{-18} cm molec^{-1} for tert-butanol [82] to 1.49×10^{-17} cm molec^{-1} (per O–H stretch) for sulfuric acid [137]. Upon observation of several simple acids and alcohols, Lange et al. [82] have discussed the correlation of the fundamental O–H stretching intensities with the electron withdrawing ability of the substituent bound to the O–H group. Theoretical work on the same set of molecules also showed the same trend that the stronger the electron withdrawing ability of the substituent, the greater the fundamental intensity [77]. Lange et al. [82] also found that molecules with more electron withdrawing substituents have a larger decrease in successive O–H overtone intensities relative to the fundamental O–H stretch. As can be seen from Figures 1 and 2, overtone intensities show much smaller variance between molecules than fundamental intensities, and this trend seen by Lange et al. [82] is probably the result of variance in the fundamental intensity. For the C–H stretching vibration, Burberry et al. [89] have mentioned the "universal intensity concept" [142], in which the $\Delta\nu_{CH} = 3$, 4, 5, and 6 transition absorption intensities per C–H oscillator become nearly equal regardless of type of molecule. A similar trend is seen for the O–H bond, where overtone intensity loses its molecular dependence, but it should be noted that in peroxide molecules (ROO–H), the theoretical results show stronger overtone intensity compared to the acids and alcohols (R–OH) [77]. Experimental results do not show clear trends as discussed and more study is needed to obtain a full understanding of the factors that determine overtone intensities.

As mentioned above, the intensity trend seen in the fundamental region is different from that seen in the overtones region. As seen in Figures 1 and 2, the O–H cross-section of sulfuric acid has the largest intensity at $\Delta\nu_{OH} = 1$ compared with the compounds investigated here, but decreases with increasing vibrational quanta more rapidly until possessing the smallest value at $\Delta\nu_{OH} = 5$. We believe this behavior is a result of the onset of dehydration reaction and Section 6 addresses this in detail.

Since theoretical values are used when experimental limitations (low vapor pressure, no laser in the absorption range, and so on) make it impossible to obtain the integrated cross-sections experimentally, it is important to gauge the accuracy of these calculations. Methods such as mean absolute percentage error and logarithmic deviation have been used to evaluate the accuracy of the calculated versus the experimental values since they span many orders of magnitude [122]. In the present paper, we compare the accuracy by using the mean absolute percentage error:

$$\text{MAPE} = \frac{1}{N_{\text{data}}} \sum_{i=1}^{N_{\text{data}}} \left| \frac{A_i^{\text{calc}} - A_i^{\text{exp}}}{A_i^{\text{exp}}} \right|. \tag{7}$$

Using all the available experimental values shown in Figure 1, we obtain an error of 45%, signifying that the calculated results are within a factor of 2 of the experimental values. It should be noted that if we only use the fundamental intensities, the error is a much smaller value of 15%, signifying that the experimental values are reproduced with high accuracy. The use of a more sophisticated and time-consuming quantum chemistry methods to obtain the PES and DMF, as well as a more detailed treatment in the vibrational calculation (such as consideration of coupling to other vibrational modes) will probably lead to a slightly better agreement with experiment, but it is expected that at the present moment the error limit for the calculated integrated cross-sections for overtone transitions

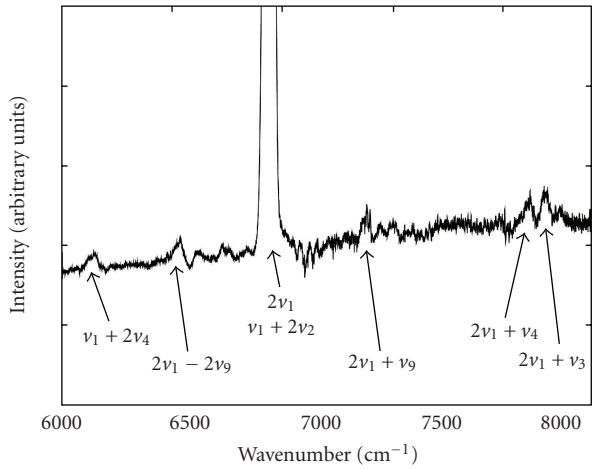

Figure 3: Illustration of combination bands observed for HNO_3 in the NIR. Assignments taken from Feierabend et al. [128, 143].

is about 30%. In systems where the relative intensities of the overtones with respect to the fundamental transition may be obtained experimentally, a hybrid method of using the theoretical fundamental intensity and the experimental relative intensities may be used to obtain an absolute cross-section for the overtones. As mentioned above for the fundamental transition, the theoretical values can reproduce experimental values with high accuracy.

5. SIGNIFICANCE OF COMBINATION BANDS

As mentioned in the introduction, product distributions of the photoinduced dissociation of HOOH showed initial state dependence [61–63]. It is expected that near the dissociation threshold, the dissociating product may show mode dependence on the band used to excite it. Therefore, Homitsky et al. [102] performed detailed analysis on the O–H stretch and torsional excitation on the overtone and combination bands of methylhydroperoxide. The observation of combination bands suggests mode coupling [144] and many combination bands involving the O–H stretching overtones of HNO_3 are shown as an example in Figure 3. Feierabend et al. [128, 143] showed that the O–H stretching overtones are not the only important absorbers in the near-IR (NIR) and visible regions; the appearance of combination bands involving the O–H stretch is also prevalent in the higher energy regions. These have fairly large absorption intensities for combination bands, although in general the local mode model often neglects mode mixing. The following mode assignments are made as shown in Figure 3: $2\nu_1$ = first O–H stretching overtone, ν_2 = NO_2 asymmetric stretch, ν_3 = NO_2 symmetric stretch, ν_4 = H–ON bend, and ν_9 = O–H torsion. A hot band of the O–H torsional mode in combination with the first O–H stretching overtone was attributed to the band centered at approximately 6500 cm^{-1}. The work of Havey et al. [145] showed that molecules which contain many low-frequency torsional modes may have significant hot band contributions.These hot band contributions can add to the total intensity of the O–H stretching overtones region. A surprising result of the HNO_3 work revealed that the intensities of the combination bands do not drop off in the O–H stretching overtone region.

Interestingly, the absorption intensities of these types of combination bands scale roughly the same as the intensities of the overtones. For example, the intensity of overtones is about the same as that of combination bands; $I\,[n\nu_{OH}/(n+1)\nu_{OH}] \sim I\,[\nu_x + \nu_{OH}/\nu_x + (n+1)\nu_{OH}]$, where ν_x is an arbitrary mode with fundamental absorption intensity. The fact that these combination modes are observed with significant absorption intensities in the NIR suggests a few key ideas. First, these combination modes should not be ruled out and regarded as bright states for overtone-induced photodissociation, especially if the vibrational mode involved is closely coupled to the reaction coordinate. Next, more local mode simulations have begun treating the coupling of the O–H stretch with other modes [43, 80, 138, 146, 147]. These types of treatments are expected to be more accurate due to the qualitative evidence for mode coupling/mixing in the observed spectra. Finally, while the combination modes cannot provide any direct quantitative measurement of mode coupling, their frequencies and intensities can serve as a test for theoretical calculations. This will allow for the assessment of the accuracy in the theoretical methods, providing information on the method to be used for calculating the spectra of molecules in which experimental determination is not possible.

6. CANDIDATES SYSTEMS OF OVERTONE-INITIATED CHEMISTRY

Previous studies [7] have revealed that overtone-induced photolysis of sulfuric acid is the source of SO_2 in the stratosphere and mesosphere [12, 13]. UV photolysis of sulfuric acid was ruled out [13, 137] because the electronic excitation lies well above the energies available from the sun in the earth's atmosphere. Sulfuric acid only absorbs in the IR and the near-IR regions, where the O–H stretching vibration plays a dominant role in its atmospheric chemistry. These studies on overtone-induced photolysis of sulfuric acid have predicted that the photochemical reaction is a concerted dehydration reaction, where the product is H_2O and SO_3 rather than a bond cleavage reaction where the product would be OH and SO_3H. This concerted reaction only requires ~32–40 kcal/mol, so, consequently, excitation of $\Delta\nu_{OH} = 4$ and higher overtones provides sufficient energy to drive the reaction and generate SO_3 and H_2O. The strong S–O (about 80 to 90 kcal/mol) [148] bond requires significantly more energy for direct bond cleavage that cannot be provided from overtone chemistry because of the low cross-sections expected for the 9th overtone required to reach this threshold. Figure 3 shows the calculated energy barrier, including the minimum and the transition state structures for the dehydration reaction of sulfuric acid $H_2SO_4 \rightarrow SO_3 + H_2O$. It should be noted that the occurrences of reactions may cause the absorption spectrum to broaden, thereby making it difficult to obtain an accurate cross-section due to the low signal-to-noise.

Table 1: Organic acids and barriers for their chemistry.

Compound	Chemical formula	Lowest energy barrier for reaction (kcal/mol)	Reaction products	OH quanta exceeding barrier	Reference
Sulfuric acid	H_2SO_4	32–40	SO_3, H_2O	$\nu_{OH} = 4$	[7, 149, 150]
Nitric acid	HNO_3	47.7	NO_2, OH	$\nu_{OH} = 5$	[57]
Pernitric acid	HO_2NO_2	21.2	HO_2, NO_2	$\nu_{OH} = 3$	[30]
Formic acid	HCOOH	41.5[(a)], 63.0[(b)]	CO, H_2O	$\nu_{OH} = 5{,}7$	[151][(a)], [152][(b)]
Glycolic acid	$OHCH_2COOH$	50.9	H_2CO, CO, H_2O	$\nu_{OH} = 6$	[153]
Lactic acid	$OHCHCH_3COOH$	47.4	$HCOCH_3$, CO, H_2O	$\nu_{OH} = 5$	[153]
Malonic acid	$HOOCCH_2COOH$	27.6	$H_2CC(OH)_2$, CO_2	$\nu_{OH} = 3$	[16]
Acetic acid	CH_3COOH	67.01[(c)], 71.5[(d)]	CH_4, CO_2	$\nu_{OH} = 7{,}8$	[154][(c)], [155][(d)]
Trifluoroacetic acid	CF_3COOH	50.3	CF_2CO_2, HF	$\nu_{OH} = 6$	[14]

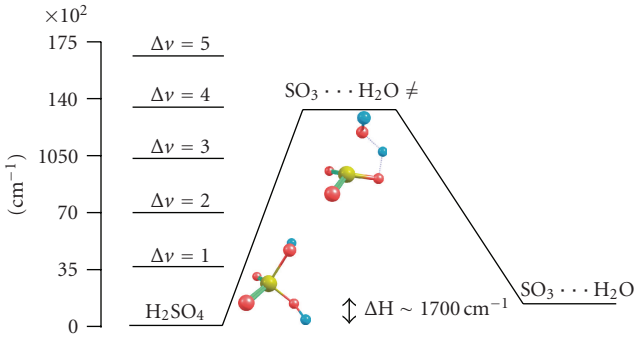

Figure 4: Calculated energy barrier for sulfuric acid dehydration.

Similar to sulfuric acid, other atmospherically relevant compounds, specifically oxidized organic species such as acids and alcohols, are capable of undergoing concerted reaction by overtone pumping of the O–H bond [2, 7, 14, 16, 18, 30, 108]. Table 1 shows several organic acids, their lowest energy barrier for reaction, the reaction products, and the minimum quanta of O–H stretch required for the chemistry to occur [7, 14, 16, 30, 57, 149–155]. The values for the energy barrier do not include the zero point energy corrections, therefore they are possibly higher than the actual reaction thresholds.

In general, if there is a lack of competing processes (such as collisional deactivation), the energy provided by overtone pumping is sufficient to drive the reaction to completion [12, 156, 157]. For example, in nitric and pernitric acid, theoretical calculations and experimental data have shown that visible wavelength excitation of O–H overtone vibrations contain sufficient energy to cleave the O–O and N–O bonds [26, 158]. Similarly, the work of Staikova et al. [16] showed that for malonic acid excitation of $\Delta\nu_{OH} \geq 3$ has the ability to decarboxylate the acid, although experimental validation of the reaction is not yet available [159]. In the case where a water molecule is available and forms a complex with the acid, it lowers the energy for reaction by one quantum of an O–H stretch [7, 16, 160]. Briefly, the presence of the water molecule forms an eight-membered hydrogen-bonded cyclic ring with the chromophore and relaxes the strain on the transition state as compared to the pure acid which forms a six-membered hydrogen-bonded cyclic ring on its own. In doing so, the transition state energy for decarboxylation of malonic acid is lowered from 25.6 to 17.6 kcal/mol [16]. The energetic difference is equal to one quantum of an O–H stretching vibrational overtone and in theory, excitation to $\Delta\nu_{OH} = 2$ can promote the reaction when a water molecule is present. Several other systems such as sulfuric acid, fluoromethanol, and perfluoromethanol have shown similar decrease in barrier heights with hydrate complex formation [160]. Abundance of water in the atmosphere point to the high possibility of the existence of hydrated complexes indicating the likelihood of water catalyzed overtone reaction being a factor in atmospheric chemistry. These hydrated clusters may serve as a model to mimic the environment that these acids are in/on the surface of aerosols. More detailed experimental investigations of these overtone-initiated concerted reactions are needed to fully assess their importance in the atmosphere.

7. CONCLUSIONS

Solar radiation provides sufficient energy to drive chemical reactions in the atmosphere and determines the earth's climate and temperature. Typically, the UV region of the solar spectrum (200–400 nm) is considered for chemical reactions since electronic transitions occur in this region and absorption in that wavelength range corresponds to normal chemical bond energies [3]. At high solar zenith angles, UV light is suppressed and low-energy visible radiation becomes important [2, 26]. Therefore, absorption of radiation in the near-IR and visible regions, which are usually dominated by X–H stretching vibrational overtones, play a significant role in determining the atmospheric chemistry and fate of certain organic compounds [7, 14, 16, 161].

Atmospheric chemistry via O–H overtone pumping can be driven by three mechanisms. In the first case, an O–H stretch (or any other strongly absorbing local mode oscillator) is excited into a vibrational overtone followed by intramolecular vibrational energy redistribution (IVR) which transfers sufficient energy into a weaker bond in the molecule to cause dissociation [2, 22, 26, 30]. Even though the O–H stretch itself is excited, it is ultimately a different weaker bond in the molecule that is broken. This is the

case for compounds such as nitric acid [57], pernitric acid [17, 32], and hydrogen peroxide [61–63] which all have relatively weak bonds. A second scenario involves exciting the O–H overtone state which is strongly coupled to the reaction coordinate [2]. Strong coupling of the excited state with the reaction coordinate allows for the concerted excitation of low-frequency modes (heavy atom motion) causing the photoexcited O–H bond to break at energies significantly lower than the bond dissociation energy at its equilibrium geometry. The mechanism is best described as a concerted reaction. In sulfuric acid, for example, excitation well above $\nu_{OH} = 6$ induces the hydrogen of the O–H bond to migrate to a different location in the molecule followed by dissociation [11]. This occurs on the timescale of picoseconds, while the process of IVR requires a significantly longer time on the order of nanoseconds [12]. Malonic acid is another example in which case the reaction is also concerted [16]. Lastly, the third process is a mechanism entailing solar radiation in sequential two-photon absorption [162]. The first photon excites a vibrational overtone into an intermediate state, while the second photon promotes the system to a repulsive dissociative first excited electronic state.

In the atmosphere, the excited species are under conditions, where deactivation can occur through collisions with water and other "cold" molecules (N_2, O_2, etc.). Therefore, the quantum yield will be defined by how fast the reaction proceeds in comparison to the deactivation time defined by collisions to these "cold" surrounding bath molecules [11, 12, 160, 163]. In discussing the time scales of overtone-induced unimolecular reaction, a key aspect to consider is whether the reaction proceeds directly or statistically. It would be expected that concerted reactions which have the excited O–H bond strongly coupled to the reaction coordinate will likely occur more directly than bond dissociation, although this will be left for future studies. Detailed study of the reaction dynamics following overtone excitation is needed in order to calculate the quantum yield and accurate J-vales for overtone-induced reactions which appear to be possible and probable in the atmosphere.

ACKNOWLEDGMENTS

The authors thank H. G. Kjaergaard and S. Yabushita for valuable input and assistance with references. Support for this work from the NSF is gratefully acknowledged.

REFERENCES

[1] R. Goody, *Principles of Atmospheric Physics and Chemistry*, Oxford University Press, Oxford, UK, 1995.

[2] D. J. Donaldson, A. F. Tuck, and V. Vaida, "Atmospheric photochemistry via vibrational overtone absorption," *Chemical Reviews*, vol. 103, no. 12, pp. 4717–4729, 2003.

[3] B. J. Finlayson-Pitts and J. N. Pitts, *Chemistry of the Upper and Lower Atmosphere: Theory, Experiments, and Applications*, Academic Press, New York, NY, USA, 2000.

[4] J. G. Calvert and J. N. Pitts, *Photochemistry*, John Wiley & Sons, New York, NY, USA, 1966.

[5] R. P. Wayne, *Principles and Applications of Photochemistry*, Oxford University Press, Oxford, UK, 1988.

[6] V. Vaida, "Review article: sunlight initiated atmospheric photochemical reactions," *International Journal of Photoenergy*, vol. 7, no. 2, pp. 61–70, 2005.

[7] V. Vaida, H. G. Kjaergaard, P. E. Hintze, and D. J. Donaldson, "Photolysis of sulfuric acid vapor by visible solar radiation," *Science*, vol. 299, no. 5612, pp. 1566–1568, 2003.

[8] K. J. Feierabend, D. K. Havey, S. S. Brown, and V. Vaida, "Experimental absolute intensities of the $4\nu_9$ and $5\nu_9$ O-H stretching overtones of H_2SO_4," *Chemical Physics Letters*, vol. 420, no. 4–6, pp. 438–442, 2006.

[9] D. K. Havey and V. Vaida, "Near infrared spectroscopy of organic acids: comparing O-H and C-H oscillator frequencies and intensities," *Journal of Molecular Spectroscopy*, vol. 228, no. 1, pp. 152–159, 2004.

[10] J. R. Lane, H. G. Kjaergaard, K. L. Plath, and V. Vaida, "Overtone spectroscopy of sulfonic acid derivatives," *Journal of Physical Chemistry A*, vol. 111, no. 25, pp. 5434–5440, 2007.

[11] Y. Miller and R. B. Gerber, "Dynamics of vibrational overtone excitations of H_2SO_4, H_2SO_4-H_2O: hydrogen-hopping and photodissociation processes," *Journal of the American Chemical Society*, vol. 128, no. 30, pp. 9594–9595, 2006.

[12] Y. Miller, R. B. Gerber, and V. Vaida, "Photodissociation yields for vibrationally excited states of sulfuric acid under atmospheric conditions," *Geophysical Research Letters*, vol. 34, no. 16, L16820, 2007.

[13] M. J. Mills, O. B. Toon, V. Vaida, et al., "Photolysis of sulfuric acid vapor by visible as a source of the polar stratospheric CN layer," *Journal of Geophysical Research*, vol. 110, no. 8, D08201, 2005.

[14] L. M. Reynard and D. J. Donaldson, "Overtone-induced chemistry of trifluoroacetic acid: an experimental and theoretical study," *Journal of Physical Chemistry A*, vol. 106, no. 37, pp. 8651–8657, 2002.

[15] N. Rontu and V. Vaida, "Vibrational spectroscopy of perfluorocarboxylic acids from the infrared to the visible regions," *Journal of Physical Chemistry B*, vol. 112, no. 2, pp. 276–282, 2008.

[16] M. Staikova, M. Oh, and D. J. Donaldson, "Overtone-induced decarboxylation: a potential sink for atmospheric diacids," *Journal of Physical Chemistry A*, vol. 109, no. 4, pp. 597–602, 2005.

[17] L. Fono, D. J. Donaldson, R. J. Proos, and B. R. Henry, "OH overtone spectra and intensities of pernitric acid," *Chemical Physics Letters*, vol. 311, no. 3-4, pp. 131–138, 1999.

[18] D. K. Havey, K. J. Feierabend, K. Takahashi, R. T. Skodje, and V. Vaida, "Experimental and theoretical investigation of vibrational overtones of glycolic acid and its hydrogen bonding interactions with water," *Journal of Physical Chemistry A*, vol. 110, no. 20, pp. 6439–6446, 2006.

[19] I. M. Konen, E. X. J. Li, M. I. Lester, J. Vázquez, and J. F. Stanton, "Infrared overtone spectroscopy and vibrational analysis of a Fermi resonance in nitric acid: experiment and theory," *The Journal of Chemical Physics*, vol. 125, no. 7, Article ID 074310, 12 pages, 2006.

[20] J. Matthews, A. Sinha, and J. S. Francisco, "Relative vibrational overtone intensity of *cis-cis* and *trans-perp* peroxynitrous acids," *The Journal of Chemical Physics*, vol. 120, no. 22, pp. 10543–10553, 2004.

[21] J. Matthews, A. Sinha, and J. S. Francisco, "The importance of weak absorption features in promoting tropospheric radical production," *Proceedings of the National Academy of Sciences of the United States of America*, vol. 102, no. 21, pp. 7449–7452, 2005.

[22] Y. Miller, G. M. Chaban, B. J. Finlayson-Pitts, and R. B. Gerber, "Photochemical processes induced by vibrational overtone excitations: dynamics simulations for *cis*-HONO, *trans*-HONO, HNO_3, and HNO_3-H_2O," *Journal of Physical Chemistry A*, vol. 110, no. 16, pp. 5342–5354, 2006.

[23] S. A. Nizkorodov, J. D. Crounse, J. L. Fry, C. M. Roehl, and P. O. Wennberg, "Near-IR photodissociation of peroxy acetyl nitrate," *Atmospheric Chemistry and Physics*, vol. 5, no. 2, pp. 385–392, 2005.

[24] S. S. Brown, R. W. Wilson, and A. R. Ravishankara, "Absolute intensities for third and fourth overtone absorptions in HNO_3 and H_2O_2 measured by cavity ring down spectroscopy," *Journal of Physical Chemistry A*, vol. 104, no. 21, pp. 4976–4983, 2000.

[25] D. J. Donaldson and J. S. Francisco, "Bimolecular reaction of molecular oxygen with overtone excited HOOH: implications for recycling HO_2 in the atmosphere," *Physical Chemistry Chemical Physics*, vol. 5, no. 15, pp. 3183–3187, 2003.

[26] D. J. Donaldson, G. J. Frost, K. H. Rosenlof, A. F. Tuck, and V. Vaida, "Atmospheric radical production by excitation of vibrational overtones via absorption of visible light," *Geophysical Research Letters*, vol. 24, no. 21, pp. 2651–2654, 1997.

[27] L. M. Haynes, K. M. Vogelhuber, J. L. Pippen, and S. Hsieh, "Effects of torsion on O-H stretch overtone spectra and direct overtone photolysis of methyl hydroperoxide," *The Journal of Chemical Physics*, vol. 123, no. 23, Article ID 234306, 9 pages, 2005.

[28] C. M. Roehl, S. A. Nizkorodov, H. Zhang, G. A. Blake, and P. O. Wennberg, "Photodissociation of peroxynitric acid in the near-IR," *Journal of Physical Chemistry A*, vol. 106, no. 15, pp. 3766–3772, 2002.

[29] R. J. Salawitch, P. O. Wennberg, G. C. Toon, B. Sen, and J.-F. Blavier, "Near IR photolysis of HO_2NO_2: implications for HO_x," *Geophysical Research Letters*, vol. 29, no. 16, 1762, 2002.

[30] M. Staikova, D. J. Donaldson, and J. S. Francisco, "Overtone-induced reactions on the HO_2NO_2 potential surface," *Journal of Physical Chemistry A*, vol. 106, no. 12, pp. 3023–3028, 2002.

[31] P. O. Wennberg, R. J. Salawitch, D. J. Donaldson, et al., "Twilight observations suggest unknown sources of HO_x," *Geophysical Research Letters*, vol. 26, no. 10, pp. 1373–1376, 1999.

[32] H. Zhang, C. M. Roehl, S. P. Sander, and P. O. Wennberg, "Intensity of the second and third OH overtones of H_2O_2, HNO_3, and HO_2NO_2," *Journal of Geophysical Research*, vol. 105, no. D11, pp. 14593–14598, 2000.

[33] P. Di Carlo, W. H. Brune, M. Martinez, et al., "Missing OH reactivity in a forest: evidence for unknown reactive biogenic VOCs," *Science*, vol. 304, no. 5671, pp. 722–725, 2004.

[34] C. L. Heald, D. J. Jacob, R. J. Park, et al., "A large organic aerosol source in the free troposphere missing from current models," *Geophysical Research Letters*, vol. 32, no. 18, L18809, 2005.

[35] Y. Rudich, N. M. Donahue, and T. F. Mentel, "Aging of organic aerosol: bridging the gap between laboratory and field studies," *Annual Review of Physical Chemistry*, vol. 58, pp. 321–352, 2007.

[36] J. Williams, "Organic trace gases in the atmosphere: an overview," *Environmental Chemistry*, vol. 1, no. 3, pp. 125–136, 2004.

[37] B. Ervens, A. G. Carlton, B. J. Turpin, K. E. Altieri, S. M. Kreidenweis, and G. Feingold, "Secondary organic aerosol yields from cloud-processing of isoprene oxidation products," *Geophysical Research Letters*, vol. 35, no. 2, L02816, 2008.

[38] R. Volkamer, J. L. Jimenez, F. San Martini, et al., "Secondary organic aerosol formation from anthropogenic air pollution: rapid and higher than expected," *Geophysical Research Letters*, vol. 33, no. 17, L17811, 2006.

[39] R. Volkamer, F. San Martini, L. T. Molina, D. Salcedo, J. L. Jimenez, and M. J. Molina, "A missing sink for gas-phase glyoxal in Mexico City: formation of secondary organic aerosol," *Geophysical Research Letters*, vol. 34, no. 19, L19807, 2007.

[40] E. B. Wilson, J. C. Decius, and P. C. Cross, *Molecular Vibrations*, McGraw-Hill, New York, NY, USA, 1955.

[41] M. S. Child, "Local mode overtone spectra," *Accounts of Chemical Research*, vol. 18, no. 2, pp. 45–50, 1985.

[42] B. R. Henry, "Use of local modes in the description of highly vibrationally excited molecules," *Accounts of Chemical Research*, vol. 10, no. 6, pp. 207–213, 1977.

[43] B. R. Henry and H. G. Kjaergaard, "Local modes," *Canadian Journal of Chemistry*, vol. 80, no. 12, pp. 1635–1642, 2002.

[44] B. R. Henry, "The local mode model and overtone spectra: a probe of molecular structure and conformation," *Accounts of Chemical Research*, vol. 20, no. 12, pp. 429–435, 1987.

[45] W. Siebrand and D. F. Williams, "Radiationless transitions in polyatomic molecules. III. Anharmonicity, isotope effects, and singlet-to-ground-state transitions in aromatic hydrocarbons," *The Journal of Chemical Physics*, vol. 49, no. 4, pp. 1860–1871, 1968.

[46] M. S. Child and L. Halonen, "Overtone frequencies and intensities in the local mode picture," *Advances in Chemical Physics*, vol. 57, pp. 1–58, 1984.

[47] L. Halonen, "Local mode vibrations in polyatomic molecules," *Advances in Chemical Physics*, vol. 104, pp. 41–179, 1998.

[48] B. R. Henry and W. Siebrand, "Anharmonicity in polyatomic molecules. The Ch-stretching overtone spectrum of benzene," *The Journal of Chemical Physics*, vol. 49, no. 12, pp. 5369–5376, 1968.

[49] R. Mecke, "Dipolmoment Und Chemische Bindung," *Zeitschrift für Elektrochemie*, vol. 54, no. 1, pp. 38–42, 1950.

[50] J. W. Perry and A. H. Zewail, "Local modes: their relaxation, polarization, and stereoselective excitation by lasers," *Journal of Physical Chemistry*, vol. 86, no. 26, pp. 5197–5205, 1982.

[51] M. Quack, "Spectra and dynamics of coupled vibrations in polyatomic molecules," *Annual Review of Physical Chemistry*, vol. 41, no. 1, pp. 839–874, 1990.

[52] M. L. Sage and J. Jortner, "Cooperative excitations of bond modes," *Chemical Physics Letters*, vol. 79, no. 1, pp. 9–14, 1981.

[53] P. R. Stannard, M. L. Elert, and W. M. Gelbart, "On the overtone-combination spectra of XY_2 moleculesa," *The Journal of Chemical Physics*, vol. 74, no. 11, pp. 6050–6062, 1981.

[54] A. Callegari and T. R. Rizzo, "State-to-state unimolecular reaction dynamics of highly vibrationally excited molecules," *Chemical Society Reviews*, vol. 30, no. 4, pp. 214–225, 2001.

[55] F. F. Crim, "Bond-selected chemistry: vibrational state control of photodissociation and bimolecular reaction," *Journal of Physical Chemistry*, vol. 100, no. 31, pp. 12725–12734, 1996.

[56] F. F. Crim, "Vibrational state control of bimolecular reactions: discovering and directing the chemistry," *Accounts of Chemical Research*, vol. 32, no. 10, pp. 877–884, 1999.

[57] A. Sinha, R. L. Vander Wal, and F. F. Crim, "State-resolved unimolecular reactions: the vibrational overtone initiated decomposition of nitric acid," *The Journal of Chemical Physics*, vol. 92, no. 1, pp. 401–410, 1990.

[58] T. Uzer, J. T. Hynes, and W. P. Reinhardt, "Classical dynamics of intramolecular energy flow and overtone-induced dissociation in HO_2H and HO_2D," *The Journal of Chemical Physics*, vol. 85, no. 10, pp. 5791–5804, 1986.

[59] E. L. Sibert III, W. P. Reinhardt, and J. T. Hynes, "Classical dynamics of energy transfer between bonds in *ABA* triatomics," *The Journal of Chemical Physics*, vol. 77, no. 7, pp. 3583–3594, 1982.

[60] E. L. Sibert III, W. P. Reinhardt, and J. T. Hynes, "Intramolecular vibrational relaxation and spectra of CH and CD overtones in benzene and perdeuterobenzene," *The Journal of Chemical Physics*, vol. 81, no. 3, pp. 1115–1134, 1984.

[61] F. F. Crim, "Selective excitation studies of unimolecular reaction dynamics," *Annual Review of Physical Chemistry*, vol. 35, pp. 657–691, 1984.

[62] T. R. Rizzo, C. C. Hayden, and F. F. Crim, "State-resolved product detection in the overtone vibration initiated unimolecular decomposition of $HOOH(6_{\nu OH})$," *The Journal of Chemical Physics*, vol. 81, no. 10, pp. 4501–4509, 1984.

[63] T. M. Ticich, T. R. Rizzo, H.-R. Dubai, and F. F. Crim, "Unimolecular reactions near threshold: the overtone vibration initiated decomposition of $HOOH(5_{\nu OH})$," *The Journal of Chemical Physics*, vol. 84, no. 3, pp. 1508–1520, 1986.

[64] I. M. Konen, E. X. J. Li, T. A. Stephenson, and M. I. Lester, "Second OH overtone excitation and statistical dissociation dynamics of peroxynitrous acid," *The Journal of Chemical Physics*, vol. 123, no. 20, Article ID 204318, 11 pages, 2005.

[65] I. M. Konen, I. B. Pollack, E. X. J. Li, M. I. Lester, M. E. Varner, and J. F. Stanton, "Infrared overtone spectroscopy and unimolecular decay dynamics of peroxynitrous acid," *The Journal of Chemical Physics*, vol. 122, no. 9, Article ID 204318, 16 pages, 2005.

[66] E. X. J. Li, I. M. Konen, M. I. Lester, and A. B. McCoy, "Spectroscopic characterization of peroxynitrous acid in cisperp configurations," *Journal of Physical Chemistry A*, vol. 110, no. 17, pp. 5607–5612, 2006.

[67] J. Matthews, A. Sinha, and J. S. Francisco, "Unimolecular dissociation and thermochemistry of CH_3OOH," *The Journal of Chemical Physics*, vol. 122, no. 22, Article ID 221101, 4 pages, 2005.

[68] E. L. Derro, C. Murray, T. D. Sechler, and M. I. Lester, "Infrared action spectroscopy and dissociation dynamics of the HOOO radical," *Journal of Physical Chemistry A*, vol. 111, no. 45, pp. 11592–11601, 2007.

[69] C. Murray, E. L. Derro, T. D. Sechler, and M. I. Lester, "Stability of the hydrogen trioxy radical via infrared action spectroscopy," *Journal of Physical Chemistry A*, vol. 111, no. 22, pp. 4727–4730, 2007.

[70] D. Bingemann, M. P. Gorman, A. M. King, and F. F. Crim, "Time-resolved vibrationally mediated photodissociation of HNO_3: watching vibrational energy flow," *The Journal of Chemical Physics*, vol. 107, no. 2, pp. 661–664, 1997.

[71] A. Sinha, R. L. Vander Wal, and F. F. Crim, "The vibrationally mediated photodissociation dynamics of nitric acid," *The Journal of Chemical Physics*, vol. 91, no. 5, pp. 2929–2938, 1989.

[72] Y. S. Li, R. M. Whitnell, K. R. Wilson, and R. D. Levine, "Solvent effects on dynamics of overtone-induced dissociation," *Journal of Physical Chemistry*, vol. 97, no. 15, pp. 3647–3657, 1993.

[73] S. Skokov, K. A. Peterson, and J. M. Bowman, "An accurate *ab initio* HOCl potential energy surface, vibrational and rotational calculations, and comparison with experiment," *The Journal of Chemical Physics*, vol. 109, no. 7, pp. 2662–2671, 1998.

[74] S. Skokov, J. Qi, J. M. Bowman, et al., "Accurate variational calculations and analysis of the HOCl vibrational energy spectrum," *The Journal of Chemical Physics*, vol. 109, no. 23, pp. 10273–10283, 1998.

[75] J. Weiss, J. Hauschildt, R. Schinke, et al., "The unimolecular dissociation of the OH stretching states of HOCl: comparison with experimental data," *The Journal of Chemical Physics*, vol. 115, no. 19, pp. 8880–8887, 2001.

[76] H. G. Kjaergaard, D. L. Howard, D. P. Schofield, T. W. Robinson, S.-I. Ishiuchi, and M. Fujii, "OH- and CH-stretching overtone spectra of catechol," *Journal of Physical Chemistry A*, vol. 106, no. 2, pp. 258–266, 2002.

[77] K. Takahashi, "XH Stretching Vibrational Spectra: A Theoretical Perspective," Ph. D. diss., Keio University, 2004.

[78] D. J. Donaldson, J. J. Orlando, S. Amann, et al., "Absolute intensities of nitric acid overtones," *Journal of Physical Chemistry A*, vol. 102, no. 27, pp. 5171–5174, 1998.

[79] N. Rontu and V. Vaida, "Vibrational spectroscopy of perfluoropropionic acid in the region between 1000 and 11 000 cm^{-1}," *Journal of Molecular Spectroscopy*, vol. 237, no. 1, pp. 19–26, 2006.

[80] D. P. Schofield, H. G. Kjaergaard, J. Matthews, and A. Sinha, "The OH-stretching and OOH-bending overtone spectrum of HOONO," *Journal of Chemical Physics*, vol. 123, no. 13, Article ID 134318, 9 pages, 2005.

[81] S. A. Nizkorodov, M. Ziemkiewicz, D. J. Nesbitt, and A. E.W. Knight, "Overtone spectroscopy of H_2O clusters in the $\nu_{OH} = 2$ manifold: infrared-ultraviolet vibrationally mediated dissociation studies," *Journal of Chemical Physics*, vol. 122, no. 19, pp. 1–11, 2005.

[82] K. R. Lange, N. P. Wells, K. S. Plegge, and J. A. Phillips, "Integrated intensities of O-H stretching bands: fundamentals and overtones in vapor-phase alcohols and acids," *Journal of Physical Chemistry A*, vol. 105, no. 14, pp. 3481–3486, 2001.

[83] J. A. Phillips, J. J. Orlando, G. S. Tyndall, and V. Vaida, "Integrated intensities of OH vibrational overtones in alcohols," *Chemical Physics Letters*, vol. 296, no. 3-4, pp. 377–383, 1998.

[84] K. Takahashi, M. Sugawara, and S. Yabushita, "Effective one-dimensional dipole moment function for the OH stretching overtone spectra of simple acids and alcohols," *The Journal of Physical Chemistry A*, vol. 109, no. 19, pp. 4242–4251, 2005.

[85] M. E. Dunn, G. C. Shields, and V. Vaida, "Experimental and theoretical study of the OH vibrational spectra and overtone chemistry of gas-phase vinylacetic acid," submitted to *The Journal of Physical Chemistry A*.

[86] D. W. Chandler, W. E. Farneth, and R. N. Zare, "A search for mode-selective chemistry: the unimolecular dissociation of t-butyl hydroperoxide induced by vibrational overtone excitation," *The Journal of Chemical Physics*, vol. 77, no. 9, pp. 4447–4458, 1982.

[87] M.-C. Chuang, J. E. Baggott, D. W. Chandler, W. E. Farneth, and R. N. Zare, "Unimolecular decomposition of t-butylhydroperoxide by direct excitation of the 6-0 O-H stretching overtone," *Faraday Discussions of the Chemical Society*, vol. 75, pp. 301–313, 1983.

[88] R. L. Swofford, M. E. Long, and A. C. Albrecht, "C-H vibrational states of benzene, naphthalene, and anthracene in the visible region by thermal lensing spectroscopy and the

local mode model," *The Journal of Chemical Physics*, vol. 65, no. 1, pp. 179–190, 1976.

[89] M. S. Burberry, J. A. Morrell, A. C. Albrecht, and R. L. Swofford, "Local mode overtone intensities of C-H stretching modes in alkanes and methyl substituted benzenes," *The Journal of Chemical Physics*, vol. 70, no. 12, pp. 5522–5526, 1979.

[90] O. S. Mortensen, B. R. Henry, and M. A. Mohammadi, "The effects of symmetry within the local mode picture: a reanalysis of the overtone spectra of the dihalomethanes," *The Journal of Chemical Physics*, vol. 75, no. 10, pp. 4800–4808, 1981.

[91] R. T. Birge and H. Sponer, "The heat of dissociation of non-polar molecules," *Physical Review*, vol. 28, no. 2, pp. 259–283, 1926.

[92] P. M. Morse, "Diatomic molecules according to the wave mechanics. II. Vibrational levels," *Physical Review*, vol. 34, no. 1, pp. 57–64, 1929.

[93] O. L. Polyansky, A. G. Császár, S. V. Shirin, et al., "High-accuracy ab initio rotation-vibration transitions for water," *Science*, vol. 299, no. 5606, pp. 539–542, 2003.

[94] D. B. Atkinson, "Solving chemical problems of environmental importance using cavity ring-down spectroscopy," *The Analyst*, vol. 128, no. 2, pp. 117–125, 2003.

[95] S. M. Ball and R. L. Jones, "Broad-band cavity ring-down spectroscopy," *Chemical Reviews*, vol. 103, no. 12, pp. 5239–5262, 2003.

[96] G. Berden, R. Peeters, and G. Meijer, "Cavity ring-down spectroscopy: experimental schemes and applications," *International Reviews in Physical Chemistry*, vol. 19, no. 4, pp. 565–607, 2000.

[97] S. S. Brown, "Absorption spectroscopy in high-finesse cavities for atmospheric studies," *Chemical Reviews*, vol. 103, no. 12, pp. 5219–5238, 2003.

[98] J. J. Scheret, J. B. Paul, A. O'Keefe, and R. J. Saykally, "Cavity ringdown laser absorption spectroscopy: history, development, and application to pulsed molecular beams," *Chemical Reviews*, vol. 97, no. 1, pp. 25–51, 1997.

[99] B. R. Henry, H. G. Kjaergaard, B. Niefer, B. J. Schattka, and D. M. Turnbull, "The local mode model and recent advances in laser based photoacoustic spectroscopyy—1992 Gerhard Herzberg Award Address," *Canadian Journal of Applied Spectroscopy*, vol. 38, no. 2, pp. 42–50, 1993.

[100] B. J. Schattka, D. M. Turnbull, H. G. Kjaergaard, and B. R. Henry, "Dependence of an acoustically nonresonant intracavity photoacoustic signal on sample and buffer gas pressure," *Journal of Physical Chemistry*, vol. 99, no. 17, pp. 6327–6332, 1995.

[101] H. D. Bruszis, "Physical foundations and application of photoacoustic spectroscopy (review)," *Industrial Laboratory*, vol. 52, no. 3, pp. 225–230, 1986.

[102] S. C. Homitsky, S. M. Dragulin, L. M. Haynes, and S. Hsieh, "O-H stretch overtone excitation in methyl and ethyl hydroperoxides," *The Journal of Physical Chemistry A*, vol. 108, no. 44, pp. 9492–9499, 2004.

[103] E. P. C. Lai, B. L. Chan, and M. Hadjmohammadi, "Use and applications of photoacoustic spectroscopy," *Applied Spectroscopy Reviews*, vol. 21, no. 3, pp. 179–210, 1985.

[104] D. L. Howard, P. Jørgensen, and H. G. Kjaergaard, "Weak intramolecular interactions in ethylene glycol identified by vapor phase OH-stretching overtone spectroscopy," *Journal of the American Chemical Society*, vol. 127, no. 48, pp. 17096–17103, 2005.

[105] S. Hsieh, B. J. Miller, A. H. Södergren, and H. G. Kjaergaard, "Vibrational overtone spectroscopy of three-membered rings," *The Journal of Physical Chemistry A*, vol. 111, no. 25, pp. 5415–5421, 2007.

[106] H. W. Rohrs, G. J. Frost, G. B. Ellison, E. C. Richard, and V. Vaida, "Fourier transform spectroscopy of radicals," in *Advances in Molecular Structure Research*, M. Hargittai and I. Hargittai, Eds., vol. 1, pp. 157–199, JAI Press, Greenwich, Conn, USA, 1995.

[107] D. L. Howard and H. G. Kjaergaard, "Influence of intramolecular hydrogen bond strength on OH-stretching overtones," *The Journal of Physical Chemistry A*, vol. 110, no. 34, pp. 10245–10250, 2006.

[108] K. L. Plath, et al., "Fundamental and overtone vibrational spectroscopy of gas phase pyruvic acid," submitted to *The Journal of Physical Chemistry A*. In preparation.

[109] P. W. Atkins and R. S. Friedman, *Molecular Quantum Mechanics*, Oxford University Press, Oxford, UK, 3rd edition, 1997.

[110] P. Echenique and J. L. Alonso, "A mathematical and computational review of Hartree-Fock SCF methods in quantum chemistry," *Molecular Physics*, vol. 105, no. 23-24, pp. 3057–3098, 2007.

[111] D. R. Hartree, "The wave mechanics of an atom with a non-Coulomb central field—part I: theory and methods," *Proceedings of the Cambridge Philosophical Society*, vol. 24, pp. 89–110, 1928.

[112] R. G. Parr and W. Yang, *Density Functional Theory of Atoms and Molecules*, Oxford University Press, New York, NY, USA, 1989.

[113] A. D. Becke, "Density-functional thermochemistry. III. The role of exact exchange," *The Journal of Chemical Physics*, vol. 98, no. 7, pp. 5648–5652, 1993.

[114] C. Lee, W. Yang, and R. G. Parr, "Development of the Colle-Salvetti correlation-energy formula into a functional of the electron density," *Physical Review B*, vol. 37, no. 2, pp. 785–789, 1988.

[115] J. Gauss and D. Cremer, "Analytical evaluation of energy gradients in quadratic configuration-interaction theory," *Chemical Physics Letters*, vol. 150, no. 3-4, pp. 280–286, 1988.

[116] J. A. Pople, M. Head-Gordon, and K. Raghavachari, "Quadratic configuration interaction. A general technique for determining electron correlation energies," *The Journal of Chemical Physics*, vol. 87, no. 10, pp. 5968–5975, 1987.

[117] E. A. Salter, G. W. Trucks, and R. J. Bartlett, "Analytic energy derivatives in many-body methods. I. First derivatives," *The Journal of Chemical Physics*, vol. 90, no. 3, pp. 1752–1766, 1989.

[118] G. D. Purvis III and R. J. Bartlett, "A full coupled-cluster singles and doubles model: the inclusion of disconnected triples," *The Journal of Chemical Physics*, vol. 76, no. 4, pp. 1910–1918, 1982.

[119] G. E. Scuseria, C. L. Janssen, and H. F. Schaefer III, "An efficient reformulation of the closed-shell coupled cluster single and double excitation (CCSD) equations," *The Journal of Chemical Physics*, vol. 89, no. 12, pp. 7382–7387, 1988.

[120] G. E. Scuseria and H. F. Schaefer III, "Is coupled cluster singles and doubles (CCSD) more computationally intensive than quadratic configuration interaction (QCISD)?" *The Journal of Chemical Physics*, vol. 90, no. 7, pp. 3700–3703, 1989.

[121] I. Shavitt, "The methods of configuration interaction," in *Methods of Electronic Structure Theory: Modern Theoretical*

Chemistry III, H. F. Schaefer, Ed., pp. 189–275, Plenum Press, New York, NY, USA, 1977.

[122] T.-K. Ha, M. Lewerenz, R. Marquardt, and M. Quack, "Overtone intensities and dipole moment surfaces for the isolated CH chromophore in CHD3 and CHF3: experiment and ab initio theory," *The Journal of Chemical Physics*, vol. 93, no. 10, pp. 7097–7109, 1990.

[123] N. M. Poulin, M. J. Bramley, T. Carrington Jr., H. G. Kjaergaard, and B. R. Henry, "Calculation of vibrational ($J = 0$) excitation energies and band intensities of formaldehyde using the recursive residue generation method," *The Journal of Chemical Physics*, vol. 104, no. 20, pp. 7807–7820, 1996.

[124] J. Tennyson and S. Miller, "A program suite for the calculation of ro-vibrational spectra of triatomic molecules," *Computer Physics Communications*, vol. 55, no. 2, pp. 149–175, 1989.

[125] J. M. Bowman, "Self-consistent field energies and wavefunctions for coupled oscillators," *The Journal of Chemical Physics*, vol. 68, no. 2, pp. 608–610, 1978.

[126] J. M. Bowman, K. Christoffel, and F. Tobin, "Application of SCF-SI theory to vibrational motion in polyatomic molecules," *Journal of Physical Chemistry*, vol. 83, no. 8, pp. 905–912, 1979.

[127] O. Christiansen, "Vibrational coupled cluster theory," *The Journal of Chemical Physics*, vol. 120, no. 5, pp. 2149–2159, 2004.

[128] K. J. Feierabend, D. K. Havey, M. E. Varner, J. F. Stanton, and V. Vaida, "A comparison of experimental and calculated spectra of HNO_3 in the near-infrared using Fourier transform infrared spectroscopy and vibrational perturbation theory," *The Journal of Chemical Physics*, vol. 124, no. 12, Article ID 124323, 6 pages, 2006.

[129] D. Neuhauser, "Bound state eigenfunctions from wave packets: time→energy resolution," *The Journal of Chemical Physics*, vol. 93, no. 4, pp. 2611–2616, 1990.

[130] H. G. Kjaergaard, B. R. Henry, and A. W. Tarr, "Intensities in local mode overtone spectra of dimethyl ether and acetone," *The Journal of Chemical Physics*, vol. 94, no. 9, pp. 5844–5854, 1991.

[131] K. Takahashi, M. Sugawara, and S. Yabushita, "Theoretical analysis on the fundamental and overtone OH stretching spectra of several simple acids and alcohols," *Journal of Physical Chemistry A*, vol. 107, no. 50, pp. 11092–11101, 2003.

[132] J. Chandrasekhar, G. W. Spitznagel, and P. V. R. Schleyer, "Efficient diffuse function-augmented basis sets for anion calculations.III. The 3-21+G basis set for first-row elements, Li-F," *Journal of Computational Chemistry*, vol. 4, no. 3, pp. 294–301, 1983.

[133] M. J. Frisch, J. A. Pople, and J. S. Binkley, "Self-consistent molecular orbital methods 25. Supplementary functions for Gaussian basis sets," *The Journal of Chemical Physics*, vol. 80, no. 7, pp. 3265–3269, 1984.

[134] M. J. T. Frisch, G. W. Schlegel, and H. B. Scuseria, "Gaussian 03," Gaussian, Wallingford, Conn, USA, 2004.

[135] R. Krishnan, J. S. Binkley, R. Seeger, and J. A. Pople, "Self-consistent molecular orbital methods. XX. A basis set for correlated wave functions," *The Journal of Chemical Physics*, vol. 72, no. 1, pp. 650–654, 1980.

[136] A. D. McLean and G. S. Chandler, "Contracted Gaussian basis sets for molecular calculations—I: second row atoms, Z=11-18," *The Journal of Chemical Physics*, vol. 72, no. 10, pp. 5639–5648, 1980.

[137] P. E. Hintze, H. G. Kjaergaard, V. Vaida, and J. B. Burkholder, "Vibrational and electronic spectroscopy of sulfuric acid vapor," *Journal of Physical Chemistry A*, vol. 107, no. 8, pp. 1112–1118, 2003.

[138] D. L. Howard and H. G. Kjaergaard, "Resonance coupling in the fourth OH-stretching overtone spectrum of formic acid," *The Journal of Chemical Physics*, vol. 121, no. 1, pp. 136–140, 2004.

[139] H. G. Kjaergaard, J. D. Goddard, and B. R. Henry, "Calculated intensity in the local mode overtone spectra of hydrogen peroxide," *The Journal of Chemical Physics*, vol. 95, no. 8, pp. 5556–5564, 1991.

[140] J. Matthews, A. Sinha, and J. S. Francisco, "High level ab initio study of the structure and vibrational spectra of HO_2NO_2," *The Journal of Chemical Physics*, vol. 121, no. 12, pp. 5720–5727, 2004.

[141] S.-I. Ishiuchi, M. Fujii, T. W. Robinson, B. J. Miller, and H. G. Kjaergaard, "Vibrational overtone spectroscopy of phenol and its deuterated isotopomers," *Journal of Physical Chemistry A*, vol. 110, no. 23, pp. 7345–7354, 2006.

[142] K. K. Lehmann and A. M. Smith, "Where does overtone intensity come from?" *The Journal of Chemical Physics*, vol. 93, no. 9, pp. 6140–6147, 1990.

[143] K. J. Feierabend, D. K. Havey, and V. Vaida, "Gas phase spectroscopy of HNO_3 in the region 2000–8500 cm^{-1}," *Spectrochimica Acta Part A*, vol. 60, no. 12, pp. 2775–2781, 2004.

[144] M. L. Sage, "High overtone C-H and O-H transitions in gaseous methanol: theory," *The Journal of Chemical Physics*, vol. 80, no. 6, pp. 2872–2879, 1983.

[145] D. K. Havey, K. J. Feierabend, J. C. Black, and V. Vaida, "Temperature-dependent infrared spectra of torsional vibrations in acetic acid," *Journal of Molecular Spectroscopy*, vol. 229, no. 2, pp. 151–157, 2005.

[146] G. M. Florio, T. S. Zwier, E. M. Myshakin, K. D. Jordan, and E. L. Sibert III, "Theoretical modeling of the OH stretch infrared spectrum of carboxylic acid dimers based on first-principles anharmonic couplings," *The Journal of Chemical Physics*, vol. 118, no. 4, pp. 1735–1746, 2003.

[147] C. D. Daub, B. R. Henry, M. L. Sage, and H. G. Kjaergaard, "Modelling and calculation of dipole moment functions for XH bonds," *Canadian Journal of Chemistry*, vol. 77, no. 11, pp. 1775–1781, 1999.

[148] http://nist.gov/srd/nsrds/NSRDS-NBS37.pdf.

[149] L. J. Larson, M. Kuno, and F.-M. Tao, "Hydrolysis of sulfur trioxide to form sulfuric acid in small water clusters," *The Journal of Chemical Physics*, vol. 112, no. 20, pp. 8830–8838, 2000.

[150] K. Morokuma and C. Muguruma, "Ab initio molecular orbital study of the mechanism of the gas phase reaction $SO_3 + H_2O$: importance of the second water molecule," *Journal of the American Chemical Society*, vol. 116, no. 22, pp. 10316–10317, 1994.

[151] K. Saito, T. Shiose, O. Takahashi, Y. Hidaka, F. Aiba, and K. Tabayashi, "Unimolecular decomposition of formic acid in the gas phase-on the ratio of the competing reaction channels," *Journal of Physical Chemistry A*, vol. 109, no. 24, pp. 5352–5357, 2005.

[152] J. S. Francisco, "A comprehensive theoretical examination of primary dissociation pathways of formic acid," *The Journal of Chemical Physics*, vol. 96, no. 2, pp. 1167–1175, 1992.

[153] L. R. Domingo, J. Andrés, V. Moliner, and V. S. Safont, "Theoretical study of the gas phase decomposition of glycolic, lactic, and 2-hydroxyisobutyric acids," *Journal of the American Chemical Society*, vol. 119, no. 27, pp. 6415–6422, 1997.

[154] O. Takahashi, K. Itoh, and K. Saito, "A theoretical study of the bifurcation reaction—II: acetic acid," *Journal of Molecular Structure: THEOCHEM*, vol. 584, no. 1–3, pp. 249–256, 2002.

[155] I. D. P. R. Moreira, "Performance of simplified G2 model chemistry approaches in the study of unimolecular mechanisms: thermal decomposition of acetic acid in gas phase," *Journal of Molecular Structure: THEOCHEM*, vol. 466, no. 1–3, pp. 119–126, 1999.

[156] M. S. Child, "Overtone spectroscopy and unimolecular reactions," *Chemical Society Reviews*, vol. 17, pp. 31–44, 1988.

[157] J. M. Jasinski, J. K. Frisoli, and C. B. Moore, "Unimolecular reactions induced by vibrational overtone excitation," *Faraday Discussions of the Chemical Society*, vol. 75, pp. 289–299, 1983.

[158] J. L. Fry, S. A. Nizkorodov, M. Okumura, C. M. Roehl, J. S. Francisco, and P. O. Wennberg, "*Cis-cis* and *trans-perp* HOONO: action spectroscopy and isomerization kinetics," *The Journal of Chemical Physics*, vol. 121, no. 3, pp. 1432–1448, 2004.

[159] T. L. Williams, *The Morphology and Processing of Models for Organic Atmospheric Aerosols*, Department of Chemistry and Biochemistry, University of Colorado-Boulder, Boulder, Colo, USA, 2004.

[160] K. Takahashi, Z. C. Kramer, V. Vaida, and R. T. Skodje, "Vibrational overtone induced elimination reactions within hydrogen-bonded molecular clusters: the dynamics of water catalyzed reactions in $CH_2FOH\cdot(H_2O)_n$," *Physical Chemistry Chemical Physics*, vol. 9, no. 29, pp. 3864–3871, 2007.

[161] C. J. Young and D. J. Donaldson, "Overtone-induced degradation of perfluorinated alcohols in the atmosphere," *Journal of Physical Chemistry A*, vol. 111, no. 51, pp. 13466–13471, 2007.

[162] L. M. Goss, V. Vaida, J. W. Brault, and R. T. Skodje, "Sequential two-photon dissociation of atmospheric water," *Journal of Physical Chemistry A*, vol. 105, no. 1, pp. 70–75, 2001.

[163] N. F. Scherer and A. H. Zewail, "Picosecond photofragment spectroscopy.II. The overtone initiated unimolecular reaction $H_2O_2(v_{OH} = 5)\rightarrow 2OH$," *The Journal of Chemical Physics*, vol. 87, no. 1, pp. 97–114, 1987.

Hindawi Publishing Corporation
International Journal of Photoenergy
Volume 2008, Article ID 604181, 11 pages
doi:10.1155/2008/604181

Research Article

Photochemistry Aspects of the Laser Pyrolysis Addressing the Preparation of Oxide Semiconductor Photocatalysts

R. Alexandrescu,[1] I. Morjan,[1] F. Dumitrache,[1] M. Scarisoreanu,[1] I. Soare,[1] C. Fleaca,[1] R. Birjega,[1] E. Popovici,[1] L. Gavrila,[1] G. Prodan,[2] V. Ciupina,[2] G. Filoti,[3] V. Kuncser,[3] and L. Vekas[4]

[1] *National Institute for Lasers, Plasma and Radiation Physics, P.O. Box MG 36, 077125 Bucharest, Romania*
[2] *Ovidius University of Constanta, P.O. Box 8600, 900527 Constanta, Romania*
[3] *National Institute of Materials Physics, P.O. Box MG 7, 077125 Bucharest, Romania*
[4] *Centre for Fundamental and Advanced Technical Research, Romanian Academy, Timisoara Branch, Bd. Mihai Viteazul 24 RO, 300223 Timisoara, Romania*

Correspondence should be addressed to R. Alexandrescu, ralexandrescu2001@yahoo.co.uk

Received 28 April 2008; Accepted 25 June 2008

Recommended by Mohamed Sabry Abdel-Mottaleb

The laser pyrolysis is a powerful and a versatile tool for the gas-phase synthesis of nanoparticles. In this paper, some fundamental and applicative characteristics of this technique are outlined and recent results obtained in the preparation of gamma iron oxide (γ-Fe_2O_3) and titania (TiO_2) semiconductor nanostructures are illustrated. Nanosized iron oxide particles (4 to 9 nm diameter values) have been directly synthesized by the laser-induced pyrolysis of a mixture containing iron pentacarbonyl/air (as oxidizer)/ethylene (as sensitizer). Temperature-dependent Mossbauer spectroscopy shows that mainly maghemite is present in the sample obtained at higher laser power. The use of selected Fe_2O_3 samples for the preparation of water-dispersed magnetic nanofluids is also discussed. TiO_2 nanoparticles comprising a mixture of anatase and rutile phases were synthesized via the laser pyrolysis of $TiCl_4$- (vapors) based gas-phase mixtures. High precursor concentration of the oxidizer was found to favor the prevalent anatase phase (about 90%) in the titania nanopowders.

1. INTRODUCTION

In recent years, research interests for the preparation and application of oxide semiconductor photocatalysts have continuously grown [1]. Particular attention is paid to the use of semiconductor materials as photocatalysts for the removal of organic and inorganic species from aqueous or gas phase. This method has been suggested in environmental protection due to its ability to oxidize the organic and inorganic substrates [2]. Several steps should characterize the heterogeneous photocatalysis reaction among which most important should be the adsorption and the reaction onto the surface [3].

Studies were made on compositions consisting mainly of various oxide semiconductors. For instance, commonly used Fe_2O_3 semiconductor oxide is known for its catalytic activity [4, 5]. TiO_2 nanoparticles offer additional advantages (low cost, chemical inertness, highly photo-activity, and suitable band gap (Eg = 3.2 eV)) [6–8].

The photocatalytic activity of a particulate semiconductor system depends on the crystal structure, crystallinity, particle size and shape, size distribution, surface area, and surface hydroxyls. Considerable enhancement of the absorption can be observed in small nanocrystals, where the surface-to-volume ratio is very high and the share of the surface atoms is sufficiently large. Consequently, the synthesis method plays a fundamental role.

A wide variety of gas-phase techniques has been developed for the fabrication of nanoparticulate structures [9] which could allow for homogeneous nucleation and may provide to some extent the control of particle size, particle shape, size distribution, particle composition, and degree of particle agglomeration. Among these synthesis procedures, the laser pyrolysis technique has been developed recently as

a powerful tool for the synthesis of technological important nanomaterials such as metallic (Fe, Ti) oxides and composites [10–13], silicon crystals [14], nanocarbon [15], and iron-siloxane polymer nanoparticles [16].

This paper represents an extension of our earlier analysis on the principles of the laser pyrolysis and its applications [17]. Here, we shortly discuss the background of the method and recent development in the field, with special emphasis on the preparation of two types of semiconductor photocatalysts: maghemite iron oxide and titanium dioxide. In Section 2, the pyrolysis of $Fe(CO)_5$-based gas mixtures and the preparation of magnetic nanofluids are presented in a sequence relevant for the phenomenology of the process and the nanopowder structure. In Section 4, main characteristics of the laser-sensitized pyrolysis of $TiCl_4$-based mixtures for producing titania and anatase titania in connection with their specific structural characteristics are discussed.

2. LASER PYROLYSIS SYNTHESIS

2.1. Photochemical aspects of the laser pyrolysis

The specific features of the CO_2 laser pyrolysis rely on the IR vibrational photochemistry. The process is based on the overlapping of the emission line of the laser (the strong 10P (20) line that peaks at 10.591 μm) with an absorption line of one or more gas precursors [17]. The molecular mechanism involves the increase of the internal energy of the ground electronic state, the evolution of the vibrational states through collisional relaxation processes, and finally the thermochemical reactions. Flynn et al. [18] show that in any environment where multiple collisions occur on the time scale of a chemical reaction, the vibrational modes of a polyatomic molecule will equilibrate, and reaction occurs without energy localization in a single mode. An additional substance, the so-called sensitizer is used in case of nonabsorbing gas precursors. It will absorb the energy and transmit it to the precursors by collisions. This energy transfer agent plays a high practical role (detailed for ethylene in what follows) because it assures the coupling between the laser radiation and the absorbing system. As a final effect of the coupling between the laser radiation and the absorbing system, the laser acts as a localized heat source. As compared to heating the gases in a furnace, the laser heating is a localized one occurring only in a small volume delimitated by the radiation cross section and the emergent gas flows. Short millisecond-scale residence times, spatial uniformity of the reaction zone, and continuous source of activation energy are the key attributes of the process.

$Fe(CO)_5$ and $TiCl_4$ are greatly used as precursors in conventional CVD or in photolytic or thermally laser-induced processes [19]. $Fe(CO)_5$ and $TiCl_4$ molecules meet also other prerequisites for CVD, like stability and relevant vapor pressure at room temperature (around 25 torr and 8 torr at 300 K, resp.). The IR spectra of both of $Fe(CO)_5$ and $TiCl_4$ present no absorption bands near the emission frequencies of the CO_2 laser.

In the sensitized CO_2 laser pyrolysis of $Fe(CO)_5/TiCl_4$, the IR radiation is used to resonantly excite C_2H_4 sensitizer. The absorption coefficient of C_2H_4 at the laser radiation wavelength of the usual CO_2 lasers is 1.7×10^{-3} torr^{-1} cm^{-1}. Ethylene is excited in a superposition of two fundamentals: ν_7 (949.3 cm^{-1}) and ν_8 (940.6 cm^{-1}). The dissociation energy H_2C-CH-H (for one hydrogen stripping) is rather high (103 Kcal/mol [20]).

Ideally, it is supposed that ethylene only transfers its energy by collisions to the other precursors, but do not participate in the reaction. However, the study of the evolution of the exhaust gases often shows that at higher temperatures ethylene could also decompose. Indeed, as a first product of decomposition, acetylene is released and appears as traces in the IR spectrum of the exhaust gases. One should note that the observed C_2H_4 dehydrogenation could be significantly promoted by the active Fe sites generated by $Fe(CO)_5$ dissociation. As shown in [21], although the thermodynamically favored process is the iron pentacarbonyl dissociation, the hydrocarbon decomposition could be speeded up by the catalytic surface of freshly formed iron nanoparticles.

2.2. Advantages and drawbacks

The laser pyrolysis processes are characterized by high temperatures, fast heating rates, and short reaction times. These features make the laser pyrolysis attractive method for the manufacture of technological useful materials at lower costs compared to conventional gas-phase processes (such as the flame spray processes). Some other advantages are (i) the relative simple equipment, (ii) the versatility—the formation of virtually any nanoproducts, provided a suitable choice of precursors, and (iii) formation of high purity products.

The drawbacks of the laser pyrolysis technique are sometimes found in the constraints imposed on the precursors [6]: the desired elements must be present in vapor phase and at least one reactant should contain an infrared absorption band for the coupling of the energy with the laser beam.

2.3. Experimental set-up

The flow reactor is the core of the laser pyrolysis technique, ensuring the practical application of the characteristic interplay between resonant and nonresonant processes. It was presented in details elsewhere [17]. A schematic view of the setup is presented in Figure 1. Briefly, the system is based on a cross-flow configuration. The reactant flow emerges in the reactor through a nozzle system where it is orthogonally intersected by the focused IR radiation beam. Pyrolysis in the gas phase occurs in the small volume defined by the radiation-gases crossing where a "flame" usually appears. It is believed that the visible emission is mainly resulting from the hot freshly nucleated particles. The confinement of gas precursors and of the particles toward the flow axis is achieved by a coaxial argon flow. Nucleated particles are kept entrained by the gas stream and collected in a removable tank at the exit of the reaction cell. Main process parameters are the nature of the gas (vapor) precursors, gas flow rates, pressure, as well as laser wavelength and laser power. For

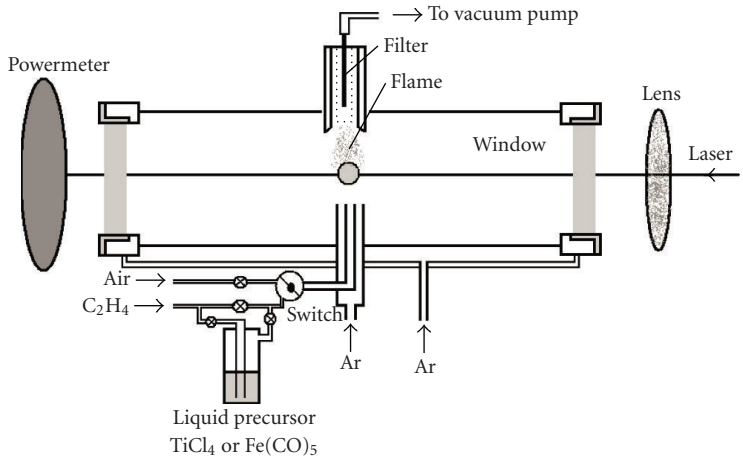

Figure 1: Schematic view of the laser pyrolysis setup for the production of iron oxide and titania nanoparticles, respectively.

liquid precursors, the bubbled vapors are entrained into the reaction zone by a carrier gas.

$Fe(CO)_5/C_2H_4$ and $TiCl_4/C_2H_4$—were alternatively used as basic precursor mixtures for the preparation of iron and titanium oxide nanoparticles, respectively. In Figure 1, both these experimental arrangements are suggested. Additives such as air were employed for obtaining specific oxide nanostructures. In order to prevent the NaCl windows from being coated with powder, they were continuously flushed with Ar. Usually, either ethylene or argon was carrying through a bubbler the vapors of the liquid metal precursor into the reaction zone. In each of these systems, the installation for laser pyrolysis was adapted to the demands imposed by the nature of the precursors and the final aim of the synthesis process. In case of titania nanoparticles, a main variable trend was the change of a double nozzle system with a triple one (not shown in Figure 1) thus trying to avoid the direct reaction of $TiCl_4$ with air.

2.4. Material characterization

After synthesis, the morphology and composition of the iron oxides nanopowders were characterized by transmission electron microscopy (TEM), selected area electron diffraction (SAED), X-ray diffraction (XRD), and Mössbauer spectroscopy. The XRD pattern was recorded on a DRON DART UM-2 diffractometer equipped with a Cu K_α radiation and a graphite monochromator in the diffracted beam. The crystallite sizes were calculated from the corrected full width and half maximum (FWHM) applying the Debye-Scherrer formula. The powdery deposits were imaged in a transmission electron microscope Philips CM120ST (Customized Microscope 120 Super Twin, 120 kV max. acceleration voltage, about 2 A resolution, Cs = ~1.2 mm). The samples were analyzed by the different electron microscopy techniques such as Bright Field Transmission Electron Microscopy (BF-TEM), Selected Area Electron Diffraction (SAED) and High Resolution Transmission Electron Microscopy (HRTEM). ^{57}Fe Mössbauer spectroscopy was used for analyzing the samples at temperatures ranging from 80 K to 230 K. Mössbauer spectra were collected in transmission geometry by inserting the sample in a bath liquid-nitrogen cryostat. A Mössbauer drive system operating in constant acceleration mode combined with conventional electronics and a ^{57}Co (Rh matrix) source of about 25 mCi activity were employed.

3. RECENT EXAMPLES OF AND ADVANCES IN THE PREPARATION BY LASER PYROLYSIS OF OXIDE SEMICONDUCTOR PARTICLES

3.1. Spinel-like iron (III) oxide (γ-Fe_2O_3)

3.1.1. The preparation of the nanoparticles and of their magnetic fluids counterparts

Nanoparticle preparation

For producing nanosized iron oxide particles, the focused continuous-wave CO_2 laser radiation (80 W maximum output power, λ = 10.6 μm) orthogonally crossed the gas flows emerging through two concentric nozzles (Figure 1). The gas mixture which contained air and $Fe(CO)_5$ vapors (about 25 Torr vapor pressure at 20°C), entrained by C_2H_4, was admitted through the central inner tube. Iron oxide samples (labeled as 01 and 02) were obtained by varying the laser power between 35 W and 55 W as presented in Table 1. The other experimental conditions, namely, the reactor pressure, the relative flow of the oxidizing agent (air), and the flow of ethylene (as $Fe(CO)_5$ carrier) were maintained constant (their values are displayed in Table 1).

Magnetic fluid preparation

The as-synthesized iron oxide nanopowders were used for the preparation of magnetic nanofluids. In what follows, the obtained magnetic fluid samples will be labeled MF01 and MF02 and are derived by dispersing in water samples 01 and 02, respectively. Water-based magnetic nanofluids are a special category of polar magnetic nanofluids showing particularities as concerning particle interactions and agglomerates formation. The synthesis of magnetic

Table 1: Experimental parameters and main crystallographic characteristics (estimated from XRD analysis) for the as-synthesized nano iron oxide samples.

Sample	$\Phi_{C_2H_4}$* (through $Fe(CO)_5$ [sccm]	Φ_{air}* [sccm]	P** [mbar]	P_L* [watt]	XRD analysis		EDAX-elemental analysis, at%		
					a (unit cell parameter) [′]	D (mean crystallite dimension) [nm]	Fe	O	C
01	145	70	300	55	8.364	4.5	36.29	52.99	10.72
02	145	70	300	35	8.377	3.0	35.09	55.12	9.79

* $\Phi_{C_2H_4}$ and Φ_{air}, are the flows of the ethylene (carrier of $Fe(CO)_5$ vapors) and of air oxidizer, respectively (in standard cubic centimeter per minute);
** P is the pressure in the reaction chamber (in mbar);
*** P_L is the laser power (in Watt).

fluids has two main stages (1) preparation of nanosized magnetic particles, in particular by laser pyrolysis, and (2) subsequent stabilization/dispersion of the nanoparticles in water carrier. Electrostatic and steric stabilization procedures are both applicable for water-based magnetic nanofluids. Double layers steric + electrostatic (combined) stabilization of magnetic nanoparticles in water carrier was experimented recently using various chain length of carboxylic acid surfactants, as well as dodecyl benzensulphonic acid (DBS) [22]. In case of magnetic nanoparticles prepared by laser pyrolysis, a complementary difficulty appears due to the large agglomerates existing already in the nanopowder state, as a consequence of the magnetic dipolar interactions between uncoated nanoparticles. The sequence of steps of the preparation procedure for water-based magnetic nanofluids may be summarized as follows: (a) addition of NaOH (6N) to the water/magnetic nanopowder mixture in order to ensure a pH value of about 8.5–9, followed by heating up the reaction medium to about 75–80°C; (b) chemisorption of the surfactant (in the present case, lauric acid (LA)); (c) magnetic organosol; (d) magnetic decantation (elimination of residual salts); (e) correction of pH (using NaOH); (f) dispersion of surface-coated magnetic nanoparticles; (g) primary magnetic nanofluid; (h) magnetic decantation/filtration; (i) water-based magnetic nanofluid (diluted, with solid volume fraction of about 5%).

3.1.2. Nanoparticle characterization

The XRD analysis of the as-synthesized nanopowders points to the presence of the spinel-like iron (III) oxide [10], namely, maghemite/magnetite iron phase (according to JCPDS 19-0629 for standard maghemite and JCPDS 39–1346 for maghemite). In Figure 2, a representative diffractogram obtained for the as-synthesized oxides is displayed. Although it refers to sample 01, its characteristic phase identification features are similar to that of sample 02 (not presented here). The unit-cell parameter (Table 1) was estimated from the 311 and 440 reflections. It presents relatively lower values to the standard magnetite value (Fe_3O_4 with $a = 8.396$ Å), suggesting the formation of a more likely maghemite phase (γ-Fe_2O_3). The broadness of the diffraction lines is associated with the formation of very small particles as well as with a high degree of structural/crystallographic disorder. The estimated mean crystallite dimension D (nm) is presented

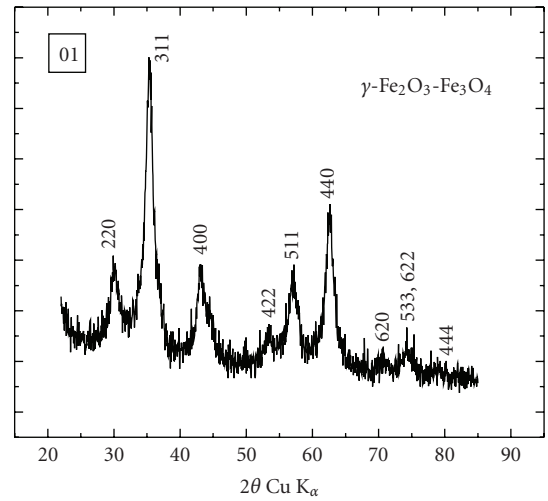

Figure 2: XRD diffraction patterns for a laser-synthesized iron oxide (sample 01): peak identification points to a chemical composition containing maghemite/magnetite iron oxide phases.

in Table 1. A higher crystallinity and slightly larger mean crystallite size may be deduced for the sample obtained at the higher laser power.

The identification of elements present in powders was performed using the energy dispersive analysis by X-rays (EDAX). The results are presented in the last column of Table 1. The stoichiometry, suggested by the relative quantities of oxygen and iron present in the synthesized powders, corresponds to a Fe^{3+} iron oxide, most probably maghemite. A rather low carbon contamination (about 10%), mainly due to the unwanted ethylene dissociation may be noticed. Although revealed by EDAX, the XRD analysis seems not able to reveal traces of carbon. It is worth to note that the sensitivity of this analysis is down to a few atomic percent and that low Z elements are detectable with limited sensitivity.

TEM analysis of samples 01 and 02 reveals an almost polycrystalline morphology (Figures 3(a), 3(b)). The nanoparticles show coalescent features. Cross-linked chains may be sometimes observed. An estimation of the particle mean sizes gives about 4.5 and 6 nm for samples 01 and 02, respectively.

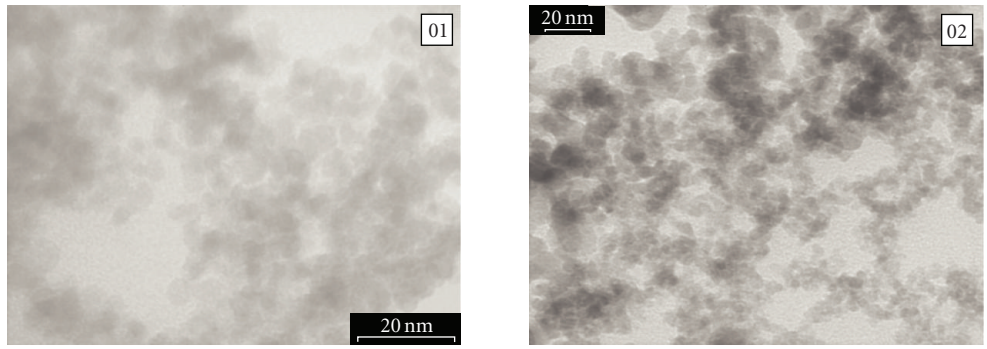

(a) (b)

Figure 3: TEM analysis for iron oxides obtained from (a) sample 01 and (b) sample 02.

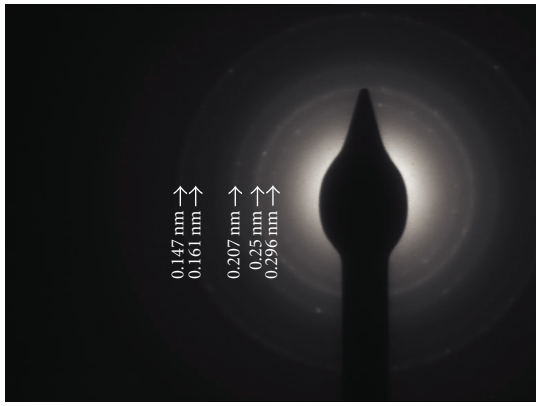

Figure 4: SAED analysis of sample 02, revealing main diffraction rings of maghemite/magnetite.

The reflections revealed by the SAED analysis (Figure 4) may be attributed to a cubic structure of the iron oxide, namely, maghemite/magnetite. The strong diffraction ring at 0.25 nm may be noticed. Although difficult to distinguish between these phases from electron diffraction patterns alone, it is probable that maghemite prevails by referring to XRD results (see, e.g., the value of the estimated lattice parameter a in Table 1). Increased crystallinity seems to characterize the nanomaterial obtained at higher laser power. This can be considered as a consequence of both the higher temperature gradients in the reactions zone and the fast quenching of the condensed nanoparticles in the condensation zone. As revealed by the characterization methods employed, this process greatly favors maghemite phase in powders.

HRTEM analysis was performed on many different domains of the nanopowders and is presented in Figure 5. Nanocrystals with different orientation and mean diameters of about 5-6 nm are displayed in Figure 5(a). From the indicated squarish areas, the Fourier transform images are presented as insets. The left-side and the right-side groups of nanocrystals in Figure 5(a) display characteristics of the cubic structure of a maghemite crystal. The lattice fringes, corresponding to the (113) (d_{113} = 0.253 nm) and to the (220) (d_{220} = 0.313 nm) planes, are evidenced. A small distribution of d-values is caused by the imperfect crystallographic structure, probably due to the quenching of the material when leaving the reaction zone. The HRTEM image of Figure 5(b) presents agglomerated nanocrystals. They seem to be surrounded by an amorphous layer.

3.1.3. *Magnetic properties for the as-synthesized particles and for the processed magnetic nanofluids*

The magnetic properties of the samples were studied by temperature-dependent Mössbauer spectroscopy. The 80 K Mössbauer spectra of the analyzed samples are shown in Figure 5. The derived probability distributions of the hyperfine field are presented at the right side. The narrow peak of the distribution, centered at about 52 T, evidences the presence of mainly maghemite in sample 01. The larger distribution peak centered at about 48 T in sample 02 might have two different reasons: (i) a starting magnetic relaxation process already present at 80 K and (ii) a much defected structure shifting structurally from maghemite to magnetite (the average magnetic hyperfine field of magnetite being lower than the one of maghemite). The magnetic relaxation process was analyzed [23] in terms of the collapsing behavior of the Mössbauer spectra at higher temperatures. From the Mossbauer spectra obtained at different temperatures, blocking temperatures of about 400 K and 200 K were derived for samples 01 and 02, respectively. Particle average sizes of about 9 nm for sample 01 and, respectively, 7 nm for samples 02 were estimated, starting from the above-mentioned blocking temperatures and considering noninteracting nanoparticles.

The ferrofluids obtained by dispersing the nanopowders in water showed blocking temperatures of 230 K and 200 K for samples MF01 and MF02, respectively. It is worth mentioning that the higher blocking temperature observed for 01 as compared to MF01 is most probably generated by nonnegligible interparticle interactions in the powder sample (e.g., the substantial presence of maghemite with its ferri-magnetic behavior). In the defected maghemite-magnetite mixtures (sample 02), a spin-glass-like structure with reduced (almost negligible) net magnetic moment per

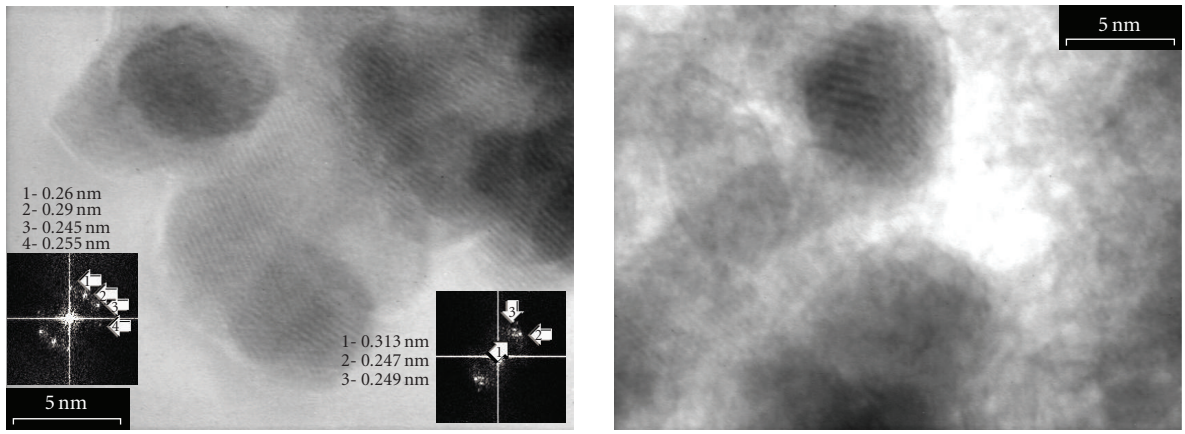

Figure 5: HRTEM images for samples: (a) 01 and (b) 02. Space representations of Fourier transform (displayed as insets on figure) seem to evidence the diffraction planes of maghemite/magnetite.

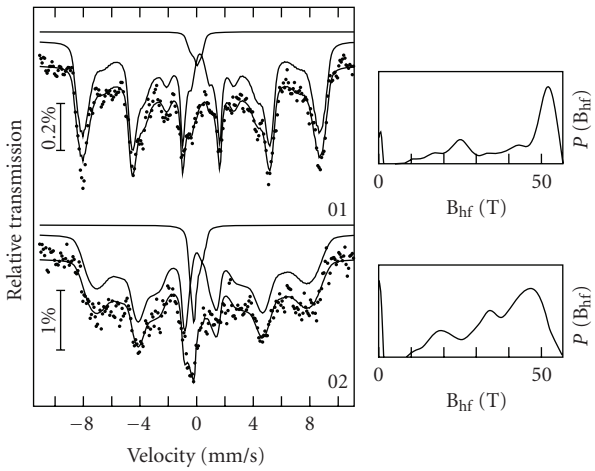

Figure 6: Mössbauer spectra (at 80 K) of the two as-synthesized nanopowder samples; at the right side, the probability distributions of the hyperfine field are also displayed.

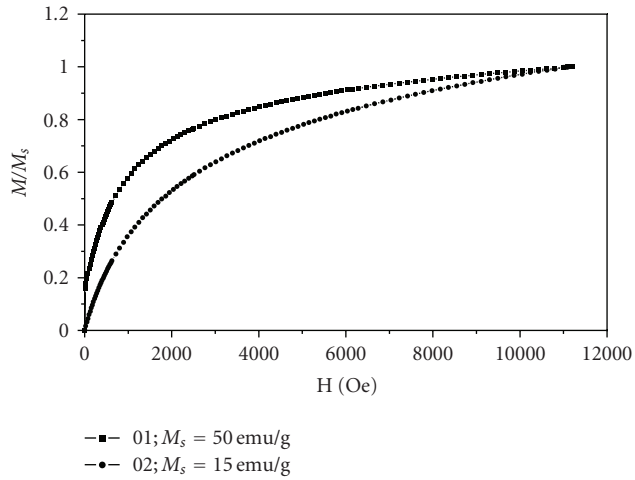

Figure 7: Reduced magnetization curves for 01 and 02 nanopowders.

particle seems to be present, affecting/reducing drastically the magnetic dipolar interactions, even in the powder form. The best magnetic performances (a maximum amount of magnetic nanoparticles at room temperature and related highest magnetization) correspond to the ferrofluid obtained by dispersing the well-formed maghemite-based nanoparticles synthesized under a laser power of 55 W.

The reduced magnetization curves of the as-synthesized nanopowders are presented in Figure 7. It is worth mentioning that none of the samples is saturated at the maximum available field of 1.1 T. This behavior can be considered an additional evidence for the disordered spin configuration, connected with the defected structure inside nanoparticles, in agreement with the Mössbauer data. Therefore, the reduced magnetization curves for the two samples were obtained with respect to the specific magnetization at the maximum field (denoted as M_s). The magnetization M_s of the 01 sample, 50 emu/g, is much greater than for sample 02 (15 emu/g) supporting a three times larger magnetic moment per particle in sample 01 as compared with sample 02 in the assumption that the particle mean sizes of the two samples are almost similar. On the other hand, the reduced magnetization of sample 01 at very low field is clearly larger than that of sample 02, providing evidence for a larger amount of magnetic state at room temperature in this sample in agreement with the larger blocking temperature evidenced by Mössbauer spectroscopy.

Following the procedures described in a previous section, the iron oxide nanopowders were subsequently synthesized as water-based magnetic fluids (MFs). TEM analysis of the ferrofluids showed that depending on the nanopowder synthesis parameters, different degrees of agglomeration are still present. The morphology of samples MF01 and MF02 may be examined in Figures 8(a) and 8(b). The

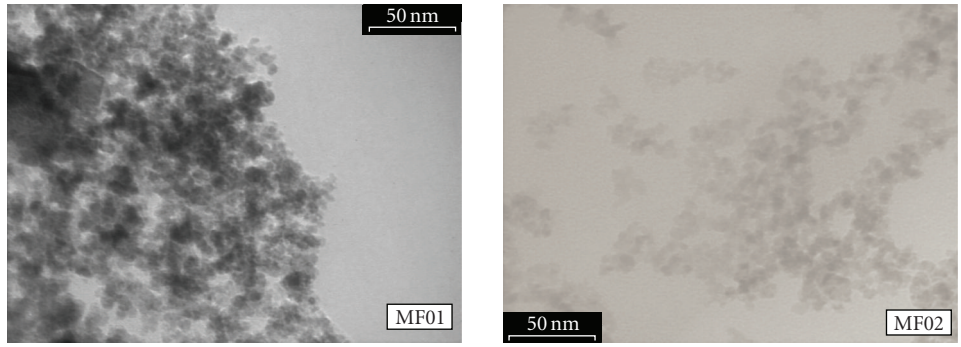

(a) (b)

Figure 8: TEM images showing the morphology of the magnetic nanofluids prepared from samples MF01 and MF02, respectively.

nanoparticles exhibit a spherical shape, confirmed by the 0.86 value of the form factor. From SAED analysis (no presented here), an iron oxide cubic structure is deduced, with lattice constants of 0.835 nm and 0.837 nm for MF01 and MF02, respectively. This estimation may indicate that the maghemite-like structure is favored in the ferrofluid-derived from the sample synthesized at high laser power. On the other hand, one may observe that the MF prepared from 02 nanoparticles (Figure 8(b)) presents a slightly lower degree of agglomeration as compared with MF02 (Figure 8(a)). The suppression of interparticle interaction in sample MF01 could be less effective, in spite of the fact that insignificant magnetic relaxation differences separate the MF samples.

The reduced magnetization curves of the ferrofluid samples MF01 and MF02, synthesized from the powders 01 and 02, respectively, are shown in Figure 9. The dependencies of the reduced magnetizations versus the applied magnetic field are quite similar to the ones of the powder samples. A major difference concerns the values of the magnetization, M_s, at the maximum field of 1.1 T. This time these are expressed in emu/cm^3 (or A/m) in order to take into account the inhomogeneous character of the ferrofluid, seen as a liquid-solid composite (M_s given in emu/cm^3 derives from the specific magnetization in emu/g times the ferrofluid density, in g/cm^3). The M_s value in sample MF01 is almost 7 times larger than the value in sample MF02, proving clearly the better magnetic performances of the ferrofluid derived from the 01 powder sample. In addition, one observes that the low field part of the reduced magnetization in the magnetic fluid sample MF01 is lower than for the 01 sample and that a certain amount of suparparamagnetic phase is to be found in this sample even at 1.1 T. Therefore, due to the cancellation of interparticle interactions, the magnetometry data infer that the magnetic relaxation at room temperature has to be more advanced in the MF01 ferrofluid sample as compared with the 01 powder sample (in agreement with the Mossbauer data showing a lower blocking temperature in the ferrofluid). Hence, the magnetic relaxation may hide the information about the static spin disorder. The specific magnetizations are not strictly related to the different degree of spin disorder in the samples but, at least qualitatively, the magnetometry results, in agreement with the Mossbauer

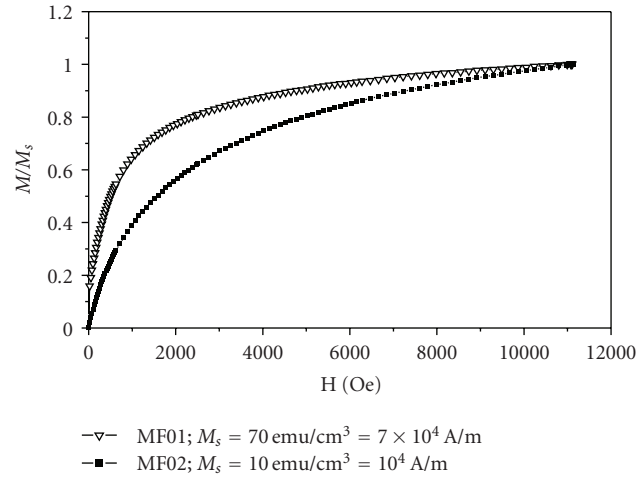

Figure 9: Reduced magnetization curves of water magnetic fluid samples prepared from 01 and 02 nanopowders.

ones, support very well the conclusion that the lowest spin disorder is present in the 01 sample and in the corresponding MF01 ferrofluid.

3.2. *Titania, with major TiO_2 anatase phase*

3.2.1. *Particle preparation and characterization*

The synthesis of TiO_2 nanopowder was performed by employing a modified version of the pyrolysis setup [24] in which $TiCl_4$ and air, as gas-phase precursors, are simultaneously allowed to emerge into the flow reactor (see also Figure 1). Ethylene served as a carrier for the $TiCl_4$ vapors and as an energy transfer agent. A special irradiation geometry employing a central triple nozzle system was used. The focused IR radiation (400 W nominal power) was intersecting at right angles the reactant flows. During all experiments, the total pressure in the reactor was held at 550 mbar.

The samples (labeled S_N, S_A, and S0) are studied relatively to the input variation of their oxygen precursors. Sample S_N was obtained by replacing air with nitrous oxide. A much

Table 2: Synthesis parameters and crystallographic parameters of nanoTiO_2 particles.

Sample	Φ_{air}* [sccm]	$\Phi_{C_2H_4}$* ($TiCl_4$) [sccm]	TiO_2-phase proportion** A (%)	R (%)	Lattice parameters** A (JCPDS 21-1272) a = 3.785 Å c = 9.513 Å		R (JCPDS 21-1272) a = 4.593 Å c = 2.959 Å		D Mean crystallite dimension [nm] A	R
					a (Å)	c (Å)	a (Å)	c (Å)		
S_N	10 (N_2O)	100	64.1	35.9	3.805	9.56	4.70	2.92	14.4	4.2
S_A	50	100	74.6	25.4	3.81	9.57	4.64	2.965	17.8	15.0
S0	150	100	92.3	7.7	3.81	9.55	4.63	2.95	18.9	21.4

* $\Phi_{C_2H_4}$ and Φ_{air}, are the flows of the ethylene (carrier of $Fe(CO)_5$ vapors) and of the air oxidizer, respectively (in standard cubic centimeter per minute);
** A and R stand for anatase and rutile, respectively; a and c are the values of the lattice parameters of titania, according to standard JCPDS 21-1272 data.

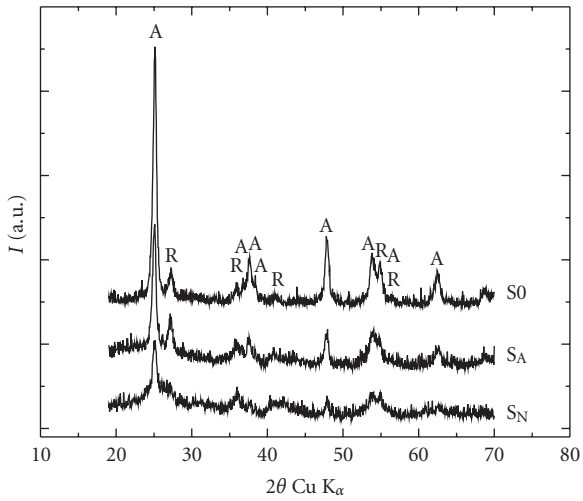

Figure 10: XRD diffraction patterns for the nanotitania samples S_N, S_A, and S0, with anatase (A) and rutile (R) peak identification.

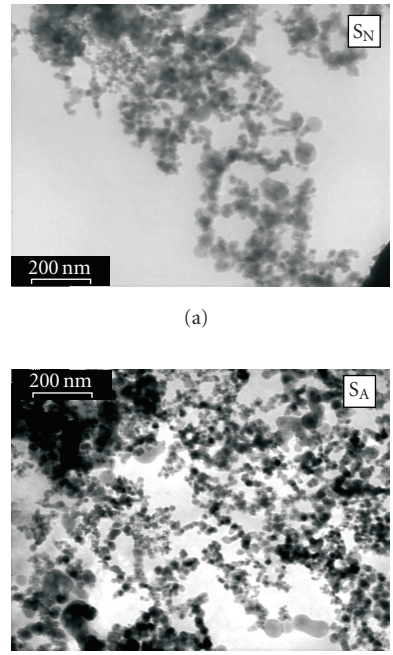

Figure 11: General TEM view of the samples S_N (a) and S_A (b).

lower air flow was used to obtain sample S_A as compared to sample S0. The main experimental parameters are listed in Table 2. In the last columns of the table are gathered the mean crystallite sizes [25] as well as the lattice parameters (a,c) as extracted from the XRD patterns (see below).

The obtained titanium oxide nanostructures were characterized by XRD, TEM, and SAED.

XRD phase analysis (Figure 10 and the last columns of Table 2) reveals an overwhelming dominancy of the anatase phase (more than about 92%) in the sample S0, obtained at the highest air precursor concentration. It was already observed [26] that for titania produced by RF thermal plasma, rutile formation is favored by oxygen-deficient gas-phase TiO_2 clusters while anatase tends to condense from oxygen-rich clusters. We should mention that for both air and nitrous oxide, at lower air flows (e.g., 10 sccm for sample S_N), the powder was gray with slight blue parts. At high air input flows (150 sccm for sample S0), the color of the powder becomes light yellow to white. Some salient features characterize the S_N, S_A, and S0 series: (i) the significant decrease of the mean particle sizes for S_N and S_A relatively to S0, particularly concerning the rutile phase; and (ii) the decrease of the total amount of the TiO_2 phases relatively to the S0 sample, especially in case of the anatase phase. For the TiO_2 S_A sample, anatase percentage is approximately 74%, which is quite close to the well-known Degussa P25 commercial sample.

Low-magnification TEM micrographsfor TiO_2 samples S_N and S_A (Figure 11) show groups of loosely-bound aggregated nanoparticles.

The SAED patterns for samples S_A and S0 are presented in Figure 12. The identification of the interplanar distances is indicated by arrows and these qualitative results can be directly compared with those obtained by means of XRD. In general, SAED analysis confirms that the titania nanoparticles are a mixture of anatase and rutile. However,

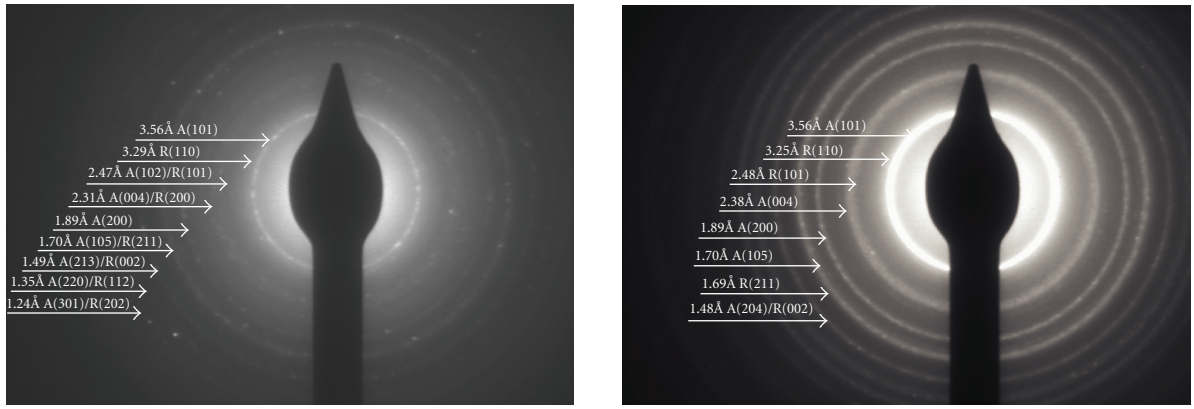

(a) (b)

Figure 12: SAED patterns for samples S_A and S0.

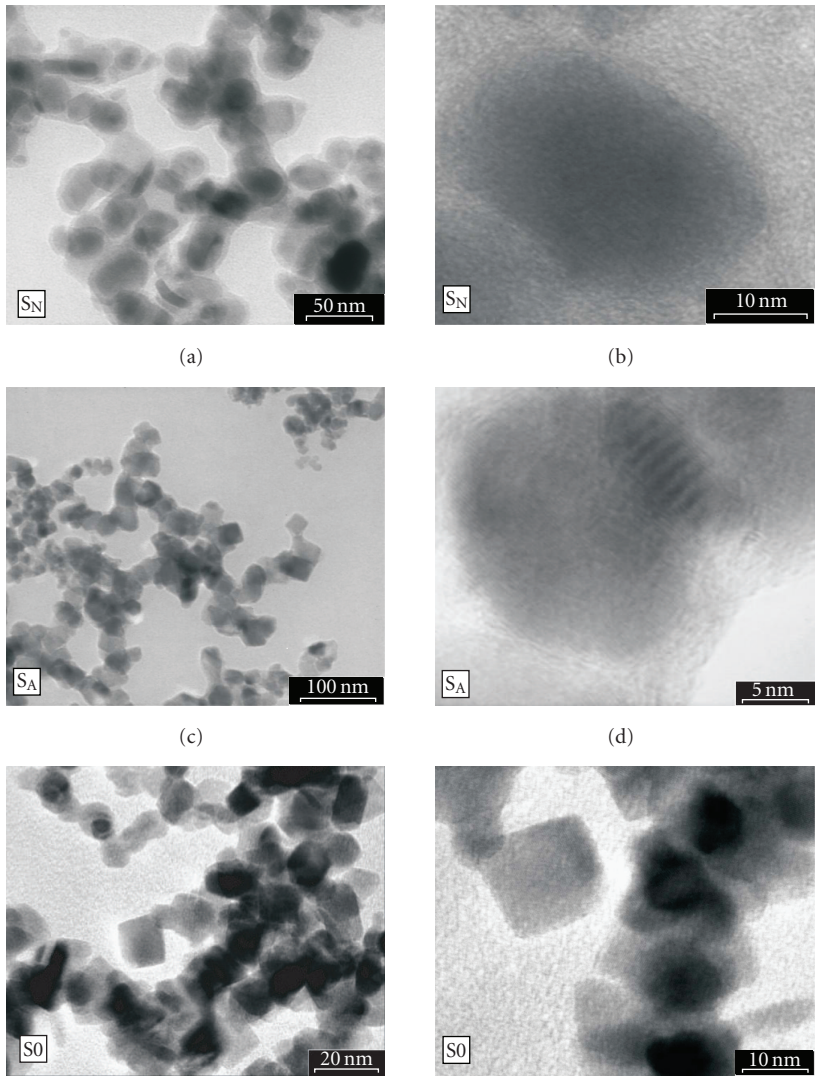

(a) (b)

(c) (d)

(e) (f)

Figure 13: Comparative TEM analysis for medium- (a, c, and e) and high-resolution (b, d, and f) images of titania samples, showing the different morphologies of S_N, S_A, and S0.

increased crystallinity and dominant anatase phase are found for the reference sample (S0). We should note that the diffusivity observed in the SAED pattern of sample S_A could be due not only to an amorphous material but also to the increased number of crystalline nanometer-sized particles [27]. The most intense diffraction rings can be assigned to the (101) anatase (at 3.52 Å) and (110) rutile (at 3.25 Å). Some rings may appear by a superposition of anatase and rutile reflections, such as the rings at 2.48 Å and 1.68 Å. In case of the better crystallinity of sample S0, the complementary ring at 1.4 Å (corresponding to rutile (007) and anatase (204)) is identified.

In Figure 13, a comparative TEM analysis for medium- (a, c, and e) and high-resolution (b, d, and f) images of S_N, S_A and S0 titania samples is performed. At a higher magnification, the TEM micrographs of samples discussed in this work exhibit both round-shaped and elongated or facetted particles with irregular shapes and sizes (Figures 13(a)–13(f)). Primary nanocrystals seem to be often present. In Figure 13(b), an isolated S_N primary nanocrystal is presented, showing an elongated (about 15 nm) shape. Particles surrounded by an amorphous layer (Figures 13(a) and 13(c)) appear in sample S_N and S_A, respectively. The rather well-defined microcrystallites of sample S0 exhibit irregular, mostly polyhedral shapes (Figure 13(f)).

4. CONCLUSIONS

Recent results obtained in the preparation of gamma iron oxide (γ-Fe_2O_3) and titania (TiO_2) semiconductor nanostructures using the laser pyrolysis method are outlined. The properties of different nanometric iron oxides prepared by laser pyrolysis were analyzed from the point of view of their morphology and magnetic behavior. The nanoparticles are characterized by a cubic maghemite/magnetite structure. Maghemite phase seems to prevail in the nanopowders obtained at the highest laser power. These nanoparticles also present a better crystallinity and slightly larger mean crystallite dimensions. The analysis of samples as water-based nanofluids shows that the best magnetic performances (a maximum amount of magnetic nanoparticles at room temperature and related highest magnetization) correspond to the ferrofluid derived from maghemite-based nanoparticles synthesized under a higher laser power.

TiO_2 nanoparticles comprising a mixture of anatase and rutile phases were synthesized via the sensitized laser pyrolysis of $TiCl_4$- (vapors) based gas-phase mixtures. TiO_2 samples were obtained by varying the amount of oxidizing agent (air). Enhanced crystallinity and larger crystallite mean sizes are observed at increased amount of the oxidizing agent. Samples with a major concentration of anatase phase (about 90%) were obtained by the same technique by using as precursors very high air flows.

ACKNOWLEDGMENT

This work was supported by the Romanian Education Ministry through CEEX (Project no. S2/C8/2005), PNCD2 (71/083/2007), and NUCLEU: LAPLACE 2 (PN 06 36/2008) programs.

REFERENCES

[1] M. R. Hoffmann, S. T. Martin, W. Choi, and D. W. Bahnemann, "Environmental applications of semiconductor photocatalysis," *Chemical Reviews*, vol. 95, no. 1, pp. 69–96, 1995.

[2] M. A. Fox and M. T. Dulay, "Heterogeneous photocatalysis," *Chemical Reviews*, vol. 93, no. 1, pp. 341–357, 1993.

[3] K. Pirkanniemi and M. Sillanpää, "Heterogeneous water phase catalysis as an environmental application: a review," *Chemosphere*, vol. 48, no. 10, pp. 1047–1060, 2002.

[4] Y. Matsumoto, "Energy positions of oxide semiconductors and photocatalysis with iron complex oxides," *Journal of Solid State Chemistry*, vol. 126, no. 2, pp. 227–234, 1996.

[5] D. G. Shchukin, E. A. Ustinovich, D. V. Sviridov, and A. I. Kulak, "Titanium and iron oxide-based magnetic photocatalysts for oxidation of organic compounds and sulfur dioxide," *High Energy Chemistry*, vol. 38, no. 3, pp. 167–173, 2004.

[6] L. Palmisano, M. Schiavello, A. Sclafani, C. Martin, I. Martin, and V. Rives, "Surface properties of iron-titania photocatalysts employed for 4-nitrophenol photodegradation in aqueous TiO_2 dispersion," *Catalysis Letters*, vol. 24, no. 3-4, pp. 303–315, 1994.

[7] B. O'Regan and M. Gràtzel, "A low-cost, high-efficiency solar cell based on dye-sensitized colloidal TiO_2 films," *Nature*, vol. 353, pp. 737–740, 1991.

[8] X. H. Wang, J.-G. Li, H. Kamiyama, and T. Ishigaki, "Fe-doped TiO_2 nanopowders by oxidative pyrolysis of organometallic precursors in induction thermal plasma: synthesis and structural characterization," *Thin Solid Films*, vol. 506-507, pp. 278–282, 2006.

[9] M. T. Swihart, "Vapor-phase synthesis of nanoparticles," *Current Opinion in Colloid & Interface Science*, vol. 8, no. 1-2, pp. 127–133, 2003.

[10] I. Morjan, R. Alexandrescu, I. Soare, et al., "Nanoscale powders of different iron oxide phases prepared by continous laser irradiation of iron pentacarbonyl-containing gas precursors," *Materials Science and Engineering C*, vol. 23, no. 1-2, pp. 211–216, 2003.

[11] R. Alexandrescu, I. Morjan, M. Scarisoreanu, et al., "Structural investigations on TiO_2 and Fe-doped TiO_2 nanoparticles synthesized by laser pyrolysis," *Thin Solid Films*, vol. 515, no. 24, pp. 8438–8445, 2007.

[12] S. Veintemillas-Verdaguer, M. Del Puerto Morales, O. Bomati-Miguel, et al., "Colloidal dispersions of maghemite nanoparticles produced by laser pyrolysis with application as NMR contrast agents," *Journal of Physics D*, vol. 37, no. 15, pp. 2054–2059, 2004.

[13] H. Maskrot, Y. Leconte, N. Herlin-Boime, et al., "Synthesis of nanostructured catalysts by laser pyrolysis," *Catalysis Today*, vol. 116, no. 1, pp. 6–11, 2006.

[14] F. Lacour, O. Guillois, X. Portier, H. Perez, N. Herlin, and C. Reynaud, "Laser pyrolysis synthesis and characterization of luminescent silicon nanocrystals," *Physica E*, vol. 38, no. 1-2, pp. 11–15, 2007.

[15] C. Jäger, F. Huisken, H. Mutschke, Th. Henning, W. Poppitz, and I. Voicu, "Identification and spectral properties of PAHs in carbonaceous material produced by laser pyrolysis," *Carbon*, vol. 45, no. 15, pp. 2981–2994, 2007.

[16] A. Tomescu, R. Alexandrescu, I. Morjan, et al., "Structural and sensing properties of a novel Fe/Fe_2O_3/polyoxocarbosilane core shell nanocomposite powder prepared by laser pyrolysis," *Journal of Materials Science*, vol. 42, no. 5, pp. 1838–1846, 2007.

[17] R. Alexandrescu, I. Morjan, I. Voicu, et al., "Combining resonant/non-resonant processes: nano-meter-scale iron-based material preparation via the CO_2 laser pyrolysis," *Applied Surface Science*, vol. 248, no. 1–4, pp. 138–146, 2005.

[18] G. W. Flynn, C. S. Parmenter, and A. M. Wodtke, "Vibrational energy transfer," *Journal of Physical Chemistry*, vol. 100, no. 31, pp. 12817–12838, 1996.

[19] R. Alexandrescu, "Laser-stimulated processes in metal carbonyls for metal-based film synthesis," *Applied Surface Science*, vol. 106, pp. 28–37, 1996.

[20] G. Herzberg, *Molecular Spectra and Molecular Structure: Infrared and Raman Spectra of Polyatomic Molecules*, vol. 2, Van Nostrand Reinhold, New York, NY, USA, 1945.

[21] K. Elihn, F. Otten, M. Boman, et al., "Size distributions and synthesis of nanoparticles by photolytic dissociation of ferrocene," *Applied Physics A*, vol. 72, no. 1, pp. 29–34, 2001.

[22] D. Bica, L. Vékás, M. V. Avdeev, et al., "Sterically stabilized water based magnetic fluids: synthesis, structure and properties," *Journal of Magnetism and Magnetic Materials*, vol. 311, no. 1, pp. 17–21, 2007.

[23] V. Kuncser, G. Schinteie, B. Sahoo, et al., "Magnetic interactions in water based ferrofluids studied by Mössbauer spectroscopy," *Journal of Physics: Condensed Matter*, vol. 19, no. 1, Article ID 016205, 16 pages, 2007.

[24] R. Alexandrescu, F. Dumitrache, I. Morjan, et al., "TiO_2 nanosized powders by $TiCl_4$ laser pyrolysis," *Nanotechnology*, vol. 15, no. 5, pp. 537–545, 2004.

[25] R. A. Spurr and H. Myers, "Quantitative analysis of anatase-rutile mixtures with an X-ray diffractiometer," *Analytical Chemistry*, vol. 29, no. 5, pp. 760–762, 1957.

[26] J.-G. Li, H. Kamiyama, X.-H. Wang, Y. Moriyoshi, and T. Ishigaki, "TiO_2 nanopowders via radio-frequency thermal plasma oxidation of organic liquid precursors: synthesis and characterization," *Journal of the European Ceramic Society*, vol. 26, no. 4-5, pp. 423–428, 2006.

[27] J. Arbiol, J. Cerdà, G. Dezanneau, et al., "Effects of Nb doping on the TiO_2 anatase-to-rutile phase transition," *Journal of Applied Physics*, vol. 92, no. 2, pp. 853–861, 2002.

Hindawi Publishing Corporation
International Journal of Photoenergy
Volume 2008, Article ID 276027, 5 pages
doi:10.1155/2008/276027

Research Article

Electro-Optical and Electrochemical Properties of a Conjugated Polymer Prepared by the Cyclopolymerization of Diethyl Dipropargylmalonate

Yeong-Soon Gal,[1] Won-Chul Lee,[1] Won Seok Lyoo,[2] Sung-Ho Jin,[3] Kwon Taek Lim,[4] Young-Il Park,[5] and Jong-Wook Park[5]

[1] *Polymer Chemistry Laboratory, College of Engineering, Kyungil University, Kyungsan 712-701, South Korea*
[2] *School of Textiles, Yeungnam University, Kyungsan 712-749, South Korea*
[3] *Department of Chemistry and Center for Plastic Information System, Pusan National University, Pusan 609-735, South Korea*
[4] *Division of Image and Information Engineering, Pukyong National University, Pusan 608-739, South Korea*
[5] *Department of Chemistry, Center for Nanotechnology Research, The Catholic University, Bucheon 420-743, South Korea*

Correspondence should be addressed to Yeong-Soon Gal, ysgal@kiu.ac.kr

Received 1 May 2008; Accepted 24 May 2008

Recommended by Mohamed Sabry Abdel-Mottaleb

The electro-optical and electrochemical properties of poly(diethyl dipropargylmalonate) were measured and discussed. Poly(diethyl dipropargylmalonate) prepared by (NBD)$PdCl_2$ catalyst was used for study. The chemical structure of poly(diethyl dipropargylmalonate) was characterized by such instrumental methods as NMR (^{1}H-, ^{13}C-), IR, and UV-visible spectroscopies to have the conjugated cyclopolymer backbone system. The microstructure analysis of polymer revealed that this polymer have the six-membered ring moieties majorly. The photoluminescence peak of polymer was observed at 543 nm, which is corresponded to the photon energy of 2.51 eV. The cyclovoltamograms of the polymer exhibited the irreversible electrochemical behaviors between the doping and undoping peaks. It was found that the kinetics of the redox process of this conjugated cyclopolymer might be mainly controlled by the electron transfer process from the experiment of the oxidation current density of polymer versus the scan rate.

1. INTRODUCTION

Considerable progress has been made in the synthesis and optical characterization of conjugated organic polymers [1–3]. Polymers having a conjugated backbone are expected to show unique properties, such as electrical conductivity, paramagnetism, migration and transfer of energy, color, chemical reactivity, and complex formation ability [3–7]. Because of these properties, polyacetylene and its homologues have been promising materials for photovoltaics, displays, lasers, nonlinear optical materials, membranes for gas separation, and for liquid-mixture separation and chemical sensors [4, 5, 8–12]. There are considerable interests in the development of electronic devices incorporating polymeric semiconductors owing to their superior properties, simplicity of fabrication, light weight, and potentially lower cost when compared to conventional inorganic semiconductors [1–3, 8, 13]. Among the various types of reported polymer semiconductors, poly(*p*-phenylenevinylenes), polythiophenes, poly(9,9-dialkylfluorenes), and their derivatives are widely used in solar cell applications as *p*-type donor materials [14, 15].

The synthesis of conjugated polymer via the cyclopolymerization of dipropargyl monomers has been very interesting method for the introduction of conjugated system in the polymer main chain via an alternating intramolecular–intermolecular chain propagation [16, 17]. 1,6-Heptadiyne itself had been polymerized by various initiator systems to give poly(1,6-heptadiyne) with a polyene cyclic structure [17]. However, the resulting poly(1,6-heptadiyne) was insoluble in any organic solvent and unstable to air oxidation as like with that of polyacetylene [17]. Thus it was difficult for practical applications to optoelectronic devices as an active material. Introduction of substituents at 4-position of 1,6-heptadiyne can enhance the processibility and stability of

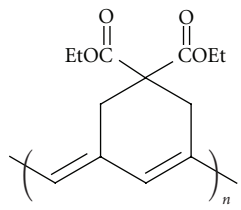

Figure 1: Chemical structure of poly(DEDPM).

the polyene systems, thus a variety of substituted poly(1,6-heptadiyne)s were designed and synthesized [5, 7, 10, 18–20].

Diethyl dipropargylmalonate (DEDPM) is a well-known cyclopolymerizable dipropargyl monomer since 1990 [21]. The polymerizations of DEDPM have been performed by $MoCl_5$, $Mo(CO)_6$, and Cp_2MoCl_2 catalyst, and high oxidation state alkylidene molybdenum complexes such as $Mo(CHCMe_2R)(N\text{-}2,6\text{-}C_6H_3\text{-}i\text{-}Pr_2)(OCMe_2CF_3)_2$ and $Mo(CHCMe_2R)(N\text{-}2,6\text{-}C_6H_3\text{-}i\text{-}Pr)_2(O\text{-}t\text{-}Bu)_2$ [21–24]. However, to date, the electro-optical and electrochemical properties of the resulting polymer from DEDPM were not systematically characterized.

Here, we prepared the conjugated cyclopolymer by the cyclopolymerization of DEDPM by $(NBD)PdCl_2$. And we report the electro-optical and electrochemical properties of poly(DEDPM), a representative conjugated cyclopolymer (Figure 1).

2. EXPERIMENTAL

(Bicyclo[2.2.1]hepta-2,5-diene)dichloropalladium(II) $(NBD)PdCl_2$ (Aldrich Chemicals) was used without further purification. Diethyl dipropargylmalonate (DEDPM) was prepared by the reaction of propargyl bromide and the sodium ethoxide solution of diethyl malonate according to the literature procedure [21]. The solvents were analytical grade materials. They were dried with an appropriate drying agent and fractionally distilled.

Poly(DEDPM) was prepared by the polymerization of DEDPM by using $(NBD)PdCl_2$ catalyst. The polymerization procedure of DEDPM by $(NBD)PdCl_2$ is as follows. In a 25 mL reactor equipped with rubber septum, 2.0 g (8.46 mmol) of DEDPM was added. Then 0.076 g of $(NBD)PdCl_2$ and 8 mL of DMF were added into the polymerization reactor (monomer to catalyst mole ratio: 30, initial monomer concentration: 0.85 M). After 24 hours at 90°C, the polymer solution diluted with 10 mL DMF was precipitated into a large excess of methanol. The precipitated polymer was filtered and dried in vacuum oven at 40°C for 24 hours. The polymer powder was obtained in 56% yield.

NMR (^{1}H- and ^{13}C-) spectra of polymer were recorded on a Varian 500 MHz FT-NMR spectrometer (model: Unity INOVA) in $CDCl_3$. FT-IR spectra were obtained with a Bruker EQUINOX 55 spectrometer using a KBr pellet. The optical absorption spectra were measured by an HP 8453 UV-visible Spectrophotometer. The photoluminescence spectra were obtained by Perkin Elmer luminescence spectrometer LS55 (Xenon flash tube) utilizing a lock-in amplifier system with a chopping frequency of 150 Hz. Electrochemical measurements were carried out with a Potentionstat/Galvanostat model 273 A (Princeton Applied Research). To examine electrochemical properties, the polymer solution was prepared and the electrochemical measurements were performed under 0.1 M tetrabutylammonium tetrafluoroborate solution; containing acetonitrile. ITO, $Ag/AgNO_3$, and platinum wires were used as a working, reference, and counter electrode, respectively.

3. RESULTS AND DISCUSSION

We used the homogeneous $(NBD)PdCl_2$ catalyst for the preparation of poly(DEDPM), which shows excellent solubility in the polymerization solvents and shows relatively stable. We had firstly used this catalyst for the cyclopolymerization of nonconjugated diyne monomers [25]. Unlike the polymerization behaviors of DEDPM by using Mo-based catalysts, which the polymerization proceeded rapidly in initial reaction stage [21, 23], the polymerization of DEDPM by $(NBD)PdCl_2$ catalyst proceeded in mild homogeneous manner to give the moderate yield of polymer (56%). And the number-average molecular weight and polydispersity of this polymer were 16,300 and 2.59, respectively. The polymers were generally soluble in such organic solvents as chloroform, 1,4-dioxane, ethyl acetate, chlorobenzene, DMF, DMSO.

We characterized the chemical structure of poly(DEDPM) by using such instrumental methods as NMR (^{1}H-, ^{13}C-), IR, and UV-visible spectroscopies. The FT-IR spectrum of polymer did not show the acetylenic C≡C bond stretching and acetylenic ≡C–H bond stretching frequencies of DEDPM. The ^{1}H-NMR spectrum of poly(DEDPM) prepared by $(NBD)PdCl_2$ showed the broad vinyl protons of conjugated polymer backbone at the region of 5.4–7.2 ppm. The proton peaks at 2.5–3.6 ppm and 3.9–4.1 ppm are originated from the methylene protons adjacent to the conjugated carbons of polymer backbone and the methylene protons of ethyl side chains, respectively. The methyl proton peak of ethyl side chains was observed at 0.9–1.5 ppm.

The ^{13}C-NMR spectrum of poly(DEDPM) did not show any acetylenic carbon peaks (72.9, 79.6 ppm) of DEDPM. Instead, the ^{13}C-NMR spectrum of polymer showed new olefinic carbon peaks of the conjugated polymer backbone at the region of 118–142 ppm. The carbonyl carbon peak was also observed at 172 ppm. We obtained more detail information for the microstructures of poly(1,6-heptadiyne)-based conjugated cyclopolymers from the studies on the resonance for the quaternary carbon atoms [26]. It has been reported that the two clusters of resonances for the quaternary carbon atoms in poly(DEDPM) can be assigned to the quaternary carbons in five-membered rings (57-58 ppm) and six-membered rings (54-55 ppm), respectively. Figure 2 shows the ^{13}C-NMR spectrum of poly(DEDPM) in the region of methine carbon peak. The peaks at 56–59 ppm were only observed, which means that the present poly(DEDPM) was majorly composed of six-membered ring moieties.

The electro-optical properties of poly(DEDPM) were measured and discussed. Figure 3 shows the UV-visible and photoluminescence (PL) spectra of poly(DEDPM) solution

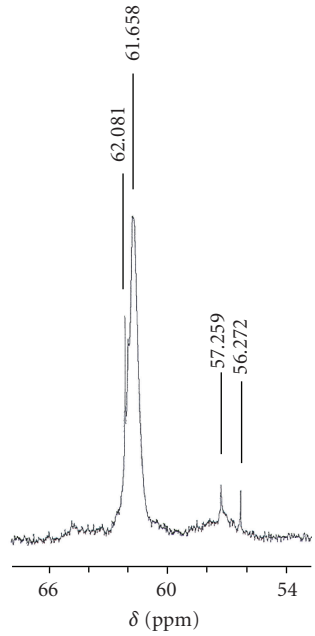

Figure 2: ^{13}C-NMR spectrum of poly(DEDPM) in the region of methine carbon.

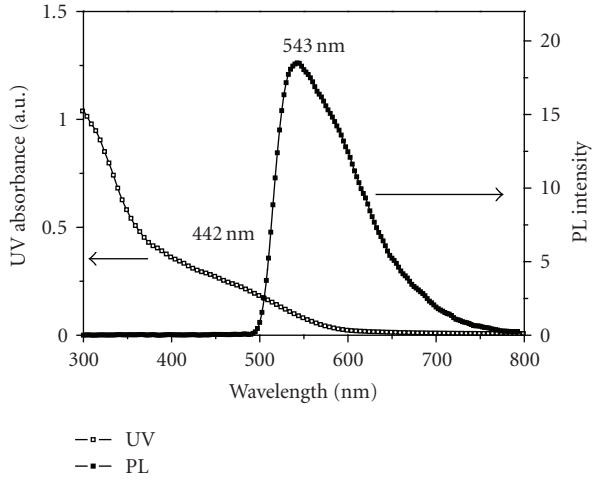

Figure 3: Optical absorption and photoluminescence spectra of poly(DEDPM) solution.

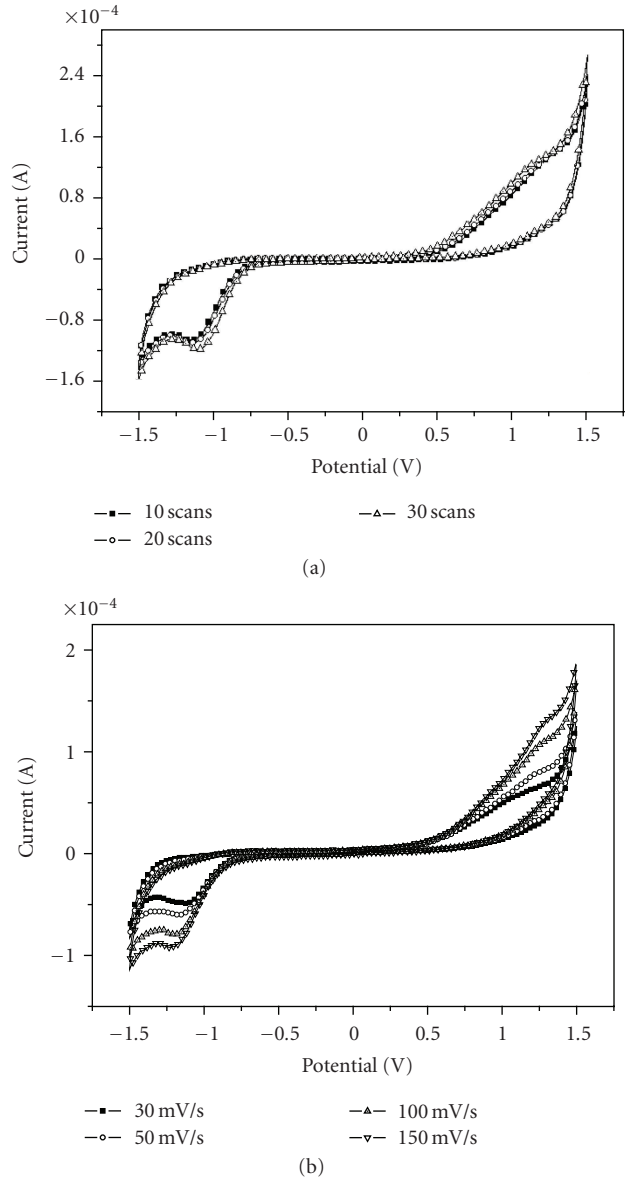

Figure 4: Cyclic voltammograms of poly(DEDPM) [0.1M (n-Bu)$_4$NBF$_4$/DMF] (a) consecutive 30 scans under 100 mV/s and (b) 30 mV/sec ~120 mV/sec with various scan rates.

(0.025 wt.%, DMF). In our previous paper [27], we had reported the UV-visible and PL spectra of poly(2-ethynyl-N-propagylpyridinium bromide) which has similar polymer backbone, conjugated polyene, and tied six-membered ring, it showed 460 nm of UV-visible maximum value and 510 nm of PL maximum value at excitation wavelength of 460 nm. Poly(DEDPM) also exhibited characteristic UV-visible absorption band at 442 nm and green PL spectrum at 543 nm corresponding to the photon energy of 2.28 eV. The reason why two polymers showed different maximum values is that poly(DEDPM) does not have an extra conjugation moiety attached to conjugated polyene which is a polymer backbone.

In order to characterize the electrochemical kinetic behaviors and an electrochemically stable window, the cyclic voltammograms (CVs) of poly(DEDPM) including a consecutive scan and various scan rates (30 mV/s ~ 150 mV/s) were recorded as shown in Figure 4(b). Typical CVs obtained at the scan rate of 100 mV/s for poly(DEDPM) solution are presented in Figure 4(a). We have observed that the shape of CVs is almost unchanged, concluding that poly(DEDPM) is fairly stable without any severe degradation up to 30 cycles of the consecutive scan. In Figure 4(b), as the speed of scan rate was increased, the peak potentials were gradually shifted to higher potentials and the current values were increased. Finally, the oxidation of poly(DEDPM) was occurred at 0.46 V (versus Ag/AgNO$_3$), where the vinylene group of conjugated polymer backbone might be oxidized in the scan. Poly(DEDPM) also shows the irreversible reduction at −0.83 V. The redox current value was gradually increased

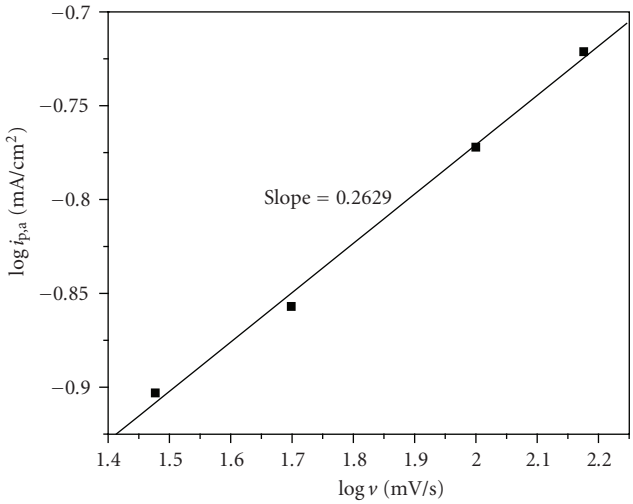

FIGURE 5: Plot of log $i_{p,a}$ versus log v for poly(DEDPM).

as the scan rate was increased. This result suggests that the electrochemical process of poly(DEDPM) is reproducible in the potential range of $-1.5 \sim +1.5$ V versus $Ag/AgNO_3$.

It has been reported that the relationship between the redox peak current and the scan rate can be expressed as a power-law type as follows [28–30]:

$$i_{p,a} = kv^x, \quad (1)$$

$$\text{Log } i_{p,a} = \log k + x \log v, \quad (2)$$

where $i_{p,a}$ = oxidation peak current density, v = scan rate, k = proportional constant, and x = exponent of scan rate.

Considering that electrode kinetics satisfies (1), the electrochemical redox reaction is controlled by either the electron transfer process, where $x = 1$, or the reactant diffusion process, where $x = 0.5$. The relationship plot of the oxidation current density (log $i_{p,a}$) as a function of the scan rate (log v) is shown in Figure 5. The oxidation current of poly(DEDPM) versus the scan rate is approximately linear relationship in the range of 30 mV/sec $\sim$ 150 mV/sec and the exponent of scan rate x value is found to be 0.262. It is explained by that the kinetics of the redox process may not reach to the diffusion-control process and not be so fast electro-active although it has very stable durability for electrochemical process.

4. CONCLUSIONS

The electro-optical and electrochemical properties of a typical conjugated cyclopolymer, poly(DEDPM), were measured and discussed. Poly(DEDPM) was prepared by $(NBD)PdCl_2$ catalyst in 56% yield. The chemical structure of poly(DEDPM) was characterized to have the conjugated polymer system with the designed repeating unit. The present poly(DEDPM) was found to be composed of six-membered ring moieties majorly from the analysis of methine carbon peaks in ^{13}C-NMR spectrum. The photoluminescence (PL) spectra of poly(DEDPM) showed that the photoluminescence peak is located at 543 nm corresponding to the photon energy of 2.51 eV. The CVs of the polymer exhibited the irreversible electrochemical behaviors between the doping and undoping peaks. It was found that the kinetics of the redox process of poly(DEDPM) might be mainly controlled by the electron transfer process from the experiment of the oxidation current density of poly(DEDPM) versus the scan rate.

ACKNOWLEDGMENT

This work was supported by Grant no. RTI04-01-04 from the Regional Technology Innovation Program of the Ministry of Knowledge Economy (MKE), South Korea.

REFERENCES

[1] V. Coropceanu, J. Cornil, D. A. da Silva Filho, Y. Olivier, R. Silbey, and J.-L. Brédas, "Charge transport in organic semiconductors," *Chemical Reviews*, vol. 107, no. 4, pp. 926–952, 2007.

[2] Y. Shirota and H. Kageyama, "Charge carrier transporting molecular materials and their applications in devices," *Chemical Reviews*, vol. 107, no. 4, pp. 953–1010, 2007.

[3] E. Menard, M. A. Meitl, Y. Sun, et al., "Micro- and nanopatterning techniques for organic electronic and optoelectronic systems," *Chemical Reviews*, vol. 107, no. 4, pp. 1117–1160, 2007.

[4] K. Tsuchihara, T. Masuda, and T. Higashimura, "Tractable silicon-containing poly(diphenylacetylenes): their synthesis and high gas permeability," *Journal of the American Chemical Society*, vol. 113, no. 22, pp. 8548–8549, 1991.

[5] S.-K. Choi, Y.-S. Gal, S.-H. Jin, and H.-K. Kim, "Poly(1,6-heptadiyne)-based materials by metathesis polymerization," *Chemical Reviews*, vol. 100, no. 4, pp. 1645–1681, 2000.

[6] S.-H. Jin, M.-Y. Kim, J. Y. Kim, K. Lee, and Y.-S. Gal, "High-efficiency poly(*p*-phenylenevinylene)-based copolymers containing an oxadiazole pendant group for light-emitting diodes," *Journal of the American Chemical Society*, vol. 126, no. 8, pp. 2474–2480, 2004.

[7] Y.-S. Gal, S.-H. Jin, H.-S. Lee, and S. Y. Kim, "Synthesis and properties of conjugated cyclopolymers bearing fluorene derivatives," *Macromolecular Research*, vol. 13, no. 6, pp. 491–498, 2005.

[8] J. W. Y. Lam and B. Z. Tang, "Functional polyacetylenes," *Accounts of Chemical Research*, vol. 38, no. 9, pp. 745–754, 2005.

[9] T. Masuda, "Substituted polyacetylenes," *Journal of Polymer Science, Part A*, vol. 45, no. 1, pp. 165–180, 2007.

[10] Y.-S. Gal, W.-C. Lee, S.-H. Jin, et al., "Cyclopolymerization of α-methylbenzyl dipropargylamine by transition metal catalysts," *Macromolecular Research*, vol. 15, no. 3, pp. 267–271, 2007.

[11] Y.-S. Gal, S.-H. Jin, and J.-W. Park, "Synthesis and properties of an ionic polyacetylene with aromatic heterocycles," *Journal of Polymer Science, Part A*, vol. 45, no. 23, pp. 5679–5685, 2007.

[12] Y.-S. Gal, W.-C. Lee, S.-H. Jin, et al., "Synthesis and electrochemical properties of poly[N-(6-azidohexyl)-2-ethynylpyridinium tetraphenylborate]," *Molecular Crystals and Liquid Crystals*, vol. 472, no. 1, pp. 271–278, 2007.

[13] K. Walzer, B. Männig, M. Pfeiffer, and K. Leo, "Highly efficient organic devices based on electrically doped transport layers," *Chemical Reviews*, vol. 107, no. 4, pp. 1233–1271, 2007.

[14] S. Günes, H. Neugebauer, and N. S. Sariciftci, "Conjugated polymer-based organic solar cells," *Chemical Reviews*, vol. 107, no. 4, pp. 1324–1338, 2007.

[15] Md. A. Karim, Y.-R. Cho, J. S. Park, et al., "Novel fluorene-based functional 'click polymers' for quasi-solid-state dye-sensitized solar cells," *Chemical Communications*, no. 16, pp. 1929–1931, 2008.

[16] G. B. Butler, "Cyclopolymerization and cyclocopolymerization," *Accounts of Chemical Research*, vol. 15, no. 11, pp. 370–378, 1982.

[17] H. W. Gibson, F. C. Bailey, A. J. Epstein, et al., "Poly(1,6-heptadiyne), a free-standing polymer film dopable to high electrical conductivity," *Journal of the American Chemical Society*, vol. 105, no. 13, pp. 4417–4431, 1983.

[18] Y.-S. Gal and S. K. Choi, "Cyclopolymerization of dipropargyl ether by transition metal catalysts," *Polymer (Korea)*, vol. 11, no. 6, pp. 563–571, 1987.

[19] B. V. K. Naidu, B.-H. Oh, D.-H. Nam, et al., "Transition-metal-catalyzed conjugated polymers of 1,6-heptadiyne derivatives in supercritical carbon dioxide," *Journal of Polymer Science, Part A*, vol. 44, no. 4, pp. 1555–1560, 2006.

[20] C. Czekelius, J. Hafer, Z. J. Tonzetich, R. R. Schrock, R. L. Christensen, and P. Müller, "Synthesis of oligoenes that contain up to 15 double bonds from 1,6-heptadiynes," *Journal of the American Chemical Society*, vol. 128, no. 51, pp. 16664–16675, 2006.

[21] M.-S. Ryoo, W.-C. Lee, and S.-K. Choi, "Cyclopolymerization of diethyl dipropargylmalonate by transition-metal catalysts," *Macromolecules*, vol. 23, no. 12, pp. 3029–3031, 1990.

[22] S.-J. Jeon, D.-J. Cho, S.-C. Shim, T.-J. Kim, and Y.-S. Gal, "$Mo(CO)_6$-catalyzed cyclopolymerization of diethyl dipropargylmalonate to give a polyene containing only five-membered rings," *Journal of Polymer Science, Part A*, vol. 37, no. 7, pp. 877–880, 1999.

[23] Y.-S. Gal, S.-H. Jin, S.-H. Kim, et al., "Cyclopolymerization of dipropargyl derivatives by Cp_2MoCl_2-$EtAlCl_2$ catalyst system," *Journal of Macromolecular Science, Part A*, vol. 39, no. 3, pp. 237–249, 2002.

[24] J. O. Krause, D. Wang, U. Anders, et al., "Stereoselective cyclopolymerization of diynes: smart materials for electronics and sensors," *Macromolecular Symposia*, vol. 217, no. 1, pp. 179–190, 2004.

[25] Y.-S. Gal, S.-H. Jin, A. R. Hyun, et al., "Electro-optical and electrochemical properties of a conjugated cyclopolymer: poly(9,9-dipropargylfluorene)," *Journal of Industrial and Engineering Chemistry*. In press.

[26] H. H. Fox, M. O. Wolf, R. O'Dell, B. L. Lin, R. R. Schrock, and M. S. Wrighton, "Living cyclopolymerization of 1,6-heptadiyne derivatives using well-defined alkylidene complexes: polymerization mechanism, polymer structure, and polymer properties," *Journal of the American Chemical Society*, vol. 116, no. 7, pp. 2827–2843, 1994.

[27] Y.-S. Gal, T. L. Gui, S.-H. Jin, et al., "Electro-optical properties of water-soluble conjugated polymer," *Synthetic Metals*, vol. 135-136, pp. 353–354, 2003.

[28] J. M. Ko, H. W. Rhee, S.-M. Park, and C. Y. Kim, "Morphology and electrochemical properties of polypyrrole films prepared in aqueous and nonaqueous solvents," *Journal of the Electrochemical Society*, vol. 137, no. 3, pp. 905–909, 1990.

[29] A. J. Bard and L. R. Faulker, *Electrochemical Methods*, chapters 3, 6 and 10, John Wiley & Sons, New York, NY, USA, 1980.

[30] Y. E. Kim, Y. S. Kwon, K. S. Lee, J.-W. Park, H. J. Seo, and T. W. Kim, "Synthesis and electrochemical properties of N-substituted bicarbazyl derivatives," *Molecular Crystals and Liquid Crystals*, vol. 424, pp. 153–158, 2004.

Hindawi Publishing Corporation
International Journal of Photoenergy
Volume 2008, Article ID 150682, 8 pages
doi:10.1155/2008/150682

Research Article

Two-Dimensional Free Energy Surfaces for Electron Transfer Reactions in Solution

Shigeo Murata,[1] Maged El-Kemary,[2] and M. Tachiya[1]

[1] *National Institute of Advanced Industrial Science and Technology (AIST), AIST Tsukuba Central 5, 1-1-1 Higashi, Tsukuba 305-8565, Japan*
[2] *Chemistry Department, Faculty of Education, Kafr ElSheikh University, Kafr ElSheikh 33516, Egypt*

Correspondence should be addressed to Shigeo Murata, shigeo.murata@aist.go.jp

Received 2 May 2008; Revised 18 June 2008; Accepted 18 August 2008

Recommended by Mohamed Sabry Abdel-Mottaleb

Change in intermolecular distance between electron donor (D) and acceptor (A) can induce intermolecular electron transfer (ET) even in nonpolar solvent, where solvent orientational polarization is absent. This was shown by making simple calculations of the energies of the initial and final states of ET. In the case of polar solvent, the free energies are functions of both D-A distance and solvent orientational polarization. On the basis of 2-dimensional free energy surfaces, the relation of Marcus ET and exciplex formation is discussed. The transient effect in fluorescence quenching was measured for several D-A pairs in a nonpolar solvent. The results were analyzed by assuming a distance dependence of the ET rate that is consistent with the above model.

1. INTRODUCTION

Electron transfer (ET) reactions have been studied extensively for many years. Fluorescence quenching is often used to study ET reactions involving excited molecules. Two types of ET reactions have been identified in fluorescence quenching: full ET from the electron donor (D) to the acceptor (A) yielding D^+ and A^- radical ions, and partial ET yielding a fluorescent complex [1]. The former mainly occurs in polar environments, and is less important in less polar environments. This process is attributed to Marcus nonadiabatic ET. The latter, on the other hand, mainly occurs in nonpolar and weakly polar environments, and is less important in more polar environments. This process is attributed to the formation of the excited-state charge-transfer complex (the exciplex). This result is supported by many other results for various D-A systems [2–4]. It was shown later [5–8] that the mechanism depends not only on the solvent polarity but also on ΔG of the reaction: quenching by exciplex formation also occurs in polar solvents for D-A pairs with smaller $-\Delta G$, the degree of charge transfer of the exciplex changes in a wide range (from ~0 to >90%) depending on ΔG and solvent polarity. These results are based on spectroscopic and dipole moment measurements.

In Marcus theory, ET occurs when the free energies of the initial and final states of ET coincide as a result of change of solvent coordinate (coordinate representing the solvent orientational polarization). The solvent orientational polarization coordinate is relevant to this type of ET. On the other hand, the coordinate relevant to exciplex formation is not clear. Exciplex formation can occur efficiently even in nonpolar solvents, where Marcus ET does not occur because of the lack of solvent orientational polarization. This indicates that some other coordinate is relevant to exciplex formation in nonpolar solvents.

In previous papers [9–13], we reported fluorescence quenching by ET between cyanoanthracenes (A) in a donor solvent. By femtosecond fluorescence upconversion experiments [12, 13], we found that the two processes, quenching of acceptor fluorescence and riseup of exciplex fluorescence, have the same time constants (~200 femtoseconds) and occur without delay. This implies that the exciplex is directly formed upon fluorescence quenching, that is, there is no intermediate process between them. Based on this observation, we proposed a mechanism of exciplex formation. According to this mechanism, the exciplex is formed as a result of mixing of the DA^* and D^+A^- states, and the exciplex state is reached when D and A^* approach each other

to contact distances. In [13], this mechanism was shown qualitatively using the potential energy surfaces of the D-A system.

Although this model can explain the exciplex formation qualitatively, a more quantitative discussion is necessary to account for the ET processes in the exciplex. Further consideration is also necessary to clarify the relation between the Marcus model of ET and the above model. In this paper, we refine our model of exciplex formation and present some experimental results on ET in a nonpolar solvent. The relation between Marcus ET and exciplex formation is also discussed briefly.

2. MECHANISM OF ET IN NONPOLAR SOLVENT

In the case of nonpolar solvent, the solvent orientational polarization is absent, and the energies E_i and E_f of the initial (DA^*) and final (D^+A^-) states of ET, respectively, do not depend on this coordinate. Except at very short distances, E_i is constant. We take $E_i = 0$ outside the contact distance. E_f is given as a function of the distance between D and A (2):

$$E_i = 0, \tag{1}$$

$$E_f = \mathrm{IP} - \mathrm{EA} - \frac{e^2}{2}\left(1 - \frac{1}{\varepsilon_{\mathrm{op}}}\right)\left(\frac{1}{a} + \frac{1}{b}\right) - \frac{e^2}{\varepsilon_{\mathrm{op}} r} \tag{2}$$

$$= E_{f\infty} - \frac{e^2}{\varepsilon_{\mathrm{op}} r}, \tag{3}$$

where IP and EA are the ionization potential of the donor and the electron affinity of the acceptor, respectively, and $\varepsilon_{\mathrm{op}}$ is the optical dielectric constant of the solvent. a and b are the radii of D and A, and r is the distance between D and A. $E_{f\infty}$ is the energy of the final state at $r = \infty$. The third term on the right-hand side of (2) gives the solvation energy of the D^+ and A^- ions. $E_{f\infty}$ can be rewritten in the following form:

$$E_{f\infty} = \Delta G^{\mathrm{AN}} + \frac{e^2}{2}\left(\frac{1}{\varepsilon_{\mathrm{op}}} - \frac{1}{\varepsilon_S^{\mathrm{AN}}}\right)\left(\frac{1}{a} + \frac{1}{b}\right), \tag{4}$$

where ΔG^{AN} and $\varepsilon_S^{\mathrm{AN}}$ are the free energy change of the reaction between D and A in AN solvent and the static dielectric constant of AN, respectively. Experimentally, it may be more convenient to use ΔG^{AN} instead of $E_{f\infty}$ because the former can be easily evaluated from the measured redox potentials of the donor and acceptor. For a pair with $a = b = 3\,\text{Å}$ in a solvent with $\varepsilon_{\mathrm{op}} = 1.88$, $E_{f\infty} = 1.65$ eV corresponds to $\Delta G^{\mathrm{AN}} = -0.85$ eV.

ET occurs when the energies of the initial and final states coincide [14, 15]. In Marcus theory, the energy coincidence occurs by the change of solvent orientational polarization, that is, the coordinate of solvent orientational polarization can be regarded as the reaction coordinate of ET reactions. This does not occur in nonpolar solvent because the solvent molecules do not have permanent dipoles. Equations (1) and (2) are plotted by broken lines in Figure 1 for a D-A pair with $E_{f\infty} = 1.65$ eV ($\varepsilon_{\mathrm{op}} = 1.88$). The two curves intersect each other at a short distance near 4.5 Å. In this case, the energy coincidence occurs by the change of intermolecular distance, and ET can occur at the intersection distance even in the absence of solvent polarization, that is, participation of solvent is not always necessary for ET to occur. This observation explains why ET can occur in nonpolar solvent. Some of the ultrafast ET that is faster than solvation may also be accounted for by the change in intermolecular distance. The coordinate of intermolecular distance can thus be regarded as another reaction coordinate of ET reactions. This point has not been stressed so far.

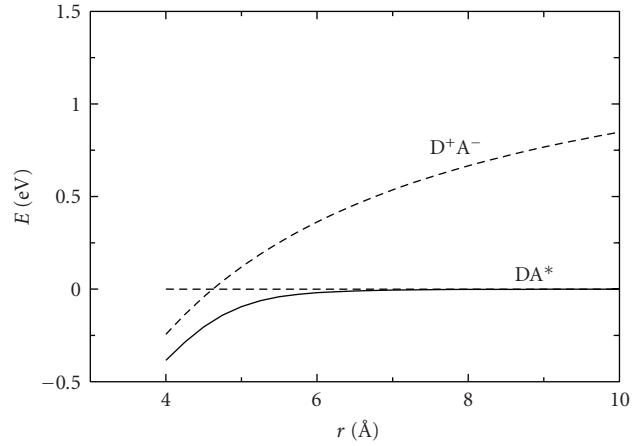

Figure 1: Potential energy curves of a D-A pair with $E_{f\infty} = 1.65$ eV ($\Delta G^{\mathrm{AN}} = -0.85$ eV) in a nonpolar solvent ($\varepsilon_S = \varepsilon_{\mathrm{op}} = 1.88$). The broken and solid curves represent the diabatic and adiabatic curves, respectively. The parameter values assumed, the molecular radii of D and A, are 3 Å, J_0 and β in (9) are 0.23 eV at 4 Å and 1 Å^{-1}, respectively. Plotting is made down to $r = 4$ Å which is smaller than $a + b = 6$ Å. This is not meaningless because D and A are often not spherical but planar and can approach to distances shorter than $a + b$.

Up to now the interactions between D and A except the Coulomb interaction have been neglected. At short distances quantum mechanical interactions between D and A become important. At such distances, the DA^* and D^+A^- states are no longer pure eigenstates but are mixed with each other. The resulting state ϕ is given by

$$\phi = c_1\psi_1 + c_2\psi_2, \tag{5}$$

where ψ_1 and ψ_2 are the diabatic states. The energies $E_\pm$ of the new adiabatic states are given using the energies E_1 and E_2 of the diabatic states

$$E_\pm = \frac{E_1 + E_2}{2} \pm \frac{\sqrt{\Delta_{12}^2 + 4H_{12}^2}}{2}, \tag{6}$$

$$\Delta_{12} = |E_1 - E_2|, \tag{7}$$

$$H_{12} = \langle \psi_1 | H | \psi_2 \rangle, \tag{8}$$

where H_{12} is the electronic coupling matrix element and is assumed to decrease exponentially with distance

$$H_{12}^2 = J_0^2 \exp[-\beta(r - r_0)]. \tag{9}$$

The energy E_- calculated from (6) with $J_0 = 0.23$ eV at $r_0 = 4\,\text{Å}$ and $\beta = 1\,\text{Å}^{-1}$ is plotted by the solid curve in Figure 1.

The adiabatic state ϕ given by (5) is the exciplex state. The electronic structure of the exciplex state changes with distance. At distances longer than the intersection distance, the exciplex state is more like the DA^* state, whereas at shorter distances, it is more like the D^+A^- state. When D and A approach each other from long distances to short distances through the intersection point, the exciplex state changes from almost neutral to an ionic one. In other words, the decrease in D-A distance induces (adiabatic) ET to form the ionic exciplex. This clearly shows that even in the absence of solvent orientational polarization, ET (or exciplex formation) can occur with the change in intermolecular distance. Thus the well-known experimental results that exciplex formation is efficient in nonpolar solvent can be understood. If D and A are close to each other when A is excited, the rate of ET induced by change of r can be of the order of the frequency of intermolecular stretching vibration in the exciplex (typically $\sim 100\,\mathrm{cm}^{-1}$). The rate can be higher than that of solvent polarization, and this mechanism can explain at least some of the ultrafast ET reported so far.

When $-\Delta G^{AN}$ is larger, the initial and final states intersect each other at longer distances (Figure 2 for $E_{f\infty} = 0.9\,\mathrm{eV}$ or $\Delta G^{AN} = -1.60\,\mathrm{eV}$), and ET is expected to occur at longer distances (R_0 is the intersection distance). In this case, however, the contribution of intramolecular vibrations to ET should also be taken into account. In Figure 2, the broken curves represent the potential energy curves of the D^+A^- state with intramolecular vibrational quanta. These curves intersect the curve of the DA^* state at shorter distances. This gives rise to ET at shorter distances in addition to ET at the original distance. On the other hand, the potential energy curves of the DA^* state with vibrational quanta gives rise to ET at longer distances. According to Tachiya and Seki [16], the first-order ET rate in this case is given by

$$k(r) = \frac{2\pi}{\hbar} J_0^2 \exp\left[-\beta(r - r_0)\right] \sum_i F_i \delta\left(ih\nu + E_{f\infty} - \frac{e^2}{\varepsilon_{op} r}\right),$$
$$F_i = \exp(-s) \exp\left(\frac{ih\nu}{2k_B T}\right) I_{|i|}(z), \tag{10}$$

where β is the attenuation coefficient of ${H_{12}}^2$ with distance, $I_{|i|}(z)$ is the modified Bessel function of the first kind:

$$s = \Lambda(2n+1) \quad n = \frac{1}{\left[\exp\left\{h\nu/(k_B T)\right\} - 1\right]},$$
$$z = 2\Lambda\sqrt{n(n+1)} \quad \Lambda = \frac{\lambda}{(h\nu)}, \tag{11}$$

where λ denotes the vibrational reorganization energy. In Figure 3, $k(r)$ is plotted as a function of r for three values of $E_{f\infty}$ with $J_0 = 100\,\mathrm{cm}^{-1}$ at 6 Å, $\beta = 1\,\text{Å}^{-1}$, $\nu = 1500\,\mathrm{cm}^{-1}$, and $\lambda = 0.3\,\mathrm{eV}$. ET occurs at discrete r values, where the potential energy curves of the initial and final states intersect. The point $r = 7.7\,\text{Å}$ of the $E_{f\infty} = 1.0\,\mathrm{eV}$ curve corresponds to the distance where the initial and final state curves with zero vibrational energies intersect. $k(r)$ decreases rapidly at distances longer than this because both H_{12} and F_i (the Franck-Condon factor) decrease with increasing distance. At distances shorter than this, H_{12} increases and F_i decreases with decreasing distance, and as a result $k(r)$ first increases and then decreases slowly. For curves with $E_{f\infty} = 0.5$ and 1.72 eV, the intersection distances are 11.2 and 4.5 Å, respectively.

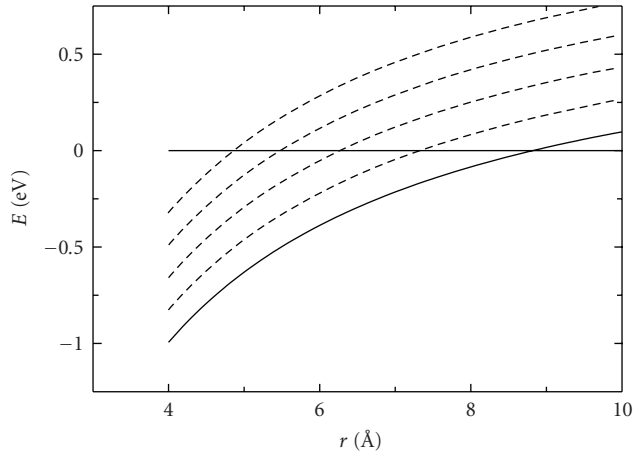

Figure 2: Potential energy curves of a D-A pair with $E_{f\infty} = 0.9\,\mathrm{eV}$ ($\Delta G^{AN} = -1.6\,\mathrm{eV}$) in a nonpolar solvent ($\varepsilon_S = 1.88$). The broken curves are the free energy curves of the final state with vibrational quanta ($\nu = 1500\,\mathrm{cm}^{-1}$).

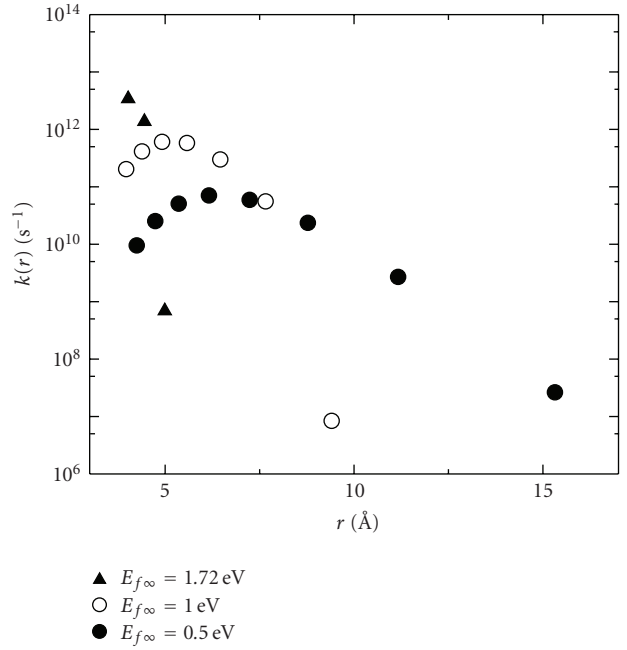

Figure 3: First-order ET rate in nonpolar solvent calculated for three values of $E_{f\infty}$ with $J_0 = 100\,\mathrm{cm}^{-1}$ at 6 Å, $\beta = 1\,\text{Å}^{-1}$, $\nu = 1500\,\mathrm{cm}^{-1}$, and $\lambda = 0.3\,\mathrm{eV}$. ET occurs at discrete r values.

3. ET REACTIONS IN POLAR SOLVENT

ET occurs when the energies of the initial and final states coincide [14, 15]. However, because the entropy does not change during ET, one can say that ET occurs when the free

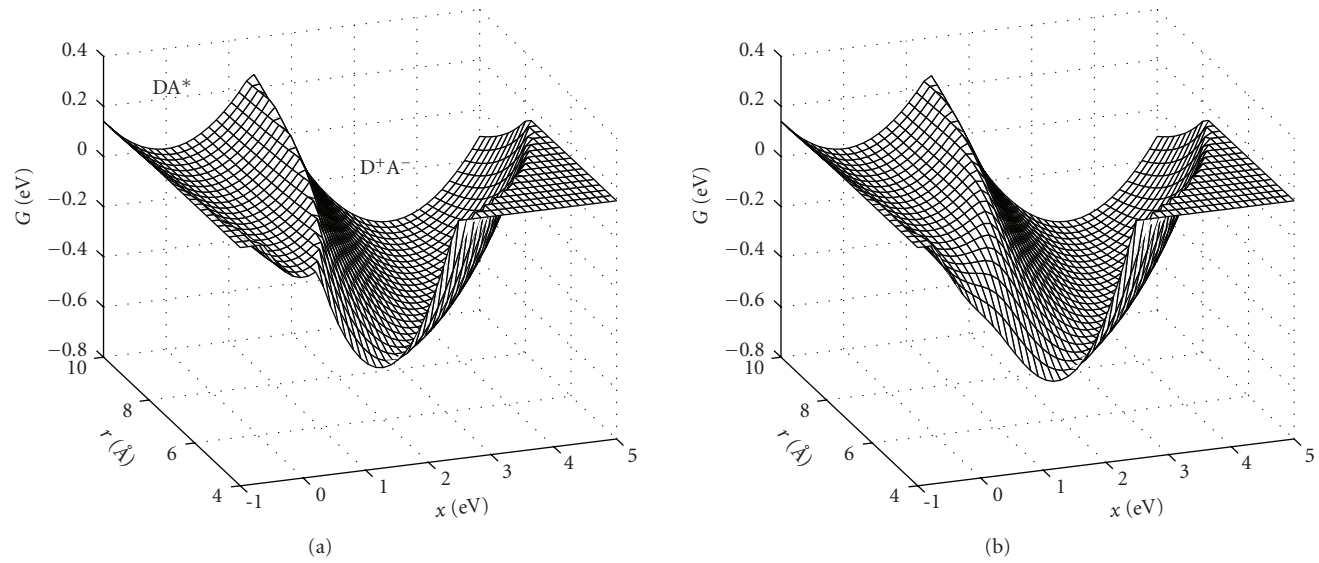

Figure 4: Free energy surfaces of a D-A pair with $\Delta G^{AN} = -0.4$ eV in AN solvent. Only the parts relevant to ET reactions are shown, (a) the mixing of the initial and final states not taken into account; (b) mixing taken into account.

energies of the initial and final states coincide. In solvents with permanent dipoles, the free energies of the initial and final states of ET are functions of both intermolecular distance r and solvent orientational polarization x. x can be given by

$$x = e\Delta V = e(V_D - V_A), \tag{12}$$

where V_D and V_A are the electrostatic potentials at the positions of D and A generated by the solvent dipoles. The free energies are given by [14, 17]

$$\begin{aligned} G_i &= \frac{1}{4\lambda}x^2, \\ G_f &= \frac{1}{4\lambda}(x - 2\lambda)^2 + \Delta G, \end{aligned} \tag{13}$$

where λ and ΔG are the reorganization energy and the free energy change of reaction, respectively, and are given by (14)

$$\begin{aligned} \lambda &= \frac{e^2}{2}\left(\frac{1}{\varepsilon_{op}} - \frac{1}{\varepsilon_S}\right)\left(\frac{1}{a} + \frac{1}{b} - \frac{2}{r}\right), \\ \Delta G &= \Delta G^{AN} + \frac{e^2}{2}\left(\frac{1}{\varepsilon_S} - \frac{1}{\varepsilon_S^{AN}}\right)\left(\frac{1}{a} + \frac{1}{b} - \frac{2}{r}\right), \end{aligned} \tag{14}$$

where ε_{op} is the optical dielectric constant of the solvent. G_i and G_f are functions of x and r, and represent 2-dimensional free energy surfaces. In this case, both x and r are regarded as reaction coordinates of ET reactions. The free energy surfaces are plotted in Figure 4(a) for a D-A pair ($\Delta G^{AN} = -0.4$ eV) in AN solvent ($\varepsilon_{op} = 1.8$ and $\varepsilon_S = 37.5$). Figure 4(b) shows the surfaces obtained by mixing the DA* and D^+A^- states corresponding to the same x and r values. In Figure 4, only the parts of the surfaces which are important for ET reactions are shown, and the surfaces in large and small x regions are artificially cut by the plane $G = 0.15$ eV so that one can see the inside of the valleys. The surfaces are smoother at shorter distances in Figure 4(b) than in Figure 4(a). This is the exciplex region, where the two states are mixed significantly. Figure 5 shows the contour plot of Figure 4(b), and some typical processes related to fluorescence quenching are also shown by arrows.

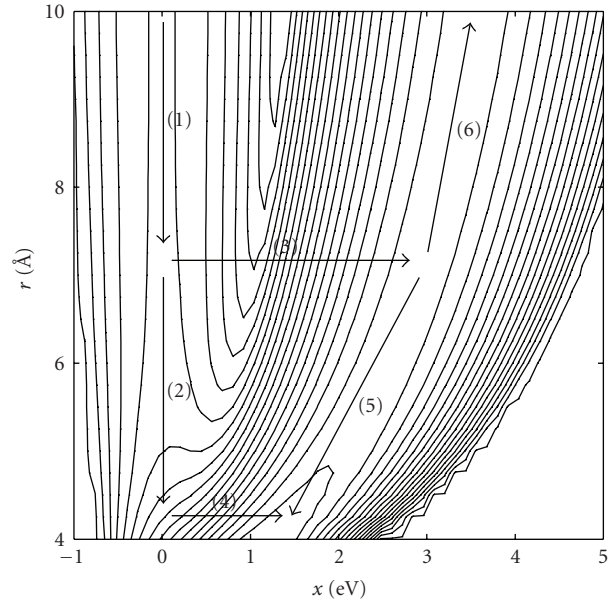

Figure 5: Contour plot of Figure 4(b). The arrows show the typical processes involved in fluorescence quenching.

From Figures 4 or 5, the relation between Marcus ET and exciplex formation is apparent. We consider a charge separation reaction. Just after excitation, the system is in the initial state DA*, and is at the bottom ($x = 0$). D and A approach each other by process (1) of Figure 5. Marcus ET

Table 1: Parameters R_0 and k_0 determined by analyzing the fluorescence decay curves.

	$E_{f\infty}$/eV	$-\Delta G^{AN}$/eV	R_0/Å	k_0/s^{-1}
C153-TMPD(0.2 M)	0.92	0.78	11.1	2.9×10^{10}
C522-TMPD(0.2 M)	0.81	0.89	12.2	3.7×10^{10}
C152-TMPD(0.2 M)	0.63	1.07	15.2	4.2×10^{8}

$E_{f\infty}$ was calculated from ΔG^{AN} using (4). $\varepsilon_S = \varepsilon_{op} = 2.16$ for liquid paraffin and $a = 3.5$ Å for TMPD and $b = 3.9$ Å for coumarins.

occurs when the system crosses the barrier that separates the initial and final states (in other words, when x changes: process (3)). The species D^+A^- generated by process (3) can either dissociate to form free ions by process (6) or form the exciplex by process (5) that involves the decrease in distance r between D^+ and A^-. The exciplex can also be formed by process (2) that occurs after process (1). Process (2) also involves the decrease in r. When r decreases, exciplex formation (charge separation) can occur even when x remains 0 (see discussion on ET in nonpolar solvent). The exciplex formed by process (2) is not in equilibrium with respect to x and can change to the equilibrated exciplex with the change in x (process (4)). This is accompanied by further charge separation within the exciplex. The rates and importances of processes (1)–(6) depend on the rate of diffusion of D and A, solvent relaxation time, interaction energy, and so forth, even for fixed ΔG^{AN}. The relative importance of Marcus ET and exciplex formation in fluorescence quenching will change with the value of ΔG^{AN}.

Some of the existing experimental results were discussed in detail elsewhere [15] on the basis of 2-dimensional free energy surfaces.

4. EXPERIMENTAL STUDY OF FLUORESCENCE QUENCHING IN NONPOLAR SOLVENT

In previous papers [9–11], we analyzed the transient effect in fluorescence quenching by ET at high quencher concentrations to determine experimentally the distance dependence of ET rates in solution. The distribution of ET distance was calculated by using the rate parameters obtained. The studies were made in polar and nonpolar solvents. In this paper, we report another study of the transient effect in a nonpolar solvent and discuss the result on the basis of the ET mechanism described in Section 2. Experimental method and data analysis have already been reported [11], and they are described briefly here.

Coumarin derivatives (C152, C153, C522; electron acceptors) were used as fluorescers and N,N,N',N'-tetramethyl-p-phenylenediamine (TMPD; electron donor) was used as quencher. The oxidation-reduction potentials of these compounds were taken from literature [18]. These values were used to calculate the free energy change ΔG^{AN} of ET reaction. Fluorescence decay curves at a quencher concentration of 0.2 M were measured by time-correlated single photon counting [9]. Fluorescence was excited using the second harmonic of a mode-locked Ti:Sa laser, and detected by an MCP-PMT. The full width at high maximum (fwhm) of the instrument response function was ~40 picoseconds. To analyze the transient effect successfully, the solvent must be highly viscous [9, 11]. We employed liquid paraffin as a viscous nonpolar solvent. Because of many restrictions (appropriate ΔG^{AN} value, high solubility in liquid paraffin, location of the absorption spectra, etc.) imposed on the D-A combinations, we could not find many D-A combinations.

The transient effect can be analyzed using the following equations [9]:

$$P(t) = \exp\left[-\frac{t}{\tau_0} - 4\pi c_0 \int_d^\infty \{1 - U(r,t)\} r^2\, dr\right], \quad (15)$$

$$\frac{\partial U(r,t)}{\partial t} = D\left(\frac{\partial^2}{\partial r^2} + \frac{2}{r}\frac{\partial}{\partial r}\right) U(r,t) - k(r)U(r,t), \quad (16)$$

where $P(t)$ is the fluorescence decay curve, $U(r,t)$ the survival probability of the D-A pair at time t that was separated by distance r when it was excited at $t = 0$. τ_0, c_0, and d are the lifetime of unquenched fluorescence, quencher concentration, and the contact distance of D and A, respectively. In obtaining (15), the initial distribution of quencher molecules is assumed to be random. D and $k(r)$ in (16) are the sum of the diffusion coefficients of D and A, and the first-order ET rate constant, respectively. Equation (16) must be solved under appropriate initial and boundary conditions. The value of D was calculated using the Stokes-Einstein equation [11].

In a previous paper [11], we analyzed the transient effect in liquid paraffin solvent, and showed that ET occurs at distances longer than the contact distances of D and A. We assumed that $k(r)$ decreases exponentially with distance

$$k(r) = A \exp[-b(r - r_0)], \quad (17)$$

where A and b are constants. From (15)–(17), we see that the shape of the fluorescence decay curve $P(t)$ is determined by the parameters A and b. Consequently, A and b can be determined by fitting the calculated decay curve (actually, its convolution with the instrument response function) to the experimental ones (it was shown that the number of parameters that can be determined by such experiment and data analysis is not more than 2) [9]. The fitting was made by a nonlinear least squares method. All the calculations were carried out numerically. Very good fittings were obtained, A and b were determined for several D-A pairs. One of the shortcomings of the use of (17) is that, if A and b corresponding to the best fit are used, $k(r)$ becomes too large at short distances. Indeed, $k(r)$ obtained from experiment exceeds 10^{15} s^{-1} for most D-A pairs at 6 Å.

In Section 2 of the present paper, we studied ET in nonpolar solvent and showed that if an intramolecular vibrational mode is taken into account, the distance dependence of $k(r)$ would be weaker when $r \leq R_0$, but $k(r)$ rapidly decrease when $r > R_0$, with R_0 being the distance where the potential energy curves of the initial and final states in the absence of intramolecular vibrational mode intersect (see Figure 3). Figure 3 shows that the dependence of $k(r)$ on r changes with $E_{f\infty}$ (or ΔG^{AN}). In Table 1 are shown the values

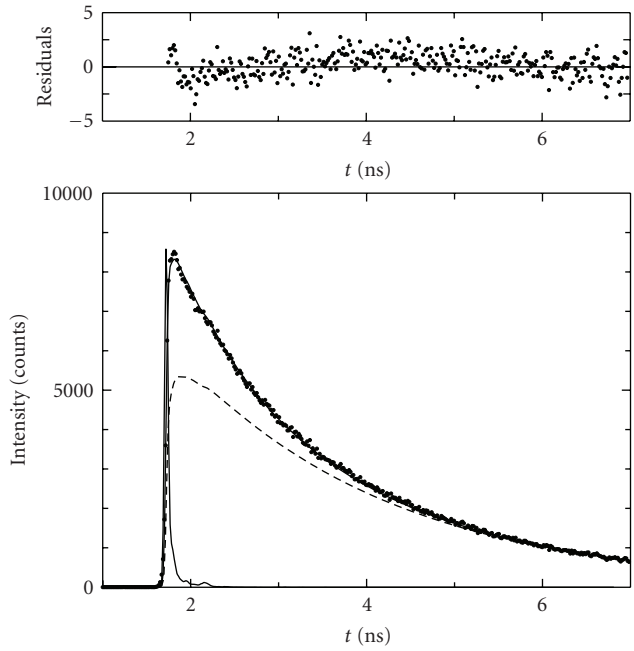

Figure 6: Observed decay curves (dots) of fluorescence of C522 quenched by TMPD (0.2 M) in liquid paraffin at 296 K, calculated best-fit to it (solid line), hypothetical decay curve (broken line), and residuals (upper dots). The thin solid line indicates the instrument response function. The ET parameters obtained are $R_0 = 12.2\,Å$ and $k_0 = 3.7 \times 10^{10}\,s^{-1}$, respectively, with $\chi^2 = 1.2786$. See the text for the hypothetical decay curve.

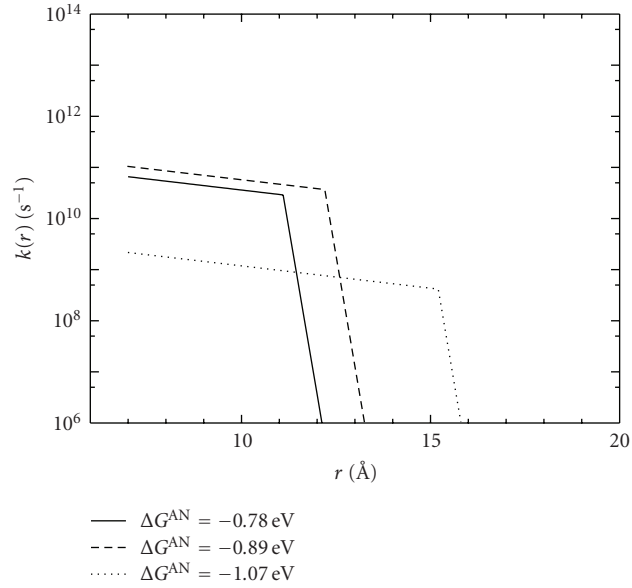

Figure 7: First-order ET rate of the three D-A pairs obtained from R_0, k_0, (18) and (19). The ΔG^{AN} values correspond to the D-A pairs given in Table 1.

of $E_{f\infty}$ and ΔG^{AN} [18] for the D-A combinations employed in this paper. These values lie in a relatively narrow range, and we can assume the same functional form for $k(r)$ for all the D-A combinations to analyze the experimental data

$$k(r) = k_0 \exp\left[-0.2(r - R_0)\right] \quad \text{for } d < r \le R_0, \tag{18}$$

$$k(r) = k_0 \exp\left[-10(r - R_0)\right] \quad \text{for } R_0 < r, \tag{19}$$

where d is the contact distance of D and A, and $k_0 = k(R_0)$. According to (18) and (19), inside the radius R_0, $k(r)$ decreases slowly with increasing distance, while outside this radius it decreases rapidly. If (18) and (19) are adopted, the parameters that determine the shape of the decay curve $P(t)$ are R_0 and k_0: they are determined from the fitting. The coefficient -0.2 in (18) was chosen to get better fittings.

The distribution $Y(r)$ of ET distance is given by the following equation [10]:

$$Y(r) = 4\pi r^2 c_0 k(r) \int_0^\infty q(r,t)P(t)\,dt, \tag{20}$$

where $q(r,t) = c(r,t)/c_0$ with $c(r,t)$ being the concentration profile of the quencher. $q(r,t)$ satisfies (16) with $U(r,t)$ replaced by $q(r,t)$. Consequently, $Y(r)$ can be calculated if the ET parameters R_0 and k_0 are determined. These calculations were also carried out numerically. $Y(r)dr$ gives the probability that ET occurs from the donor to the acceptor over a distance between r and $r + dr$. Integration of $Y(r)$ over r gives the quantum yield of ET reaction.

The fluorescence decay is faster for D-A pairs with higher $-\Delta G^{AN}$ values. This is also true for the decay due to ET reaction only (i.e., the decay after eliminating the monomolecular decay of the excited fluorescer). The transient effect is more pronounced for pairs with higher $-\Delta G^{AN}$ values. Figure 6 shows the experimental decay curve (dots) and the calculated best-fit one (solid curve, actually this is the convolution of the calculated curve with the instrument response function [9]) of the C522-TMPD(0.2 M) pair. Also is shown in Figure 6 a hypothetical decay curve (broken curve) that would be observed if there was no transient effect. This curve was obtained by calculating the convolution of the instrument response function with an exponential function with the same decay time as that in the longer time region of the observed decay. The difference between the observed and hypothetical decay curves found in the shorter-time region is due to the transient effect that we analyze. The fit of the calculated decay curve with the observed one is satisfactory, that is, the transient effect is reproduced well by the analysis. The parameters R_0 and k_0 corresponding to the best fit were $12.2\,Å$ and $3.7 \times 10^{10}\,s^{-1}$, respectively. The fit for C152-TMPD pair is not as good as for C522-TMPD pair. This might be because $k(r)$ of the same functional form, in particular, the slope in the longer distance range, has been used. However, if functions with smaller slopes are used, the fitting calculation becomes unstable and it does not give reasonable results. So we did not change the functional form of $k(r)$ for different D-A pairs. The parameters obtained from experiment are summarized in Table 1. The stronger transient effect found experimentally for D-A pairs with higher $-\Delta G^{AN}$ values is reflected on the larger R_0 values of these pairs. Figure 7 shows the distance dependence of $k(r)$

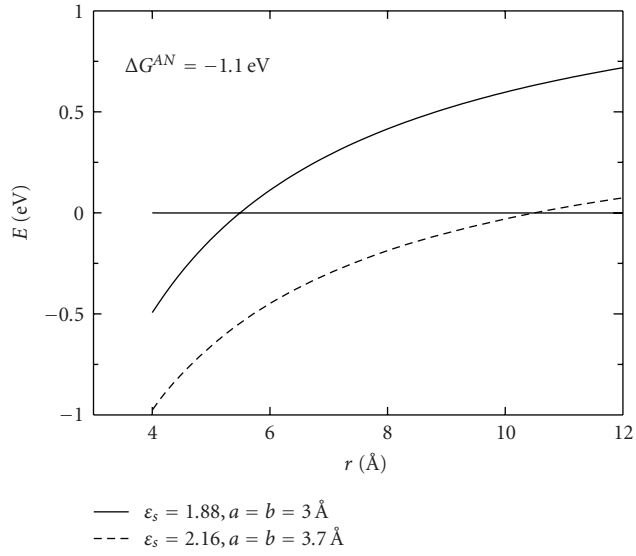

Figure 8: Free energy curves of a D-A pair with $\Delta G^{AN} = -1.1$ eV in a nonpolar solvent. Curves for pairs with different molecular radii and in different solvents are compared.

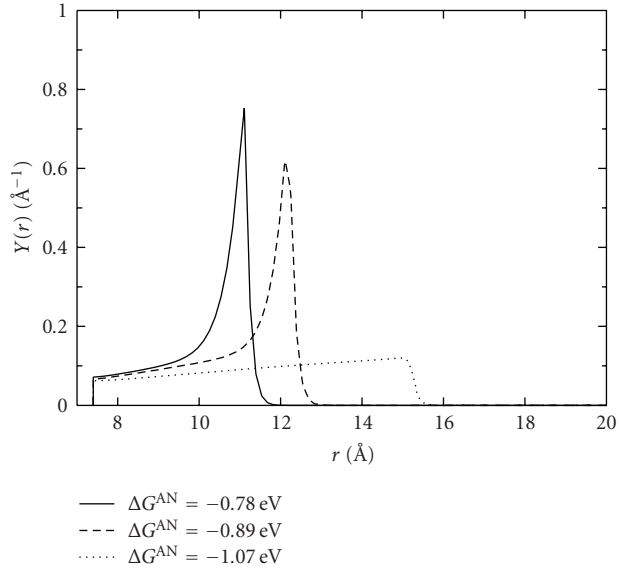

Figure 9: Distribution of ET distance at a quencher concentration of 0.2 M calculated from (20) using R_0 and k_0 determined experimentally.

obtained using R_0 and k_0. The largest value of $k(r)$ obtained is $\sim 1 \times 10^{11}$ s^{-1} in the whole range of r: we have obtained good fits with reasonable values of $k(r)$.

It is clear from Table 1 that R_0 increases with increasing $-\Delta G^{AN}$ of the D-A pair. This is expected from the model already described in Section 2. The same model predicts that k_0 decreases with increasing R_0. The experimental result seems to be consistent with this, although k_0 of the C522-TMPD pair ($R_0 = 12.2$ Å) is slightly larger than that of the C153-TMPD pair ($R_0 = 11.1$ Å). Thus the experiment and the prediction from the model are in qualitative agreement.

R_0 is the distance where the free energy curves in the absence of intramolecular vibrational mode intersect each other, and it can readily be obtained from (1) and (3). Figure 8 shows the potential energy curves for a D-A pair with $\Delta G^{AN} = -1.1$ eV (corresponding to the C152-TMPD pair). The solid E_f curve gives $R_0 \sim 5.5$ Å, which is much smaller compared with that (15.2 Å) experimentally found for C152-TMPD pair. For this case, however, the parameter values ($a = b = 3$ Å, $\varepsilon_S = 1.88$) used so far are not appropriate. More realistic values are $a = 3.9$ Å (for coumarins), $b = 3.5$ Å (for TMPD) (both calculated empirically [19, 20]), and $\varepsilon_S = 2.16$. The broken E_f curve using these parameters gives R_0 ($\sim$10.5 Å) that is much larger than the previous one and closer to the experiment. The agreement, however, is not quantitative. The disagreement may be caused by insufficient accuracy of the calculation of potential energy surfaces, and also by possible nonrandom distribution of quencher molecules in liquid paraffin solvent that consists of large molecules compared to solute molecules. These are problems to be solved in the future.

Figure 9 shows the distribution of ET distance at $c_0 = 0.2$ M calculated from (20). ET occurs at distances longer than the contact distance of D and A, as has been reported in a previous paper [10, 11]. We see from Figure 9 that each $Y(r)$ curve has a maximum at distance R_0, in spite of the assumption that $k(r)$ increases with decreasing r. This can be understood as follows [10]. Before excitation, the distribution of D and A is random (or uniform). After excitation, the reaction first occurs between D and A with initial intermolecular distances smaller than R_0. This is because the solvent is highly viscous and D and A cannot approach quickly by diffusion. This results in a decrease in the concentration of D-A pairs with $r < R_0$, and in the time following, other D and A can approach by diffusion to the $r < R_0$ region. Because $k(r)$ suddenly increases to a high value at $r = R_0$ (except for C152-TMPD pair), the reaction occurs efficiently near this point yielding a large value of $Y(r)$ near $r = R_0$, and only a small fraction of D-A pairs is left for further approach. In the case of C152-TMPD, because $k(r)$ is not large enough in $r < R_0$, the reaction at R_0 is not very efficient and a larger fraction of D-A pairs can reach the $r < R_0$ region to react there.

Figure 7 indicates that $k(r)$ of the C522-TMPD pair ($\Delta G^{AN} = -0.89$ eV, pair 1) is larger than that of the C153-TMPD pair ($\Delta G^{AN} = -0.78$ eV, pair 2) at any value of r. However, the maximum value of $Y(r)$ of pair 1 is smaller than that of pair 2. This can be interpreted in the following way. Because R_0 and $k(r)$ of pair 1 are larger than those of pair 2, the reaction of pair 1 just after excitation is more efficient than that of pair 2. This implies that a smaller number of pairs is available for reaction near $r = R_0$ in the time following. These features can explain why the maximum value of $Y(r)$ of pair 1 is smaller than that of pair 2. The quantum yield of ET reaction is 0.74, 0.81, and 0.73 for C153-TMPD, C522-TMPD, and C152-TMPD pairs, respectively, at $c_0 = 0.2$ M.

5. CONCLUDING REMARKS

In nonpolar solvents, where solvent orientational polarization is absent, ET can occur by the change in intermolecular D-A distance. Efficient exciplex formation in nonpolar solvents, a well-known experimental result, can thus be understood. Intermolecular distance can be regarded as the reaction coordinate of ET reactions. In polar solvents, the free energies are functions of both intermolecular distance and solvent orientational polarization. The relation between Marcus ET and exciplex formation was discussed on the basis of 2-dimensional free energy surfaces. Some experimental results were presented on the transient effect in fluorescence quenching in a nonpolar solvent. The results were analyzed by assuming a distance dependence of the ET rate that is consistent with the above model.

REFERENCES

[1] H. Leonhardt and A. Weller, "Elektronenübertragungsreaktionen des angeregten Perylens," *Berichte der Bunsen-Gesellschaft für Physikalische Chemie*, vol. 67, no. 8, pp. 791–795, 1963.

[2] M. Gordon and W. R. Ware, Eds., *The Exciplex*, Academic Press, New York, NY, USA, 1975.

[3] H. Beens and A. Weller, "Excited molecular z-complexes in solution," in *Organic Molecular Photophysics*, J. B. Birks, Ed., vol. 2, pp. 159–215, John Wiley & Sons, New York, NY, USA, 1975.

[4] N. Mataga, "Photochemical charge transfer phenomena-picosecond laser photolysis studies," *Pure and Applied Chemistry*, vol. 56, no. 9, pp. 1255–1268, 1984.

[5] I. R. Gould, R. H. Young, L. J. Mueller, and S. Farid, "Mechanisms of exciplex formation. Roles of superexchange, solvent polarity, and driving force for electron transfer," *Journal of the American Chemical Society*, vol. 116, no. 18, pp. 8176–8187, 1994.

[6] I. R. Gould, R. H. Young, L. J. Mueller, A. C. Albrecht, and S. Farid, "Electronic structures of exciplexes and excited charge-transfer complexes," *Journal of the American Chemical Society*, vol. 116, no. 18, pp. 8188–8199, 1994.

[7] Y. L. Chow and C. I. Johansson, "Exciplexes of (dibenzoylmethanato)boron/benzenes: the control of exciplex electronic structure," *The Journal of Physical Chemistry*, vol. 99, no. 49, pp. 17558–17565, 1995.

[8] K. N. Grzeskowiak, S. E. Ankner-Mylon, S. N. Smirnov, and C. L. Braun, "Exciplex dipole moments: excited cyanoanthracenes in neat methylbenzene solvents," *Chemical Physics Letters*, vol. 257, no. 1-2, pp. 89–92, 1996.

[9] S. Murata, S. Y. Matsuzaki, and M. Tachiya, "Transient effect in fluorescence quenching by electron transfer. 2. Determination of the rate parameters involved in the Marcus equation," *The Journal of Physical Chemistry*, vol. 99, no. 15, pp. 5354–5358, 1995.

[10] S. Murata and M. Tachiya, "Transient effect in fluorescence quenching by electron transfer. 3. Distribution of electron transfer distance in liquid and solid solutions," *The Journal of Physical Chemistry*, vol. 100, no. 10, pp. 4064–4070, 1996.

[11] L. Burel, M. Mostafavi, S. Murata, and M. Tachiya, "Transient effect in fluorescence quenching by electron transfer. 4. Long-range electron transfer in a nonpolar solvent," *The Journal of Physical Chemistry A*, vol. 103, no. 30, pp. 5882–5888, 1999.

[12] S. Iwai, S. Murata, and M. Tachiya, "Ultrafast fluorescence quenching by electron transfer and fluorescence from the second excited state of a charge transfer complex as studied by femtosecond up-conversion spectroscopy," *The Journal of Chemical Physics*, vol. 109, no. 14, pp. 5963–5970, 1998.

[13] S. Iwai, S. Murata, R. Katoh, M. Tachiya, K. Kikuchi, and Y. Takahashi, "Ultrafast charge separation and exciplex formation induced by strong interaction between electron donor and acceptor at short distances," *The Journal of Chemical Physics*, vol. 112, no. 16, pp. 7111–7117, 2000.

[14] M. Tachiya, "Generalization of the Marcus equation for the electron-transfer rate," *The Journal of Physical Chemistry*, vol. 97, no. 22, pp. 5911–5916, 1993.

[15] S. Murata and M. Tachiya, "Unified interpretation of exciplex formation and Marcus electron transfer on the basis of two-dimensional free energy surfaces," *The Journal of Physical Chemistry A*, vol. 111, no. 38, pp. 9240–9248, 2007.

[16] M. Tachiya and K. Seki, "Energy gap law of electron transfer in nonpolar solvents," *The Journal of Physical Chemistry A*, vol. 111, no. 38, pp. 9553–9559, 2007.

[17] M. Tachiya and S. Murata, "Non-Marcus energy gap dependence of back electron transfer in contact ion pairs," *Journal of the American Chemical Society*, vol. 116, no. 6, pp. 2434–2436, 1994.

[18] H. Shirota, H. Pal, K. Tominaga, and K. Yoshihara, "Substituent effect and deuterium isotope effect of ultrafast intermolecular electron transfer: coumarin in electron-donating solvent," *The Journal of Physical Chemistry A*, vol. 102, no. 18, pp. 3089–3102, 2000.

[19] J. T. Edward, "Molecular volumes and the Stokes-Einstein equation," *Journal of Chemical Education*, vol. 47, no. 4, pp. 261–270, 1970.

[20] A. Bondi, "Van der Waals volumes and radii," *The Journal of Physical Chemistry*, vol. 68, no. 3, pp. 441–451, 1964.

Hindawi Publishing Corporation
International Journal of Photoenergy
Volume 2008, Article ID 131702, 6 pages
doi:10.1155/2008/131702

Research Article

Electrochemiluminescence Study of Europium (III) Complex with Coumarin3-Carboxylic Acid

Stefan Lis, Krzysztof Staninski, and Tomasz Grzyb

Department of Rare Earths, Faculty of Chemistry, Adam Mickiewicz University, Grunwaldzka 6, 60 780 Poznan, Poland

Correspondence should be addressed to Stefan Lis, blis@amu.edu.pl

Received 4 May 2008; Revised 12 June 2008; Accepted 22 July 2008

Recommended by Mohamed Sabry Abdel-Mottaleb

The europium (III) complex of coumarin-3-carboxylic acid (C3CA) has been prepared and characterized on the basis of elemental analysis, IR, and emission (photoluminescence and electrochemiluminescence) spectroscopy. The synthesised complex having a formula $Eu(C3CA)_2(NO_3)(H_2O)_2$ was photophysically characterized in solution and in the solid state. Electrochemiluminescence, ECL, of the system containing the Eu(III)/C3CA complex was studied using an oxide-covered aluminium electrode. The goal of these studies was to show the possibility of the use of electrochemical excitation of the Eu(III) ion in aqueous solution for emission generation. The generated ECL emission was very weak, and therefore its measurements and spectral analysis were carried out with the use of cut-off filters method. The studies proved a predominate role of the ligand-to-metal energy transfer (LMET) in the generated ECL.

1. INTRODUCTION

Coumarins and their derivatives due to their biological activities, interesting photophysical and photochemical, and metal binding properties have been a subject of numerous investigations [1–12]. This group of compounds is known to have diverse applications in biology and medicine, due to their anticancer, antibiotic, anticoagulant, and anti-inflammatory [1, 2] properties. It has been found that the binding of a metal to the coumarin moiety retains or even enhances its biological activity [2, 3].

The coumarin-3-carboxylic acid (HC3CA) has previously been used as a ligand in complexation reactions with d-electron metal ions [5–7] and series of lanthanide cations (Dy(III), Er(III), Eu(III), Gd(III), Tb(III), and Sm(III)) [8–12]. The binding mode of coumarin-3-carboxylic acid in its La (III) complex has been investigated both experimentally and theoretically [8], the studies indicated strong ionic metal-ligand bonding in La-C3CA complex and insignificant donor acceptor interaction. A sensitized emission and an effective ligand to metal energy transfer in the samarium complex with 7-acetoxy coumarin 3-carboxylic acid [9], and efficient emission with long lifetimes although with low quantum yield values in the systems of Eu^{3+} and Tb^{3+} with crown ethers and iminodiacetic subunits attached to 3-aroylcoumarins in methanol [10] have been observed. The samarium (III) complex of coumarin-3-carboxylic acid proved to be the most active antiproliferative agent among the complexes [11]. Erbium (III) and europium (III) luminescent lanthanide complexes based on a coumarin showing effective energy transfer between the coumarin ligand and the lanthanide ions were designed and characterized by Kim et al. [12].

Coumarin derivatives have been a subject of electrochemiluminescence its mechanisms, induced by injection of hot electrons into aqueous electrolyte solution [13]. The studies showed that coumarins can be suitable candidates as ECL labels for bioaffinity assays or other analytical applications [13].

In our recent investigations, we have applied specific electrogenerated luminescence, ECL, which can be observed in Ln (III) (Ln = Tb, Dy and Eu) complexes with organic ligands containing aromatic rings forming stable complexes, in studying mechanisms of energy transfer [14, 15]. The ECL was obtained by producing highly oxidizing and reducing species as: hydrated electrons, hydroxyl, and sulfate radicals. These strong redox reactants efficiently excite the complexed Ln (III) ions by ligand to metal energy transfer.

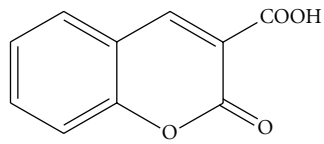

Figure 1: The structure of the ligand (coumarin-3-carboxylic acid, C3CA) studied.

The present work contains results of photoluminescence (PL) and electrochemiluminescence (ECL) studies concerning the complex of Eu (III) with the C3CA ligand. The goal of these studies was to show the possibility of ECL generation with the use of electroexcitation resulting in the ligand-to-metal energy transfer (LMET) in aqueous solution with participation of the Eu (III) ion.

2. EXPERIMENTAL

2.1. Synthesis of compounds

All chemicals were used of AR grade. The europium oxide Eu_2O_3 (Merck 99.99%, KGaA, Germany) was dissolved in a slight excess of HNO_3 or H_2SO_4. Obtained europium nitrate was dried and its appropriate amount dissolved in ethanol (spectroscopic grade) and europium sulphate was dried and dissolved in water (doubly distilled).

Synthesis of Eu(III) complex with coumarin-3-carboxylic acid.

The complex was synthesized by reaction of the Eu (III) salt, Eu $(NO_3)_3$, with coumarin-3-carboxylic acid (Merck, Figure 1) in a 1:2 metal to ligand molar ratio. The complex was prepared by adding ethanol solution of Eu $(NO_3)_3$ into ethanol solution of the ligand. The reaction mixture was stirred for 2 hours at room temperature. The precipitate was filtered, washed four times with ethanol, and dried in a desiccator to constant weight. The obtained Eu/C3CA complex was very limited soluble in water and ethanol ($<10^{-4}$ mol×dm^3).

2.2. Methods

The carbon, hydrogen, and nitrogen content of the compounds were determined by elemental analysis on an elemental analyser model VARIO ELIII. The IR spectra (4000–400 cm^{-1}) were obtained by means of an FTIR Bruker IFS 113v spectrophotometer (resolution 1 cm^{-1}), and the samples (~2 mg) were prepared in KBr. The water content was determined by luminescence lifetime measurement of the solid complex and was confirmed by TGA.

The luminescence lifetime measurements were carried out using the detection system consisting of a nitrogen laser (KB6211) and a tuneable dye laser [16].

The fluorescence spectra were recorded using a Perkin-Elmer MP3 and Aminco Bowman AB2 spectrofluorimeters.

ECL measurements were carried out using the experimental setup described recently [14]. Detection of the emitting light was possible through the use of a spectrometer Triax 180 (Horiba Jobin YVON GmbH, Germany) and a photon-counting head Hamamatsu H4730-01. The spectrometer allows for spectral recording in the range of 200–800 nm with a step of 0.15 nm. The spectrometer control is executed using a built-in digital controller. This controller enables one to operate the position of a diffraction grating and the width of the entrance and exit slits by controlling of the respective stepping motors. It also allows for sharp tuning of an emission wavelength and its change during measurements. The detection module of this system also allows the measurements of ultra weak emission (chemi- and electrochemiluminescence) spectra with a standard resolution of a moderate quality spectrofluorimeter. The recording module of this equipment consists of a photon-counting head Hamamatsu H4730-01 and a scalar cart attached to a PC. The ECL spectra, because of their weak emission, were recorded using the method of cut-off filters [17]. The ECL measurements were made in a double electrode system: Al/Al_2O_3 as the working electrode and a Pt-wire as the counter electrode, in aqueous solution. The aluminium plate electrode (5 mm × 25 mm × 1 mm) was covered with a natural oxide film (ca. 2 nm thick) and was made of an aluminium stripe (99.999%, Merck). The platinum anode was made of a Pt-wire (1.5 mm diameter). The ECL measurements were recorded with the use of the earlier described equipment [14].

3. RESULTS AND DISCUSSION

Characterization of the Eu (III) complex with coumarin-3-carboxylic acid.

The elemental analysis of the Eu/C3CA compound showed the following data: C = 39.07%; H = 2.14%; N = 2.16%, which are in a very good agreement with the calculated values, C = 38, 23%; H = 2.25%; N = 2.24%, for Eu $(C3CA)_2(NO_3)(H_2O)_2$, EuC20H14NO13. The formation of this Eu (III) complex was also confirmed by IR spectroscopy (see Figure 2) and luminescence of lifetime measurement.

3.1. FTIR spectra analysis

Detailed analysis of vibrational frequencies, the IR spectra of the HC3CA ligand and its Eu (III) complex, showed a very good agreement with the literature data [8] and gave evidence for bidentate coordination of C3CA ligand to Eu (III) ions through the carbonylic oxygen and the carboxylic oxygen. The bands in the 3580–3440 cm^{-1} range are observed in the Eu/C3CA complex IR spectrum due to the ν(OH) modes of the coordinated water molecules, while the broad band at ~3180 cm^{-1} in the IR spectrum of the ligand is assigned to the ν(OH) vibrational mode. This band is not observed in the spectra of the complexes, indicating that the deprotonated ligand form participates in the complexes.

The following bands, observed in the IR spectra of the Eu/C3CA complex, are assigned to the vibrational modes of the NO_3 group: 1260 cm^{-1} for $\nu(NO)_{bonded}$; 790 cm^{-1} and 725 cm^{-1} for δ(ONO). These bands indicate the presence of the nitrate group in the Eu/C3CA complex molecule. On the basis of the above detailed vibrational study, we

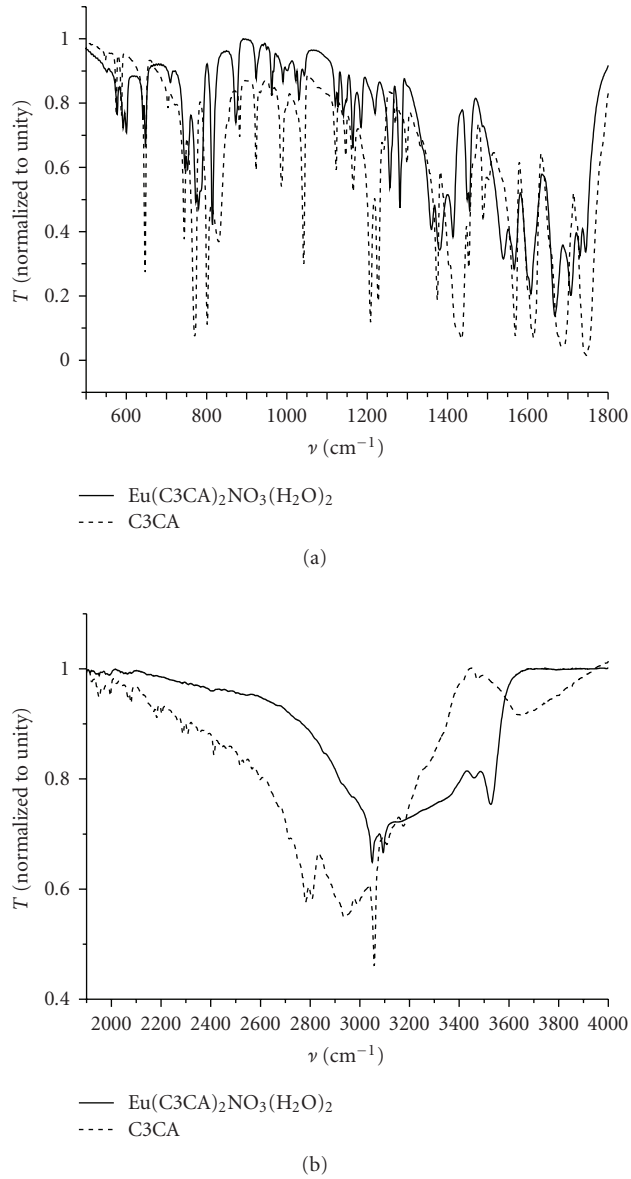

Figure 2: FTIR spectra of the C3CA ligand and $Eu(C3CA)_2(NO_3)(H_2O)_2$ complex recorded in the range of 500–1800 cm^{-1} (a) and 2000 and 4000 cm^{-1} (b).

can conclude that the metal-ligand bonding in Eu(III) complexes of coumarin-3-carboxylic acid appeared to be strongly ionic with very small donor-acceptor character, which is in agreement with the previously reported data for the Gd (III), Sm (III), and Dy (III) complexes with the C3CA ligand [11].

3.2. Luminescence and electrochemiluminescence studies

The Eu(III) luminescence lifetime measured as 411 ± 6 microseconds (average of 6 measurements) for the solid Eu/C3CA complex was used to calculate the number of water molecules, bond in the inner sphere of the Eu(III) ion, from the equation below [18]:

$$n_{H_2O} = 1.05 \times \tau^{-1} - 0.7. \quad (1)$$

The decay rate ($k = 1/\tau$, τ in milliseconds) of the $5D_0 \rightarrow 7F_j$ emission is proportional to the number of aqua ligands, coordinating the Eu(III) ion, due to the vibronic coupling of the $5D_0$ excited state with vibrational states of the high frequency OH oscillators of the aqua ligands. The calculated n_{H_2O} based on the value of τ (0.411 millisecond) measured for the Eu/C3CA complex indicates the presence of two water molecules in the Eu(III) inner coordination sphere. This hydration number ($n_{H_2O} \approx 2$) confirms the formula $Eu(C3CA)_2(NO_3)(H_2O)_2$ of the complex-formed Eu(III) with coumarin-3-carboxylic acid ligand. The studied complex $Eu(C3CA)_2(NO_3)(H_2O)_2$ is weakly soluble in water and alcohol ($< 10^{-4}$ mol/dm^3 in water).

The electrochemiluminescence of the europium(III) ion is the least known among the lanthanide series [13, 19]. Studies being done so far, considering europium chelates with the use of cathodic-generated ECL in aqueous solution, indicate two possible mechanisms of excitation of the Eu(III) ions: (1) in the process of energy transfer from electrochemically exited ligand the Eu(III) ion, or (2) in the electroreduction process of Eu^{3+} to Eu^{2+} following its oxidation with the use of a strong radical oxidizer generated as a result of decomposition of a coreactant (e.g., $S_2O_8^{2-}$). It has been previously shown that this oxidizing excitation process of Eu(II) occurs mainly in chemiluminescence systems [20, 21].

Luminescence excitation and emission spectra of the solid $Eu(C3CA)_2(NO_3)(H_2O)_2$ complex are presented in Figure 3. These photoluminescence studies show that the emission spectrum of the complex ($\lambda_{ex} = 370$ nm) exhibits typical narrow sharp emission bands corresponding to the characteristic $^5D_0 \rightarrow {}^7F_j$ transition of Eu(III) ion with the strongest emission band of the characteristic $^5D_0 \rightarrow {}^7F_2$ transition of the Eu(III) ion at 615 nm. This observation confirms the crucial role of the C3CA ligand in the transfer of the absorbed energy to the central ion of the complex.

In order to find optimal conditions for the ECL process, we studied the dependence of pH on the photoluminescence (PL) intensity of Eu(III) in the solution of Eu/C3CA complex. As shown in Figure 4, the PL intensity of Eu(III) in the complex solution considerably decreases above the value of pH > 5 with a simultaneous change of the intensity ratio of the bands $^5D_0 \rightarrow {}^7F_1$ and $^5D_0 \rightarrow {}^7F_2$. The observed changes, especially in the range of pH > 6, indicate ligand replacements in the inner coordination sphere of the Eu(III) ion, due to progressive hydrolysis occurring in the aqueous solution of the complex.

The ECL studies of systems containing the Eu(III) ion, both in the complex with C3CA ligand and uncomplexed (as $Eu_2(SO_4)_3$), were investigated.

The quantum yield of the ECL utraweak emission is assessed (as $\sim 5 \times 10^{-8}$, for $Eu_2(SO_4)_3$). The quantum yield of this utraweak emission is given as the ratio of the number of electric charges introduced into the system, resulting of ECL process, to the number of photons generated in the

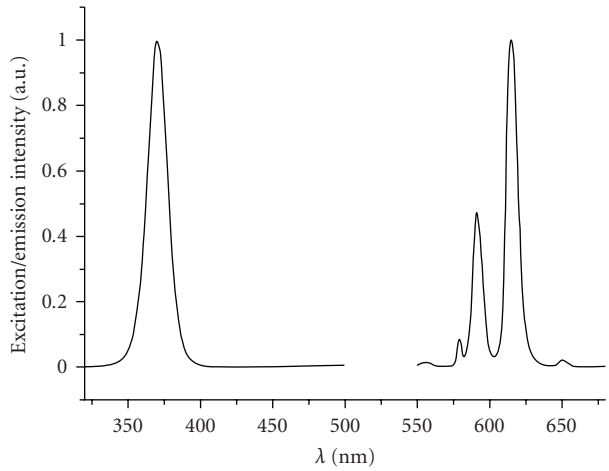

FIGURE 3: Normalized excitation and emission spectra of solid state of $Eu(C3CA)_2(NO_3)(H_2O)_2$ complex (5×10^{-5} mol×dm^{-3}), λ_{exc} = 365 nm.

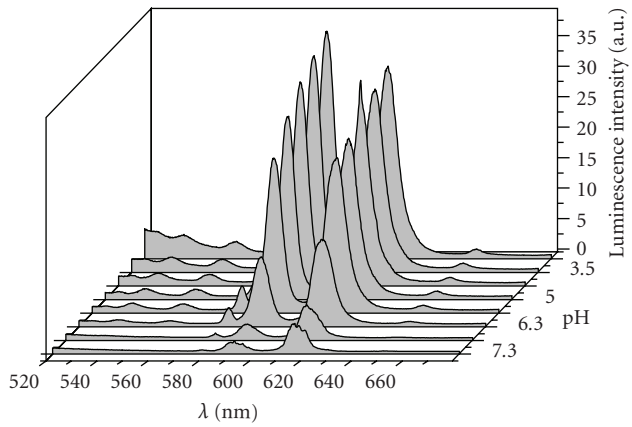

FIGURE 4: Photoluminescence spectrum of aqueous solution of (5×10^{-5} mol × dm^{-3}), λ_{exc} = 355 nm as a function of pH.

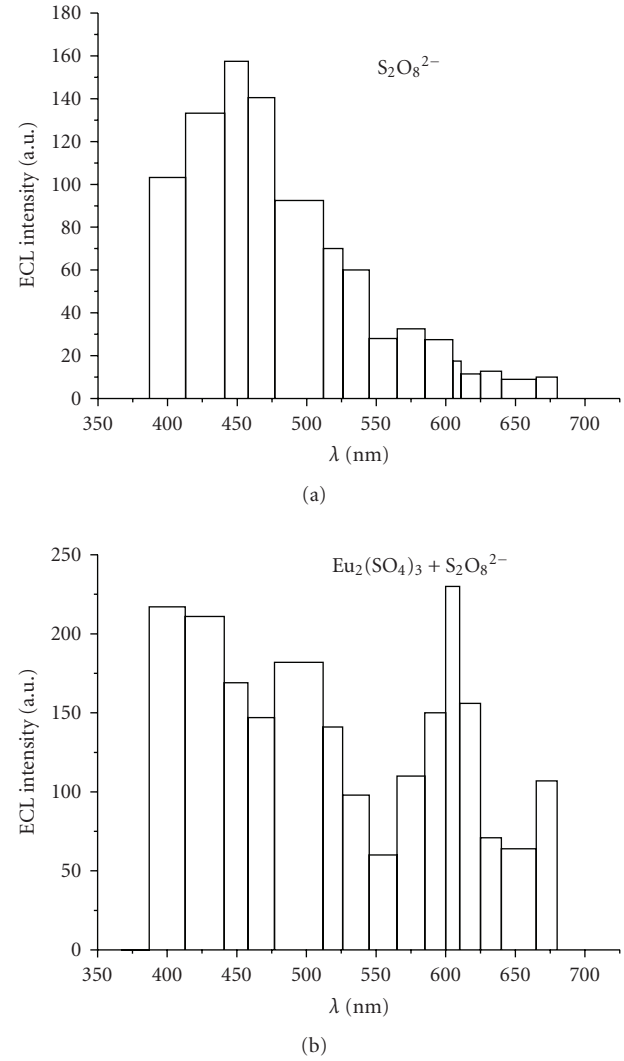

FIGURE 5: ECL spectra of system containing $K_2S_2O_8$ (2×10^{-2} mol × dm^{-3}). (a) and $K_2S_2O_8$ + $Eu_2(SO_4)_3$(5×10^{-2} mol × dm^{-3}). (b) Experimental conditions: Al/Al_2O_3 as a working electrode, Pt wire as a counter electrode, applied pulse voltage −50 V, frequency 40 Hz, pulse charge 30 μC, pH of solution 4.5.

process, in the same geometrical conditions. The excitation mechanism of the coumarin 3-carboxylic acid molecules via the ECL method involves emission of "hot" electrons from the electrode into the Eu(III) complex. This assists in the formation of active radicals on the electrode surface in solutions containing peroxodisulfate $S_2O_8^{2-}$ ions, as a coreactant, which can be easily decomposed in the following reaction:

$$e_{aq}^- + S_2O_8^{2-} \longrightarrow SO_4^{\bullet -} + SO_4^{2-}. \quad (2)$$

Under air-saturated solutions, and due to oxygen evolution at the counter electrode, oxyradicals and hydrogen peroxide can be formed, if hydrated electrons are produced at the working electrode [13]. The ECL spectra were recorded in aqueous solution containing: only the coreactant $K_2S_2O_8$ (Figure 5(a)), and $Eu_2(SO_4)_3$ (as uncomplexed Eu(III)) plus the coreactant $K_2S_2O_8$ (see Figure 5(b)). The ECL spectra and spectral analysis, due to a very weak ECL intensity observed in the studied system, were complete using the method of cut-off filters [17].

In the case of ECL, spectrum recorded for the coreactant ($K_2S_2O_8$) predominates a band with maximum at ~450 nm, corresponding to radiative relaxation from the ^{3}P excited state to the ^{1}S ground state of the active F-center in Al_2O_3 [22]. The ECL spectrum containing additionally the Eu(III) ions exhibits characteristic emission in the region around 600 nm. The ECL spectrum characteristic for Eu(III), generated in the system without an organic ligand, shows that Eu(III) can be excited by the reduction-oxidation process. The Eu(III) ions are easily reduced to Eu(II) (E_0 for Eu(III)/Eu(II) = −0.35 V) and then are oxidized by sulfate

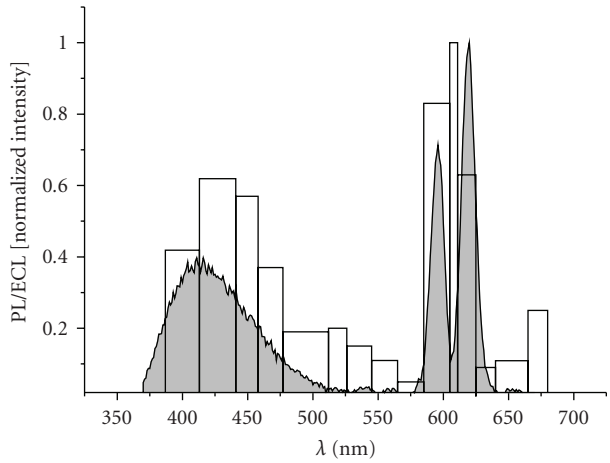

FIGURE 6: Photoluminescence (λ_{exc} = 355 nm) and electrochemiluminescence spectra of $Eu(C3CA)_2(NO_3)(H_2O)_2$ complex in aqueous solution. Experimental conditions: Al/Al_2O_3 as a working electrode, Pt wire as a counter electrode, applied pulse voltage −50 V, frequency 40 Hz, pulse charge 30 μC, pH of solution 4.5, concentration of the complex 5×10^{-5} mol × dm^{-3}.

and hydroxyl radicals present in solution leading to Eu(III) excitation

$$\begin{aligned} e^-_{aq} + Eu^{3+} &\longrightarrow Eu^{2+}, \\ Eu^{2+} + SO_4^{\bullet -} &\longrightarrow SO_4^{2-} + (Eu^{3+})^*, \\ (Eu^{3+})^* &\longrightarrow Eu^{3+} + h\nu\,(595, 615\,\text{nm}). \end{aligned} \tag{3}$$

The ECL spectrum of the $Eu(C3CA)_2(NO_3)(H_2O)_2$ complex shows, additionally to the characteristic emission of Eu(III), also a broad emission band in the range of 370–500 nm, corresponding to radiative transitions in the ligand molecule (see Figure 6). In the case of complexes containing phenyl group(s), the radical excitation of the aromatic ring can be accomplished on the way of redox reactions. Therefore, the studied system consisting of $Eu(C3CA)_2(NO_3)(H_2O)_2$ complex and $S_2O_8{}^{2-}$ the central ion can be potentially excited according to two ways:

(I) as a result of energy transfer from the excited state (singlet or triplet) of the ligand to the Eu(III) ion:

$$\begin{aligned} Eu(III)\text{-}L + SO_4^{\bullet -} &\longrightarrow Eu(III)\text{-}L_{OX} + SO_4^{2-}, \\ Eu(III)\text{-}L_{OX} + e^-_{aq} &\longrightarrow Eu\text{-}L^*, \\ Eu\text{-}L^* \longrightarrow Eu^*\text{-}L &\longrightarrow Eu\text{-}L + h\nu\,(595, 615\,\text{nm}), \end{aligned} \tag{4}$$

(II) on the way of reduction and oxidation of the complexed Eu(III):

$$\begin{aligned} e^-_{aq} + Eu(III)\text{-}L &\longrightarrow Eu(III)\text{-}L_{RED}, \\ Eu(III)\text{-}L_{RED} &\longrightarrow Eu(II)\text{-}L, \\ Eu(II)\text{-}L + SO_4^{\bullet -} &\longrightarrow Eu(III)^*\text{-}L + SO_4^{2-}, \\ Eu^*\text{-}L &\longrightarrow Eu\text{-}L + h\nu\,(595, 615\,\text{nm}). \end{aligned} \tag{5}$$

The ECL intensity (λ = 615 nm) observed in the system containing the complex studied is over one order of magnitude higher than in that with the uncomplexed Eu(III) ions. This observation proves the predominate role of the ligand to metal energy transfer on the total efficiency of the electrochemiluminescence.

4. CONCLUSIONS

Eu(III) forms with the ligand of coumarin-3-carboxylic acid (C3CA) the complex of composition $Eu(C3CA)_2(NO_3)(H_2O)_2$. This complex is one of a few examples in which ECL characteristic for the Eu(III) ion can be observed [13, 15, 19]. The mechanism of excitation of the central ion can be completed as a result of energy transfer from the excited state of the ligand to the Eu(III) ion (LMET), which is predominant, and on the way of reduction and oxidation reactions of the complexed Eu(III) ion. The observed ECL in this system is utraweak, due to a very limited solubility of C3CA, and therefore can be detected with the use of a single photon counting method. Coumarin derivatives having important biological activities, of better than C3CA solubility in aqueous solution should exhibit more intensive ECL. This ECL generated with the participation of the LMET, can be potentially used in analytical applications of biologically active agents, for example, in pharmaceutical preparations, as we recently have shown using the chemically generated emission for the determination of tetracycline derivatives [23].

REFERENCES

[1] G. Kokotos, V. Theodorou, C. Tzougraki, D. Deforce, and E. Van den Eeckhout, "Synthesis and in vitro cytotoxicity of aminocoumarin platinum(II) complexes," *Bioorganic & Medicinal Chemistry Letters*, vol. 7, no. 17, pp. 2165–2168, 1997.

[2] A. Karaliota, O. Kretsi, and C. Tzougraki, "Synthesis and characterization of a binuclear coumarin-3-carboxylate copper(II) complex," *Journal of Inorganic Biochemistry*, vol. 84, no. 1-2, pp. 33–37, 2001.

[3] I. Kostova, I. Manolov, I. Nicolova, S. Konstantinov, and M. Karaivanova, "New lanthanide complexes of 4-methyl-7-hydroxycoumarin and their pharmacological activity," *European Journal of Medicinal Chemistry*, vol. 36, no. 4, pp. 339–347, 2001.

[4] T. Wolff and H. Görner, "Photodimerization of coumarin revisited: effects of solvent polarity on the triplet reactivity and product pattern," *Physical Chemistry Chemical Physics*, vol. 6, no. 2, pp. 368–376, 2004.

[5] S. W. Ng and V. G. Kumar Das, "Tetramethylammonium bis(coumarin-3-carboxylato)triphenylstannate ethanol solvate," *Acta Crystallographica C*, vol. 53, no. 8, pp. 1034–1036, 1997.

[6] S. W. Ng, "Coordination complexes of triphenyltin coumarin-3-carboxylate with *O*-donor ligands: (coumarin-3-carboxylato)triphenyltin-*L* (*L* = ethanol, diphenylcyclopropenone and quinoline *N*-oxide) and bis[(coumarin-3-carboxylato)triphenyltin]-*L* (*L* = triphenylphosphine oxide and triphenylarsine oxide)," *Acta Crystallographica C*, vol. 55, no. 4, pp. 523–531, 1999.

[7] A. L. El-Ansary and M. M. Omar, "Formation constants and molecular structure of vanadium (IV), cobalt (II), nickel (II), copper (II) and zinc (II) chelates with 8-(arilazo)-7-hydroxy-4-methylcoumarin dyes," *Egyptian Journal of Chemistry*, vol. 31, pp. 511–520, 1988.

[8] Tz. Mihaylov, N. Trendafilova, I. Kostova, I. Georgieva, and G. Bauer, "DFT modeling and spectroscopic study of metal-ligand bonding in La(III) complex of coumarin-3-carboxylic acid," *Chemical Physics*, vol. 327, no. 2-3, pp. 209–219, 2006.

[9] E. Bakier and M. S. A. Abdel-Mottaleb, "Factors affecting light energy transfer in some samarium complexes," *International Journal of Photoenergy*, vol. 7, no. 1, pp. 51–58, 2005.

[10] M.-T. Alonso, E. Brunet, O. Juanes, and J.-C. Rodríguez-Ubis, "Synthesis and photochemical properties of new coumarin-derived ionophores and their alkaline-earth and lanthanide complexes," *Journal of Photochemistry and Photobiology A*, vol. 147, no. 2, pp. 113–125, 2002.

[11] I. Kostova, G. Momekov, and P. Stancheva, "New samarium(III), gadolinium(III), and dysprosium(III) complexes of coumarin-3-carboxylic acid as antiproliferative agents," *Metal-Based Drugs*, vol. 2007, Article ID 15925, 8 pages, 2007.

[12] S.-G. Roh, N. S. Baek, K.-S. Hong, and H. K. Kim, "Synthesis and photophysical properties of luminescent lanthanide complexes based on coumarin-3-carboxylle acid for advanced photonic applications," *Bulletin of the Korean Chemical Society*, vol. 25, no. 3, pp. 343–344, 2004.

[13] M. Helin, Q. Jiang, H. Ketamo, et al., "Electrochemiluminescence of coumarin derivatives induced by injection of hot electrons into aqueous electrolyte solution," *Electrochimica Acta*, vol. 51, no. 4, pp. 725–730, 2005.

[14] K. Staninski, S. Lis, and D. Komar, "Electrochemiluminescence on Dy(III) and Tb(III)-doped Al/Al_2O_3 surface electrode," *Electrochemistry Communications*, vol. 8, no. 7, pp. 1071–1074, 2006.

[15] K. Staninski and S. Lis, "Electrogenerated luminescence of chosen lanthanide complexes at stationary oxide-covered aluminium electrode," *Journal of Alloys and Compounds*, vol. 451, no. 1-2, pp. 81–83, 2008.

[16] S. Lis, Z. Hnatejko, and Z. Stryla, "Device for measurements of selective luminescence excitation spectra of europium (III) based on a nitrogen and dye laser system," *Optica Applicata*, vol. 31, no. 3, pp. 643–648, 2001.

[17] M. Kaczmarek and S. Lis, "Luminescence characterisation of the reaction system histidine-$KBrO_3$-Tb(III)-H_2SO_4," *Journal of Fluorescence*, vol. 16, no. 6, pp. 825–830, 2006.

[18] P. P. Barthelemy and G. R. Choppin, "Luminescence study of complexation of europium and dicarboxylic acids," *Inorganic Chemistry*, vol. 28, no. 17, pp. 3354–3357, 1989.

[19] M. M. Richter and A. J. Bard, "Electrogenerated chemiluminescence. 58. Ligand-sensitized electrogenerated chemiluminescence in europium labels," *Analytical Chemistry*, vol. 68, no. 15, pp. 2641–2650, 1996.

[20] K. Staninski, M. Kaczmarek, and M. Elbanowski, "Kinetic and spectral aspects in chemiluminescence system Eu(III)/HCO_3^-/H_2O_2," *Journal of Alloys and Compounds*, vol. 380, no. 1-2, pp. 177–180, 2004.

[21] M. Elbanowski, B. Mąkowska, K. Staninski, and M. Kaczmarek, "Chemiluminescence of systems containing lanthanide ions," *Journal of Photochemistry and Photobiology A*, vol. 130, no. 2-3, pp. 75–81, 2000.

[22] A. Hakanen, E. Laine, M. Latva, T. Ala-Kleme, and K. Haapakka, "Quenching of cathodic electrogenerated F-center luminescence of aluminium oxide by lanthanide cations at the electrode/electrolyte interface," *Journal of Alloys and Compounds*, vol. 275–277, pp. 476–479, 1998.

[23] M. Kaczmarek, A. Idzikowska, and S. Lis, "Europium-sensitized chemiluminescence of system tetracycline-H_2O_2-Fe(II)/(III) and its application to the determination of tetracycline," to appear in *Journal of Fluorescence*.